Contribution à la compréhension de l'action des agents réducteurs de retrait dans les matériaux cimentaires : étude expérimentale et modélisation

Hafsa Rahoui

UNIVERSITÉ PARIS-EST

ÉCOLE DOCTORALE SCIENCE INGÉNIERIE ET ENVIRONNEMENT

THÈSE

présentée pour l'obtention du diplôme de

DOCTEUR

DE

L'UNIVERSITÉ PARIS-EST

Spécialité: *Génie Civil*

par

Hafsa RAHOUI

Sujet de la thèse :

Contribution to understanding the action of shrinkage reducing admixtures in cementitious materials: experiments and modeling

Thèse soutenue le 17/12/2018 devant le jury composé de :

Rapporteurs :	**Prof. Pietro LURA**
	Prof. Jason WEISS
Examinateurs :	**Dr. Patrick DANGLA**
	Prof. Ippei MARUYAMA
	Dr. Martin MOSQUET
	Dr. Matthieu VANDAMME
Directeur de thèse :	**Prof. Jean-Michel PEREIRA**

Acknowledgments

This work wouldn't have seen light without the support of LafargeHolcim. I am grateful for the financial and scientific support, which allowed me to go through this journey.

I would like to thank the members of the jury Prof. Pietro Lura, Prof. Jason W. Weiss and Dr. Patrick Dangla. I am humbled by their review of the work. I sincerely thank you for our enriching exchange and constructive comments. My thoughts go for late Dr. Ellis Gartner, who was at the launching of the work and his enthusiastic contribution.

I would like to express my sincere gratitude to my supervisors: Matthieu Vandamme, Ippei Maruyama, Jean-Michel Pereira and Martin Mosquet. From the poromechanics class during the master degree to our everyday interaction during the PhD, Matthieu's enthusiasm, availability and guidance were essential. The three years were stimulating and full of learning thanks to his rigor and precision. His significant counseling in poromechanical modeling helped the model see the light. I would like to thank Maruyama sensei, Ippei, who made my integration in the laboratory at Nagoya University effortless. Our discussions were motivating as he welcomed my 'ambitious' ideas, and was excited to new findings genuinely. I came to love experimental work, although laborious, through my several stays at the laboratory, and came to appreciate its peculiarities when it works and when it does not. His expertise in SRAs and shrinkage of cementitious materials helped guide the work in the right direction. My gratitude also goes to Jean-Michel, who directed this work, who was available through our multiple PhD meetings, providing a vision extrapolating from cementitious materials to soils. His kindness was always there when needed, during the finishing line and throughout the entire work. His patience during the writing and review of the work, and his pertinent questions and comments benefited greatly this study. My sincere appreciation also goes for Martin, his large expertise in admixtures helped guide the work optimally. His support during my visits to the LafargeHolcim Centre de Recherche at Lyon made it possible to conduct a significant part

Abstract

Cement-based materials are complex multiscale porous materials that are sensitive, among other things, to the surrounding relative humidity. The changes of the relative humidity induce a macroscopic deformation of the materials. This phenomenon is referred to as drying shrinkage. Drying shrinkage of cement-based materials may lead to their cracking. Not only do these cracks impact the aesthetic aspect, they are also a source of vulnerability of structures, as the ingress of harmful substances may be enhanced, hence leading to a potential weakening of the structural performance. The addition of shrinkage reducing admixtures (SRAs) is a way to mitigate of drying shrinkage of cement-based materials, which allows to reduce the risk of cracking. Although SRAs have proven beneficial in reducing drying shrinkage, their mechanisms of action are still debated.

In this thesis, we aim at providing a better understanding of the mechanisms of action of SRAs, by combining a comprehensive experimental campaign with poromechanical modeling of drying shrinkage of cement pastes. We study the impact of one SRA (hexylene glycol) on the first drying shrinkage of thin cement paste samples and on their subsequent re-humidification, which allows investigation of the irreversibility of drying shrinkage. The performance of the SRA in terms of reduction of drying shrinkage and its dependence on the alkali content of the cement pastes and on the range of relative humidity are investigated. Two methods of drying are employed: long-term drying of samples of 3 mm thickness, and short-term drying of samples of 0.5 mm thickness. Drying shrinkage isotherms of cement pastes containing SRA show little or no irreversibility. The reduction of drying shrinkage due to the SRA is highest in the relative humidity range [33%-75%] and at low alkali content.

These measurements are complemented with microstructural characterization: the phase assemblage is assessed based on X-ray diffraction (XRD) and thermogravimetric analysis (TGA) and the pore structure is analyzed with mercury intrusion porosimetry (MIP), nitrogen sorption isotherms and

water sorption isotherms. The impact of the SRA on the microstructure before the long-term drying is examined, as well as the evolution of pore structure after long-term drying. The SRA is found to alter the pore structure of cement pastes before drying, as well as how the pore structure evolves upon drying.

The experimental measurements served as a database for the modeling of how water content and drying shrinkage evolve with relative humidity. The relationship between the amount of the various types of water present in the pore system and relative humidity is modeled based on the knowledge of the pore structure. If the pore structure is characterized by water sorption measurements, we propose a model that resolves the pore water into two types, namely water adsorbed on solid surfaces and water in capillary pores. In contrast, if the pore structure is characterized by nitrogen sorption measurements, we propose a model that resolves water into three types, namely water in the micropores, water adsorbed on solid surfaces, and water in capillary pores.

To model drying shrinkage, two approaches are presented. A first approach consists in developing a phenomenological model enabling the prediction of drying shrinkage for a cement paste that contains given contents of alkali and SRA and at a given relative humidity. The second approach consists in a poromechanical model of adsorption-induced strains. The strain is modeled as resulting from capillary forces (impacted by capillary water), Bangham-type surface forces (impacted by water adsorbed on solid surfaces), and, if water is resolved into three types, the effect of the variation of the water content in the micropores.

To the light of the experimental and modeling results, the mechanisms of action of SRA on drying shrinkage are discussed. SRA is found to act on drying shrinkage by reducing the strain induced by capillary effects and the range of relative humidity over which they occur, as well as by reducing the Bangham-type strains due to adsorption on solid surfaces.

Keywords: drying shrinkage, SRA, alkali, length change isotherms, mass change isotherms, irreversibility, poromechanics.

Résumé

Les matériaux cimentaires sont des matériaux multiéchelles sensibles aux conditions environnantes et notamment à l'humidité relative ambiante. Les variations de l'humidité relative induisent une déformation macroscopique du matériau. Ce phénomène, dit retrait de séchage, peut induire la fissuration des matériaux cimentaires. Non seulement ces fissures nuisent à l'aspect esthétique, mais elles peuvent aussi fragiliser les structures en facilitant leur attaque par des substances agressives. Les agents réducteurs de retrait (ARRs) ont prouvé leur efficacité pour la réduction du retrait et de la fissuration des matériaux cimentaires en résultant. Cependant, leurs mécanismes d'action sont encore le sujet de nombreuses questions. Dans ce travail, nous visons à apporter une meilleure compréhension des mécanismes d'action des ARRs, en combinant un programme expérimental exhaustif et une modélisation poromécanique du retrait de séchage des pâtes de ciment. Nous étudions l'impact d'un ARR (hexylène glycol) sur le premier retrait de séchage et sur la re-humidification des pâtes de ciments de faible épaisseur, ce qui nous permet d'étudier l'irréversibilité du retrait de séchage. La performance des ARRs en termes de réduction du retrait de séchage, sa dépendance à la teneur en alcalin et à la gamme d'humidité relative est analysée. Deux méthodes de séchage sont employées : séchage long-terme d'échantillons de 3 mm d'épaisseur, et séchage court-terme d'échantillons de 0.5 mm d'épaisseur. L'irréversibilité des isothermes de retrait de séchage des pâtes de ciment se voit considérablement réduite en présence des ARRs. La réduction de retrait de séchage induite par l'ARR est maximale dans la gamme d'humidité relative entre 33% et 75% et pour une faible teneur en alcalins. Nous étudions également l'impact des ARRs sur la microstructure. L'assemblage de phase est déterminé en combinant la diffraction aux rayons X (DRX) avec l'analyse thermogravimétrique (ATG). La structure poreuse est examinée par la porosimétrie mercure, les isothermes de sorption à l'azote, et les isothermes de sorption à l'eau. L'impact de l'ARR sur la microstructure avant le séchage

long-terme est analysé, ainsi que l'évolution de la structure poreuse après le séchage long-terme. L'ARR modifie la structure poreuse avant séchage, ainsi que l'évolution de cette structure poreuse au cours du séchage long-terme. Les résultats de cette caractérisation expérimentale constituent une base de données pour la modélisation de la teneur en eau et du retrait de séchage en fonction de l'humidité relative. Nous modélisons la teneur en eau des pâtes de ciment en fonction de l'humidité relative, basé sur la connaissance de la structure poreuse. Si la structure poreuse est évaluée par des isothermes de sorption à l'eau, nous proposons un modèle distinguant l'eau en deux contributions : de l'eau adsorbée sur les surfaces solides et de l'eau condensée dans les pores capillaires. Si la structure poreuse est évaluée par des isothermes à l'azote, nous proposons un modèle qui distingue l'eau en trois contributions : de l'eau adsorbée dans les micropores, de l'eau adsorbée sur les surfaces solides, et de l'eau condensée dans les pores capillaires. Nous élaborons ensuite deux approches pour modéliser le retrait de séchage. Une première approche consiste à développer un modèle phénoménologique permettant de prédire le retrait de séchage d'une pâte de ciment à une teneur en alcalins et en SRA donnée, et séchée à une humidité relative donnée. La deuxième approche consiste à élaborer un modèle poromécanique des déformations induites par adsorption. Nous considérons la déformation des pâtes de ciment comme le résultat de forces capillaires (impacté par l'eau capillaire), de forces de surfaces de type Bangham (impacté par l'eau adsorbée sur les surfaces solides), et dans le cas où l'eau est répartie en trois contributions, de variations de la teneur d'eau dans les micropores. A la lumière des résultats expérimentaux et de modélisation, nous identifions les mécanismes d'action des ARRs sur le retrait de séchage. L'ARR réduit notamment le retrait de séchage par deux biais : 1) en réduisant le retrait induit par les effets capillaires et la gamme d'humidité relative sur laquelle ces effets sont présents, et 2) en réduisant les déformations de type Bangham induites par adsorption sur les surfaces solides.

Mots clefs : retrait de séchage, agent réducteur de retrait ARR, alcalins, isotherme de déformation, isotherme de variation de masse, irréversibilité, poromécanique.

Contents

CONTENTS

List of Figures

15

19

21

23

27

List of Tables

Chapter 1

Introduction

1.1 Context

Concrete is the most consumed material on Earth, with a volume of 10 km^3 per year (Flatt et al., 2012). This material has been around since the Roman empire, although the raw materials of which the hydraulic binder of this era were different from the modern Portland cement as we know it today (Hewlett, 2003). The reasons making concrete the most widely used construction material are the availability of the raw materials and their low cost. Portland cement is made by the grinding and calcination of mix of around 80% of limestone with around 20% of clays. Concrete cost can vary between \$60 to \$100 per cubic meter (Mehta and Monteiro, 2001). Our understanding and targeted uses of concrete for housing and infrastructure have evolved through the years (Aïtcin, 2000). With the increasing appetite to build challenging structures, concrete today is required to conform to higher standards of durability and structural performance, while meeting environmental requirements (Aïtcin, 2000) and reducing the carbon dioxide emissions of the cement industry (evaluated to 5–8% of all human made emissions (Sharp et al., 2010)).

Drying shrinkage of concrete occurs due to the changes of surrounding relative humidity. When the relative humidity decreases, the material dries and consequently shrinks. This drying shrinkage, when restrained by the

presence of aggregate or reinforcement, can lead to cracks (Damgaard Jensen and Chatterji, 1996). Not only do these cracks degrade the aesthetic aspect of the structure, they also impact its structural performance (Sasano et al., 2018) and represent a source of vulnerability for the structure. Consequently, strategies to minimize the drying shrinkage can prove beneficial for the overall enhancement of the performance of structures.

Facing increasing demands to make sustainable and durable concrete (Van Damme, 2018), concrete is made of a mix of not only water, cement, sand and aggregates, but also includes chemical admixtures. Chemical admixtures are used to tune the performance of concrete depending on targeted properties (e.g., workability, setting time).

Among the chemical admixtures, one finds shrinkage reducing admixtures (SRAs) which come in handy to reduce drying shrinkage. These admixtures were patented in the early 80s in Japan (Goto et al., 1985) to reduce drying shrinkage of cement-based materials. SRAs have proven efficient in reducing drying shrinkage of cement-based materials, and were employed in infrastructures (e.g., Nair et al. (2016) for bridges). The SRAs are typically at a liquid state at ambient temperature, and are usually added to the concrete mix by replacing the equivalent amount of water by SRA. These SRAs are usually composed of one or a mixture of non-ionic surfactants, and possibly other components (e.g., dispersing agents, accelerators or air entrainers) (Eberhardt, 2010). The non-ionic surfactants may be composed of monoalcohols, glycols, alkylether oxyalkylene glycols or polymeric surfactants (Eberhardt, 2010).

1.2 Research significance

Although SRAs are efficient in reducing drying shrinkage, their mechanisms of action are not fully understood. Industrial suppliers (e.g., Sika (2012)) and part of the research community (e.g., Ai and Young (1997)) state that these admixtures act on drying shrinkage by reducing the surface tension of pore solution of cement-based materials, which would translate into a reduction of capillary effects and thus into a reduction of the total drying

shrinkage. However, this mechanism alone does not justify the need for high dosage (industrial suppliers recommend 1% to 2% in mass of cement) to reach optimal reduction of drying shrinkage. Further, the secondary effects of these admixtures on other properties of cement-based materials are not comprehensively stated. In fact SRAs are reported to impact the mechanical properties (e.g., Shah et al. (1992); Maltese et al. (2005)), the degree of hydration (e.g., Bentz (2006); Sant et al. (2006)), the microstructure of cement pastes (e.g., Saliba et al. (2011); Eberhardt (2010)), and the transport properties of the cement-based materials (Bentz et al., 2001; Sant et al., 2010; Pour-ghaz et al., 2010). Facing this incomplete image on the effects of SRAs, the high recommended dosage, their cost and availability, and the potential issues related to the low saturation vapor pressure/low flamming point of some SRAs (Eberhardt, 2010) and the potential impact on the air voids, their practical use in construction is refrained.

Providing a clear understanding of the mechanisms of action of SRAs requires understanding the physical origins of drying shrinkage of cement-based materials. Although several workers studied drying shrinkage, no consensus is drawn with regards to the physical processes that intervene and dominate when the material is dried at various ranges of relative humidity. Among others, Kovler and Zhutovsky (2006), Scherer (2015) and Ye and Radlińska (2016) presented an overview on drying shrinkage. Drying shrinkage is usually attributed to capillary pressure, adsorption-induced stress and disjoining pressure effects. Furthermore, the microstructure of cement paste evolves through drying, during which the surface area and the pore volume undergo dramatic changes (e.g., Parrott et al. (1980); Maruyama et al. (2014)). In our attempt to better understand drying shrinkage, we are confronted to various challenges: the material presents a wide pore size distribution and a complex morphology, several potential physical origins for drying shrinkage are proposed, and the potential interaction of the chemical admixtures with the cement hydrates is poorly understood.

The industry aims at minimizing the amount of SRA it adds to the mix, while guaranteeing its efficiency in reducing drying shrinkage. To help this optimization, a model of how the SRA reduces shrinkage would be useful.

However, the drying shrinkage of cement pastes is known to depend on the clinker composition in general (e.g., Maruyama (2010)), and on its content of alkali in particular (e.g., Ye and Radlińska (2017)). Consequently, a good model should take into account the content of alkali of the mix.

1.3 Research objectives

In this work we aim at identifying the mechanisms of action of SRA on drying shrinkage of cement pastes and how its efficiency is impacted by the alkali content, through a thorough experimental campaign and subsequent modeling.

Experimentally, we aim at:

- Evaluating the impact of SRA and alkali on drying of cement pastes in terms of length change and mass change, by means of long-term drying and short-term drying.

- Assessing the irreversibility of drying shrinkage of cement pastes at various contents of SRA and of alkali by means of length change measurements, upon drying and subsequent re-humidification.

- Investigating the impact of SRA and alkali on the hydration of cement pastes.

- Evaluating the impact of SRA and alkali on the pore structure of cement pastes before drying.

- Examining the evolution of pore structure of cement pastes with various contents in SRA and in alkali upon a long drying.

- Investigation of the potential interaction of SRA with cement hydrates.

The results of this comprehensive experimental campaign on cement pastes at various SRA and alkali content will serve as a database for the modeling of both water content and length change of cement pastes upon variations of relative humidity. For what concerns this modeling, we aim at:

- Providing a model usable by the cement and concrete industry to predict how much SRA needs to be added to reach a given shrinkage reduction, depending on the environmental conditions (i.e., relative humidity).

- Providing a model that separates water content of cement paste into various types (water in capillary pores, water adsorbed on surfaces and water in micropores when necessary), where each type contributes to the strain of cement paste.

- Through a combined discussion of model and experimental results, discuss the mechanism (or mechanisms) through which the SRA reduces drying shrinkage.

1.4 Layout of the thesis

The manuscript is organized into a succession of 8 chapters, as follows:

- Chapter 2 is a review of the state of the art on drying shrinkage of cement-based materials and on shrinkage reducing admixtures. In this chapter, we also introduce the concepts that will be used in the following chapters, with regards to the methods for the experimental campaign and to the modeling of drying shrinkage of cement pastes.

- Chapter 3 presents the results of the experimental campaign dedicated to the measurement of drying isotherms of cement pastes at various contents in SRA and in alkali. The drying of cement pastes is conducted based on two methods: long drying and short drying. The impact of SRA on drying shrinkage is examined, and its ability to reduce drying shrinkage is investigated depending on the considered mix design (i.e., content of SRA and content of alkali) and on the range of relative humidity.

- Chapter 4 is devoted to the characterization of microstructure of the cement pastes already considered, before the long drying and after the

long drying. The impact of SRA on the microstructure (both chemically and physically) is examined, as well as its impact on the evolution of the pore structure through drying.

- Chapter 5 describes the characterization of the interactions between SRA and cement paste by means of leaching experiments and pore solution extractions.

- Chapter 6 deals with a model for predicting the adsorption isotherm (i.e., the relation between water content and relative humidity), based on the knowledge of the pore structure. The water is separated into 3 types of water (i.e., water in micropores, water adsorbed on surfaces and water in capillary pores) or 2 types of water (i.e., water adsorbed on surfaces and water in capillary pores), depending on how the microstructure is characterized (i.e., by water or nitrogen adsorption). Identification and quantification of the various types of water will be used as an input to the drying shrinkage model in the subsequent chapter.

- Chapter 7 focuses on a modeling of drying of cement pastes that contain various contents in alkali and in SRA. Both a phenomenological and a physics-based model are proposed. The physics-based model is derived to the light of how water was modeled in the previous chapter: strains induced by water in micropores, water adsorbed on solid surfaces, and water in capillary pores are all taken into account.

- Chapter 8 summarizes the conclusions of the work and presents perspectives for future research.

Chapter 2

State of the art

We present in this chapter an overview of cement-based materials. We introduce first the microstructure of cement pastes. The hydration of cement and the resulting pore structure are presented, to the light of the commonly adopted models for the microstructure of C-S-H, the main hydrate of cement. Then the experimental techniques to characterize the pore structure that will be employed in this work are introduced. A phenomenological review of drying shrinkage is presented. The physical origins of drying shrinkage are detailed, along with the major phenomenological features of drying shrinkage of cement-based materials, among which the irreversibility of the first drying shrinkage. The modeling approaches for drying shrinkage are then reviewed. Finally, we review the proposed mechanisms of action of shrinkage reducing admixtures as well as the experimental observations regarding their impact on the properties of cement-based materials.

2.1 Microstructure of cement paste

2.1.1 Hydration of cement

Clinker is a hydraulic binder, which reacts with water through a process of dissolution-precipitation to form a cement paste. The cement paste represents the "glue" binding aggregates to make concrete. Portland cement is

made of four major phases[1]: alite (impure tricalcium silicate C_3S), belite (impure dicalcium silicate C_2S), aluminate (C_3A) and ferrite (C_4AF). An ordinary Portland clinker contains mass fractions in the range of 45 to 60%, 15 to 30%, 6 to 12% and 6 to 8%, for C_3S, C_2S, C_3A and C_4AF, respectively (Mehta and Monteiro, 2001). Other minor phases can also be present such as gypsum ($C\overline{S}H_2$) that regulates the hydration kinetics. Hydration of silicate phases (C_3S and C_2S) produces C-S-H and calcium hydroxide CH (also referred to as portlandite). The hydration reactions of silicate phases occur as follows:

$$C_3S + (3 - x + y)H \rightarrow C_xSH_y + (3 - x)CH \qquad (2.1)$$

$$C_2S + (2 - x + y)H \rightarrow C_xSH_y + (2 - x)CH \qquad (2.2)$$
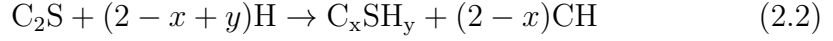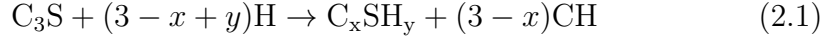
The parameters x and y refer to C/S and H/S molar ratio of C-S-H, because C-S-H stoichiometry is poorly defined and depends strongly, among others, on the hydration conditions (pressure, temperature, water-to-cement mass ratio w/c) and drying history. C-S-H gel occupies 50 to 60% in volume of the solids of hydrated cement paste and portlandite occupies 20 to 25% in volume of the solids of hydrated cement paste (Mehta and Monteiro, 2001).

The hydration of aluminate phases depends on the presence of sulfates. In the absence of sulfates, C_3A reacts as follows (Gartner et al., 2001):

$$2C_3A + 27H \rightarrow C_4AH_{19} + C_2AH_8 \rightarrow 2C_3AH_6 \qquad (2.3)$$

The aluminate first reacts in presence of gypsum to produce ettringite (AFt) $C_6A\overline{S}_3H_{32}$. Once sulfate is depleted, the reaction continues to form monosulfoaluminate (AFm) $C_4A\overline{S}H_{12}$, following (Gartner et al., 2001):

$$C_3A + 3C\overline{S}H_2 + 26H \rightarrow C_6A\overline{S}_3H_{32} \qquad (2.4)$$

$$2C_3A + C_6A\overline{S}_3H_{32} + 4H \rightarrow 3C_4A\overline{S}H_{12} \qquad (2.5)$$

---
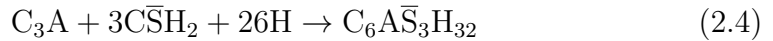
[1]Cement chemistry nomenclature is adopted: C stands for CaO, S stands for SiO_2, A for Al_2O_3, F for Fe_2O_3, H for H_2O and $\overline{S}$ for SO_3
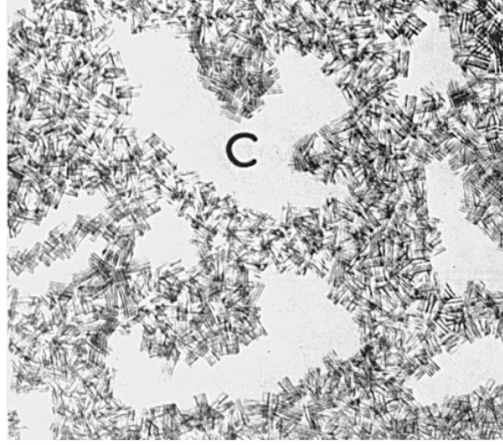
Figure 2.1: An illustration of C-S-H gel with capillary pores (marked by C) (after Powers, 1958).

The hydration reaction of C_4AF is similar to that of C_3A (Gartner et al., 2001). In the absence of gypsum, C_2AH_8 and $C_4(A,F)H_{19}$ form, and produce $C_3(A,F)H_6$. In the presence of gypsum, the hydration of C_4AF produces AFt with iron substitution, that converts into AFm form.

2.1.2 Cement paste: a multiscale porous material

In this section we review some of the models of the microstructure of C-S-H widely reported in the literature.

Powers (1958) established the first model of microstructure of the C-S-H gel. His work proposed that cement paste is composed of a cement gel, and spaces between those particles. The cement gel is made of fibrous particles with straight edges. Although highly disordered, the C-S-H was approximated by tobermorite crystal. The spaces between the gel particles are identified as capillary pores, and the interstices inside them (i.e., inside the gel particles) are identified as gel pores. An illustration of the proposed model can be found in figure 2.1.

Feldman and Sereda (1968) proposed a model of hydrated cement pastes based on length change and sorption measurements, and supported by mechanical characterization. The structure of C-S-H is considered to be made

A – Interparticle Bonds
X – Interlayer Hydrate Water
B – Tobermorite Sheets
O – Physically Adsorbed Water
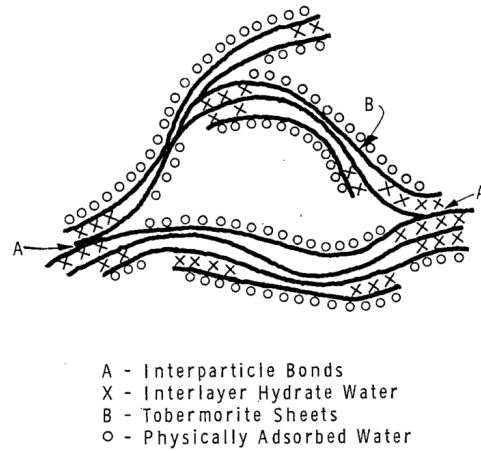
Figure 2.2: Proposed structure of C-S-H (after Feldman and Sereda, 1968).

of a layered and highly disordered structure. Water is present between the layers as structural water and chemical water. The removal of this water is considered to be at the origin of the irreversibility of drying shrinkage (detailed in section 2.3.3) and of the sorption isotherms, and explains the changes in mechanical properties observed with relative humidity (RH). An illustration of the proposed model can be found in figure 2.2.

Later, Jennings (2000) proposed a model, referred to as CMI, with the aim of providing not only a qualitative description, but also a quantitative one, reconciling the disparities of values of specific surface area (SSA) and density of C-S-H reported in the literature. The model is based on a basic building block that assembles into a globule. The globules aggregate into a loose packing forming the low density C-S-H (LD C-S-H) with a porosity of 28% and into a dense packing forming the high density C-S-H (HD C-S-H) with a porosity of 13%. These porosities are related to the spaces between the globules but do not include the pore space inside the gobules. Tennis and Jennings (2000) quantify the volume fractions of LD C-S-H and HD C-S-H versus the w/c ratio and the degree of hydration.

Jennings (2008) later proposed a refinement CMII of his CMI model (Jennings, 2000), where focus was on smallest gel pores, and attempted to link the microstructure to the behavior observed at macroscopic level in drying experiments. The model lies on the continuity of the model CMI, and sheds
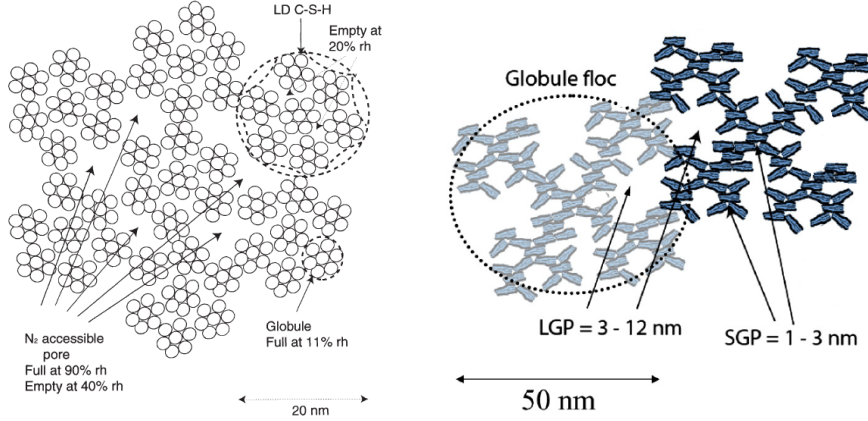
Figure 2.3: Structure of LD C-S-H (left) phase based on model CMI (after Jennings, 2000), and C-S-H schematic (right) based on model CMII (after Jennings, 2008).

light on LD C-S-H. C-S-H is considered of granular or particulate nature. C-S-H particles are viewed as platelets with layered structure, and in which porosity is identified at various scales. In the C-S-H globule (particle), water can be present at two locations, in interlayer space and in intraglobular pores (IGP) of size lower than 1 nm. The spaces between globules, which are part of gel water space, are interglobular pores. The gel pore space is further differentiated into small gel pores (SGP) of size between 1 nm and 3 nm and large gel pores (LGP) of size between 3 nm and 12 nm, as illustrated in figure 2.3. The gel pore space consists of both intraglobular and interglobular pores.

Recently, Gartner et al. (2017) attempted to elucidate the structure of C-S-H, as some questions remained with the previous models. A major question that the authors address is why the C-S-H incorporates a large amount of gel water. They attempt to establish a model of the structure of C-S-H from a chemical point of view. The C-S-H is seen here as made initially from single sheets with adsorbed calcium cations, the sheets stacking upon each other with incorporated calcium cations and their hydration shells agglomerate, forming the C-S-H gel.

47
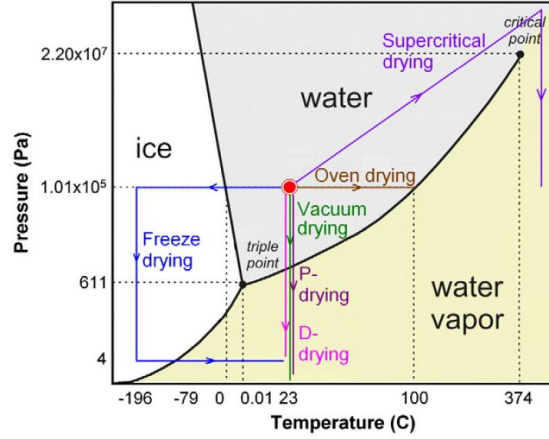
Figure 2.4: Drying techniques of cement-based materials as illustrated on phase diagram of water (after Zhang and Scherer, 2011). The red point represents the starting point.

2.2 Characterization of pore structure

In this section we present the experimental techniques for the characterization of pore structure of cement pastes, that are used in this work, namely mercury intrusion porosimetry, gas sorption measurements, and the pre-drying techniques required prior to these measurements. For each technique, the principle of the measurement is introduced as well as the information that can be retrieved from it.

2.2.1 Impact of drying on pore structure characterization

The most commonly used techniques for pore structure characterization (eg., MIP, gas sorption) of cement pastes require drying of the sample prior to measurements. Drying conducted prior to measurements alters the pore structure. A multitude of techniques are used for drying cementitious materials, such as oven drying, vacuum drying, freeze drying, solvent exchange and recently also supercritical drying (Zhang and Scherer, 2017) as illustrated in figure 2.4.

Regardless of the diversity of drying techniques, there is no general agree-

ment on the technique that best preserves the pore structure of the cement paste. Concluding over this issue requires a reference technique that indeed preserves pore structure, whereas most studies adopt a comparative approach. Drying even affects the structure of anhydrous clinker: Mantellato et al. (2015) found that the nitrogen specific surface area of anhydrous clinker varies significantly with the type of degassing (vacuum or under N_2 flow, temperature, pressure and duration), as these drying techniques dehydrate gypsum in their case, leading to crack formation.

Gallé (2001) found that freeze drying is less damaging compared to oven drying (at 105 °C and 60 °C), and to vacuum drying, as a finer porosity is identified in MIP results for freeze dried samples. Collier et al. (2008) also investigated the impact of freeze drying, oven drying, vacuum drying and solvent exchange using acetone, and found that the studied drying methods were comparable, and that pore structure appears to be better preserved by acetone quenching. Zhang and Scherer (2011) reviewed and conducted a comparative study of various drying techniques (freeze drying, solvent exchange using various solvents), and found that solvent exchange using isopropanol preserved the pore structure best, this method was previously recommended by several authors (Feldman and Beaudoin, 1991; Konecny and Naqvi, 1993; Snoeck et al., 2014). Moreover, Muller (2014) investigated vacuum drying, oven drying at 50 °C and 110 °C, freeze drying and solvent exchange. Muller (2014) also confirmed that solvent exchange using isopropanol preserved the pore structure best, comparing measured pore volume to capillary pore volume obtained by 1H-NMR measurements (note that 1H-NMR does not require a pre-drying, since water is used to probe the pore space of cement paste).

In the following, we introduce techniques for characterization of pore structure that will be used later in this study.

2.2.2 Mercury intrusion porosimetry

Mercury intrusion porosimetry (MIP) is based on the intrusion of mercury in the porous medium (here cement paste). MIP consists in placing a sam-
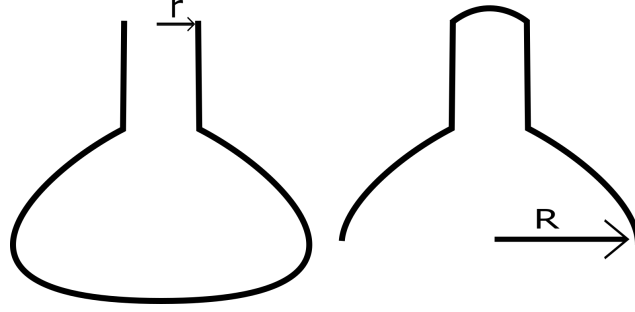
Figure 2.5: An illustration of a constricted pore of radius R and of an entry radius r (left) and a non-constricted pore (right).

ple in a cell under vacuum, then introducing the mercury into the cell, and increasing the pressure of mercury gradually. The volume of intruded mercury is recorded at each step of pressure. The required pressures to intrude mercury are related to the pore entry diameter by the Washburn equation (Washburn, 1921):

$$d = \frac{4\gamma \cos\theta}{P} \tag{2.6}$$

where: d is the pore diameter, P the applied pressure, γ the surface tension of mercury taken here as γ=0.485 N/m, θ the contact angle of mercury taken as 130°.

Note that MIP measurements (when dealing with intrusion of mercury) enable to assess a pore entry size instead of a pore size (Diamond, 2000). In fact, when intruding mercury into a constricted pore (connected to the outside by a small entry of radius r) as shown on figure 2.5-left, the pressure required to intrude the pore is the pressure needed to intrude the entry of the pore. The corresponding pore volume in this case is the pore volume of the large pore and the corresponding diameter is that of the small entry, since intruded mercury will access both small entry and large pore. The pore volume in this case corresponds to the pores of an entry size of radius r. In the case of figure 2.5-right, the pressure required to intrude the pore is that required to intrude large pore, and the obtained pore volume corresponds well to the volume of large pore only. This phenomenon is related to the ink-bottle effect and will be further detailed in the next section.

2.2.3   Gas sorption measurements

Principle of measurement

The pore structure can also be analyzed by gas adsorption techniques. When a solid (denoted adsorbent) is exposed to a gas (denoted adsorbate), the gas molecules are attracted to the surface and adsorbed on it. During a sorption measurement, the adsorbed volume is measured in terms of the pressure of the gas to which the solid is exposed to. The sample is dried prior to the measurement, and further degassed when placed in the device for measurements. With increasing gas pressure, the adsorption branch is measured, and with decreasing pressures, the desorption branch is measured.

A measured sorption isotherm consists of the adsorbed volume on the adsorption branch and desorption branch as a function of p/p_0 (i.e., the relative pressure of the gas to its saturation vapor pressure p_0), as shown in figure 2.6 illustrating typical nitrogen or water sorption isotherms of a plain cement paste respectively. Two methods are possible to acquire the sorption isotherm (both will be used in this work): volumetric method and gravimetric method. The volumetric method is based on the exposition of the porous material to a finite volume of gas, and monitoring the pressure within the cell where the porous material is placed; the adsorbed volume can then be inferred. This is particularly of good use when the adsorbate boiling point is low, as is the case for nitrogen whose boiling temperature is 77 K (Aligizaki, 2006). However the measurement near the saturation vapor pressure of the adsorbate is less accurate, compared to the gravimetric method, because controlling the pressure near the saturation vapor pressure can be challenging, and because the errors accumulate through the measurements of successive points of the isotherm. The gravimetric method is based on the monitoring of the mass of the sample (degassed prior to measurement or not) at the various relative pressures to which the sample is exposed.

Figure 2.6-top shows a typical nitrogen sorption isotherm. The adsorption branch is below the desorption branch and a hysteresis is observed at relative pressures larger than 0.42. This hysteresis is due to the ink-bottle effect (that will be detailed in the next section).
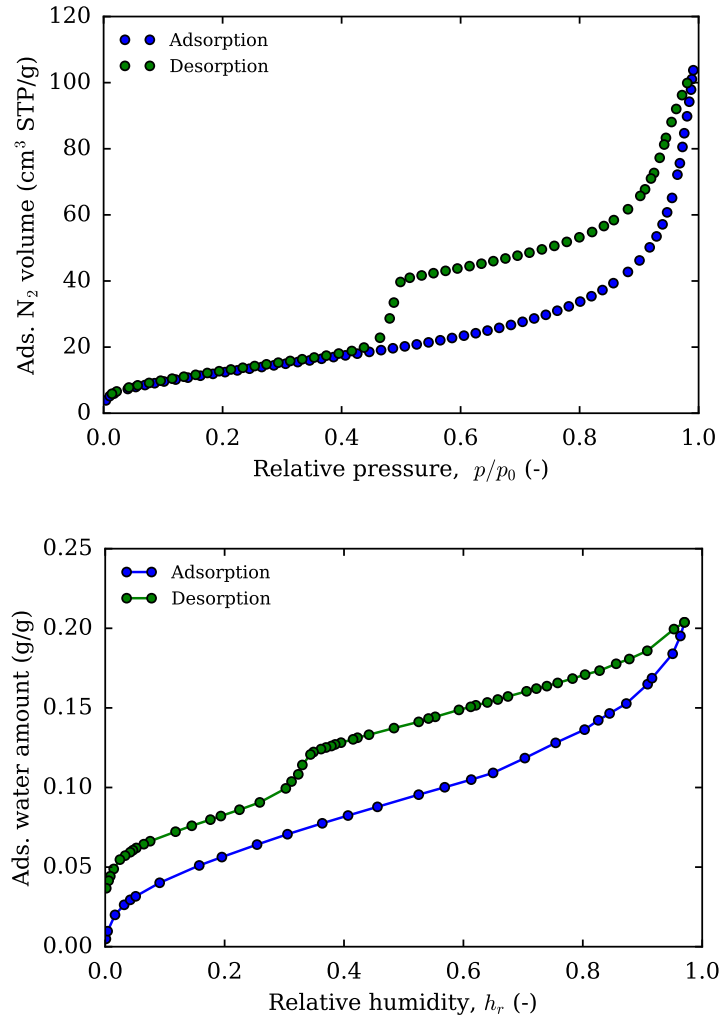
Figure 2.6: A typical nitrogen sorption isotherm (top) for a plain cement paste of this study and a typical water sorption isotherm (bottom).

$$p_d\,(r) < p_{cav}\,(R_c) \qquad p_{cav}\,(R_c) < p_d\,(r) < p_e\,(R_c)$$
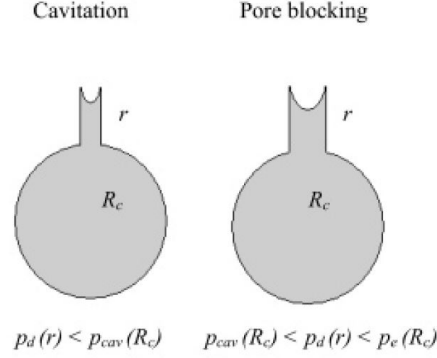
Figure 2.7: A constricted pore where the entry size is small sufficiently for cavitation to occur on drying (on the left): on drying the pore pressure $p_d(\mathrm{r})$ is greater than the characteristic cavitation pressure $p_{cav}(R_c)$, and a constricted pore where a pore blocking is observed without cavitation (on the right), on drying the pore pressure $p_d(\mathrm{r})$ is lower than the characteristic cavitation pressure $p_{cav}(R_c)$ and greater than the pressure of equilibrium of the liquid-air interface $p_e(R_c)$ (after Ravikovitch and Neimark, 2002). Note that the absolute value of pressures is discussed here.

Furthermore, at relative pressure of 0.42, a jump is observed on the desorption branch due to cavitation (as proven for porous materials at comparable relative pressures (Ravikovitch and Neimark, 2002; Thommes et al., 2006; Rasmussen et al., 2010)). When a pore is constricted, i.e., connected to the outside by a small entry, and the entry radius is smaller than a critical threshold as illustrated in figure 2.7, the large negative pressures caused on drying of the constricted pore can lead to the cavitation of the saturating liquid. In fact, cavitation occurs when the liquid phase is under significant tensile stress, at which the liquid reaches a metastable state, and a phase change occurs: liquid to vapor. Nucleation of gaseous bubbles occurs and the condensate is emptied. The cavitation depends on the properties of the considered adsorbate (which are nitrogen and water for the sorption isotherms we consider in this study). The cavitation translates on the isotherm into a marked jump on the desorption branch: for nitrogen desorption this corresponds to a relative pressure of 0.42.

Figure 2.6-bottom shows an example of a water sorption isotherm measured on a plain cement paste prepared in this study. Similarly to nitrogen
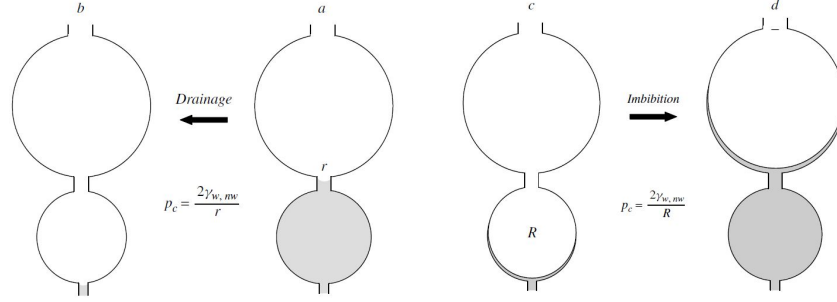
Figure 2.8: Drainage and imbibition of ink-bottle pores (after Coussy, 2010).

sorption isotherm, the adsorption branch of the water sorption isotherm also falls below the desorption branch. Furthermore, a hysteresis is observed over the entire range of relative humidity. Jennings (2008) states in his model that removal of water within the globules of C-S-H occurs such that water is removed at low RH (at 11%) but re-enters only at high RH (higher than 40%) causing the hysteresis observed in water sorption isotherms (the low range hysteresis).

Similarly to nitrogen sorption isotherms, a jump is observed at a relative pressure of 0.35, due to the cavitation of water in the pores of cement paste (Maruyama et al., 2018b; Pinson et al., 2018).

Ink-bottle effect

Let us consider a porous medium composed of constricted pores as illustrated in figure 2.8. When this system is intruded by a non-wetting phase, e.g., when this system is being dried, intrusion is controlled by the size of the entry of the pore. However, when the wetting phase is intruding the pore space, the intrusion is controlled by the pore size. When conducting a nitrogen desorption or water desorption measurement, the non-wetting phase is vapor nitrogen (respectively water vapor) and the wetting phase is liquid nitrogen (respectively liquid water). The desorption is controlled by the pore entry size, while the adsorption branch is controlled by the pore size, this effect being known as the ink-bottle effect.

Measurement of specific surface area with BET method

To evaluate the specific surface area, we use the Brunauer-Emmett-Teller (BET) method. Brunauer et al. (1938) assumed that adsorption occurs through a multilayer process. They also assumed that the adsorption sites are identical on an energetic level, that there is no adsorbate-adsorbate interaction, and that there is no variation of properties of adsorbed layers after the first one. The BET theory helps relating the monomolecular layer capacity to the sorption isotherm following:

$$\frac{p}{V(p_0 - p)} = \frac{1}{V_m C} + \frac{(C-1)p}{V_m C p_0} \tag{2.7}$$

where V is the adsorbed volume at pressure p (m^3/g), V_m is the volume of the adsorbed monomolecular layer (m^3/g), C is the BET constant (unitless), p is the pressure (N/m^2), and p_0 is the saturation vapor pressure of the adsorbate.

Plotting $p/(V(p_0 - p))$ vs. p/p_0 yields a linear plot at the low range of relative pressures [0.05-0.35]. Computing the slope and intercept enables determining the monomolecular layer capacity V_m and the BET constant C.

The specific surface area is computed following:

$$S_{ssa} = \frac{V_m N_A A_m}{V_M} \tag{2.8}$$

where S_{ssa} is the specific surface area (m^2/g), V_m is the volume of the adsorbed monomolecular layer (m^3/g), N_A is the Avogadro constant, A_m is the average area occupied by one molecule of adsorbate (m^2/molecule), and V_M is the molar volume (m^3/mol).

For water and nitrogen the surface area per molecule is taken as A_m=0.162 nm^2 for nitrogen (Aligizaki, 2006), and A_m= 0.114 nm^2 for water (Mikhail and Selim, 1966).

Note that the BET constant C provides an insight into the solid-adsorbate interaction, since it is related to the net heat of adsorption $q_1 - q_L$ following:

$$C = \exp\left(\frac{q_1 - q_L}{RT}\right) \tag{2.9}$$
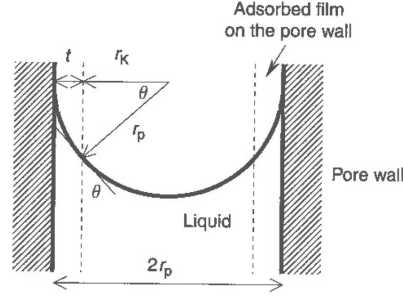
Figure 2.9: Pore of radius r_p in which are present an adsorbed film layer of thickness t and capillary meniscus of radius r_k (after Aligizaki, 2006).

where q_1 is the energy of adsorption of the first layer and q_L is the heat of liquefaction of the adsorbate.

Measurement of pore size distribution with BJH method

Barrett-Joyner-Halenda (BJH) method allows to characterize the pore (or pore entry) size distribution when adsorption branch (or desorption branch) is analyzed (Barrett et al., 1951). They consider that pore fluid is present under two forms: adsorbed on the solid surfaces and liquid in capillary pores, as illustrated in figure 2.9. The pore size is corrected for the adsorbed film layer following:

$$r_k = r_p - t \tag{2.10}$$

where r_k is the Kelvin radius, t is the thickness of adsorbed film layer and r_p is the pore size, as illustrated in figure 2.9.

Kelvin radius r_k can be assessed as follows:

$$r_k = \frac{-2M_v\gamma\cos(\theta)}{\rho_w RT \ln(p/p_0)} \tag{2.11}$$

where M_v is the molar mass of liquid adsorbate, γ is the surface tension of the liquid adsorbate, θ is the contact angle taken as null (i.e., the pore solution is considered perfectly wetting), ρ_w is the mass density of liquid adsorbate, R is the ideal gas constant, T is the absolute temperature, and p/p_0 is the pressure of the gas relative to its saturation vapor pressure p_0.

To determine the thickness t in equation 2.11, a t-curve is implemented. The t-curve is the average thickness of the adsorbed layer on a plane surface as a function of relative pressure. The t-curve is a characteristic curve of the adsorbate, and considered not dependent on the nature of solid surfaces. Several researchers measured this characteristic curve of the considered adsorbate on various non-porous materials. When the adsorbate is nitrogen, t-curves of de Boer (Lippens et al., 1964) measured on aluminum hydroxides and oxides and of Cranston and Inkley (Cranston et al., 1957) for several non-porous materials are commonly used. Empirical equations are also proposed for the t-curve of nitrogen, among which Harkins and Jura t-curve (Harkins and Jura, 1944) following:

$$t = \sqrt{\frac{A_{HJ}}{B_{HJ} - \log(p/p_0)}} \tag{2.12}$$

with $A_{HJ} = 13.99$ Å^2 and $B_{HJ} = 0.034$, thickness t here is expressed in Å.

When the adsorbate is water, various t-curves can be found in the literature, among which the t-curve proposed in Hagymassy et al. (1969) where the authors propose t-curves depending on the parameter C of the heat of adsorption as evaluated by the BET theory. Results of Hagymassy et al. (1969) are based on measurements conducted on zirconium silicate, rutile, silica and silica gel, quartz barium sulfate, among others. Badmann et al. (1981) proposed also a t-curve based on measurements on anhydrous silica phases C$_2$S and C$_3$S, following:

$$t = K_1 - K_2 \ln(-\ln(h_r)) \tag{2.13}$$

where $K_1 = 0.385$ nm and $K_2 = 0.189$ nm, and h_r is the relative humidity.

Wu et al. (2014) report that the choice of the t-curve impacts the obtained pore size distribution analyzed by BJH on water sorption isotherms: the smaller the considered thickness of the t-curve, the more the pore size distribution is shifted towards smaller pores.

To analyze the pore structure based on the BJH method, the porosity of

the porous material is discretized into n intervals of radii r_i, where:

$$r_i = r_k + t \tag{2.14}$$

Let us consider two families of pores of mean radius r_i and r_{i+1}. On the desorption branch, when the relative pressure decreases from p_i to p_{i-1}, the capillary condensate of the family of pores of mean radius r_i is emptied and a layer of adsorbed liquid remains on the pore walls. When the relative pressure is further decreased, the family of pores of radius r_{i-1} is emptied of its capillary condensate, and a layer of adsorbed layer remains, similarly to the first step. Furthermore, the first remaining adsorbed layer becomes thinner as the relative pressure decreases.

Each family of pores is described by a characteristic size $\bar{r}_i$ such that:

$$\begin{aligned} \bar{r}_1 &= (r_1 + r_0)/2 \\ \bar{r}_n &= (r_n + r_{n-1})/2 \end{aligned} \tag{2.15}$$

Assuming that the pores are cylindrical, the volume v_1 of the first family of pores can be computed (Rouquerol et al., 2003), following:

$$v_1 = (\bar{r}_1/(\bar{r}_1 - t_1))^2 (\delta v_{l,1}) \tag{2.16}$$

where $\delta v_{l,1}$ is the desorbed volume inferred from the sorption isotherm at the first step.

The volume of subsequent family of pores of smaller radii can be also computed following:

$$v_n = \left(\frac{\bar{r}_n}{\bar{r}_n - t_n} \right)^2 \left[\delta v_{l,n} - \delta t_n \sum_{i=1}^{n-1} \delta a_i \left(1 - \frac{t_n}{\bar{r}_i} \right) \right] \tag{2.17}$$

where:

$$\delta a_i = \frac{2\delta v_i}{\bar{r}_i} \tag{2.18}$$

In analyzing sorption isotherms, family of pores of size lower than about 35 nm are considered; this size limit corresponds for example in case on

nitrogen sorption isotherm to a relative pressure of 0.97. This choice is motivated by the fact that at high relative pressures, an insignificant variation of pressure translates into a large variation of the pore size. Being limited by the precision of the relative pressure, the pore size distribution may not be reliable above this limit.

Characterization of pore structure with t-plot method

The pore structure can also be analyzed by transforming the sorption isotherm into a t-plot, without having to assume a pore geometry in contrast to the BJH method, which assumes pore geometry (namely, that pores are cylindrical) to infer quantitative information on the pore structure (namely the pore size distribution). The t-plot consists of a plot of the adsorbed volume in terms of thickness of adsorbed layer, as shown in figure 2.10. The adsorbed volume is measured experimentally as a function of the relative pressure, and the thickness of adsorbed layer based on the t-curve reported in literature. The t-curve depends on the considered adsorbate and expresses a thickness of the adsorbed layer in terms of the relative pressure for a non-porous material. In this work we use the t-plot to derive qualitative description of the pore structure, without necessarily assuming a pore geometry. The t-plot may indicate some features of the pore structure such as the presence of micropores filling and of capillary condensation, as detailed in figure 2.10.

Discrepancies revealed by adsorption of water and nitrogen

Adsorption measurements on cement-based materials give rise to significant differences of values of specific surface area (SSA) and pore volume when the adsorbate is nitrogen or water vapor. SSA based on water adsorption is consistently greater than the SSA measured by nitrogen adsorption as illustrated in figure 2.11. Moreover, SSA assessed by nitrogen increases with w/c ratio, while that measured with water is found unvarying (Mikhail et al., 1964). It should be noted however that Litvan (1976) found, by means of nitrogen adsorption, surface areas as large as 250 m^2/g for cement pastes. Litvan (1976) argued that the preparation method can give rise to large

59
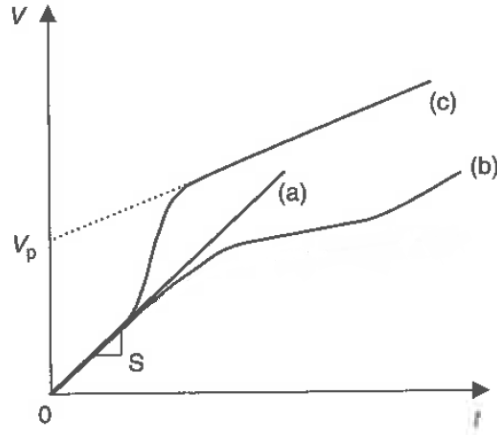
Figure 2.10: Possible types of t-plots: a) for a material presenting multilayer adsorption with no vapor condensation, b) for a material presenting micropores filling as the line diverges below the straight line, c) for a mesoporous material with capillary condensation (after Aligizaki, 2006).

discrepancies of the obtained SSA based on nitrogen adsorption.

The fact that the measured SSA depends on the adsorbate can be linked to several causes (Aligizaki, 2006). The smaller size of water molecules (3 Å) compared to nitrogen molecules (3.5 Å) may lead to inaccessibility of nitrogen to some pore space in cement paste that is accessible to water molecules. Odler et al. (1972) and Odler (2003) also suspect that nitrogen adsorption measurements need years to reach equilibrium. Since large pores may be connected to the outside by small entries, the filling of the large pores through the small entries occurs by activated diffusion, referred to by activated entry process. This process presents an energy barrier which depends on the temperature, and assuming this barrier similar for both adsorbates, the water adsorption takes two to three weeks to reach equilibrium, while nitrogen adsorption would need longer durations (given that the nitrogen boiling temperature is low compared to water). Further, the dipolar nature of water makes it strongly attracted to the ionic surfaces of the hydrates, while nitrogen is less attracted to these surfaces because of its quadrupolar nature. Feldman and Sereda (1968) indicated that measuring specific surface area with nitrogen allows measurements of "true" surface area, since water can
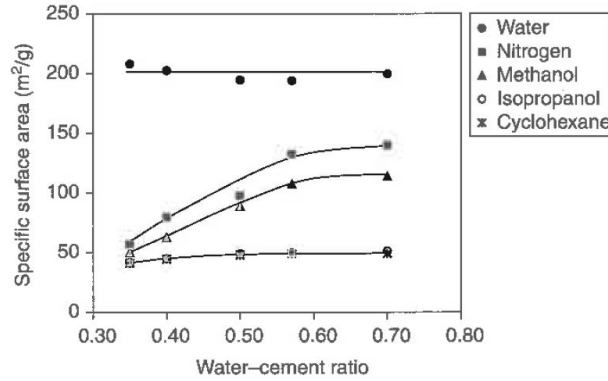
Figure 2.11: Specific surface area of hardened cement pastes at various water to cement ratios measured with different adsorbates (after Aligizaki, 2006 according to (Mikhail and Selim, 1966)).

enter C-S-H interlayer while nitrogen cannot. However Odler (2003) finds that SSA measured by water adsorption is closer to the total surface area of cement-based materials, compared to SSA measured by nitrogen adsorption.

2.3 Drying shrinkage of cementitious materials

In this section, we present an introduction of the various shrinkage types to which cement-based materials are subjected. Then we focus on drying shrinkage, the mechanisms proposed to explain it, and some of its major features. Finally, the modeling approaches to predict drying shrinkage are presented.

2.3.1 Overview

Through their service life, cement-based materials are subject to various forms of shrinkage originating from various origins (Kovler and Zhutovsky, 2006). In what follows we present the major types of shrinkage that cement-based materials experience during their life service.

- Chemical shrinkage is a shrinkage that the cement paste undergoes due

to the decrease in volume of the hydrates with regards to the volume
of clinker and water. It is also referred to as Le Chatelier contraction.

- Plastic shrinkage: this type of shrinkage occurs when cement or con-
  crete are fresh, i.e., in their plastic phase. It is caused by the evapora-
  tion of moisture from the surface.

- Thermal Shrinkage: caused by the temperature gradients due to both
  the environmental conditions and cement hydration. In fact, the hy-
  dration of cement is an exothermic reaction leading to a rise in tem-
  perature. As the hydration rate decreases, the concrete temperature
  decreases back and the hardened cement undergoes a thermal shrink-
  age.

- Autogenous shrinkage: this type of shrinkage occurs when the 3 fol-
  lowing conditions are met: sealed (to prevent exchange of moisture
  with the surroundings), unrestrained, and isothermal. It is due to the
  self-desiccation of the material: the water in the cement paste is con-
  sumed by hydration. Hence, the capillary pores are no more saturated,
  which leads to a decrease of relative humidity. This phenomenon is
  more pronounced at w/c $<$ 0.44 (Taylor, 1990) than at larger w/c.
  The autogenous shrinkage of a concrete at w/c below 0.40 can reach
  up to about $3{\times}10^{-4}$ while for a concrete at w/c $>$0.45 the autogenous
  shrinkage is usually lower than 10^{-4} (Acker and Ulm, 2001).

- Drying shrinkage: it occurs under unsealed conditions, thus moisture
  transfer with the surroundings is allowed. This shrinkage type occurs
  during considerably long periods (months and years depending on the
  geometry and the environmental conditions). The drying shrinkage
  of concrete may vary between about 2 and 6 $\times10^{-4}$ (Acker and Ulm,
  2001). The physical processes at the origin of drying shrinkage are
  detailed in section 2.3.2.

- Carbonation shrinkage: the carbon dioxide present in the atmosphere
  reacts with the cement hydrates. The carbonation concerns not only

portlandite (with which the reaction results in the formation of calcium carbonate), but also C-S-H. This chemical reaction leads to a reorganization of the microstructure, causing an increase in mass of samples and a decrease in porosity, but paradoxically, a decrease in total volume. The physical origin of this type of shrinkage is still debated, and is sometimes attributed to the carbonation of portlandite (Kovler and Zhutovsky (2006) citing Powers (1962)), and sometimes to the carbonation of C-S-H leading to its decalcification and dehydration (Swenson and Sereda, 1968).

In this work, we focus on drying shrinkage of cement pastes. In the next section we provide a literature review of the physical origin of drying shrinkage.

2.3.2 Mechanisms of drying shrinkage

The physical origin of drying shrinkage in cement paste was long argued, but no consensus was made over which mechanism is dominant in what range of RH. The difficulty in reaching a consensus is due to the complexity of the material, of its interactions with water, and of how these interactions translate into a strain. In what follows, we summarize the most commonly accepted mechanisms of drying shrinkage, which are:

- Capillary forces;

- Surface effects;

- Disjoining pressure;

- Movement of interlayer water.

Capillary forces

When a porous material is dried, i.e., subjected to a relative humidity lower than 100%, a capillary meniscus develops in the pores of the material, allowing the liquid phase and gaseous phase to be in equilibrium at RH lower than

100%. The pore solution is under tensile stresses, and pulls the pore wall closer, causing the shrinkage of the material. The capillary pressure p_{cap} is related to the imposed relative humidity through Kelvin equation, following:

$$p_{cap} = -\frac{RT}{\overline{V}_L} \ln h_r \tag{2.19}$$

where R is the ideal gas constant, T is the absolute temperature, $\overline{V}_L$ is the molar volume of water and h_r the relative humidity.

The capillary pressure in a cylindrical pore of radius r partially filled with a pure liquid of surface tension γ can be assessed following Laplace equation:

$$p_{cap} = p_{nW} - p_W = \frac{2\gamma cos\theta}{r} \tag{2.20}$$

where p_{nW} and p_W are the pressure of the non-wetting phase and of the wetting phase, respectively. The non-wetting phase here is the gaseous phase in the pore space, and its pressure p_{nW} is equal to the atmospheric pressure in the case of drying under ambient conditions. The wetting phase is the liquid.

In the presence of solutes in the pore solution, equation 2.19 is modified as follows to account for the effect of the solutes:

$$p_{cap} = -\frac{RT}{\overline{V}_L} \ln \frac{h_r}{1-x} \tag{2.21}$$

where x is the molar fraction of solute in aqueous solution. Equation 2.21 shows that, at a given relative humidity, the presence of solutes in the pore water reduces the capillary pressure.

Effect of capillary depression is generally assumed to take place at the high range of relative humidity. Hansen (1987) indicated that capillary stress effects are active above 25% RH, while Baroghel-Bouny and Godin (2000) considers that it is the dominant effect to explain drying shrinkage for RH above 44%.

Surface effects

With decreasing RH, at some point, all capillary pores are emptied: surface effects are then considered significant. In fact, the free energy of the solid surfaces varies during the sorption process: it decreases during adsorption and increases during desorption. The changes in surface energy $\Delta\gamma$ are assessed with the Gibbs adsorption isotherm, following:

$$\mathrm{d}\gamma = -\Gamma d\mu \qquad (2.22)$$

where $\Gamma = N_{ads}/S$ is the excess adsorbed amount per unit area, and μ is the chemical potential of adsorbed liquid.

The changes in surface energy lead to a variation of the length of the porous material. These surface effects were studied by Bangham et al. (1932), who focused on the swelling of charcoal in contact with various vapors. The strain was found proportional to the change of surface energy originating from adsorption on surfaces of the solid. The strain ε can hence be accounted for by the Gibbs-Bangham equation following:

$$\varepsilon = \lambda \Delta\gamma \qquad (2.23)$$

where γ is the surface tension and λ is the proportionality factor linking the changes of surface energy to the strain at the macro level. λ is function of the surface area of the solid, its Young's modulus, and its solid density, and depends on the considered geometry of the pore network (Scherer, 1986).

Baroghel-Bouny and Godin (2000) considers that surface effects are prominent in the range of RH below 44% RH. Hansen (1987) considers that these surface effects act over the entire range of RH. However, this author points out that these effects can only account for a small fraction (about 33% of the first drying shrinkage at 50% RH of pastes with w/c=0.6) of the drying shrinkage of cement pastes.

Disjoining pressure

Derjaguin and Churaev (1978) defined the disjoining pressure Π for the equi-

librium of thin planar films at mechanical equilibrium following:

$$\Pi = p_{mechanic} - p_{thermodynamic} \tag{2.24}$$

where $p_{mechanic}$ is the mechanical pressure applied to the film, and $p_{thermodynamic}$ its thermodynamic pressure. The disjoining pressure is the excess pressure (counted from the thermodynamic pressure) that maintains a thin film of liquid at equilibrium. This disjoining pressure depends on the thickness of the layer in question.

The drying shrinkage of cement-based materials was also attributed to disjoining pressure effects by workers. Wittmann (1973) considers that drying shrinkage above 50% RH is governed by disjoining pressure. Ferraris and Wittmann (1987) verified experimentally the role of disjoining pressure on the separation between two spherical adjacent quartz surfaces placed in a chamber where the RH was controlled. The length change at RH above 40% is linked to disjoining pressure. Beltzung and Wittmann (2005) consider that the length change observed at RH above 50% is associated to the dominant impact of disjoining pressure, based on the idea that, since the nanopores of C-S-H are filled with structured water, a capillary meniscus cannot be formed. They indicate that the disjoining pressure is influenced by Na^+ and K^+ content in pore solution. Maruyama (2010) also proposed that drying shrinkage originates from hydration pressure effects. The hydration pressure is the disjoining pressure linked to hydration forces built up within adsorbed water film. Based on experimental correlations, Maruyama (2010) derived a phenomenological model that links this disjoining pressure to the observed shrinkage, based on measurements performed on cement pastes prepared at various mix parameters (w/c ratio and cement type).

Movement of interlayer water

Some authors also suggest that movements of interlayer water can be responsible for drying shrinkage in general, and for first drying shrinkage. Hansen (1987) found that Gibbs-Bangham effect can only account for a small fraction of the observed drying shrinkage and suggested that interlayer water removal

may be responsible for the remaining fraction of the shrinkage. Feldman and Sereda (1968) also indicate that this mechanism is related to the irreversibility accompanying the first drying shrinkage. In the next section we address the irreversibility of drying shrinkage.

2.3.3   On the irreversibility of drying shrinkage

A specific feature of drying shrinkage of hardened cement-based materials is that the first drying is irreversible, meaning that a cement paste that is dried and re-humidified exhibits a residual strain: it does not recover its initial length, as shown in figure 2.12. The specific nature of the first drying shrinkage, i.e., its irreversibility, was first highlighted by Helmuth and Turk (1967). Both cement pastes and alite pastes exhibit a reversible and an irreversible drying shrinkage, these features of drying shrnkage may be induced by the drying shrinkage behavior of C-S-H. Helmuth and Turk (1967) link the irreversibility of the drying shrinkage followed by the reversible drying to a stabilization process of the cement hydrates (in the sense that the shrinkage and swelling of pastes are identical on cycles of drying and re-humidification) caused by the shrinkage of the solid phases. Once subjected to a prolonged first drying, cement pastes exhibit similar shrinkage and swelling, independently of the porosity (Helmuth and Turk, 1967). The authors also suggested that the reversible shrinkage is due to shrinkage of solid phases, while the irreversible shrinkage is due to a decrease of pore volume. Bentur et al. (1979) explains the irreversible strain by the creation of silicates bonds in C-S-H.

The models for C-S-H structure (presented in section 2.1.2) also addressed this first drying shrinkage and the irreversibility that accompanies it. Feldman and Sereda (1968) related this irreversibility to the layered nature of C-S-H, and the probable rearrangement of the layers on drying and rewetting. Jennings (2008) linked the irreversibility of first drying shrinkage to a rearrangement of the globules of C-S-H at relative humidities from 100% down to 50%, and to a possible increase of the degree of polymerization of the silicates. Further, Jennings (2008) stated that when cement paste is dried, the large gel pores diminish due to a rearrangement of particles (Jennings,
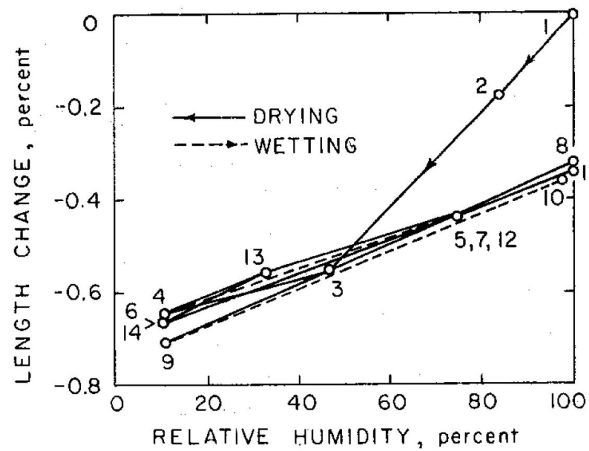
Figure 2.12: First drying shrinkage and subsequent drying-wetting cycles of hardened cement pastes prepared at a water-to-cement ratio w/c=0.6 (after Helmuth and Turk, 1967).

2004). Gartner et al. (2017) suggested that the irreversibility originates from the calcium ion bridging in C-S-H sheets, leading to their cross-linking during the drying process, and eventually to a definitive reduction of space between interlayers.

2.3.4   Factors impacting drying shrinkage

Drying shrinkage depends on mix design, cement composition, environmental conditions and admixtures. For what concerns mix design and environmental conditions, drying shrinkage usually increases with increasing w/c ratio and with decreasing RH (Helmuth and Turk, 1967; Chanvillard, 1999).

Cement composition also influences drying shrinkage. In fact, Maruyama (2010) report that low heat Portland cement exhibits a drying shrinkage larger than ordinary Portland cement. The alkali content is reported to impact the drying shrinkage behavior of cement pastes. Garci Juenger and Jennings (2002) report that increasing alkali content (by addition of sodium hydroxide to mix water) reduces the rate of shrinkage (i.e., how fast the sample shrinks over time) of cement pastes dried at 50% RH. However the shrinkage reached after 80 days of drying is similar to the one of the reference
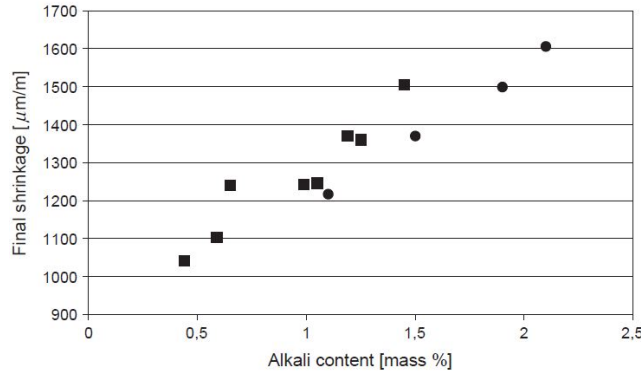
Figure 2.13: Shrinkage measurements on mortars prepared at water-to-cement ratio w/c=0.40 and sand-to-clinker ratio s/c=1.44 and dried at RH of 60% (after Beltzung and Wittmann, 2005). The measurements started after 1 week of mixing.

mix. By performing experiments on mortars prepared at a water-to-cement ratio of 0.40, Beltzung and Wittmann (2005) found that drying shrinkage increases with alkali content (controlled by addition of sodium and potassium hydroxide to water), as illustrated in figure 2.13.

Ye et al. (2017) found that cement pastes enriched in alkali (by addition of NaOH, NaCl and KOH to the mix water) dried at 50% RH exhibit larger shrinkage than ordinary Portland cement pastes. The authors propose that the impact of alkalis on drying shrinkage is due to an impact of the alkalis on the saturation degree at a given RH, or on the creep properties of the cement paste. However, it should be noted that the clinker used in their study already contained a total equivalent alkali content of 0.89% before enrichment in alkali, such that the enrichment in alkali led to alkali contents larger than for regular clinkers. Indeed, the alkali content of regular clinkers, expressed in equivalent Na_2O (alkali content of both sodium and potassium is converted to a sodium equivalent following $Na_2O + 0.658K_2O$), usually ranges from 0.2 to 1.5% (Mehta and Monteiro, 2001).

2.4 Poromechanics

2.4.1 Introduction: isotropic linear poroelasticity

In this section we present poromechanics-based modeling approaches of drying shrinkage, which aim at linking the physical mechanisms mentioned earlier to the drying shrinkage.

Let us consider a porous material, made of a solid matrix and of pores. The porous material is considered to be saturated, i.e., filled with a unique fluid. Following Coussy (2010), for a linear isotropic poroelastic porous material under isothermal conditions, the constitutive equations can be written as follows:

$$\sigma = K\epsilon - bp \qquad (2.25a)$$

$$\varphi = b\epsilon + p/N \qquad (2.25b)$$

$$s_{ab} = 2Ge_{ab} \qquad (2.25c)$$

where σ and ϵ are the volumetric stress and strain respectively, s_{ab} and e_{ab} are the deviatoric stress and strain respectively, p is the pressure of the pore fluid, $\varphi = \phi - \phi_0$ is the change of Lagrangian porosity, K is the bulk modulus of the porous material, b is its Biot coefficient, N is its Biot modulus, G is its shear modulus. The Biot coefficient b is related to the bulk modulus K of porous material and to the bulk modulus K_s of the solid skeleton (assumed to be homogeneous) following:

$$b = 1 - \frac{K}{K_s} \qquad (2.26)$$

When the porous material is only partially saturated, i.e., when its pore space is occupied by more than 1 fluid, the set of equations 2.25 is no more valid, as the pressure in the pore space is no more homogeneous. In the case of drying, where part of the pore space is occupied by a gas at pressure p_g and part of the pore space is occupied by a liquid at pressure p_l, one can adapt the set of equations 2.25 by considering that the pore space is submitted to

an apparent pore pressure $p = S_l p_l + S_g p_g$, where S_l and S_g are the degrees of saturation of the liquid and of the gas, respectively: in such a case, the apparent pore pressure is in fact equal to the volume-averaged pressure of the fluids in the pore space. Such approximation has been shown to be valid only under the assumption of pore iso-deformation (Coussy, 2010), i.e., under the assumption that, when an isotropic confining stress is applied to the material, the relative volume variation of all pores is identical.

In the next section, we provide a literature review of the models used to predict drying shrinkage. Some of them rely on poromechanics for partially saturated media.

2.4.2 Models of drying shrinkage

In this section we present some models of drying shrinkage of cement-based materials, for both elastic and non-elastic approaches. The models (Coussy et al., 2004; Vlahinić et al., 2009; Rougelot et al., 2009) consider that the material is poroelastic and are based on the capillary pressure as the driving force for drying shrinkage, then viscoelastic models are presented addressing the first irreversible drying shrinkage. We also present the model considering disjoining pressure as the driving force of drying shrinkage.

Biot-Bishop model

For a partially saturated porous medium, such as a drying porous medium whose pore space is occupied by air at pressure p_g and liquid at pressure p_l, the apparent pore pressure p is a contribution of those both pressures. If one uses the assumption of pore iso-deformation (see section 2.4.1), the apparent pore pressure p can be approximated by :

$$p = S_l p_l + S_g p_g \tag{2.27}$$
$$= S_l(p_l - p_g) + p_g \tag{2.28}$$
$$= -S_l p_{cap} + p_g \tag{2.29}$$

where S_l and S_g are the saturation degree of the liquid and gas respectively, and where $p_{cap} = p_g - p_l$ is the capillary pressure. The saturation degrees verify: $S_l + S_g = 1$. By counting all pressures relatively to the atmospheric pressure, the apparent pore pressure p can be approximated by $-S_l p_{cap}$.

Considering a stress-free sample (i.e., $\sigma=0$ in equation 2.25) along with $p = -S_l p_{cap}$, the strain generated by capillary stresses is a function of saturation and capillary pressure (Bentz et al., 1998), as follows:

$$\varepsilon = \frac{b S_l p_{cap}}{K} \tag{2.30}$$

where S_l is the saturation degree of the liquid phase, K is the bulk modulus of the porous material, and b is the Biot coefficient. Using the definition of the Biot coefficient, the linear strain can therefore be written as follows (Mackenzie, 1950; Bentz et al., 1998):

$$\varepsilon = \frac{S_l p_{cap}}{3} \left(\frac{1}{K} - \frac{1}{K_s} \right) \tag{2.31}$$

where K_s is the bulk modulus of solid skeleton.

Coussy et al. (2004) model

Coussy et al. (2004) pointed out that equation 2.30 neglects the impact of interfaces. In fact, when the porous solid is dried, its saturation decreases and the capillary pressure increases, as the menisci penetrate into smaller and smaller pores. An energy density $U = \int_{S_l}^1 p_{cap}(S) dS$ is needed as well for the creation of interfaces between liquid and gas, liquid and solid, and solid and gas. An equivalent pore pressure $\Pi_{cap} = -S_l p_{cap} - U$ is proposed for the apparent pore pressure acting on the partially saturated porous medium, which takes into account the energy stored in the interfaces. Equation 2.30 was modified to account for these effects too, resulting in the following equation:

$$\varepsilon = \frac{b}{K} \int S_l dp_{cap} \tag{2.32}$$

The authors pointed out that this modified equation does not require surface properties to be known. Coussy et al. (2004) found that this equation captures well the drying shrinkage behavior down to 50% RH. For what concerns the divergence of the model at lower relative humidity (observed on experimental data obtained on an ordinary cement paste), they attributed it to surface effects that would be dominant at low RH.

Vlahinić et al. (2009) and Rougelot et al. (2009) model

Another approach to model drying shrinkage was proposed in the work of Vlahinić et al. (2009) and Rougelot et al. (2009). Instead of considering an apparent pore pressure in a partially saturated porous material, the porous material is seen as a saturated material where the mechanical properties are dependent on the saturation degree. Vlahinić et al. (2009) proposed a constitutive model based on capillary pressure in the framework of poroelasticity, and in which the effective stress is formulated by accounting for a weakening of the solid matrix upon drying (instead of considering an averaged pore pressure, like in Coussy et al. (2004) model). In fact, upon drying, the partially saturated porous material is seen as a saturated porous material and a weakened matrix, for which the emptied pores are considered as part of a "new" weakened solid matrix. They account for this weakening by considering a first-order approximation, with which the effective bulk modulus of the weakened matrix depends linearly on the porosity of this weakened material: at a null porosity, the bulk modulus is the bulk modulus K_s of the solid skeleton, and at a porosity equal to that of the non-weakened material, the effective modulus is the bulk modulus K of the porous solid. Therefore, the effective bulk modulus follows:

$$K = K_s - \frac{(K_s - K)(1 - S_l)}{(1 - S_l\phi)} \tag{2.33}$$

where S_l is the saturation degree of the liquid and ϕ is the porosity. They confronted their model to drying shrinkage data gathered on hardened cement paste (second drying) and Vycor, and found good agreement at high RH.

Rougelot et al. (2009) also proposed a model for drying of cement-based materials (cement pastes and mortar) in a similar approach to Vlahinić et al. (2009), in which the porous material is modeled as a combination of an "equivalent" solid matrix made of the solid skeleton, of the emptied pores, and of the saturated pores. The properties of this "equivalent" solid matrix depend on the saturation degree of the material. Hence, they proposed that Biot coefficient and bulk modulus depend on the saturation degree, such that:

$$K = S_l K_{(S_l=1)} + (1 - S_l) K_{(S_l=0)} \tag{2.34}$$

where $K_{(S_l=1)}$ and $K_{(S_l=0)}$ were assessed experimentally. The strain ε generated is computed following:

$$\varepsilon = p_{cap} \left(\frac{1}{K(S_l)} - \frac{1}{K_s} \right) \tag{2.35}$$

Viscoelastic models

As noted in section 2.3.3, the first drying shrinkage of cement paste is marked by an irreversibility, for which the physical mechanisms are still debated. Grasley and Leung (2011) modeled drying shrinkage of cement pastes under the scope of poromechanics and aging viscoelasticity. Benboudjema et al. (2007) developed a model for drying shrinkage of cement pastes with a viscoelastic approach. The model attempts to capture the irreversibility of drying shrinkage (intrinsic drying shrinkage dissociated from the structural effect of microcracks induced by drying) and its dependency on the drying rate considering an elastic contribution and a creep component under the action of capillary forces and disjoining pressure. The model is confronted to measurements of drying shrinkage for RH>50%, and reproduces the tendencies of drying shrinkage.

Maruyama (2010) model

Maruyama (2010) considered that drying shrinkage originates from disjoining pressure, which is referred to as hydration pressure. He proposes that water in

cement paste is adsorbed on surfaces, then infers an empirical model linking the disjoining pressure and the thickness of adsorbed film following:

$$\Pi(e) = \Pi_0 \exp(-d/\lambda_0) \tag{2.36}$$

where Π_0=4500 MPa, λ_0=0.95 nm, $d = 2e$ and e is the statistical thickness of the adsorbed film.

The uniaxial strain ε of the cement pastes is related to the incremental changes $\Delta\Pi$ of disjoining pressure as follows:

$$\varepsilon = \frac{w}{3K}\Delta\Pi \tag{2.37}$$

where w is the volumetric water content (i.e., the volume of liquid water per volume of material) and K is the bulk modulus of the cement paste.

2.5 Shrinkage reducing admixtures (SRAs)

The use of SRA is motivated by the fact that these admixtures can reduce drying shrinkage, and hence potentially the risk of cracking that this drying can induce. When the drying is restrained, drying shrinkage can lead to cracking (Bažant and Raftshol, 1982). However, the link between use of SRA and induced cracking is not straightforward. Several investigated experimentally the impact of SRA on fracture development: from restrained shrinkage tests, the conclusion was that SRA mixtures cracked at later ages and the crack width showed considerable reduction, when compared to mix designs with no SRA (Shah et al., 1992; Folliard and Berke, 1997; Saliba et al., 2011).

SRAs were first patented by Goto et al. (1985) in 1982, in Japan. Typically consisting of glycol ethers, they are known for decreasing both the autogenous shrinkage and the drying shrinkage, which helps reducing the risk of cracking of the cement-based materials. Dosages of 0.5% to 2% in cement weight are usually recommended. The cost of the SRA is around 4 euros to 5 euros/kg (Collepardi et al., 2005). The cost of the SRA, together with the high recommended dosages, translate into an increase of cost of concrete of around 12-20 euros per m^3 (Collepardi et al., 2005).

In this section, we first detail the observed effects of SRAs on various types of shrinkage of cement-based materials, namely plastic shrinkage, autogenous shrinkage and drying shrinkage. Then, the proposed mechanisms of action of these organic molecules are presented. Finally, the influence of SRAs on other properties (e.g., mechanical properties, hydration) is discussed.

2.5.1 Shrinkage of cement-based materials and SRAs

The influence of SRAs on drying shrinkage was studied thoroughly in the literature. SRAs reduce the magnitude of drying shrinkage by up to 50% (Ai and Young, 1997; Saliba et al., 2011; Shah et al., 1992; Gettu et al., 2002; Rongbing and Jian, 2005; Eberhardt and Kaufmann, 2006; Eberhardt, 2010).

Several studies (Tazawa and Miyazawa, 1995; Bentz and Jensen, 2004; Rongbing and Jian, 2005; Sant et al., 2006; Bentz et al., 2001; Weiss et al., 2008; Saliba et al., 2011) also found that SRAs can reduce autogenous shrinkage. Moreover, an early-age expansion is commonly observed for pastes containing SRA (Pease, 2005; Weiss et al., 2008; Sant et al., 2011). Sant et al. (2011) reported that this early-age expansion contributes to the observed reduction of autogenous drying shrinkage, and may be explained by a pore solution that is more supersaturated with regards to portlandite in presence of SRA than in absence of it, leading to higher crystallization pressures, and hence generating expansion of cement paste.

It was also reported that these admixtures can reduce the plastic shrinkage (Holt and Leivo, 2000, 2004; Mora-Ruacho et al., 2009; Saliba et al., 2011). The reduction is found to range from 25% (Saliba et al., 2011) to 50% (Holt and Leivo, 2000, 2004).

Further, a synergistic effect of SRA and expansive agents was observed, for the reduction of both drying shrinkage (Collepardi et al., 2005; Maltese et al., 2005) and autogenous shrinkage (Oliveira et al., 2014).

2.5.2 Mechanisms of action of SRAs

The first studies on SRAs stated that these organic molecules act on drying shrinkage and autogenous shrinkage by means of their action on capillary

forces. Many (among which the suppliers of SRAs such as Sika, Mapei or Chryso) claim that the shrinkage mitigation is due to the ability of the SRAs to decrease the surface tension of the pore solution. Since the SRAs decrease the surface tension of the pore solution (e.g., Rajabipour et al. (2008)), they decrease the compressive stresses to which the solid matrix is subjected at a given saturation level, and hence its shrinkage. In fact, when a porous material is conditioned at a given RH, the capillary pressure is set according to equation 2.19. At a given RH, reducing the surface tension leads to a reduction of radius of the meniscus. Consequently, at a given RH, the meniscus is localized in pores with smaller radii when the paste contains SRAs, compared to the plain paste. Hence, for a porous material with a given pore size distribution and at a given RH, a larger fraction of pores empties when the surface tension of the pore solution decreases: said otherwise, at a given RH, the saturation degree S_l should decrease in presence of SRA. Therefore, based on equation 2.30, the strain generated by capillary stresses is reduced. Such mechanism is the mechanism widely reported for the action of SRAs on drying shrinkage and autogenous shrinkage (Balogh, 1996; Ai and Young, 1997). Note that the same reasoning can be applied if the contact angle between pore solution and solid surface increases, at a constant surface tension and relative humidity. This increase of contact angle leads to a reduction of the saturation degree, and, consequently, to a decrease of the strain generated by capillary stresses. Bentz (2006) reported that the contact angle of a SRA solution on hardened cement paste is 7°, while that of distilled water is 28°.

However, the contribution of this sole mechanism (action on capillary forces through the reduction of surface tension) does not justify the high concentrations recommended to optimally reduce shrinkage, which are larger than the threshold concentration above which the surface tension of the pore solution reaches an asymptotic value. Furthermore, the reduction of drying shrinkage is not correlated to surface tension, as shown in figure 2.14, after Maruyama et al. (2018a). Therefore, other mechanisms of action must play a role.

Recent studies investigated further the mechanisms of action of SRA.
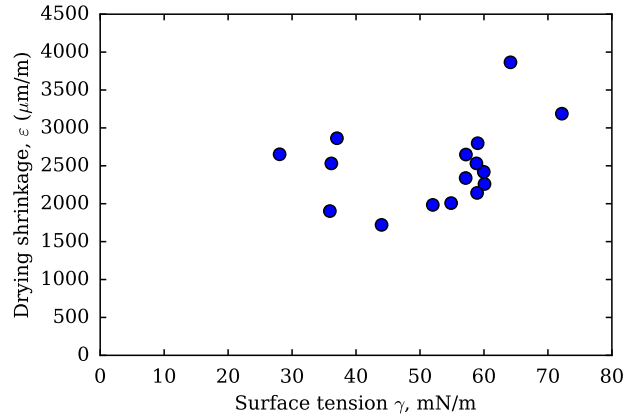
Figure 2.14: Drying shrinkage of cement pastes at (w+SRA)/c mass ratio of 0.55 dried at a RH of 60% containing potential SRAs (alcohol-ethylene oxide polymers), in terms of measured surface tension of aqueous SRA solution, based on data from Maruyama et al. (2018a).

Eberhardt (2010) identified a mobile part of SRAs and an immobile one, based on leaching experiments. Eberhardt (2010) suggests that SRAs (7 different SRAs were studied which were commercial SRAs, and potential SRAs based on surfactants and cleaning agents. Among the commercial SRAs a SRA majorly composed of DPTB=dipropylene-tert-buthylether, and a commercial SRA composed of 2-dimethyl-1.3propandiol in majority) act on shrinkage by reduction of capillary stresses by the mobile fraction of SRAs, while the immobile fraction increases the disjoining pressure. Maruyama et al. (2016) reported that SRA (SRA studied here is a synthesized SRA with the formula R-O- $(EO)_2$- $(PO)_2$-H, EO is oxirane, PO is methyl oxirane and R a butyl group) act through two mechanisms. At RH above 70%, drying shrinkage is reduced by reduction of capillary forces, through the reduction of surface tension. Below 70% RH, SRAs reduce drying shrinkage by means of the immobile fraction, which is suspected to change the morphology of portlandite which may have a restraining effect on the drying shrinkage. Gartner et al. (2017) suggest a novel mechanism of action in the light of the model of C-S-H established in the same work (Gartner et al., 2017). The SRAs are suggested to play a kinetic role inhibiting the formation of

bridging bonds between C-S-H sheets and dehydrated calcium ions. Such inhibition prevents the microstructural changes at the level of C-S-H and thus the length change observed at the macro level. Recently, Maruyama et al. (2018a) studied the alcohol-ethylene oxide polymers and their action on drying shrinkage of cement pastes. The authors studied 15 molecules with three different alphatic alcohols and various poly-ethylene-oxide chain lengths. Molecules with balanced hydrophilic-lipophilic properties are able to reduce optimally drying shrinkage. These molecules act on drying shrinkage, specifically in the range of RH between 75% and 40%. SRAs are able to reduce mainly the irreversible shrinkage. Maruyama et al. (2018a) proposed that SRAs act on drying shrinkage by inhibiting the agglomeration of C-S-H sheets, as the SRAs are suspected to be positioned in the vicinity of C-S-H.

The mechanisms proposed in the literature, and by which SRAs act on drying shrinkage, are summarized as follows:

- Reduction of the capillary effect.

- Reduction of disjoining pressure effect.

- Inhibition of the microstructural collapse and of the re-arrangement of the microstructure.

In the next section, we detail other aspects over which SRAs have an influence, namely the microstructure, the mechanical properties and the transport properties.

2.5.3 Other impacts of SRAs

Impact of SRA on microstructure

Hydration of cement is reported to be modified in presence of SRA. Cement paste with SRA (made of propyleneglycol ether) are observed to contain a lower quantity of portlandite at early age (Maltese et al., 2005). However, Ai and Young (1997) reported no significant change in the chemistry of formed hydrates or the rate of formation. Moreover, many report the retarding effect

of the SRA on the hydration kinetics (Bentz, 2006; Sant et al., 2006; Eberhardt, 2010; Saliba et al., 2011). This was further investigated by Rajabipour et al. (2008) (where SRA studied was a commercial SRA consisting mainly of poly-oxyalkylene alkyl ether), who linked this retardation of hydration to changes of composition of the pore solution in the presence of SRA mixtures, leading to a lowering of alkali sulfates dissolution. Increasing content of alkali is linked to an increase the hydration rate of cement.

SRAs are reported to affect the pore structure of cement-based materials, but experimental observations do not always agree with each other. Saliba et al. (2011) and Shah et al. (1992) (based on a study of three SRAs: commercial SRA containing an alkoxylated alcohol, alkoxylated alcohol based oligomer, and an alcohol based SRA) found that addition of SRA reduces the volume of macropores (i.e., pores between 50 nm and 10 μm) and that this reduction depends on the type of SRA used (Shah et al., 1992). Maltese et al. (2005) assessed specific surface area and found it to increase for cement pastes containing SRA. Eberhardt (2010) found that mature cement and mortar pastes with SRA exhibited larger specific surface area and larger gel porosity (estimated from mass loss between 50 °C to 110 °C) than plain pastes or plain mortars. This increase in gel porosity is attributed to an increase of pores smaller than 4 nm, concluded from nitrogen adsorption measurements. However, Ai and Young (1997) found that, for a cement paste, no significant change is observed in size distribution of mesopores, or in the specific surface area, when SRA is added to the paste.

Further, Maltese et al. (2005) and Eberhardt (2010) report an impact of the SRA on the morphology of the hydrates. In fact, Maltese et al. (2005) observed significant morphology changes when SRA is used: prismatic needles are detected, but their chemical composition was not identified. (Eberhardt, 2010, p. 126) found that portlandite formed a layered structure in the presence of SRA. Maruyama et al. (2016) investigated the morphology of portlandite precipitated in solution in presence of SRA and found that smaller crystals are formed compared to portlandite precipitated in the absence of SRA, as illustrated in figure 2.15.
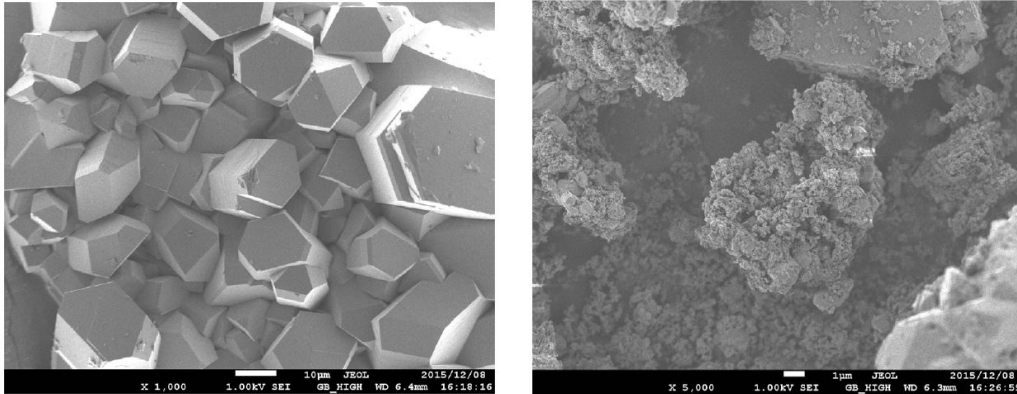
Figure 2.15: Morphology of precipitated portlandite in (left) water without SRA and (right) in solution with SRA (after Maruyama et al., 2016).

Impact of SRA on mechanical properties

Maltese et al. (2005) and Saliba et al. (2011) found that samples containing SRA exhibit lower compressive strength than samples containing no SRA, by up to 25% (Maltese et al., 2005). Ribeiro et al. (2006) reported that a decrease in compressive strength is noted only at early ages, while at the mature state the decrease is small. The elastic modulus is reported to decrease in presence of SRA (Saliba et al., 2011). Shah et al. (1992) found that the tensile strength decreases, by up to 30%, depending on the used SRA and its content in the mix. One may wonder if the observed decrease in mechanical properties may not be caused by the retardation of hydration of samples containing SRA reported by some authors as detailed in section 2.5.3.

The impact of SRA on creep properties was little investigated. D'Ambrosia et al. (2001) report a slight reduction of total tensile creep for concrete containing SRA. Gettu et al. (2002) report that the drying creep coefficient is reduced in presence of SRA, and that the basic creep does not depend on SRA.

Impact of SRA on transport properties

SRAs may also impact the transport properties of water in cement-based materials, by acting on the pore fluid and the material matrix. SRA is

observed to increase the viscosity of fluid up to 50% for a 10% addition of SRA (Bentz, 2006; Sant et al., 2010). For mortars containing SRA, with respect to mortars containing no SRA, Pour-ghaz et al. (2010) (the SRA studied here is a commercial SRA based on poly-oxyalkylene alkyl ether mainly) report slower drying rate at high RH (when liquid diffusion is prevalent), and lower diffusivity when subjecting mortar specimens to drying from one side. Sant et al. (2010) concluded that SRA (a commercial SRA based on poly-oxyalkylene alkyl ether) reduces the rate of water absorption (assessed by subjecting dried samples to one-dimensional water absorption by placing water on top of the samples). Ribeiro et al. (2006) found that, for mortars, a large reduction in the oxygen permeability was observed in the materials containing SRA (two SRAs were studied composed mainly of a high molecular weight polyglicol and an alkyl-ether), which also exhibited a lower capillary suction (i.e., the water uptake by submerged samples in water through time), in spite of the fact that the open porosity was similar for samples with or without SRA. Further, Bentz et al. (2001) found that, when subjecting a sample to 8 hours of drying, a drying front develops in the cement pastes containing SRA (a commercial SRA), in contrast to plain pastes for which a uniform front is observed. It should be noted that in this work, drying starts at an early age (i.e., 3 hours after setting), so that the pastes contain more free evaporable water relative than if they were in their mature states.

2.6 Conclusions

In this chapter, we introduced a literature review of the various aspects of the microstructure of cement-based materials, drying shrinkage and shrinkage reducing admixtures. We also introduced the concepts related to the characterization of the pore structure of cement-based materials and to the modeling of drying shrinkage, which will be used in this work.

Through their service life, cement-based materials endure several types of shrinkage, among which drying shrinkage. Drying shrinkage is induced by transfer of moisture from the specimen to its surroundings. Cement-based materials are multiscale porous materials, and a variety of experimental tech-

niques can be used to probe their pore space. The pore structure of cement pastes spans a wide scale from nanometers to micrometers. The removal of water occupying the pore space contributes to the shrinkage of the cement paste, and the physical mechanism through which this removal translates into a strain depends on the size of the pores from which this water is removed. The most reported mechanisms of drying shrinkage are: capillary forces, surface effects and disjoining pressure. Moreover, the first drying shrinkage of cement pastes is characterized by an irreversibility: when a cement paste is dried for the first time, and re-humidified to high relative humidities, the cement paste does not recover its length before the first drying, i.e., a residual strain of the cement paste is observed. Drying shrinkage is of large interest in the scientific community, and was extensively studied using both experimental approaches and modeling approaches. The drying shrinkage of cement-based materials is influenced, among others, by the environmental conditions, the mix design and admixtures.

Shrinkage reducing admixtures are one way to mitigate drying shrinkage. Although their ability to reduce drying shrinkage is confirmed by a variety of studies, the mechanisms of action underlying this ability are not yet clarified. In this chapter, we also reviewed the impact of SRAs on other features of the material (e.g., microstructure properties, mechanical properties and transport properties).

Chapter 3

Impact of SRA on drying shrinkage isotherms

In this chapter, we examine the impact of SRA on drying and the subsequent re-humidification of cement pastes at various contents of alkali. 9 types of cement paste with various contents of alkali and SRA are dried and re-humidified on a wide range of relative humidities (RH). Mass of cement pastes and their length change were monitored at each set relative humidity. The investigation of drying shrinkage behavior was conducted using long-term measurements on relatively large sized samples (thickness of 3 mm), and using short-term measurements on samples of a smaller size (thickness of 0.5 mm). The performance of SRA in terms of shrinkage reduction is found to depend on range of RH and on content of alkali. We examine the impact of SRA and alkali on the reversible shrinkage and irreversible shrinkage, by studying 2 initial conditions: 1) samples that were kept under sealed conditions until measurements, and 2) samples that were equilibrated at RH of 11%. SRA impacts significantly the irreversibility of drying shrinkage isotherms. Finally, the possibility of implementing SRA as a curing agent is studied by short-term measurements, and may prove as promising for drying shrinkage reduction of cementitious materials.

3.1   Materials and methods

In this section, we present the materials used in our study and the adopted method of preparation. We also present the methods for drying procedure of cement pastes using both long-term measurements and short-term measurements.

3.1.1   Materials

We manufactured 9 types of samples with various contents of alkali and SRA. The samples had in common:

- One solution to clinker ration (in mass) of 0.55, where mass of solution is the sum of mass of water and SRA in case of samples containing SRA.

- Type of SRA added. One type: hexylene glycol, also known as 2-Methyl-2,4-pentanediol.

The cement pastes differed by:

- Clinker used. 3 types are considered: ordinary Portland cement low in alkali content, and 2 other alkali enriched cements with medium and high alkali content.

- Amount of SRA added. 3 contents are considered: 0%, 4%, and 8% of the mass of clinker.

3 types of clinker are studied here, considering their alkali content: ordinary Portland cement provided from "Le Teil" (historically the first plant and quarry of Lafarge, in southern France) is enriched in alkali with potassium sulfate K_2SO_4 at a content of 1.4% and 2.8% in clinker mass, corresponding to low alkali content (0% addition of K_2SO_4), medium (1.4% addition of K_2SO_4), and high (2.8% addition of K_2SO_4), corresponding to a content of alkali expressed in equivalent Na_2O of 0.2, 0.7 and 1.2% respectively. The potassium sulfate is added to mixing water in order to reach desired alkali

Composition from XRF		Composition from XRD	
Component	Mass fraction, %	Phase	Mass fraction, %
SiO_2	22.5	Alite C_3S	69.4
Al_2O_3	2.9	Belite C_2S	17.6
Fe_2O_3	2.25	Ferrite C_4AF	7.1
CaO	66.97	Aluminate C_3A	1.1
MgO	0.85	Calcite $C\overline{C}$	1.9
K_2O	0.17	Gypsum $C\overline{S}H_2$	0.5
Na_2O	0.12	Anhydrite $C\overline{S}$	1.2
SO_3	2.22	Hemihydrate $C\overline{S}H_{0.5}$	0.4

Table 3.1: Chemical composition of the Ordinary Portland cement clinker used, in mass fraction. XRF and XRD stand for X-ray fluorescence and X-ray diffraction, respectively.

content. Composition of clinker is provided in table 3.1. The cementitious system considered in this study is the hardened cement paste.

The shrinkage reducing admixture (noted 'SRA') used in this study is: hexylene glycol, 2-Methyl-2,4-pentanediol. This SRA can be found in a pure state, and its physico-chemical characterization is well stated in the literature. It is also among the main components of commercialized SRAs. In fact, the company Grace has patented the hexylene glycol as SRA, namely Eclipse 4500 which contains [50%-100%] hexylene glycol. Major characteristics of this molecule are reported in table 3.2.

3.1.2 Method of preparation of samples

A total of 9 types of samples was prepared. They were labeled based on the following logic. Considering the two cases: plain paste or mixture containing SRA, the labeling adopted is the following:

1. for plain paste with no added SRA: [PP-type of cement].

2. for pastes with added SRA: [SRX-type of cement], with X the content of SRA (without % symbol).

Type of cement will be referred to as [L, M, H], relatively to the alkali content [low, medium, high]. Note that throughout this work the content of
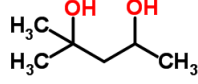
Chemical name	2-Methyl-2,4-pentanediol
Common name	Hexylene Glycol
Chemical formula	$C_6H_{14}O_2$
Topological formula	
Molecular weight	118 (g/mol)
Density at 20 °C	0.92 [b]
Boiling point/range	197.1 °C [a]
Solubility	Soluble in water and ethanol [a]
Surface tension at 20 °C	33.1 mN/m [b]
Saturated vapor pressure	0.003-0.007 kPa [b]

Table 3.2: Properties of the studied shrinkage reducing admixture. References correspond to (*a*) (Lide, 2003, p=521) and (*b*) (Whim and Johnson, 2012, p=309).

SRA is expressed in % of the mass of clinker. The list of all types of materials prepared is provided in table 3.3.

The samples preparation is conducted through 3 main stages:

1. Mixing: de-ionized water is kept over night at room temperature 20 °C. The water is pre-mixed with the appropriate amount of SRA, when an SRA mixture is considered, as well as the potassium sulfate for alkali enriched cement. The SRA equivalent amount is reduced from the water in mass. The solution (water, potassium sulfate and SRA) is then added to clinker, and mixed following the procedure detailed below for each alkali content:

   - For low alkali cement paste: water is separated in two parts. A first part corresponding to a w/c ratio of 0.3, that is mixed with clinker for 2 minutes. SRA is added to the remaining and second part of water. Obtained solution is added to the premixed paste, and is mixed again for 2 minutes. We use a Renfert twister mixer with a rate of 250 rpm.

   - For medium alkali cement paste: potassium sulfate is first added

Label of material	Clinker	s/c	SRA content, %
PP-L	OPC-L	0.55	0
SR4-L	OPC-L	0.55	4
SR8-L	OPC-L	0.55	8
PP-M	OPC-M	0.55	0
SR4-M	OPC-M	0.55	4
SR8-M	OPC-M	0.55	8
PP-H	OPC-H	0.55	0
SR4-H	OPC-H	0.55	4
SR8-H	OPC-H	0.55	8

Table 3.3: List of prepared samples. Note that s/c designates the ratio of the mass of solution (i.e., of the mix of water with the SRA) to the mass of clinker. OPC-L, OPC-M, and OPC-H designate ordinary Portland cement low in alkali content, Portland cement with medium alkali content and Portland cement with high alkali content, respectively.

    to water, and well agitated until added salt is dissolved. Then, for the SRA containing pastes, SRA is added. The same mixing procedure as that of the low alkali paste is adopted.

- For high alkali cement paste: a different approach for mixing is used for high alkali pastes since using the mixing procedure described for low and medium alkali contents did not allow to obtain homogeneous pastes. In fact lumps (for which illustration and investigation is given in appendix A), identified as syngenite, formed during the mixing and a homogeneous mixing could not be reached until a high rate mixer was used. Here planetary centrifugal mixer "thinky mixer" type ARE 500 is used. Solution is first prepared mixing water, alkali and SRA added in this order, then added to clinker. We first mix for two minutes at 1000 rpm, then paste is mixed manually with a spatula, and re-mixed again for one minute.

Afterwards the paste is remixed manually every 30 minutes using a plastic spatula, until creamy consistency is obtained, this process can take from 4 to 10 hours for the considered cement pastes. The stainless

steel bowl in which the cement paste is resting is covered to prevent
drying during this mixing process (except at the moments when we
need to remix the preparations). The paste is then cast in the molds,
which are subject to external vibration to minimize trapped air bubbles.
An illustration of molds used here can be found in figure 3.1. Then
the molds are wrapped with a damp cloth and plastic sheet, to avoid
drying the samples before being removed from the molds. The molds
give specimens of dimensions 3 mm×13 mm×300 mm. Furthermore,
we verify that the cloth is still damp after 5 days when the specimens
are removed from the molds. We note that the molds were not greased
prior to casting which helps avoiding the impact of grease on the drying
shrinkage behavior, given that the prepared samples are of a thickness
of 3 mm the effect of grease may not be marginal.

2. Cutting: the pastes were removed from their molds after 5 days, every
   sample is cut twice with a diamond saw, with a rotational speed of 70
   rpm, to render specimens of dimensions of 3 mm×13 mm×100 mm.
   De-ionized water is used during the cutting process. The presence of
   water lubricates the surfaces which facilitates cutting process, and also
   allows to cool the surface and prevents overheating. Some water can
   be absorbed on the edges of the samples during this process. How-
   ever given that samples have a high w/c ratio, and that samples are 5
   days-old when they are cut, samples can be considered saturated, the
   absorbed water hence is negligible with regards to the evaporable water
   of cement pastes.

3. Curing: samples are cured in sealed aluminum bags, kept in a room of
   20 °C for 90 days. The 90 days curing period helps obtaining mature
   pastes at high degree of hydration. This sealed curing conditions helps
   avoiding the leaching of SRA as opposed to curing under lime saturated
   solution.

Post hydration addition of SRA
To study the impact of addition of SRA after hardening of cement pastes, a

Figure 3.1: Mold used for cement pastes preparations. The mold may give up to 10 samples of dimensions 300 mm×13 mm×3 mm.

subset samples are prepared based on plain paste to which SRA was added after the paste was mature. Plain paste with low alkali content of a size 3 mm × 3 mm × 0.5 mm (cut using a diamond saw) and age over 6 months was immersed in SRA solution of concentration of ∼18% in mass (SRA to water ratio), paste to solution (water+SRA) mass ratio is ∼18%. The sample is immersed in SRA solution for at least 3 days, after which drying shrinkage and mass change are measured by short-term measurements.

In order to estimate the SRA content, organic carbon amount in cement pastes was measured after short-term drying measurements were achieved. The abundance of carbon, hydrogen, and oxygen of cement pastes was measured with an elemental analyzer (elementar vario MICRO cube, Elementar Inc.). We used sulfanilamide ($NH_2C_6H_4SO_2NH_2$) as a standard for the measurement of carbon and hydrogen contents in mass percentage.

3.1.3 Methods of drying shrinkage and sorption measurements

In the following section methods for measurements of drying shrinkage isotherms and sorption isotherms are presented. First, we introduce methods for long-term measurements. Then, methods for short-term isotherms are introduced.

Long-term drying shrinkage measurements

The dimensions of samples used for drying shrinkage are chosen to reduce the time needed to reach equilibrium. In the measurements conducted by Hansen (1987), drying of cement paste of thickness 2-3 mm at RH of 50%
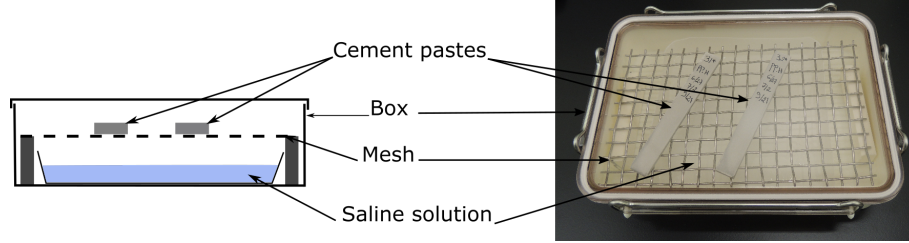
Figure 3.2: A schematic of side view (left hand) of the box used for long-drying measurements and a picture (right hand) of the box for drying (box A used for monitoring)

.

and 75% did not reach equilibrium after 200 days drying. Samples may also crack due to the moisture gradient in samples, Bisschop and Wittel (2011) found however that cement pastes of thickness 2 to 4 mm are not impacted in terms of cracking induced by drying shrinkage. Further, the shape of cement based specimen can also impact the drying shrinkage behavior. Samouh et al. (2018) found that prisms, compared to cylinders, had lower mass loss and drying shrinkage, and the difference was explained by the impact of size on moisture diffusion. The measurements in the study of Samouh et al. (2018) were conducted on concrete specimens of 7 cm thickness. The dimensions of samples used in this work allow reducing gradients and resulting microcracks, as well as reducing the time required to reach equilibrium in terms of length change and mass change.

Drying of samples starts after the end of curing period of 3 months under sealed conditions. Samples are put in boxes of dimensions $210 \times 150 \times 45$ mm^3, containing a saturated salt solution over which a mesh was placed as illustrated in figure 3.2. Saturated salt solutions enable controlling the relative humidity. We note that in the preparation of saline solutions we aimed at reaching saturation not only by surpassing the theoretical solubility of salts but also until visible salt crystals were detected. We also made sure that salt crystals are well covered by the liquid saline solution to ensure targeted RH is met, since exposed dry salt crystals lead to lower values of RH (Multon et al., 1991). Both the salts and the targeted RH are detailed in table 3.4. The samples are then put on the mesh to avoid direct contact with the saturated

salt solution. A relative humidity sensor is inserted in each of 18 boxes, used for drying of chosen three types of cement pastes at the considered 8 RH, in order to monitor and confirm the relative humidity inside the box during the drying. For every relative humidity and type of samples, two boxes are considered:

1. A box, referred to as box A, containing at least 2 samples for measurement of the drying shrinkage and the weight loss periodically. The samples of box A serve to determine if equilibrium is reached.

2. A box, referred to as box B, containing at least 5 samples. The drying shrinkage and mass of these samples are measured only twice: before drying (after the curing period of 3 months under sealed conditions is achieved, and before the samples are placed in the box where RH is controlled), and after drying (after the samples reach equilibrium with relative humidity).

This method allows avoiding the carbonation of the samples of the second box (box B), since it is opened a limited number of times. Thus, renewing air inside of the box is limited as well, and so is the accumulated amount of CO_2. As for the first box, it contains sacrificial samples used to monitor weight loss and shrinkage of samples over time, and determine when equilibrium is reached. We assume that if carbonation occurs, it will not significantly affect the rate at which samples equilibrate with relative humidity. Results of the monitoring of weight loss and mass change on drying and re-humidification can be found in appendix B.2.

Samples of size 100 mm×13 mm×3 mm serve for the long-term drying shrinkage measurements. As for the short-term measurements, a sample of dimensions 3 mm×3 mm×0.5 mm is cut from the larger samples using a diamond saw. An illustration of the samples for long-term and short-term measurements can be found in figure 3.3. Details will be provided about both long-term and short-term measurements in the next section.

Once the samples were prepared, and left under sealed curing for 3 months, they were left to reach equilibrium for at least 6 months under targeted relative humidities from 95% down to 11%. Another batch of samples is left

Salt	Relative humidity (%)
LiCl	11*
$MgCl_2$	30
NaI	40*
$Mg(NO_3)_2$	54*
NaBr	60*
NaCl	75*
KCl	85
KNO_3	95*

Table 3.4: Salts used and the corresponding targeted relative humidity. All the relative humidity marked with a star * are considered for the first adsorption and the second drying.
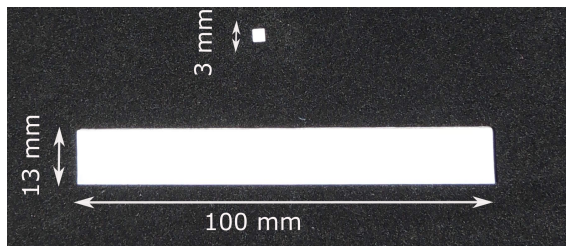
Figure 3.3: A picture of an upper view of sample for short-term measurements (top) and of a sample for long-term measurements (bottom).

to dry at 11%, and subsequently put at higher relative humidities for re-humidification measurements. We remind that measurement of length and mass of a type of cement paste equilibrated at a given RH, on drying or re-humidification branch, is conducted on at least 5 companion specimens.

The length is measured by a contact displacement meter with a precision of $\pm$ 0.5 μm for 1 mm, and a reference made of ceramic (Cera block provided by Mitutoyo) of length 100 mm. The length before and after drying is measured. Samples are also weighted before and after drying, to obtain the sorption isotherm of studied cement paste. The final measurements of mass change and length change are measured on the samples in boxes B, containing at least 5 samples, when the mass change of samples in the box A destined for equilibrium monitoring, is below 0.01% per day. The uniaxial strain ε is measured as follows:

$$\varepsilon = \frac{l - l_{ref}}{l_{ref}} \tag{3.1}$$

where l is the measured length of cement specimen, and l_{ref} stands for the reference length of cement specimen. This reference length can refer to sealed state or to state of samples equilibrated at RH 11% or 95%. It will be stated when the reference state is taken at a given RH. If not precised the reference is taken under sealed state.

The mass change w_l is computed as follows:

$$w_l = \frac{m - m_{ref}}{m_{ref}} \tag{3.2}$$

where m is the measured mass of cement specimen, and m_{ref} is the reference mass of cement specimen after curing under sealed conditions, to state of samples equilibrated at RH 11% or 95%. As for length change measurements, if the reference is not stated then the reference corresponds to sealed state. If the reference is that of a given RH, the reference will be clearly stated.
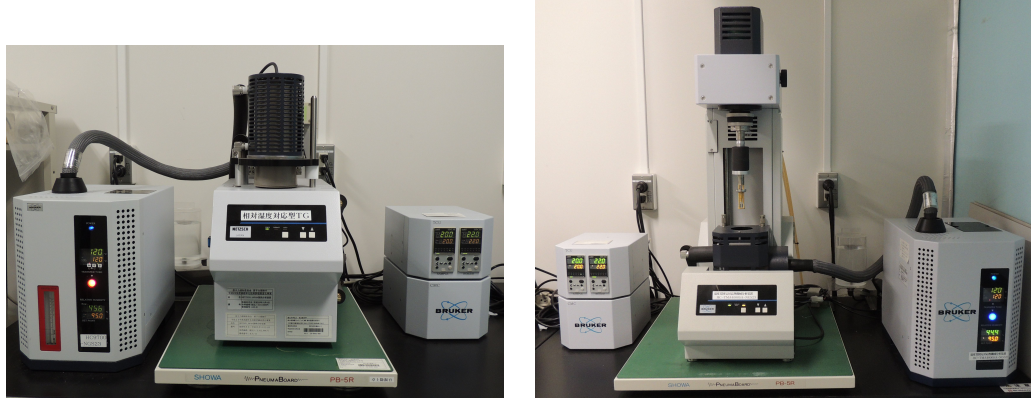
Figure 3.4: Experimental set-up for short-term measurements, TGA coupled
with RH generator (left) and TMA coupled with RH generator (right).

Short-term drying shrinkage measurements

Chosen samples are used for short-term measurements. Studied cement
pastes are recapitulated in table 3.5. A sample of dimensions of 3 mm×3
mm×0.5 mm is dried under a RH-controlled air flow. The length changes
are obtained by means of a thermomechanical analyzer (TMA) coupled with
a RH generator (AXS TMA4000SA and HC9700, Bruker, figure 3.4-right),
where the length variations are measured by a linear variable differential
transducer (LVDT) with a precision of 0.5 μm and a contact load of 0.098
N. The length change of these samples are measured. For measuring short-
term sorption isotherms, 2 samples of the same dimension as for short-term
length-change isotherm measurements were used in a thermogravimetric an-
alyzer (TG-DTA 2000SA and HC9700, Bruker AXS, figure 3.4-left) coupled
with a relative humidity generator similarly to TMA measurements. The
choice of using 2 samples is motivated by increasing the precision of the
measurement. Since one sample weighs roughly 7 grams, variation of mass
during drying and re-humidification can be in the range of precision of device.

Two initial conditions for samples are considered:

1. sealed curing for at least 3 months.

2. samples that were dried at RH 11% on long-term measurements after
   the sealed curing of 3 months.

Sample	Condition before measurement	Measurements
PP-L	sealed	short-term drying, long-term drying
SR4-L	sealed	long-term drying
SR8-L	sealed	short-term drying, long-term drying
PP-M	sealed	short-term drying, long-term drying
SR4-M	sealed	short-term drying, long-term drying
SR8-M	sealed	long-term drying
PP-H	sealed	short-term drying, long-term drying
SR4-H	sealed	long-term drying
SR8-H	sealed	short-term drying, long-term drying
PP-L-SRA	SRA added after hydration	short-term drying
PP-L-11	prolonged drying at RH 11%	short-term drying
PP-H-11	prolonged drying at RH 11%	short-term drying
SR8-L-11	prolonged drying at RH 11%	short-term drying
SR8-H-11	prolonged drying at RH 11%	short-term drying

Table 3.5: Types of samples for long-term measurements and short-term measurements.

These two initial conditions help investigation of the irreversible drying shrinkage (based on measurement on sealed state samples) and the reversible drying shrinkage behavior (based on measurement on dried samples).

The relative humidity imposed to the samples is as follows for both drying and re-humidification [95%, 75%, 55%, 35%, 5%] for all samples (pre-dried and never dried). Each step of RH is kept for 8 hours. Exceptions are noted for RH of 55%, 35% and 5% on desorption and 95% on re-humidification where RH is kept for an additional 8 hours, because approaching equilibrium takes longer. Hence an 8 hour span does not allow sample to approach equilibrium similarly to other steps of RH. We note also for dried cement pastes that sample is allowed for an additional 8 hours at the initial RH of 95%. A measurement of desorption and subsequent adsorption is completed in almost 5 days. We note that length change and weight loss are computed for short-term measurements relatively to RH of 95% imposed at the start of the cycle.
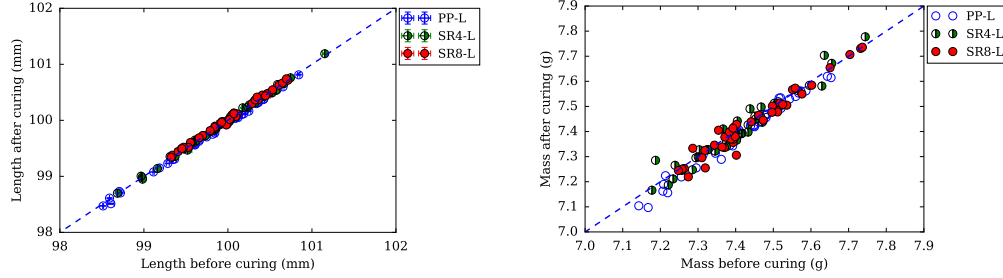
Figure 3.5: Length and mass of samples before and after curing under sealed
conditions for pastes at low alkali content.

3.1.4 Validation of sealed curing and of relative humidities of drying

To validate the conditions of sealed curing of samples, some samples are
chosen randomly to monitor their mass and length before and after the curing
period. This procedure will serve to confirm the absence of drying during
the curing process.

Results for plain paste low alkali and paste containing SRA at 4% and
8% content at low alkali content are shown in figure 3.5 for length of sample
before and after curing, and for mass of sample before and after curing.
Results indicate that length of samples is not impacted by the curing period.
This goes well in line with the fact that samples are prepared at high w/c
ratio, allowing to avoid the autogenous shrinkage. Moreover, mass of samples
before and after curing shows some scattering. This indicates that some water
redistribution in samples takes place, and might be related to the possible
evaporation of water and uptake of water during preparation of samples.
During the curing period water of samples is redistributed, however total
mass of samples varies little during curing validating the sealed conditions of
curing of samples (largest variation of total mass was found to be less than
0.15%). Results confirm the curing conditions of samples.

Relative humidity within the boxes used for drying of cement paste was
monitored using two methods:

- Digital relative humidity sensor inserted inside the boxes and kept in-
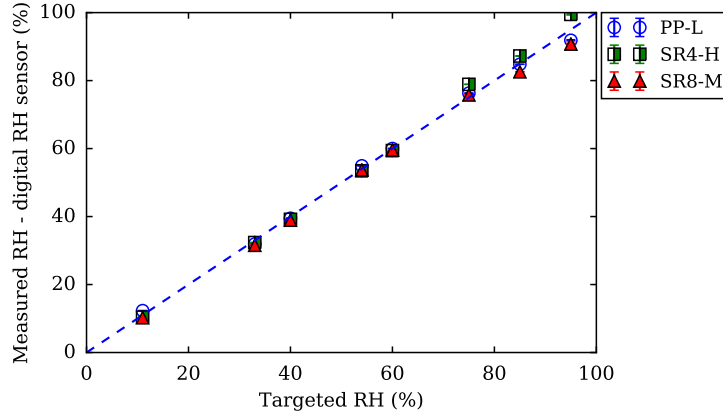
Figure 3.6: Measured relative humidity by digital sensors inserted in boxes for drying of three chosen cement pastes.

side during the whole period of drying.

- Water activity measurement using Aqualab 4TE of saline solutions of boxes.

Some of the boxes were chosen for relative humidity monitoring by digital sensors. Given the reduced number of sensors we only monitor using this method drying boxes for PP-L, SR8-M, and SR4-H. Results of measured relative humidity as a function of targeted RH is shown in figure 3.6. As for monitoring by measurement of water activity of saline solution, all of the drying boxes were tested. Results using this method are shown in figure 3.7.

Measurements based on digital sensors inserted in the boxes show an overall agreement of measured RH and targeted RH, except for measurement at RH larger than 75%, and most particularly for one measurement at targeted RH 95% inserted in box for drying of paste SR4-H as shown in figure 3.6, where measured RH is close to 100% RH. This variability of the measurement is linked to the error of measurement of the sensors at high RH, where potential condensation of water vapor may lead to variable measurement of the RH inside the box.

Overall, both methods for monitoring of RH inside the boxes used for drying shrinkage measurements concur, and confirm agreement of theoretical

99
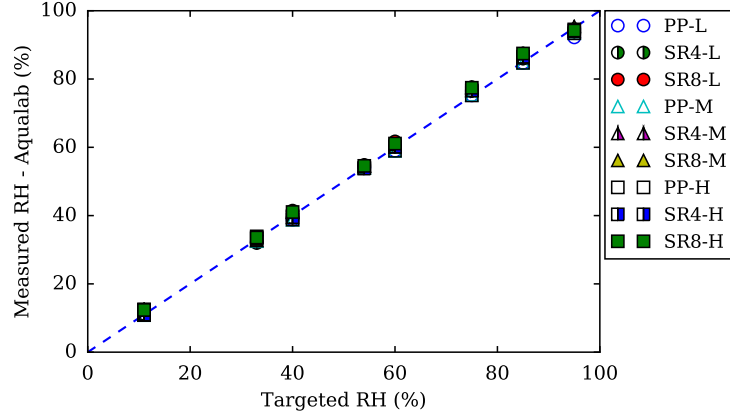
Figure 3.7: Measured relative humidity by Aqualab inserted on sampled saline solutions of boxes for drying of 9 types of cement pastes.

	Long-term drying	Short-term drying
Size of sample	100×13×3 mm³	3×3×0.5 mm³
RH on drying	8 RH-[95%-11%]	5 RH-[95%-5%]
RH on re-humidification	5 RH-[11%-95%]	5 RH-[5%-95%]
Samples	a sample for each RH	a sample for all cycles
Measurements	Mass and length of samples subjected to RH controlled by saline solutions	TMA and TGA coupled with RH generator

Table 3.6: Measurements of drying and specifications of each measurements (short-term and long-term drying).

and experimental values for targeted RH using saline solutions.

3.1.5 Summary of experimental measurements

In this section we summarize the experimental program that is discussed in this chapter regarding drying shrinkage measurements. In table 3.6 we summarize the measurements of drying of cement pastes detailed in table 3.5.

3.2 Long-term drying measurements

In this section we present the results of long-term drying shrinkage and weight loss measurements of the 9 types of cement paste, tuned in alkali and SRA contents. The impact of SRA and alkali on the long-term drying shrinkage is investigated and discussed.

3.2.1 Length and mass change results

Results of drying shrinkage measurements and mass change of samples of the 9 types of cement paste studied during first desorption and subsequent re-humidification are shown in figures 3.8, 3.9 and 3.10 for low alkali content, medium alkali content, and high alkali content respectively.

First we examine results of mass change of cement pastes shown on the right hand side of figures 3.8, 3.9 and 3.10. During first desorption weight loss of cement paste is observed. For RH larger than 54%, weight loss occurs in a fast manner then slower as the RH decreases. When samples are subjected to RH that is lower than 40%, weight loss of samples coincide on the desorption branch and adsorption branch, except for plain paste at high alkali content and paste containing SRA at content of 8% at low alkali content (see SR8-L in figure 3.8 and PP-H in figure 3.10).

Let's examine the hysteresis and irreversibility of weight loss of cement pastes. Hysteresis is defined here by the fact that a measured parameter (here weight loss) follows a different path on desorption and adsorption as shown in figure 3.11 (the left hand sub-figure and the middle sub-figure). Irreversibility is defined here by the fact that a parameter does not regain its initial value after a desorption-adsorption cycle, as shown in figure 3.11 (the left hand sub-figure) where the initial value at A and final value at B after a cycle of drying and re-humidification are different. The right hand sub-figure in figure 3.11 corresponds to a reversible and without hysteresis cycle. When samples are dried from the sealed state to a relative humidity of 11% then re-humidified to higher relative humidities, the weight loss does not coincide with the weight loss measured on first drying for RH higher than 40%. The weight loss shows an hysteresis for RH higher than 40%.

101
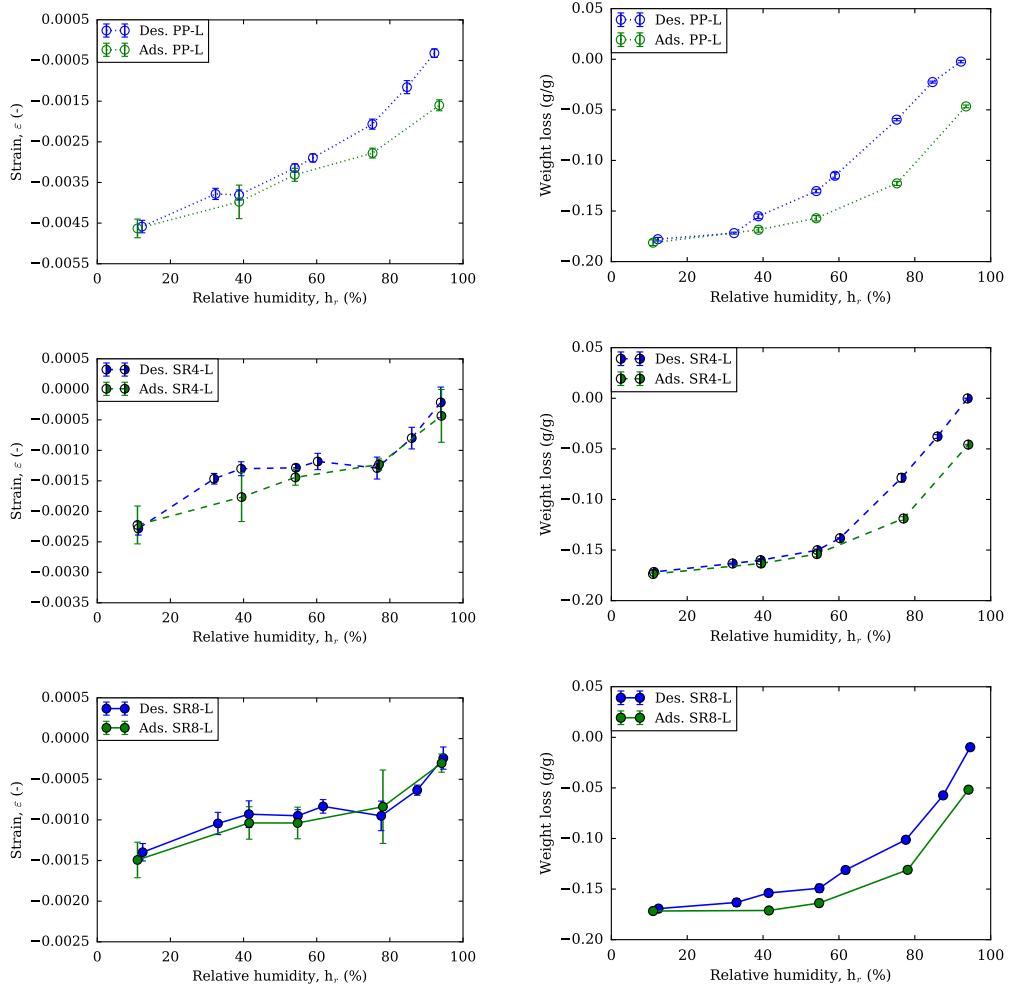
Figure 3.8: Length change (left) and mass change (right) of samples at low
alkali content with no SRA (PP-L) and with SRA at a content of 4% (SR4-L)
and 8% (SR8-L). Results of drying (blue) and subsequent re-humidification
(green) are shown.
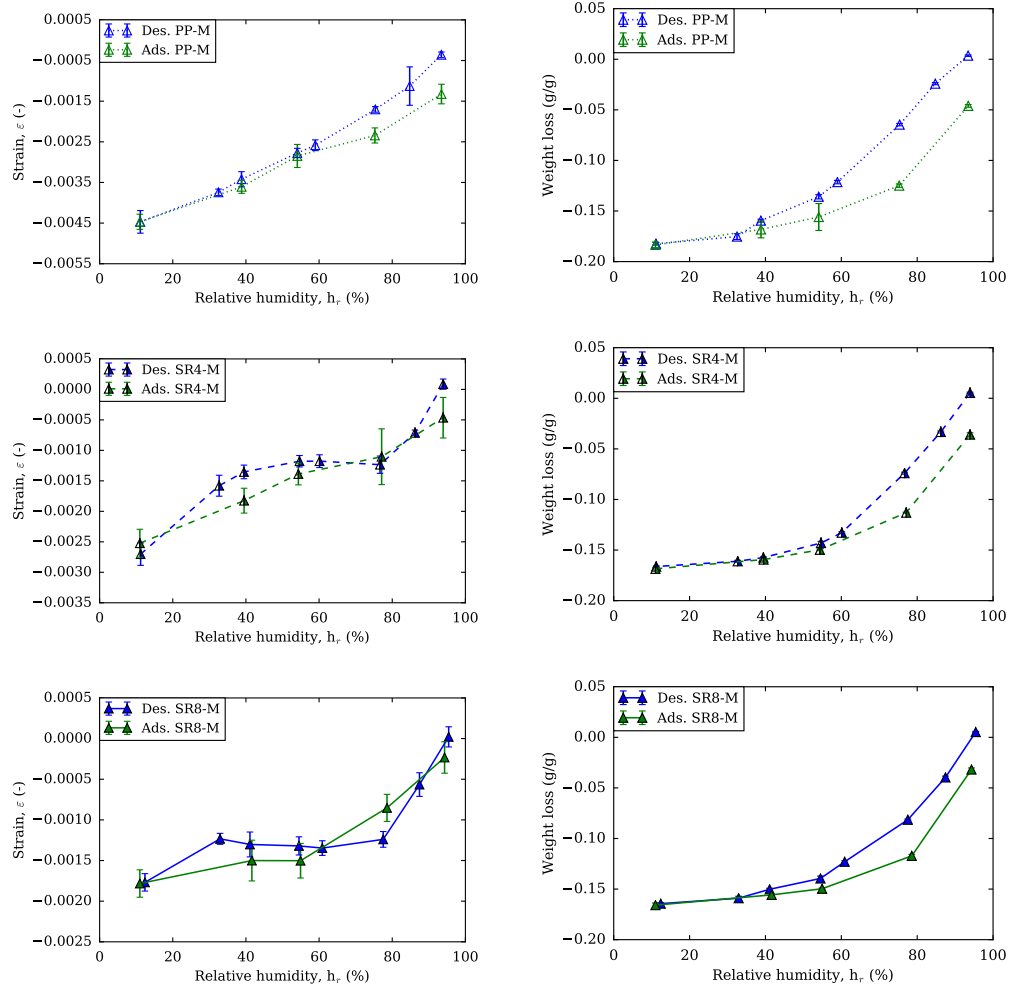
Figure 3.9: Length change (left) and mass change (right) of samples at medium alkali content with no SRA (PP-M) and with SRA at a content of 4% (SR4-M) and 8% (SR8-M). Results of drying (blue) and subsequent re-humidification (green) are shown.
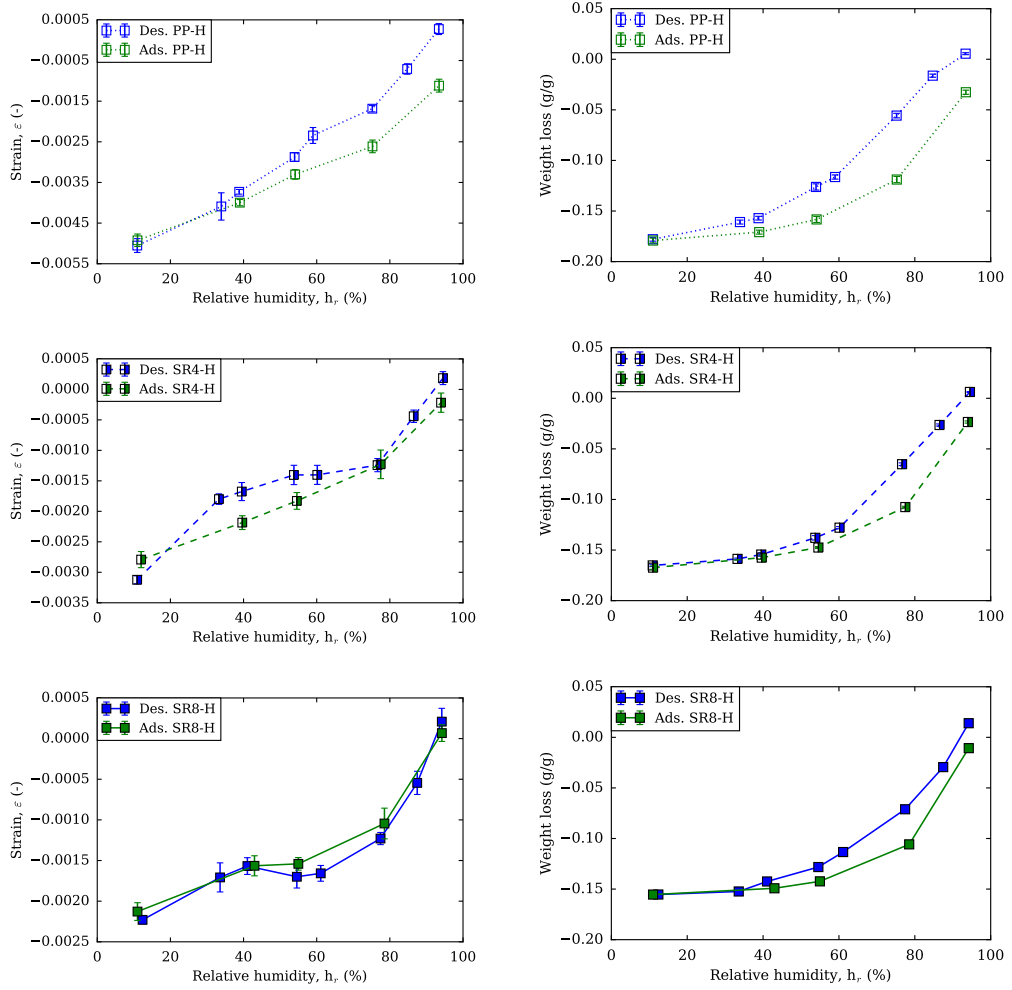
Figure 3.10: Length change (left) and mass change (right) of samples at high alkali content with no SRA (PP-H) and with SRA at a content of 4% (SR4-H) and 8% (SR8-H). Results of drying (blue) and subsequent re-humidification (green) are shown.
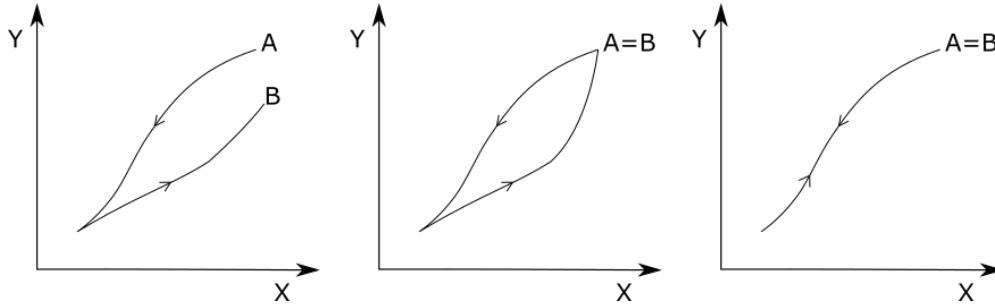
Figure 3.11: A schemtatic for the variations of parameter Y with regards to parameter X during a cycle of drying and re-humidification starting at the intial value A and returning to final value B after a cycle of drying and re-humidification. The left hand figure corresponds to an irreversible behavior with hysteresis (A≠B). The middle figure corresponds to a reversible (A=B) with hysteresis behavior. The right hand figure corresponds to a reversible (A=B) and without hysteresis behavior (path during drying is the same as during re-humidification.

Further, the samples do not regain their initial weight when dried to 11% and re-humidified to 95%. The weight loss shows an irreversibility.

Let us examine the impact of SRA on mass change of cement pastes on drying and re-humidification. We compare weight loss of samples at low alkali content for plain paste and paste containing SRA in figure 3.12. Weight loss of pastes containing SRA is higher than weight loss of plain paste at RH higher than 40%. For RH larger than 60%, paste at 8% content of SRA has a larger weight loss, below 60% weight loss is comparable. On the re-humidification branch, cement pastes regain water at a comparable manner, except for cement paste at 8% content of SRA which shows a lower weight gain on the re-humidification branch.

Drying shrinkage of cement pastes is shown on the left side of figures 3.8, 3.9 and 3.10. For plain pastes, drying shrinkage decreases linearly with decreasing RH. At RH lower than 54% length change of samples on the first desorption and subsequent re-humidification is almost equal: no or little hysteresis is observed. When sample is re-humidified to RH larger than 54%, we observe that plain paste does not recover all shrinkage: an irreversible shrinkage is noted. We compare drying shrinkage of first desorption of plain
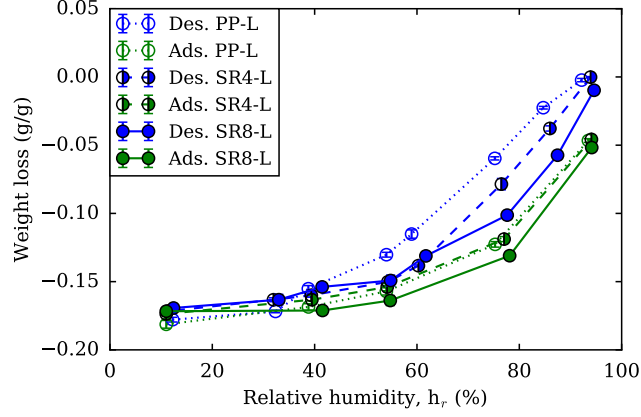
Figure 3.12: Mass change during drying and re-humidification of paste at low
alkali content, with and without SRA: plain paste (PP-L), paste containing
4% SRA (SR4-L) and paste containing 8% SRA (SR8-L).

paste and pastes with SRA at various contents of alkalis in figure 3.13. Drying shrinkage of pastes containing SRA is consistently lower relatively to
plain pastes at RH range below 75%. For RH higher than 75%, reduction
of shrinkage is lower (for low alkali and medium alkali content) than the
reduction of shrinkage on the RH lower than 75%, if not absent (for high
alkali content). Moreover, a plateau is observed on the range of RH [33%-
75%]. This behavior is observed for all 6 pastes containing SRA regardless of
their alkali content. Furthermore, upon re-humidification samples with SRA
regain almost all the shrinkage as shown in figures 3.8, 3.9 and 3.10. The
drying shrinkage isotherm is reversible for pastes containing SRA, although
weight loss is not recovered upon re-humidification to RH of 95%.

We combine weight loss measurements and shrinkage measurements in
figure 3.14 for plain pastes at various alkali content, to investigate the role of
alkalis in drying shrinkage behavior of plain pastes. Alkalis do not impact the
weight loss of plain pastes during drying and re-humidification. Alkalis impact the drying shrinkage, however no clear tendency can be generalized over
the entire range of investigated RH. As an illustration, at 54% RH shrinkage is comparable between cement pastes with medium and high content of
alkali, whereas cement pastes with low alkali content shows largest drying

106
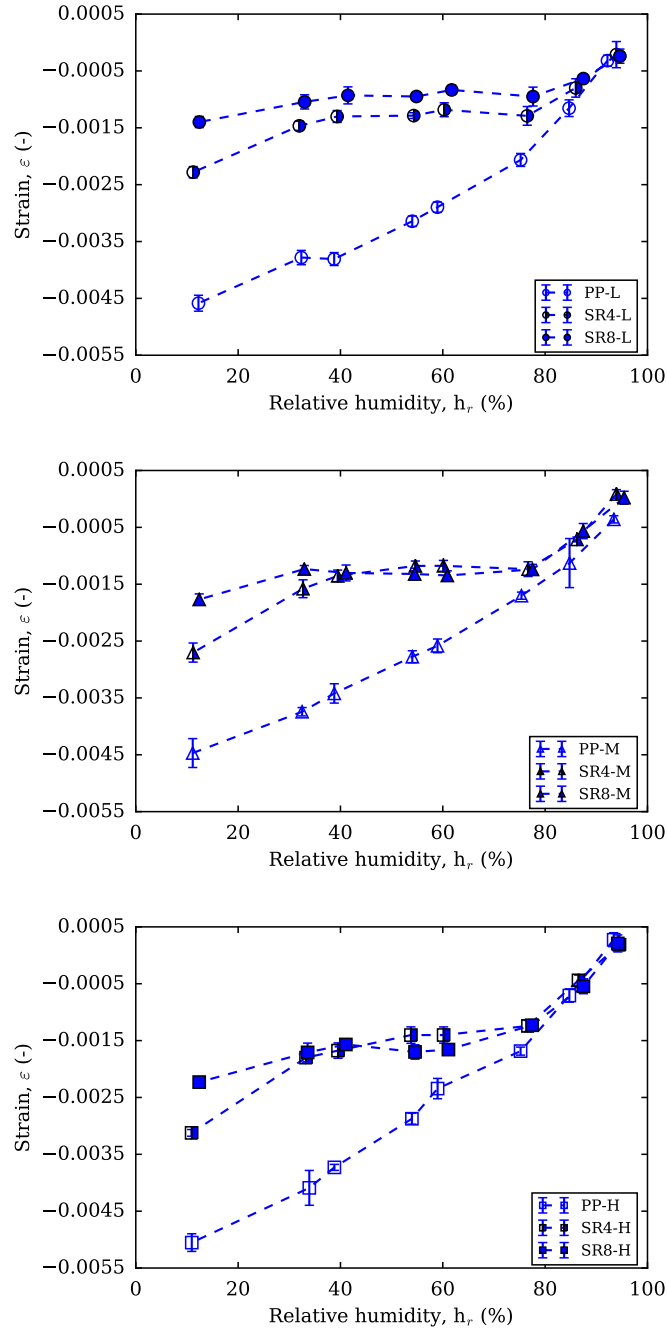
Figure 3.13: Drying shrinkage of plain paste (PP) and paste at various SRA contents (4% content and 8% content) at low alkali content (upper figure), medium alkali content (middle figure) and high alkali content (lower figure).
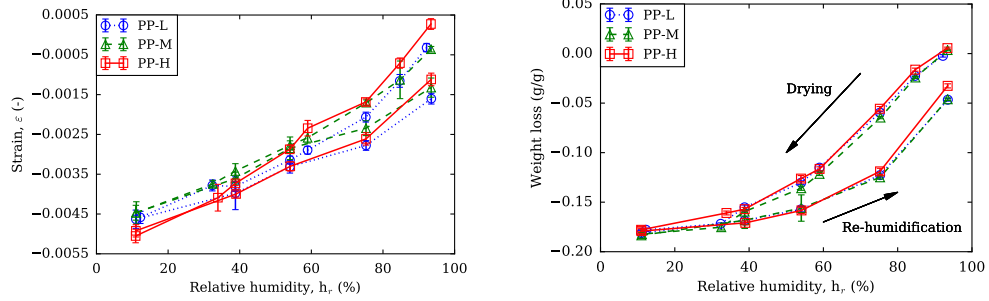
Figure 3.14: Length (left) and mass change (right) with relative humidity
of plain pastes at low alkali content (PP-L), medium alkali content (PP-M)
and high alkali content (PP-H).
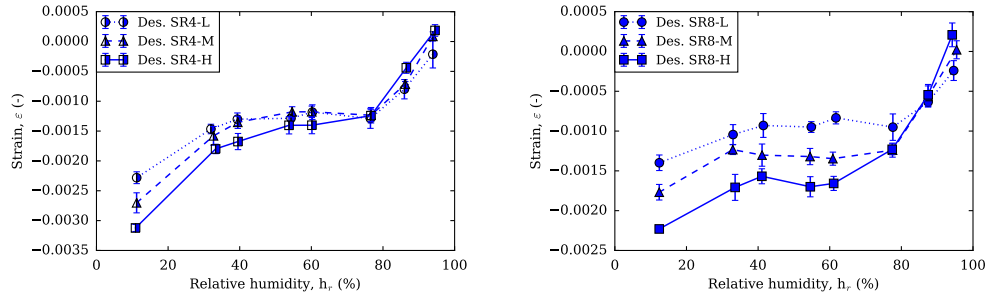
Figure 3.15: Length change of pastes containing SRA (4% content on the
left, 8% content on the right) at various contents of alkali.

shrinkage. When cement pastes dried at 11% RH, cement pastes with high
alkali content have larger drying shrinkage compared to cement pastes with
lower content of alkali.

As for pastes containing SRA, cement pastes at increasing alkali content
showed a higher drying shrinkage during desorption as shown in figure 3.15.
Moreover, at medium alkali content and high alkali content, samples con-
taining 4% SRA and 8% SRA have similar drying shrinkage values on the
range of RH of [95%-33%] as displayed in figure 3.13. At this range of RH,
and at the medium and high content of alkali, increasing SRA content does
not lead to a decrease of drying shrinkage.

To better understand the impact of SRA on drying shrinkage and weight
loss and how these two quantities are related, we plot the strain observed
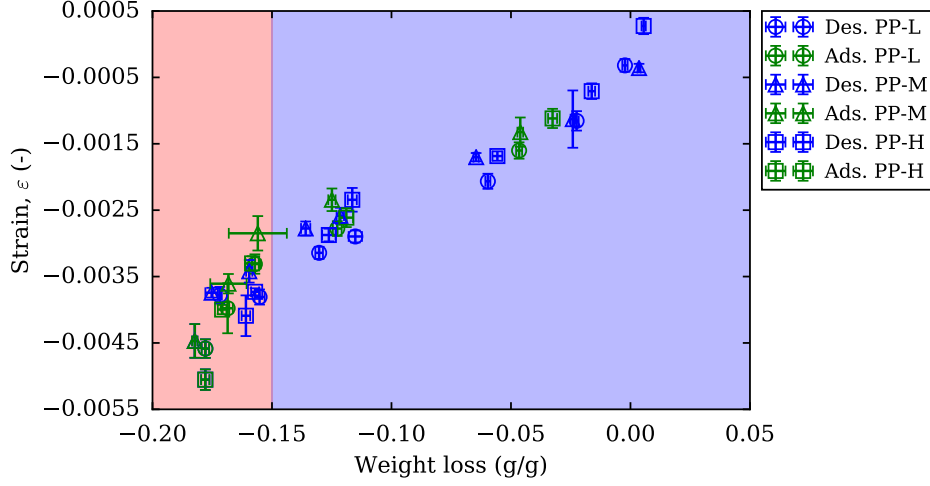
Figure 3.16: Strain in terms of weight loss of plain pastes for various alkali contents under drying (indicated by blue symbols) and re-humidification (indicated by green symbols) paths. Blue shade indicates linear behavior range and red shade affine behavior with an increased slope of drying shrinkage with regards to weight loss.

in terms of the weight loss reported. Results of this representation is shown in figures 3.16 and 3.17 for plain pastes, pastes containing SRA at 4% and 8% content respectively. Results show that regardless of alkali content and of humidity change path, all points follow a master curve. Results of plain paste shown in figure 3.16 show that plain paste follows a linear behavior when weight loss is lower than 0.15 g/g, beyond this value slope of shrinkage with regards to weight loss increases, that is to say that for a small weight loss a large variation of strain is observed, a variation of weight loss of 0.01 g/g induces a shrinkage of 500 to over 1000 μm. Results for pastes containing SRA presented in figure 3.17 show that strain follows three regimes. A first regime is observed when weight loss is lower than 0.05 g/g during which strain follows a linear behavior. A second regime is observed at weight loss lower than 0.15 g/g during which weight loss does not generate a shrinkage. A third regime is observed when weight loss is larger than 0.15 g/g and for which slope of strain vs. weight loss increases.
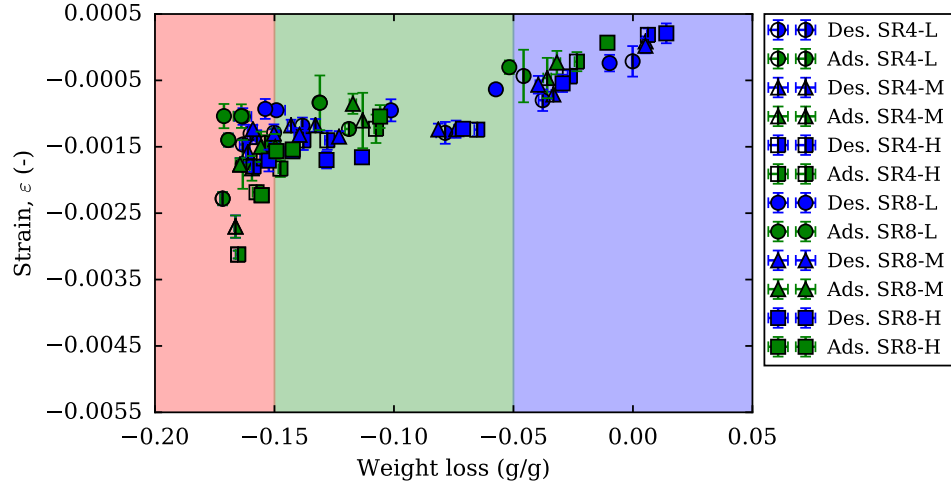
Figure 3.17: Strain in terms of weight loss of samples containing SRA for
various alkali contents under drying (indicated by blue symbols) and re-
humidification (indicated by green symbols) path. Blue shade indicates linear
behavior range, green shade a constant behavior and red shade an increased
slope of drying shrinkage with regards to weight loss.

3.2.2   Discussion of impact of SRA on weight loss

Impact of SRA on weight loss was reported by several authors. Bentz et al.
(2001) studied the effect introduced by addition of SRA to evaporation of
both bulk water, and evaporable water of cement paste with w/c=0.35. They
confirmed that addition of SRA to bulk water leads to a higher rate of evap-
oration, however addition of SRA to cement paste leads on the contrary to
lower rates of evaporation. The equilibrium values of weight loss are not
reported as the results reported stand for 48 hours drying. They relate the
influence of SRA on drying rate to the modification of drying kinetics of ce-
ment paste in presence of SRA, as they found that cement paste with SRA,
when dried from an isolated surface, develops a drying front, in contrast to
plain pastes. Therefore, water vapor diffuses through the pore network be-
fore reaching the surface, while for plain pastes, it reaches the surface by
maintained capillary network of films.

By means of short-term measurements, SRA addition to {Vycor+SRA}

and to cement pastes was also found to lead to larger weight loss on desorption in the range of RH [60-80%] for the first and down to a RH of 20% for the second (Maruyama et al., 2016), which agrees with results presented in the previous section. Weiss et al. (2008) also found that for RH higher than 50% mass loss of samples are either larger or comparable to mass loss of plain pastes. The impact of SRA on weight loss of samples may be explained by its ability to lower surface tension. In fact, at thermodynamic equilibrium, when samples are dried at a given relative humidity RH, the size of meniscus that can form in the pore network of cement paste is related to the surface tension by the Kelvin equation 2.11. At a given RH, reducing the surface tension comes to a reduction of the size of equilibrium of formed meniscus. For a given pore structure, when surface tension of pore solution is reduced, volume of family of pores emptied of their condensate is therefore larger, which corresponds to larger weight loss (Weiss et al., 2008).

3.2.3 Discussion of impact of SRA and alkali contents on drying shrinkage

The ability of SRA to reduce the drying shrinkage is confirmed in our study. Moreover, we find that SRA reduces significantly irreversibility of drying shrinkage and suppresses it in some cases. The ability of SRA to reduce drying shrinkage is highest at the range of RH [33%-75%] where drying shrinkage of cement paste is almost constant while weight loss is increasing: weight loss and shrinkage are not correlated in this range of RH. Supported by findings of short-term measurements we provide an interpretation for this behavior in section 3.4.

The ability of SRA to decrease the drying shrinkage also depends on the content of alkali. In fact, at the same content of SRA, the higher the alkali content, the higher the drying shrinkage experienced by cement pastes during desorption. Moreover, for high alkali content, drying shrinkage measurements of plain pastes and pastes containing SRA at RH above 75% is almost identical. Hence, in this case the addition of SRA to the mixing water does not lead to additional drying shrinkage reduction. This observation

raises questions on the commonly reported mechanism of action of SRA on the capillary effects explained in section 2.5.2. If the role of SRA in drying shrinkage reduction is solely through its ability to reduce surface tension of pore solution, then the addition of SRA to mixing water would lead to a reduction of drying shrinkage regardless of alkali content, and this reduction would be observed on the high range of RH where capillary effects are dominant, whereas experimental measurements goes against this behavior.

The interaction of SRA with the pore solution and how the alkali may reduce its efficiency is of interest here. SRAs reduce the surface tension by adsorbing on liquid-air interfaces. Rajabipour et al. (2008) studied the interaction of a commercial SRA in pore solution, and found that critical micellar concentration (CMC) of SRA in synthetic pore solution is moved toward lower concentrations of SRA compared to SRA in deionized water. This means that SRA starts to combine into micelles at lower concentrations in the synthetic pore solution, instead of adsorbing on liquid-air interface. This may suggest that part of SRA in high alkali medium may not be adsorbed on liquid-air interfaces, and present rather in the bulk pore solution. However this explanation is not satisfactory because Rajabipour et al. (2008) found that although CMC is moved toward lower concentrations the reached surface tension is also lower in the synthetic pore solution. Addition of SRA to material with high content of alkali does not necessarily impact the ability of SRA to reduce the surface tension of the pore solution of the material, hence the impact of SRA on drying shrinkage of cement pastes at high contents of alkali may not be explained by the change of surface tension. In section 5.3.2, we confirm by measurements of surface tension of extracted pore solution of the studied cement pastes that content of alkali does not influence the surface tension of pore solution of cement pastes containing SRA.

In section 5.3, we investigate the composition of extracted pore solution of cement pastes, and the depletion of alkalis in presence of SRA is observed and confirms the finding of previous studies (Rajabipour et al., 2008), one may wonder if the depleted alkalis are intermixed with C-S-H, and the presence of the alkali ions in the vicinity of the C-S-H, and as such the drying shrinkage of C-S-H increases for pastes with high alkali contents. This may explain

why the SRA performance in high alkali media degraded.

In the next section, we investigate the drying and re-humidification of chosen cement pastes at short-term, by means of TMA-RH and TGA-RH measurements. We study samples kept under sealed conditions until the measurements and samples dried slowly at 11% RH. These measurements allow to assess the irreversible shrinkage and reversible shrinkage respectively.

3.3 Short-term drying measurements

Short-term length change measurements and mass change of studied cement pastes previously reported in table 3.5 are discussed in this section. We investigate the drying shrinkage behavior of samples that were not dried prior to measurements, denoted non-pre-dried to refer to their condition prior to measurements, and samples that were subject to long and slow drying at 11% RH, denoted pre-dried cement pastes.

3.3.1 Short-term measurements of non-pre-dried cement pastes

Figures 3.18 and 3.19 show results of plain pastes and pastes with SRA respectively. These samples were kept under sealed conditions prior to measurements. Results for drying shrinkage on plain pastes presented in figure 3.18 show that plain pastes share the following features, regardless of alkali content:

- Length change measurements shows an irreversible shrinkage of the order of 2500 μm/m since cement paste does not recover all its length change upon re-humidification to RH of 95%.

- Length change measurements shows little or no hysteresis below 35% RH.

- Increase of length change on desorption branch is higher in the range of RH>35% than in the range of RH below 35%.

113
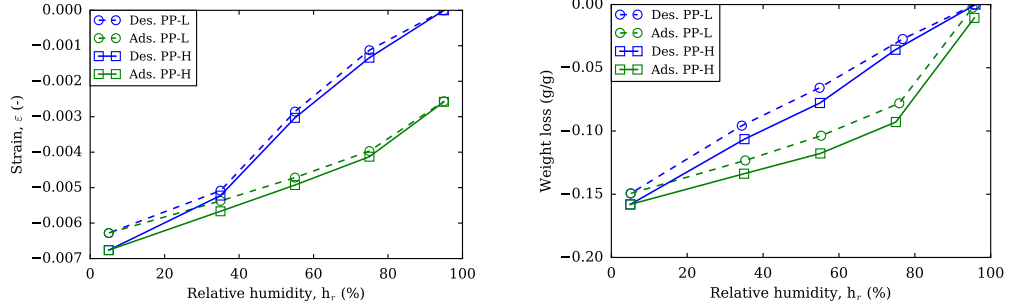
Figure 3.18: Short-term results of plain pastes at low alkali content (PP-L)
and high alkali content (PP-H). Length change is presented on left, and mass
change on right, upon desorption (blue) and adsorption (green).

- Length change is linear with regards to RH on re-humidification branch.

- Mass change is reversible: weight loss upon drying is regained upon
  re-humidification to 95%.

- Hysteresis is observed for mass change on the entire range of RH [5%-
  95%].

- Mass change is linear on desorption branch on the investigated range
  of RH.

- Mass change is also linear on the adsorption branch on RH range of
  [5%-75%], for RH>75% the increase of water uptake is significantly
  larger.

Length change and weight loss of samples containing SRA are presented
in figure 3.19. Results show that samples containing SRA share the following
features regardless of alkali content:

- Length change shows smaller irreversibility compared to plain paste,
  irreversible shrinkage is lower than 1000 μm/m.

- Length change has a hysteresis on the entire range of studied RH.

- Increase of length change is lowest at mid range of RH ([35%-75%] for
  content of SRA of 8% and [35%-55%] for content of SRA of 4%).

114
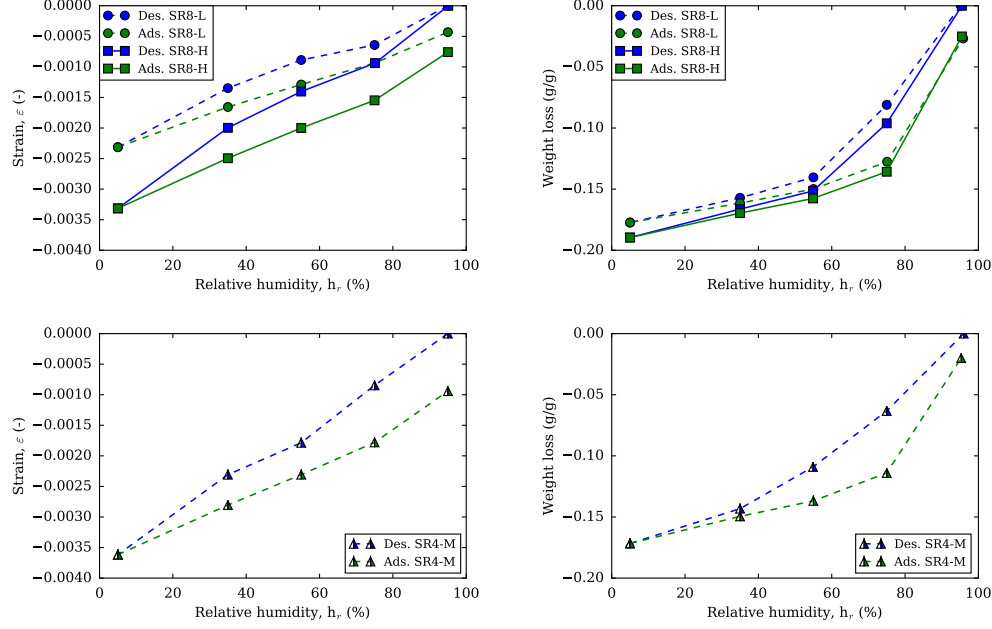
Figure 3.19: Short-term results of pastes at low alkali content and 8% content of SRA (SR8-L), at high alkali content and 8% content of SRA (SR8-H) and at medium alkali content and 4% content of SRA (SR4-M).

- Increase of weight loss is high at RH>55% for pastes with SRA content 8% and at RH>35% for content of SRA of 4%.

- Increase of weight gain on the adsorption branch is higher at RH>75% compared to range of RH<75%.

To verify the impact of SRA on drying shrinkage, we compare in figure 3.20 results of short-term measurements for plain paste and pastes containing 8% SRA, at low alkali content and high alkali content. Results confirm ability of SRA to reduce significantly drying shrinkage. Namely when sample is dried at 5%, a reduction of drying shrinkage of 63% and of 51% is reached for low alkali content and high alkali content respectively with regards to plain pastes. SRA in alkali medium reduces less the drying shrinkage compared to lower alkali contents, which is consistent with long-term drying shrinkage results.
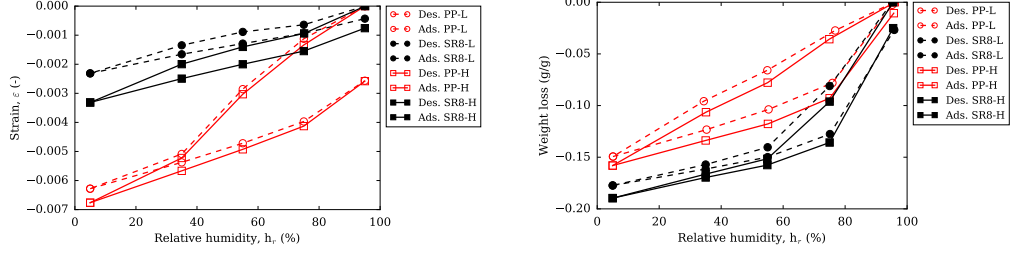
Figure 3.20: Short-term results of pastes at low alkali content plain paste (PP-L) and 8% content of SRA (SR8-L), at high alkali content plain paste (PP-H) and 8% content of SRA (SR8-H). Length change is presented on the left, and mass change on the right.

3.3.2 Short-term measurements of pre-dried cement pastes

Length change and weight loss of pre-dried plain pastes with various alkali contents are presented in figure 3.21. Results show that plain pastes share the following features regardless of alkali content:

- Length change is reversible, residual strain at RH of 95% on re-humidification is lower than 250 μm/m.

- Increase of length change is largest at RH range [55%-35%].

- Mass change is reversible: lost water upon desorption is regained after re-humidification to 95%.

- Mass change shows hysteresis over the entire range of studied RH: that is to say samples lose more water upon desorption than what it regains upon adsorption.

Length change and weight loss for pastes containing SRA at various alkali contents pre-dried at RH of 11%, are presented in figure 3.22. Results show that samples containing SRA have similar features observed for cement pastes that were not dried as shown in figure 3.19 and discussed in the previous section. We remind briefly these features:

116
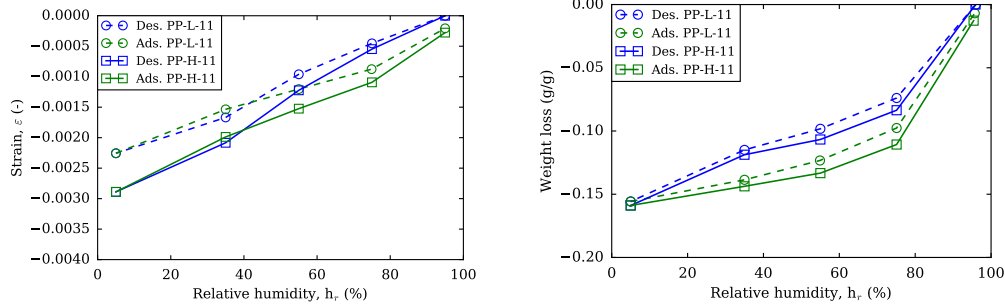
Figure 3.21: Short-term results of pre-dried plain pastes at low alkali content (PP-L-11) and at high alkali content plain paste (PP-H-11).

- Length change shows smaller irreversibility compared to plain paste, and exhibits a hysteresis on the range of RH investigated.

- Increase of length change is lowest at mid range of RH, that is [35%-55%].

- Increase of weight loss is high at RH>55% for pastes with SRA content 8% and at RH>35% for content of SRA of 4%.

- Increase of weight gain on the adsorption branch is higher at RH>75% compared to range of RH<75%.

Impact of prolonged drying on drying of cement pastes

In this section we investigate further the drying shrinkage behavior of pastes containing SRA that were kept under sealed conditions and pastes containing SRA that were dried slowly at 11% RH prior to measurements. Strain observed during short-term drying and subsequent re-humidification plotted in terms of weight loss is shown in figure 3.23 for samples containing SRA, that were not dried and that were subjected to drying at 11% prior to measurements.

Drying shrinkage isotherms are comparable for cement pastes containing SRA, both at pre-dried state and non-pre-dried state. However, for plain pastes, the long drying at 11% RH impacts the drying shrinkage isotherms of cement pastes as shown in figure 3.24. Results indicate that prolonged drying

117
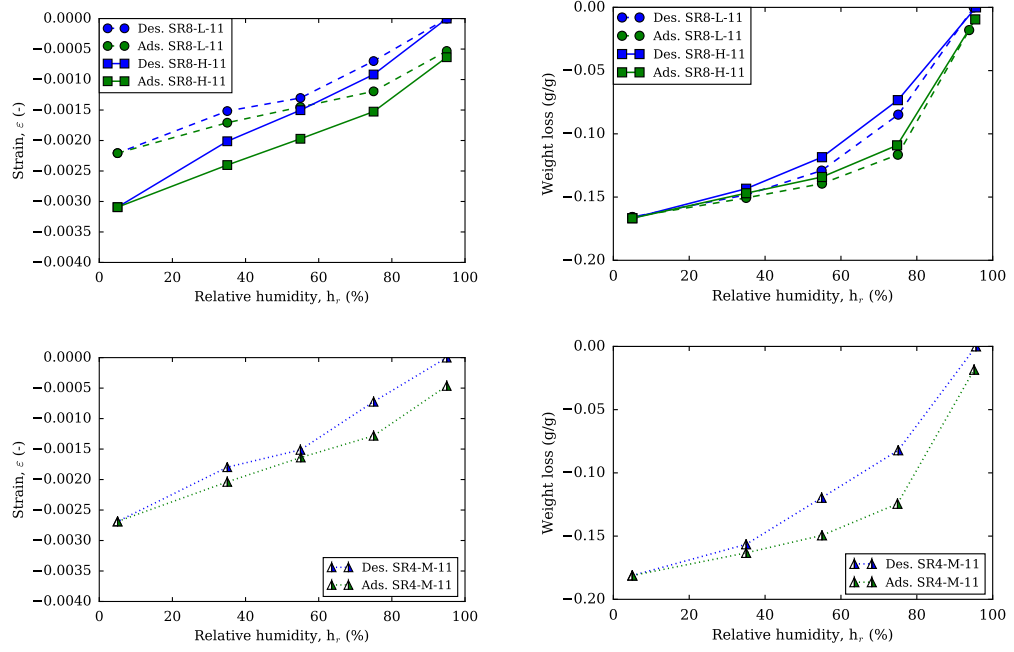
Figure 3.22: Short-term results of pre-dried pastes at low alkali content and
8% content of SRA (SR8-L-11), at high alkali content and 8% content of SRA
(SR8-H-11) and at medium alkali content and 4% content of SRA (SR4-M-
11).
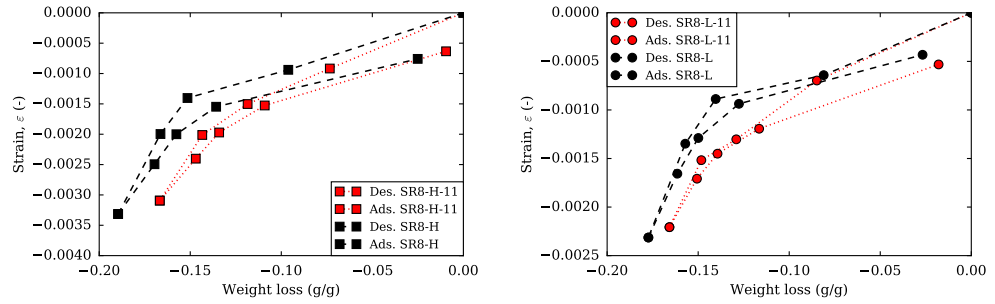
Figure 3.23: Short-term length change vs. mass change of pastes at low alkali
content and 8% content of SRA (SR8-L) and pre-dried to 11% (SR8-L-11),
at high alkali content and at 8% content of SRA (SR8-H) and pre-dried to
11% (SR8-H-11).
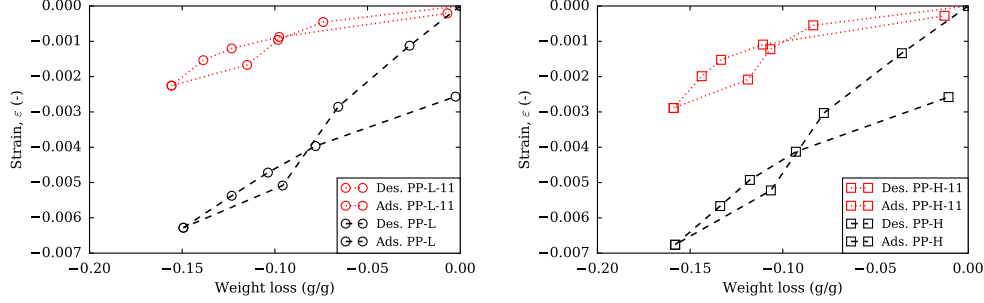
Figure 3.24: Short-term length change vs. mass change of plain pastes at low alkali content (PP-L) and pre-dried to 11% (PP-L-11), at high alkali content (PP-H) and pre-dried to 11% (PP-H-11).

at 11% RH of samples does not impact the drying shrinkage behavior and mass change behavior in contrast to plain pastes. Pore structure of samples containing SRA may not be altered significantly by the prolonged drying. Further investigations are made in section 4.4 confirming this explanation.

3.3.3 Analogies between prolonged drying and SRA addition

We notice that strain reached after the desorption branch by plain pastes pre-dried to 11% RH and by non-pre-dried pastes containing SRA have similar order of magnitude (as shown in figures 3.19 and 3.21). Let us investigate further the similarities shared by pre-dried plain pastes and non-pre-dried pastes containing SRA, as shown in figures 3.25 and 3.26 for low alkali content and high alkali content respectively. Length change of plain pastes that were dried slowly at 11% RH and that of pastes containing SRA show little irreversibility (below 750 μm/m). On the adsorption branch, increase of strain are similar for pre-dried plain paste and pastes containing SRA (except for plain paste low alkali range at the RH step from 75% to 95% RH). Increase of water uptake on adsorption branch is comparable for pre-dried cement paste and non-pre-dried pastes containing SRA.

These observations lead us to question the role of SRA in drying shrink-age, and how the prolonged drying at RH of 11% leads to similar features
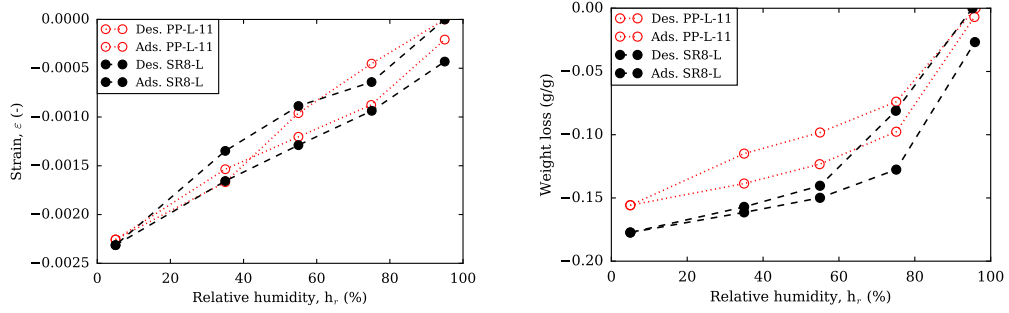
Figure 3.25: Short-term results of pastes at low alkali content and 8% content
of SRA (SR8-L) and plain paste pre-dried to 11% RH (PP-L-11).
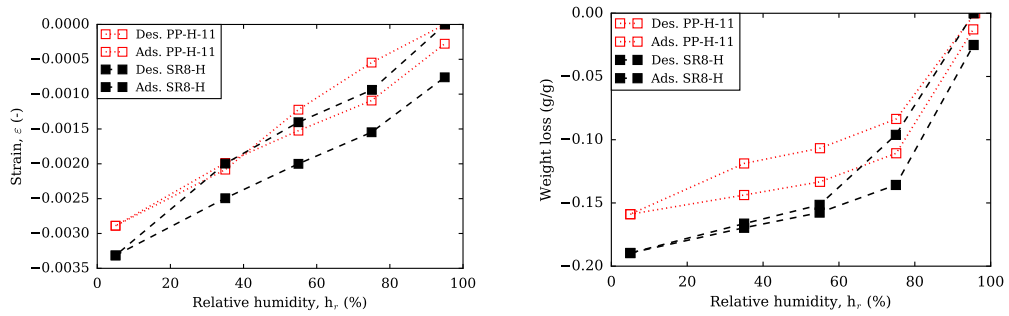
Figure 3.26: Short-term results of pastes at high alkali content and 8% con-
tent of SRA (SR8-H) and plain paste pre-dried to 11% RH (PP-H-11).

of drying shrinkage to addition of SRA. Two hypothesis may explain these analogies between pre-dried plain cement pastes and cement paste containing SRA (non-pre-dried and pre-dried):

1. SRA hinders the collapse of microstructure, assuming this collapse of microstructure contributes to the observed length change of cement paste.

2. Water is distributed in pore space of pre-dried plain pastes and non-pre-dried SRA pastes in similar manner.

Let us look at the first assumption. This assumption considers that the collapse of pore structure contributes to shrinkage. Pore structure of pre-dried plain pastes is stabilized as it was subject to a microstructural collapse (Maruyama et al., 2014). In case of pastes containing SRA, SRA may hinder this pore structure collapse, since short-term drying shrinkage isotherms of non-pre-dried SRA pastes and pre-dried SRA pastes are comparable, and they both show a small irreversibility. Thus, reduction of pore structure collapse may lead to a reduction of shrinkage and explains partly the analogies of pre-dried plain pastes and SRA pastes, since other mechanisms play a role in the drying shrinkage of cement pastes as introduced in section 2.3.2. The question that needs to be addressed is how the length change is related to pore structure changes, and whether length change leads to a pore structure change or the inverse, or rather both phenomena occur simultaneously. To have an indication on the link of length change and pore structure evolution, we study the reversibility of the pore structure. We find in section 4.5 that when plain paste is re-humidified to 95% RH after being dried to 11% RH (long-term drying, corresponding to pre-dried pastes) it recovers its surface area and its pore volume, whereas strain is not recovered. Changes of pore structure are found to be reversible. This supports the fact that pore structure changes are more likely a result of drying shrinkage of cement paste and the mechanisms of drying shrinkage than the inverse, since a sample that is re-humidified presents a similar pore structure (as will be later discussed in 4.5) but has a residual strain relatively to a cement paste with no drying history.
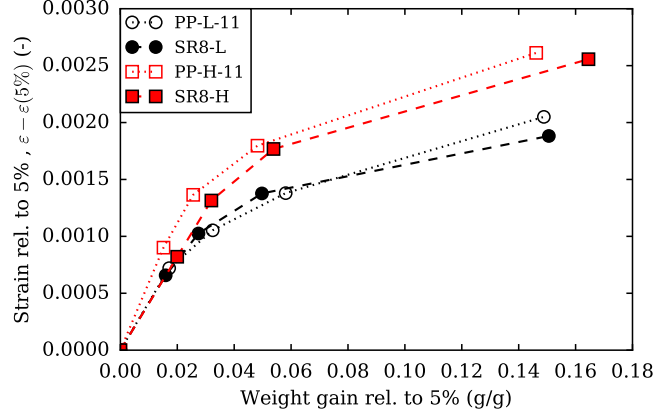
Figure 3.27: Short-term length change relative to 11%RH on the adsorption branch for a pre-dried plain paste at low alkali content (PP-L-11) and a paste at 8% content of SRA and low alkali content (SR8-L).

For the second assumption, let us examine the adsorption branch. We note that increase of length change and mass change of a pre-dried plain paste and non-pre-dried paste containing SRA are comparable, as shown in figure 3.27. Since uptake of water is made by surface adsorption on the low range of RH, by capillary condensation on the high range of RH, and possibly micropores filling, the similarities in water adsorption on both pastes may suggest that water is distributed in pore space of these cement pastes in similar manner. The removal/uptake of water from pore space of cement pastes leads to macroscopic length change. The differences of weight loss on drying of pastes containing SRA and pre-dried plain pastes may be linked to the action of SRA on the way the samples are emptied of their water content.

3.3.4   Post-hydration addition of SRA

In this section, we examine the impact of SRA on drying shrinkage with addition of SRA after hardening of cement paste. This allows to bypass the effects induced by SRA on pore structure of cement pastes when added during mixing (see section 4.2).

The amount of SRA in cement paste after measurements is assessed by es-

timation of organic carbon in sample. Samples contain an equivalent amount of 4.5 g per 100 g of cement paste $\pm$ 0.3, using mix design conditions it corresponds to $4.5 \times 1.55 = 6.9\%$ in mass of clinker.

Results of length change and mass change of plain paste at low alkali content to which SRA was added after hydration are shown in figure 3.28. We show also on the same plot results obtained for plain paste and paste containing 8% SRA at low alkali content for comparison purposes. Results show that SRA reduces the drying shrinkage of samples when added after hydration. The reduction is more significant in the mid range of RH 75% down to 55% than in the range of relative humidities below 55% or higher than 75%. The mass change is also modified by the SRA. In fact on the desorption branch the weight loss of cement paste with added SRA is higher in the RH range of 55% down to 35% and comparable at 75% and 5% compared to weight loss of plain paste at the same RH. However on the adsorption branch it regains water similarly to the plain paste. This observation is a strong indicator that a major role of SRA in cement paste is on the manner the water is removed from pore network of cement paste. Moreover we note that the increase of drying shrinkage on desorption branch from 35% to 5% is slightly larger for the plain paste with added SRA compared to plain paste, this may be explained by the possibility that SRA does not diffuse to the smallest pores of cement paste, compared to when SRA is present during the hydration of cement paste.

This finding suggests another practical use of SRA as curing agent (in the sense that SRA is added after hydration/hardening of cement paste) of cement paste enabling the reduction of drying shrinkage, and also avoiding drawbacks of reduction of hydration degree and pore structure changes. In fact Bentz (2005) found interest in this alternative use of SRA. Bentz (2005) tested the addition of SRA as a curing agent to mortar by spraying an SRA solution at concentrations of 10% and 20%. Their results focused on the availability of water for hydration in cement pastes relative to a plain paste subject to same RH condition. The length change however was not of interest in this study. Dang et al. (2013) later investigated the virtues of using SRA as a curing agent applied to mortar. Their results corroborate the results
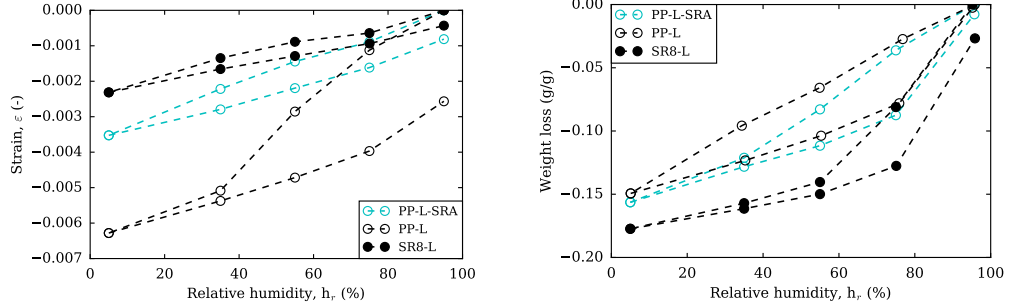
Figure 3.28: Length change (right) and mass change (left) of plain paste with added SRA after hydration (PP-L-SRA), a plain paste (PP-L) and paste with 8% content of SRA (SR8-L). All pastes are at low alkali content.

obained in this section, where addition of SRA as a curing agent leads to lower drying shrinkage. Morevoer, Dang et al. (2013) find that a combination of SRA and a curing compound proves more efficient than the use of each component separately.

3.4 Lessons learned from short and long-term measurements

3.4.1 Differences between short and long-term measurements

In this section we compare long-term measurements and short-term measurements of length change and mass change. Long-term measurements are accompanied by significant microstructural changes linked to the colloidal alteration of C-S-H as detailed in Maruyama et al. (2014, 2017). Short-term measurements enable the investigation of drying shrinkage behavior separately from these changes of pore structure.

Let us examine how long-term measurements and short-term measurement compare for the plain pastes and pastes containing SRA in figures 3.29 and 3.30. Drying shrinkage of plain pastes is larger for short-term measurements than for long-term measurements while weight loss shows an inverse

Figure 3.29: Short-term measurements and long-term measurements of plain
paste at low alkali content (PP-L) and high alkali content (PP-H). Length
change and mass change are computed relatively to 95% RH.

tendency for plains pastes. Weight loss of pastes containing SRA is compara-
ble for short-term measurements and long-term measurements. We also note
that for all studied samples, long-term measurements lead to lower length
change at RH lower than 55%, except for paste containing SRA at 8% con-
tent at high alkali content.

The differences between short-term measurements and long-term mea-
surements may originate from the aforementioned microstructural changes:
when cement paste is dried for prolonged periods its surface area decreases,
and its pore volume also varies (as will be detailed in section 4.4). If we
assume that surface effects govern drying shrinkage in the low range RH,
reducing the surface effects comes to a reduction of drying shrinkage. If we
consider a Gibbs-Bangham surface effects, then reducing the surface area
affected by an adsorbed film leads to a reduction of these surface effects.
Since prolonged drying leads to an evolution of the pore structure of plain
pastes, manifested by a reduction of surface area, the surface effects may be
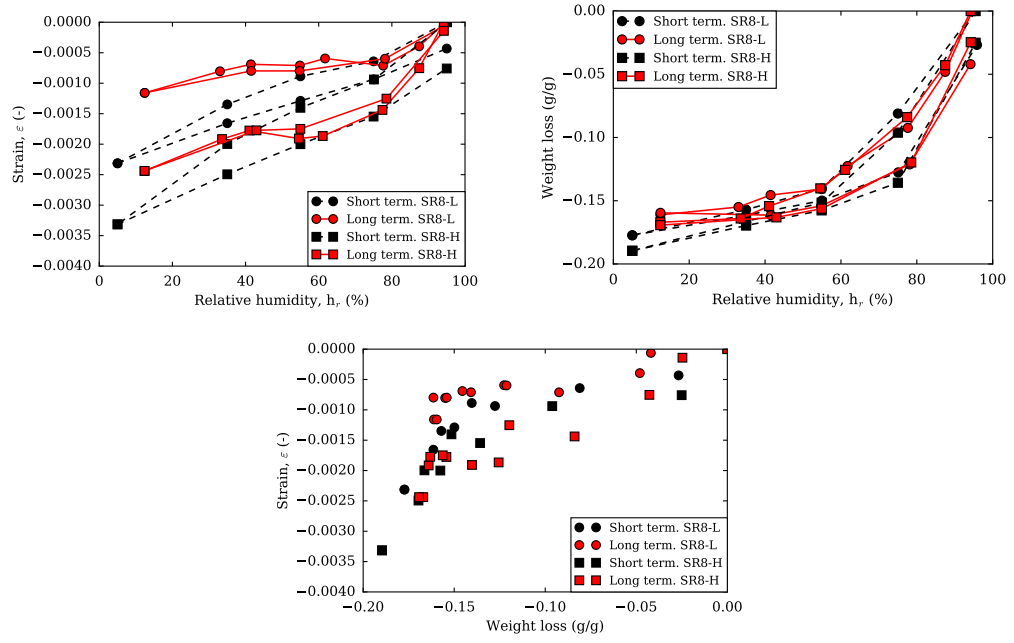
Figure 3.30: Short-term measurements and long-term measurements of paste containing 8% SRA at low alkali content (SR8-L) and high alkali content (SR8-H). Length change and mass change are computed relatively to 95% RH.
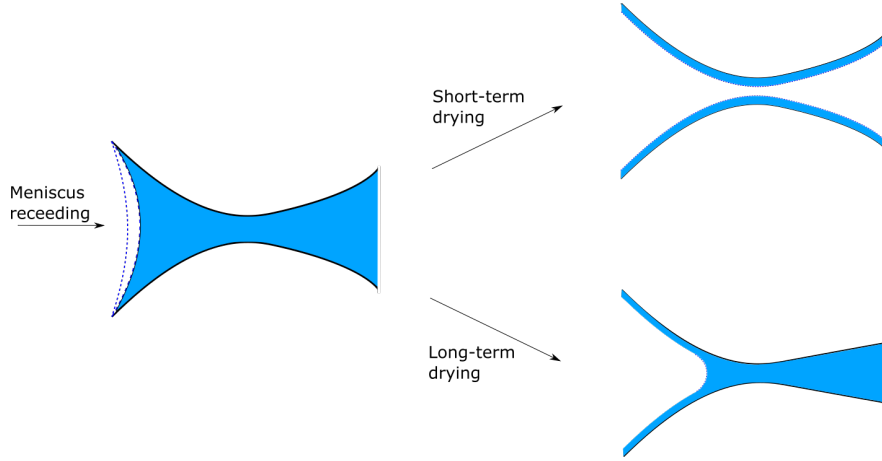
Figure 3.31: Schematic of the drying of pore on the short-term drying and
long term-drying. Long term-drying allows pore structure to evolve through
drying in contrast to the short-term measurements.

reduced as such. For pastes containing SRA, changes of pore structure dur-
ing the long-term drying are significantly reduced (as will be later detailed
in section 4.4). Long-term drying and short-term drying of pastes contain-
ing SRA are more comparable than those of plain paste. The comparability
of short-term drying and long-term drying of pastes containing SRA goes
in line with comparability of short-term drying shrinkage of non-pre-dried
pastes and pre-dried pastes. Figure 3.31 shows a schematic of how the pore
drying is imagined to take place in a pore of cement paste on the short-term
drying and the long-term drying.

3.4.2 Irreversibility of drying shrinkage

Let us recapitulate the observations regarding the irreversible shrinkage made
from previous measurements shown in this chapter:

- For plain pastes, drying shrinkage is irreversible for long-term measure-
  ments and short-term measurements, and the irreversitbility is larger
  for short-term drying than long-term drying, as shown in figures 3.8,
  3.9 and 3.10 for long-term measurements and figure 3.18 for short-term
  measurements.

- For pastes containing SRA, shrinkage shows little or no irreversibility, as measured by long-term measurements and short-term measurements, as shown in figures 3.8, 3.9 and 3.10 for long-term measurements and figure 3.19 for short-term measurements.

- For plain pastes, mass change is reversible for short-term measurements but irreversible for long-term measurements.

- For pastes containing SRA, mass change shows some irreversibility for both short-term measurements and long-term measurements.

One may suspect that the irreversibility of drying shrinkage of plain pastes is linked to the pore structure evolution and the potential partial collapse of porosity. However, as mentioned earlier and will be detailed in section 4.5, pore structure evolution are found reversible. A tentative explanation of the irreversibility of drying shrinkage is the ink-bottle effect occurring upon drying. The large irreversible shrinkage obtained for short-term drying may be explained by the fact that pore structure is highly disordered compared to the pore structure of paste that was dried. On drying the pore structure of cement pastes is reorganized and potentially the connectivity of the pores evolves to an "organized" configuration. As such, the ink-bottle effect would be more prominent in the non-pre-dried plain cement pastes compared to the pre-dried plain cement pastes. The origin of the irreversibility will be further detailed in modeling of drying shrinkage in 7.4.4.

3.4.3 Changes of surface properties by SRA

Water is often assumed wetting for cement pastes. However, SRA may change the surface properties of cement paste, and modify its wettability. Short-term drying shrinkage measurements show that reduction of drying shrinkage is largest in the range of RH of [35%-75%]. Moreover, results of long-term drying shrinkage isotherms and mass change isotherms show that weight loss and drying shrinkage at the range of RH [33%-75%] are not correlated, since removal of water in this range of RH does not induce a length change. This range is the same range where surface effects are dominant as explained in

section 2.3.2. This observation raises questions over how SRAs modify the surface properties, and how this possible modification leads to reduction of drying shrinkage.

Organic molecules are known to modify the wettability of surface of porous materials. In fact, presence of organic molecules in soils is at the origin of their water repellency (Doerr et al., 2000). When grafted by organic molecules silica gel becomes hydrophobic, drying shrinkage of these systems is reduced which proves beneficial for industrial production (Deshpande et al., 1992; Prakash et al., 1995; Zhou et al., 2008; Sarawade et al., 2010). The link of the changes of surface properties and shrinkage for these materials is explained by the elimination of the irreversible shrinkage which is caused by chemical cross-linking (Prakash et al., 1995; Sarawade et al., 2010) and the reduction of the capillary forces due to a reduction of surface tension (Zhou et al., 2008). SRA may adsorb on surfaces of cement pastes, forming hydrophobic patches. This may explain as well the changes in kinetics of drying observed by Bentz et al. (2001) where a drying front develops in the drying process of cement pastes, since this feature is observed when a hydrophobic porous material is dried (Shokri et al., 2008). However, Bentz (2006) measured contact angle on hardened cement paste of 7° for a SRA solution (concentration of 10%) and 28° for distilled water, which does not support the hydrophobicity of cement surfaces in presence of SRAs. We point that these measurements are conducted at the macro level, and may not reflect the nature of surfaces at the mesoporosity scale of cement paste. The adsorption of SRA may minimize the changes of surface energy: assuming that surface effects on length change can be accounted for by Gibbs-Bangham mechanism, reducing the surface energy allows reduction of drying shrinkage. The investigation of changes of surface properties induced by SRA will be examined in the following chapter by means of nitrogen and water adsorption.

3.5 Conclusions

In this chapter we have investigated the impact of SRA on drying shrinkage behavior of cement paste at the various alkali contents considered in this

study. This investigation was carried out using two methods: 1) long-term measurements and 2) short-term measurements. The first method corresponds to the classical approach of studying relatively large sized specimens (thickness of 3 mm) equilibrated for long periods of time ($\sim$ 6 months) at set relative humidities, controlled here by saline solutions. The second method corresponds to measurements of small sized samples (thickness of 0.5 mm) studied by TMA and TGA coupled with RH generator. The two methods enable to confirm the ability of studied SRA to reduce significantly the drying shrinkage of cement pastes, regardless of alkali content. The two methods were employed to study cement pastes that were never dried and cement pastes that were subjected to long-term drying. During this long-term drying, microstructure of cement pastes evolves (as introduced in 2.3.3 and studied in the next chapter 4.4). The use of two methods allows to dissociate the pore structure evolution observed during drying of cement pastes from the drying shrinkage.

The major results regarding the length change and mass change behavior are as follows:

- Cement pastes containing SRA show little or no irreversibility of drying shrinkage isotherms (as shown in figures 3.8, 3.9, 3.10 for long-term measurements, and figure 3.19 for short-term measurements), in contrast to the irreversibility observed for plain pastes (as shown in figures 3.8, 3.9, 3.10 for long-term measurements, and figure 3.18 for short-term measurements).

- SRA reduces drying shrinkage significantly at the range of RH of [33%-75%], where shrinkage is almost constant, while weight loss increases as shown in figure 3.13.

- For plain pastes, increasing alkali content does not impact on the mass change on drying and re-humidification, while it has little impact on the drying shrinkage as shown in figure 3.14.

- Performance of SRA in terms of drying shrinkage reduction is degraded in high alkali media as discussed in section 3.2.3.

- The addition of SRA to plain paste after hardening also enables the reduction of drying shrinkage, as shown in figure 3.28.

- Short-term measurements of plain pastes lead to a larger length change during drying for RH<54% compared to long-term measurements and the difference is larger as the drying RH decreases, as shown in figure 3.29.

Chapter 4

Impact of SRA on microstructure

In this chapter we investigate the effects of SRA on microstructure of cement paste. First, we analyze the impact of SRA on the hydration of cement paste. Through a combination of X-ray diffraction measurements (XRD) with Rietveld analysis, and thermogravimetric measurements (TGA), we assess the influence of SRA on the degree of hydration and the formed hydrates. Second, we investigate the impact of SRA on the developed pore structure before the prolonged drying. Two pre-drying techniques are used, namely solvent exchange and vacuuming at room temperature. The two pre-drying methods tested allowed evaluation of developed pore structure and gave insight into the location of SRA in cement paste. Pore structure is also analyzed after prolonged drying at various relative humidities. We analyze the impact of SRA on pore structure, as evaluated by pore size distribution and specific surface area (SSA), by means of mercury intrusion porosimetry (MIP), nitrogen sorption isotherms and water sorption isotherms (volumetric method).

4.1   Methods

In this section we present the methods employed in this work to analyze microstructure of cement pastes. The methods enable characterizing the

microstructure from chemical and physical points of view:

- The hydration degree is estimated for cement pastes by combining measurements of XRD and TGA. The phase assemblage is also obtained by combination of these two techniques. The amount of portlandite and calcite can be evaluated as well by TGA measurements.

- The pore structure is analyzed by means of MIP giving a pore entry size distribution. Nitrogen sorption measurements and water sorption measurements also help estimating a pore size distribution and specific surface area. The pore volume can also be evaluated by these measurements.

4.1.1 Methods of phase assemblage analysis

In this section we introduce the methods of phase assemblage analysis. Two techniques are employed:

1. X-ray diffraction with Rietveld analysis (XRD)

2. Thermogravimetric method analysis (TGA)

X-ray diffraction is a method that allows identification of crystalline phases present in the tested sample. Rietveld analysis allows the quantification of the present phases. Thermogravimetric method analysis consists in putting the sample in a set environment (nitrogen, dioxygen..) and subjecting it to increasing temperatures. The phases present in the sample decompose at characteristic ranges of temperatures, and the mass loss of the sample is monitored. This mass loss helps quantifying the identified phases.

The hydration degree is estimated for cement pastes by combining measurements of XRD and TGA. The phase assemblage is also obtained by combination of these two techniques, allowing to quantify the phases of cement pastes, namely portlandite, ettringite, calcite and the amorphous phase. The amount of portlandite and calcite can be evaluated as well by TGA measurements.

We detail in the following the preparation method conducted prior to XRD and TGA measurements. We do note that the same preparation method was used prior to XRD and TGA measurements. Samples were cured in sealed aluminum bags until the desired age is reached (namely 7, 14, 28 days, 3 months, 6 months and 1 year). The samples were dried to stop the hydration from progressing. The hydration stoppage is required for the early ages for which the progress of hydration is significant compared to older ages (>28 days) where hydration progresses at slower rates. The drying method to stop hydration efficiently used here was freeze drying (Aligizaki, 2006, p. 37). This method consists in reducing the temperature of the cement paste by liquid nitrogen quenching, then decreasing pressure by placing the sample under vacuum, and finally increasing gradually the temperature to the ambient temperature while keeping the sample under vacuum (the vacuum pump could reach a theoretical value of 6.7×10^{-4}mbar). This process allows to sublimate the formed ice. All samples were freeze dried except for samples of age of 6 months. These samples were not dried prior to XRD and TGA measurements to enable identifying the impact of SRA on formed hydrates independently from the pre-drying impact (Scrivener et al., 2016, p. 22). The samples were crushed and sieved below 100 μm for TGA measurements and below 63 μm for XRD measurements. The powder was then tested directly in XRD and TGA, to quantify the formed hydrates, and assess the degree of hydration of samples.

We used the X-ray diffractometer X'Pert Pro X'Celerator detector, the 2θ ranges scanned from 5° to 65° with a scan speed of 0.016°/min. We used an internal reference to quantify identified phases: powder cement paste is mixed with a known quantity of corrundum, that serves as a reference to quantify the crystalline phases, and the amorphous phases.

Thermogravimetric analysis was conducted on the crushed cement pastes. Unless specified otherwise, the measurements were conducted under nitrogen environment with a flow of 20 mL/min and heating rate of 10 K/min, using an open vessel. The range of temperature was from 20 °C to 1000 °C.

XRD measurements and TGA measurements are combined to assess the

degree of hydration, following (Termkhajornkit et al., 2015):

$$\alpha = 1 - \frac{W(t)/(1 - W_w)}{W(t = 0)} \tag{4.1}$$

where $W(t)$ is the mass fraction of anhydrous phases (C_3S, C_2S, C_3A and C_4AF) of the hydrated cement paste at the given time t, $W(t = 0)$ is the mass fraction of anhydrous phases of the clinker before hydration $W(t = 0) \simeq 1$. $W(t)$ and $W(t = 0)$ are evaluated by XRD measurements. W_w stands for the mass fraction of evaporable water (if cement paste is not dried before the measurement) and non-evaporable water of the hydrated cement paste. W_w is evaluated by TGA measurements and is equal to the mass loss $W_{TGA}(20°C - 550°C)$ between 20 °C and 550 °C following:

$$W_w = W_{TGA}(20°C - 550°C) \tag{4.2}$$

Note that for pastes containing SRA, W_w includes also the mass loss $W_{TGA}(180°C - 200°C)$ due to SRA as will be justified later.

Degree of hydration of each of the anhydrous phases is computed as follows:

$$\alpha_x = 1 - \frac{W_x(t)/(1 - W_w)}{W_x(t = 0)} \tag{4.3}$$

where α_x is the degree of hydration of the phase x that stands for C_3S, C_2S, C_3A or C_4AF. $W_x(t)$ and $W_x(t = 0)$ are the mass fractions of anhydrous phase x of the hydrated cement paste at the given time t and of the clinker before hydration respectively.

Phase assemblage of cement pastes is based on results of XRD for identification and quantification of phases, and makes use of TGA to normalize with regards to mass of ignited cement. The mass fraction f_x of phase x with regards to this ignited mass is computed as follows:

$$f_x = \frac{W_x(t)}{1 - W_w} \tag{4.4}$$

where W_w is evaluated following equation 4.2.

Note that only major phases are reported and normalized to mass of

ignited cement (approximating mass of clinker). This means that sum of all phases is larger than 100%. We normalize to mass of ignited mass to enable comparison of plain pastes and pastes containing SRA.

The C/S ratio of the amorphous phase can be evaluated by mass balance of the phases of clinker and of the phases of hydrated cement paste. Let $C_C(t)$ be the molar amount of CaO originating from the clinker phases which are the anhydrous phases and other phases (i.e., calcite, gypsum, hemihydrate and anhydrite, calcium hydroxide). $C_C(t = 0)$ corresponds to the molar amount of CaO in the clinker (before hydration) and $C_C(t)$ the molar fraction of CaO in the hydrated cement pastes, determined following:

$$C_C(t = 0) = 3n_{C_3S} + 2n_{C_2S} + 3n_{C_3A} + 4n_{C_4AF} + n_{C\bar{C}} + n_{C\bar{S}H_2} + n_{C\bar{S}H_{0.5}} + n_{C\bar{S}} \tag{4.5}$$

$$C_C(t) = 3n_{C_3S} + 2n_{C_2S} + 3n_{C_3A} + 4n_{C_4AF} + n_{C\bar{C}} + n_{CH} + n_{C_6A\bar{S}_3H_{32}} \tag{4.6}$$

where n_X is the molar amount of phase X.

$C_S(t)$ is the molar amount of SiO_2 of the hydrated cement paste and the clinker, originating from C_3S and C_2S, we can write:

$$C_S(t) = n_{C_3S} + n_{C_2S} \tag{4.7}$$

The molar ratio of C/S of the cement paste can be evaluated by attributing the remaining CaO or SiO_2 of the initial composition of clinker and the hydrated cement to the amorphous phase following:

$$\text{C/S} = \frac{C_C(t = 0) - C_C(t)}{C_S(t = 0) - C_S(t)} \tag{4.8}$$

Portlandite $Ca(OH)_2$ and calcite $CaCO_3$ are also evaluated by using TGA measurements. In fact, porltandite dehydroxylates following:

$$Ca(OH)_2 \rightarrow CaO + H_2O \tag{4.9}$$

and calcite decarbonates following:

$$CaCO_3 \rightarrow CaO + CO_2 \tag{4.10}$$

The mass fraction of portlandite m_{CH} and calcite $m_{C\bar{c}}$ per mass of cement paste are measured following:

$$m_{CH} = W_{CH} \times \frac{M_{CH}}{M_H} \tag{4.11}$$

where W_{CH} is the mass loss associated to portlandite, M_{CH} is the molar mass of portlandite, and M_H is the molar mass of water;

$$m_{C\bar{c}} = W_{C\bar{C}} \times \frac{M_{C\bar{C}}}{M_{\bar{C}}} \tag{4.12}$$

where $W_{C\bar{C}}$ is the mass loss associated to calcite, $M_{C\bar{C}}$ is the molar mass of calcite, and $M_{\bar{C}}$ is the molar mass of carbon.

Molar masses M_{CH}, $M_{C\bar{C}}$, M_H and $M_{\bar{C}}$ of portlandite, calcite, water and carbon dioxide respectively are given in table 4.1.

Phase	Formula		Molar mass (g/mol)
Calcium hydroxide	CH	$Ca(OH)_2$	74.1
Calcite	$C\bar{C}$	$CaCO_3$	100.1
Water	H	H_2O	18
Carbon dioxide	$\bar{C}$	CO_2	44

Table 4.1: Molar mass of phases portlandite, calcite, water and carbon dioxide.

The range of temperature where portlandite dehydroxylates is between $\sim$400 °C and $\sim$500 °C. Calcite decarbonates in a range between $\sim$600 °C and $\sim$800 °C (Scrivener et al., 2016, p.190). The exact delimitation of the range of decomposition of the phases is conducted based on the differential thermogravimetric (DTG) curve. Furthermore, the mass loss of the phases is assessed based on the stepwise method.

The ESEM observations were also performed on polished sections with energy dispersive X-Ray analysis with a FEG quanta 400F, with a beam

current of 1 nA, an accelerating voltage of 15 kV and a 10 mm working distance.

4.1.2 Methods of pore structure analysis

The pore structure is analyzed by multiple techniques. The cement pastes are characterized by means of:

1. Mercury intrusion porosimetry allowing to evaluate the pore entry size distribution;

2. Nitrogen sorption isotherms to estimate pore size distribution and specific surface area;

3. Water sorption isotherms to evaluate specific surface area.

These 3 techniques enable the evaluation of the pore volume as well.

Prior to mercury intrusion porosimetry, nitrogen sorption isotherms and water sorption isotherms measurements, cement paste needs to be dried. In our study two drying methods are used:

- Solvent exchange;

- Vacuuming at room temperature.

For solvent exchange, we used the same protocol as defined in Muller (2014). Samples were sawed to small pieces of 2 mm thickness. They were then immersed in isopropanol for 1 week. The isopropanol was renewed after 1 day, then after 3 days. After isopropanol immersion, the samples were placed in a dessicator for 1 week and subjected to vacuum (vacuum pump with theoretical pressure 6.7×10^{-4} mbar) at room temperature.

As for vacuuming at room temperature, the procedure is adapted for each targeted measurements. For nitrogen sorption measurements and mercury intrusion porosimetry, the samples were coarsely crushed into pieces of a size below 1.1 mm. An amount of 100 mg is then placed under vacuum condition for nitrogen sorption measurements. For MIP measurements, the amount needed is around 1 g. The sample is left under vacuum condition for 24

hours. For water sorption measurements, the sample was ground manually with a mortar and pestle and then sieved. The fraction of sample with a size larger than 25 μm and smaller than 75 μm was used for the measurements. An amount of $\sim$25 mg was dried under vacuum at room temperature for 45 min prior to measurement.

The device used for MIP measurements is of type Autopore IV provided by Micromeritics, the maximum reached pressure is 414 MPa, corresponding to a pore entry diameter of 3 nm.

Nitrogen sorption measurements were conducted by a Belsorp Mini 2 provided by Microtrac-bel, and the range of relative pressure p/p_0 ranges from 0.01 to 0.99.

Note that for nitrogen, the kink volume, corresponding to the volume of fluid that cavitates, is assessed from desorption branch by computing the difference of adsorbed volume at relative pressure of 0.51 and 0.42. This volume is the volume of pores connected to the outside by an entry radius of $\sim$ 2.1 nm. This size is estimated for a relative pressure 0.51 as the sum of Kelvin radius and thickness of adsorbed layer (evaluated by Harkins and Jura (1944)).

Water sorption measurements were conducted by a VSTAR vapor sorption analyzer (Quantachrome Instruments) at a temperature of 20 °C. At least two measurements per sample were conducted for samples that were conditioned prior to pre-drying under sealed conditions. For samples conditioned at various relative humidities, measurements were repeated for chosen samples, hence error bars (corresponding to standard deviation of the measurements) are shown for measurements that were repeated. Samples for water sorption measurements were vacuumed at room temperature prior to measurements.

4.2 Results of impact of SRA on microstructure

In this section, we examine the impact of SRA and alkali on the degree of hydration of the 9 types of cement pastes, at the various contents of alkali and SRA. The degree of hydration is examined with regards to its correlation to the content of SRA and alkali, as well as its evolution through time. The phase assemblage obtained by XRD will then be discussed.

4.2.1 Impact of SRA on degree of hydration

Degree of hydration of the 9 types of cement paste at ages of 3 months and 6 months is computed. Degree of hydration of cement pastes in terms of the SRA content for the various alkali contents is shown in figure 4.1. The degree of hydration of cement paste (average degree of hydration) decreases with the addition of SRA. This decrease is observed regardless of the alkali content, and can reach 15% in case of low alkali content cement pastes containing 8% SRA at the age of 3 months. We remind that the solution to clinker mass ratio (e.g., the ratio of SRA and water to clinker in mass) is 0.55, and that the samples were cured under sealed conditions for 3 months.

Degree of hydration of pastes at chosen ages (7 days, 3 months and 6 months) is shown in figure 4.2. Higher contents of alkali lead to higher degree of hydration of pastes at 7 days. At ages of 3 months and 6 months, degree of hydration does not depend on the content of alkali.

Since a decrease of degree of hydration with SRA content is observed for cement pastes at an age of 6 months, let us investigate the evolution of the degree of hydration through curing time, from 7 days to a 1 year span. Figure 4.3 shows the degree of hydration of plain pastes and pastes containing 8% SRA content at low alkali, medium alkali and high alkali content, respectively. At 1 year, the degree of hydration of cement pastes with 8% SRA content is slightly lower than the degree of hydration of plain pastes. The hydration of the cement pastes in the presence of SRA is significantly retarded at low ages, however it is not "stopped" since it progresses through
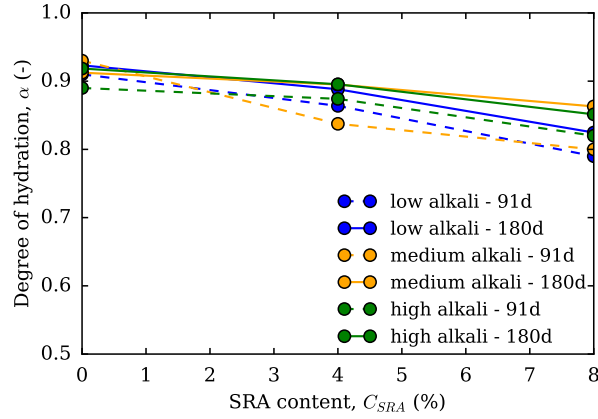
Figure 4.1: Degree of hydration of cement pastes at two ages: 3 months and 6 months, at the low alkali content, medium alkali content and high alkali content.
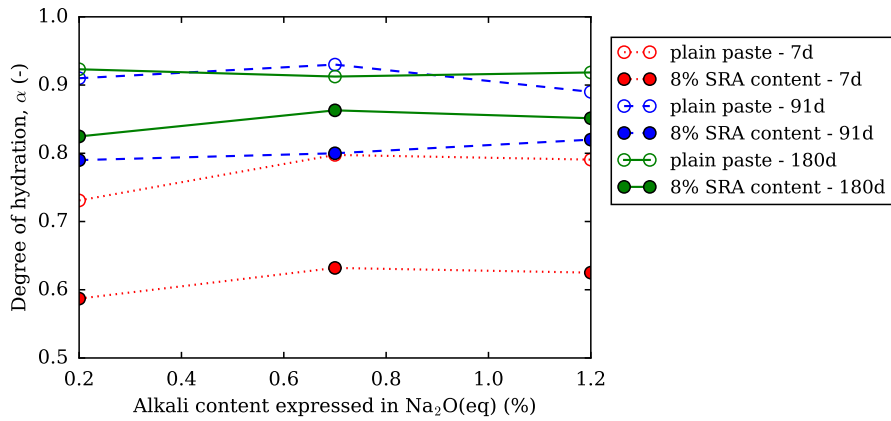
Figure 4.2: Degree of hydration of cement pastes at three ages (7 days, 3 months and 6 months) in terms of alkali contents for plain pastes and pastes containing 8% SRA content.
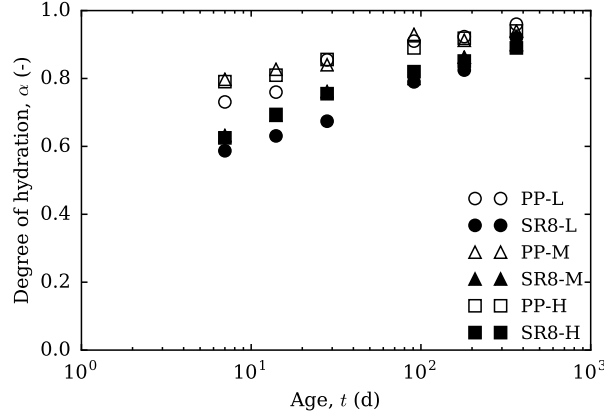
Figure 4.3: Degree of hydration of pastes at various alkali contents, for plain pastes (hollow symbols) PP-L, PP-M and PP-H at low alkali content, medium alkali content an high alkali content respectively, and pastes at 8% SRA content (filled symbols) SR8-L, SR8-M and SR8-H at low alkali content, medium alkali content an high alkali content respectively.

curing time.

The retardation of the hydration in presence of SRA being confirmed, let us examine in more depth the impact of SRA on the degree of hydration of the anhydrous phases. Average degree of hydration of the cement paste, as well as of each anhydrous phase -both silicate and aluminate phases- is shown in figure 4.4 for pastes at low alkali content, medium alkali content and high alkali content. The aluminate phase C_3A is hydrated for 9 types of cement paste. The degree of hydration of ferrite phase C_4AF is the most impacted by the addition of SRA. The degree of hydration of the silicate phases C_3S and C_2S is reduced for cement pastes containing SRA compared to plain pastes.

The alkali impacts the degree of hydration only at the early ages. These results support findings of Jawed and Skalny (1978) that reported the acceleration of hydration in presence of alkalis. Juenger and Jennings (2001) also reported an increase of hydration of cement paste with high content of alkali (alkali content was modified by addition of NaOH to mix water in this study) only at early age (less than 1 day), however at later ages Juenger and

143
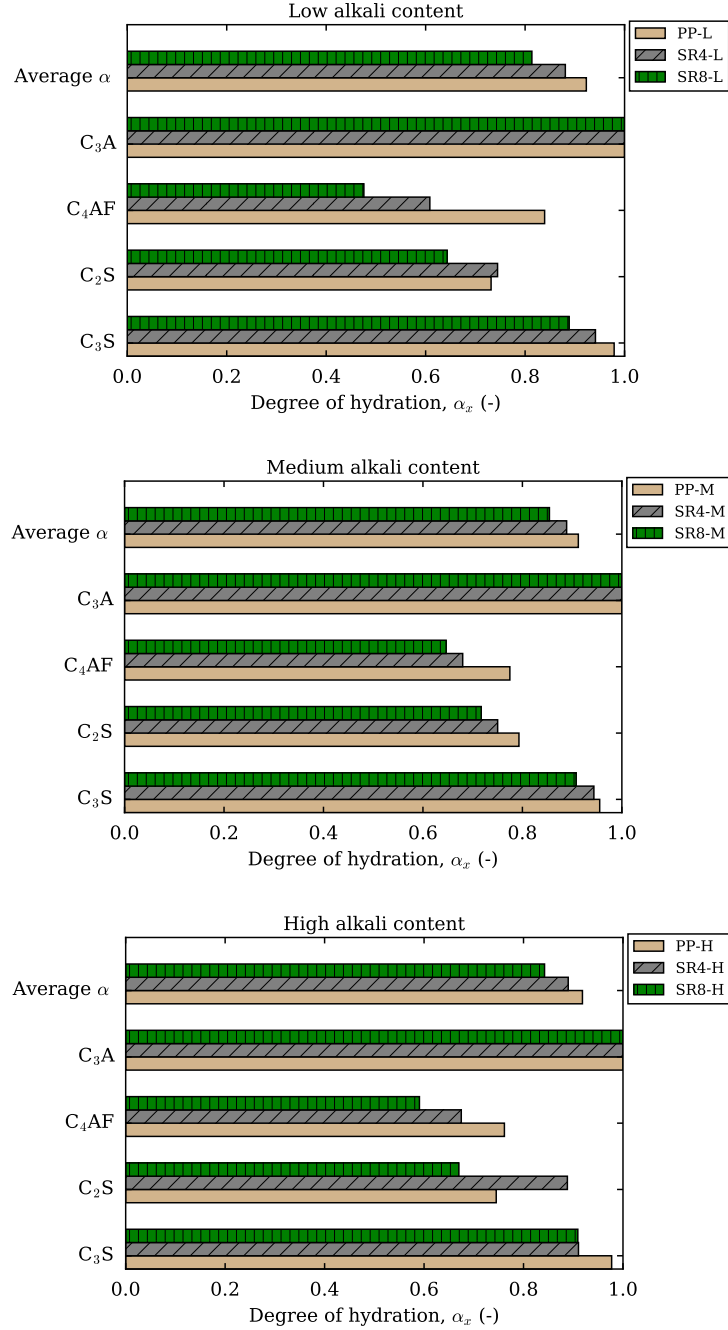
Figure 4.4: Degree of hydration of the anhydrous phases and of the cement paste at low alkali content, medium alkali content and high alkali content. Results are shown for plain paste PP-(L,M,H), paste at 4% content SR4-(L,M,H) and paste at 8% content SR8-(L,M,H).

Jennings (2001) report that hydration is retarded by the presence of alkali.

Although the impact of SRA on hydration of cement pastes was reported by several authors (detailed in section 2.5.3), few investigated causes of this retardation of hydration. It should be reminded that addition of SRA to mixing water was done by replacing equivalent mass of water by SRA. This means that actual water to clinker ratio is lower than for plain paste: it decreases from 0.55 in the case of plain paste to 0.47 in case of pastes containing 8% SRA. The water to clinker ratio remained higher than 0.42 to 0.44, which is necessary to reach complete hydration (Taylor, 1990, p. 120). Therefore, complete hydration of cement pastes may not be hindered due to the decrease of w/c ratio. The possible adsorption of the SRA on anhydrous phases or hydrates may also lead to decrease of hydration. However, Ai and Young (1997) found no evidence of adsorption of SRA (commercial SRA based on DPTB) on cement hydrates or anhydrous phases. Finally, Eberhardt (2010) found by means of leaching experiments that SRA (several SRAs among which a commercial SRA composed mainly of DPTB) does adsorb on cement hydrates, portlandite mostly. This adsorption provides an explanation for retardation of hydrates of silicate phases in his study. Since the hydration of cement pastes containing SRA is only retarded, and does progress through time, the impact of SRA on hydration through adsorption on anhydrous phases, or on formed hydrates may not be enough to explain the retardation of hydration, if we assume that adsorption occurs in an irreversible manner. The adsorption of SRA on hydrates for the SRA studied here will be further investigated in section 5.4. Rajabipour et al. (2008) studied the impact of SRA (SRA studied was a commercial SRA consisting mainly of poly-oxyalkylene alkyl ether) on the pore solution of cement paste. Their results showed that the presence of SRA in extracted pore solution of cement pastes led to a lowering of dissolution of alkalies in the pore solution, which may explain the decrease in the hydration rate of cement paste containing SRA. In our study, the impact on the hydration was observed for cement pastes containing high alkali content as well. The impact of SRA on the composition of pore solution will be further investigated in section 5.

4.2.2 Phase assemblage of pastes

Phase assemblage of 9 types of cement pastes studied at the age of 6 months is shown in figure 4.5. Amount of anhydrous phases is larger in the case of cement paste containing SRA since SRA reduces the degree of hydration. Amount of ettringite increases in case of low alkali content in the presence of SRA, and increases at increasing content of alkalis as observed for paste at an age of 6 months. For pastes at an age of 3 months, ettringite is not detected because of the preparation method consisting of freeze drying, which leads to strong dehydration of ettringite (Mantellato et al., 2016). Amount of portlandite is not significantly impacted by hydration retardation. Portlandite is produced by the hydration reaction of the silicate phases C_3S and C_2S, the amorphous phase is also a product of these hydration reactions. Reducing the hydration degree of the silicate phases in presence of SRA at almost constant amount of portlandite suggests that SRA impacts the stoichiometry of the formed C-S-H gel. We will detail the potential impact of SRA on the stoichiometry of C-S-H in the next section.

4.2.3 Impact of SRA on stoichiometry of C-S-H

Mass balance of cement paste composition before and after hydration based on XRD and TGA measurements allowed estimation of C/S ratio of cement pastes. Results are shown in figure 4.6. Results suggest that C/S ratio decreases form ~ 1.7 to ~ 1.4 in case of cement paste containing SRA at low alkali content.

A tentative measurement to confirm the impact of SRA on C/S ratio of the amorphous phase was conducted by means of scanning electron microscopy with X-ray analysis (SEM-EDS). Results are shown in figure 4.7. Results show that a large distribution of C/S ratio of values larger than 1.7, since the molar ratio of Si/Ca is around 0.4-0.5, linked to a C/S larger than 1.7. The high C/S ratio may be due to the intermixed portlandite with C-S-H gel (Chen et al., 2010), and to the limitations of the technique where scanning zone includes a large fraction of the hydrates and may not accurately scan C-S-H only. In the appendix D, we show the histogram of
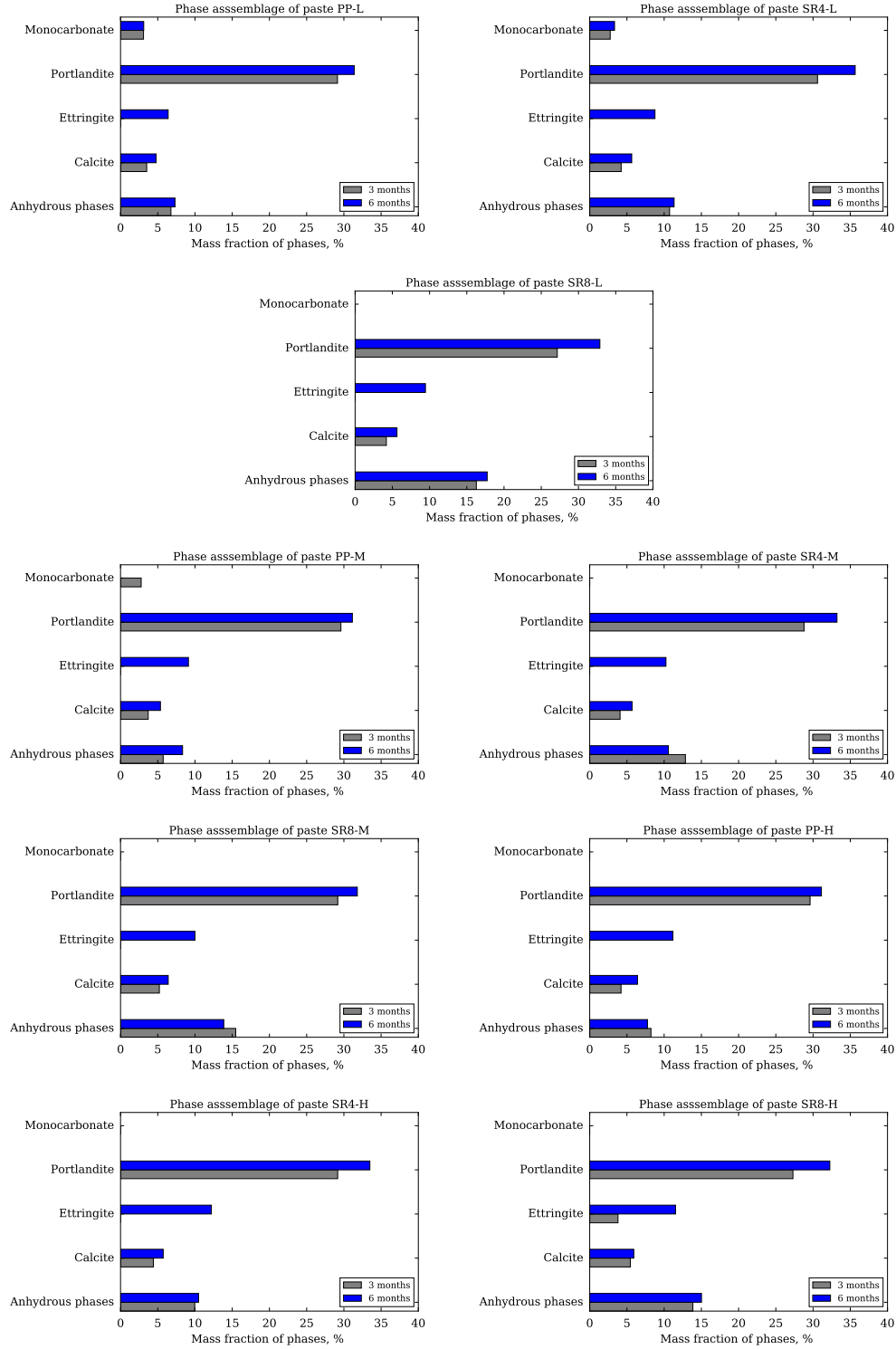
Figure 4.5: Amount of anhydrous phases, and major phases of hydrated cement pastes at an age of 3 months and 6 months.
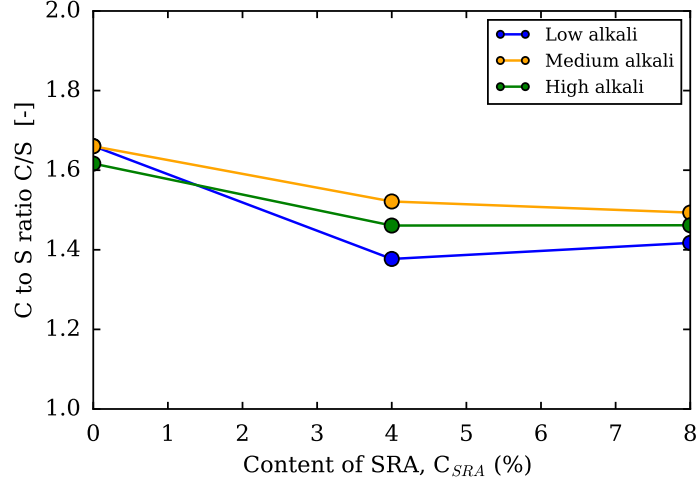
Figure 4.6: Evaluated C/S ratio of the amorphous phase in terms of the SRA content, for the various alkali contents, based on mass balance of cement pastes.

distribution of the obtained ratio of Si/Ca. Using this technique we are not able to confirm the suspected effect of SRA on composition of formed C-S-H. This result needs further investigation to confirm impact of SRA on composition of C-S-H, other experimental techniques such as transmission electron microscopy (TEM) may prove useful in this case.

4.2.4 Impact of SRA on TGA measurements

In this section, we examine the influence of SRA on the results of TGA measurements. Figure 4.8 shows TG and DTG curves obtained from TGA measurements for low alkali plain cement paste and cement pastes containing SRA at contents of 4% and 8%. A particular peak on DTG curves of only pastes containing SRA is observed at temperatures 180 °C to 210 °C. In fact this peak is associated to the boiling point of SRA, for which the theoretical boiling temperature is 197 °C. This was further confirmed by testing SRA only in TGA; results are shown in figure 4.9.

Figure 4.10 is the combination of results of 4 TGA measurements. Amount of portlandite and calcite of paste at low alkali content and 8% content of
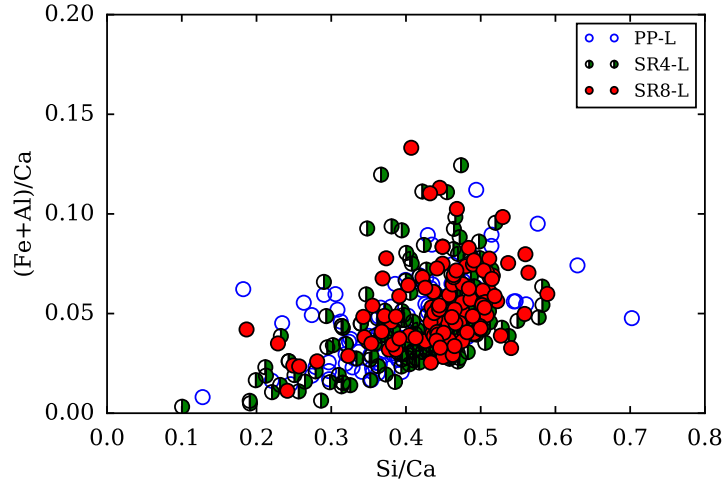
Figure 4.7: The molar ratio of (Fe+Al)/Ca in terms of Si/Ca based on SEM-EDS analysis of plain paste (PP-L), paste at 4% SRA content (SR4-L) and paste at 8% SRA content (SR8-L), at low alkali content.
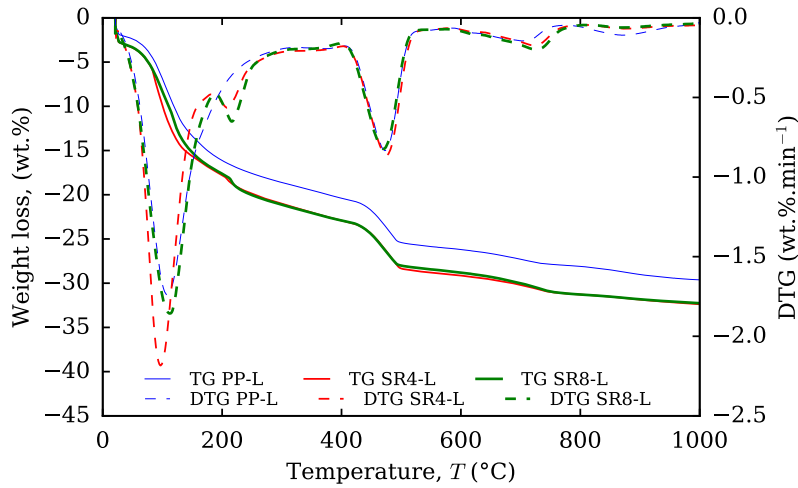
Figure 4.8: TGA results and DTG results for low alkali content samples for a plain paste (PP-L), paste containing 4% SRA (SR4-L) and 8% SRA (SR8-L).

149
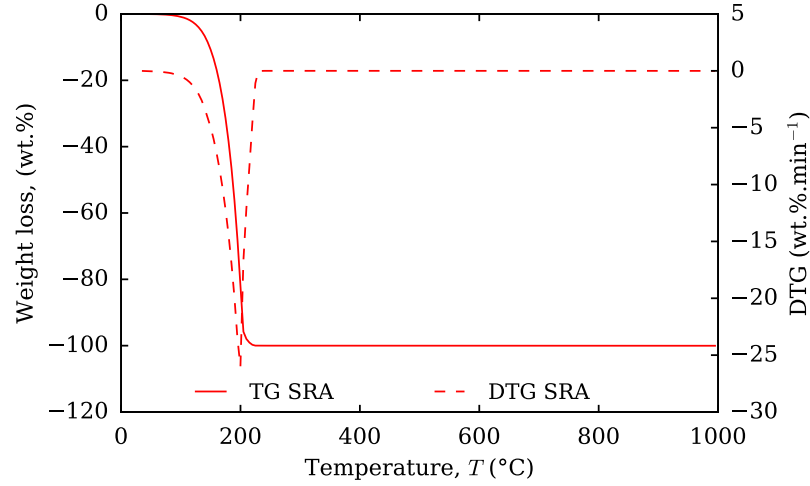
Figure 4.9: TGA results and DTG results for SRA only.

SRA was assessed under 2 heating rates $10\,°C/min$ and under $30\,°C/min$, and under two environments nitrogen and dioxygen. At a given heating rate, the amount of calcite increases and the amount of portlandite decreases, when the TGA measurement is conducted under dioxygen instead of nitrogen. In addition to that, the amount of calcite increases with increasing heating rate, while the portlandite amount decreases. In fact, SRA ($C_6H_{14}O_2$, 2-Methyl-2,4-pentandiol) used in our study contains 6 molecules of carbon, 2 molecules of oxygen and 14 molecules of hydrogen. A rudimentary approach consists in considering that one molecule of SRA may produce one molecule of carbon dioxide, or in the presence of another source of dioxygen, can give up to 6 molecules of carbon dioxide. This may explain why conducting TGA measurements under oxygen leads to lower portlandite amounts and higher calcite amount for the same cement paste compared to conducting TGA measurement under nitrogen flow. Furthermore, if we assume that SRA releases CO_2 molecules that carbonate the cement paste, increasing the rate of heating means that at a given temperature, the amount of CO_2 molecules is higher relative to a lower rate, as the flow of protecting gas (nitrogen or dioxygen) is kept constant in all 4 measurements. This may explain why increasing the rate of heating leads to lower portlandite amount and higher

calcite amount for the same cement paste. These observations show that the SRA contributes to the carbonation during the TGA measurements, by producing CO_2 that reacts with hydrates of the cement paste, in particular portlandite.

Several authors (e.g., Taylor (1990); Zhang and Scherer (2011)) observed that organic molecules may cause an in-situ carbonation of cement pastes during TGA meausrement. In particular, when the cement paste is soaked in solvent to stop hydration or to dry before TGA measurement, larger amounts of calcite are reported. Zhang and Scherer (2011) observed that when solvent exchange (using ethanol and acetone) is conducted previous to TGA measurements larger carbonation is observed compared to other drying techniques such as freeze-drying. Deeper investigations were carried out by Mitchell and Margeson (2006) and Knapen et al. (2009). Mitchell and Margeson (2006) showed that a chemical reaction of acetone occurs with portlandite. The authors speculate that the reaction occurs on heating of the samples, through release of CO_2 that would react with portlandite. Knapen et al. (2009) also studied the impact of solvent exchange, among other drying techniques, on carbonation by means of Fourier transform infrared spectroscopy (FT-IR), among various experimental techniques. The authors studied a Portland cement paste by solvent exchange using methanol, ethanol and ethanol+ether, and also studied FT-IR spectroscopy profiles of cement paste with solvent exchange heated to 550 °C. The authors found that solvents react strongly with cement paste when heated, and form carbonate-like phases.

The chemical composition of cement pastes at various contents of alkali and SRA were examined. In the next section, we explore the impact of SRA on pore structure of cement paste after curing under sealed conditions for 3 months, and after drying to various relative humidities. The pore structure developed after re-humidification is also examined for chosen samples.
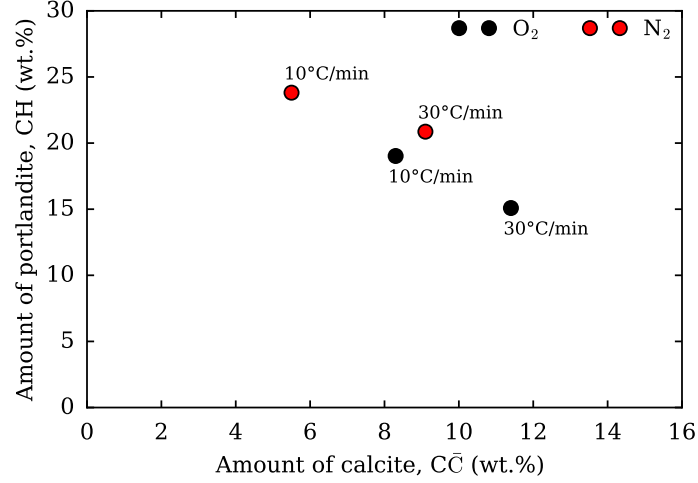
Figure 4.10: Portlandite amount and calcite amount evaluated by TGA measurements for low alkali content plain paste and paste with 8% SRA content under dioxygen and nitrogen environments and under two heating rates (10 °C/min and 30 °C/min).

4.3 Pore structure of cement pastes after curing under sealed conditions

In this section we present results of pore structure analysis of the 9 types of cement paste with various contents of SRA and alkali. Pore structure of cement pastes is characterized by mercury intrusion porosimetry, where cement pastes are pre-dried by two methods (solvent exchange and vacuuming at room temperature). Nitrogen sorption isotherms and water sorption isotherms are also obtained for the 9 types of cement pastes.

4.3.1 Impact of SRA on specific surface area

Specific surface area of cement pastes evaluated by nitrogen adsorption analyzed by BET model are shown in figures 4.11 and 4.12, where specific surface area is plotted in terms of the content of SRA of cement pastes and in terms of the content of alkali, respectively. Cement pastes containing SRA have a lower specific surface area relative to plain pastes. Specific surface area de-

Figure 4.11: Specific surface area evaluated by BET model applied to nitrogen adsorption of cement pastes as a function of SRA content.

creases with increasing content of SRA, regardless of alkali content as shown in figure 4.11. The decrease of specific surface area is significant in case of low alkali content, and can reach up to 60% decrease in case of samples containing 8% SRA. Moreover, increasing alkali content also leads to a decrease of the specific surface area as shown in figure 4.12. This decrease is larger for the plain pastes than for the pastes containing SRA.

In figure 4.13 we plot BET constant in terms of SRA content. The BET constant of plain pastes has a value in the range of [71-83] and decreases significantly as well in the presence of SRA. We remind that the BET constant is related to the affinity of the gas to the solid. In fact, for samples of SRA content of 4% the constant C_{BET} reaches a value of ~ 30, for samples of SRA content of 8% the constant C_{BET} reaches a value of ~ 22. This impact of SRA on BET constant C_{BET} is an indicator that for cement pastes containing SRA, when samples are pre-dried by vacuuming at room temperature, an adsorbed amount of SRA may remain on the solid surfaces.

Specific surface area was also assessed by BET model applied to water sorption. The BET constant is examined as well as the pore volume. Results of specific surface area, shown in figure 4.14, confirm that specific surface
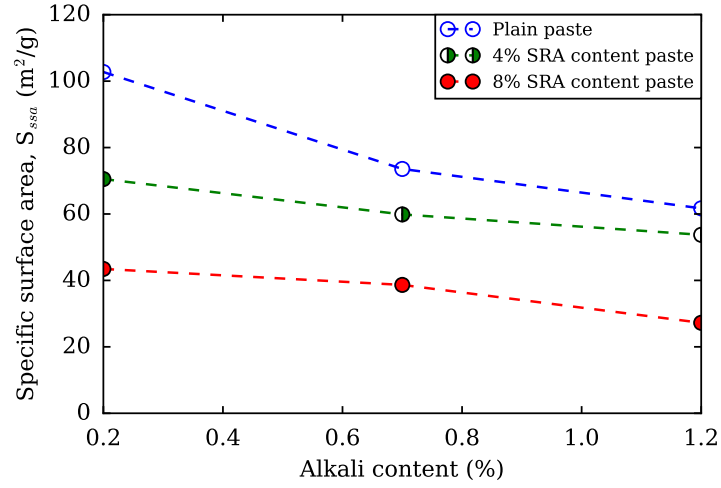
Figure 4.12: Specific surface area evaluated by BET model applied to nitrogen adsorption of cement pastes as a function of alkali content.
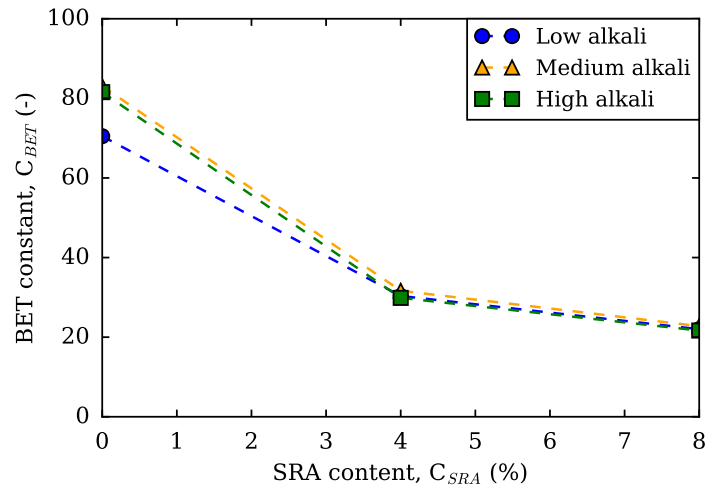
Figure 4.13: BET constant evaluated on nitrogen adsorption of cement pastes as a function of SRA content.
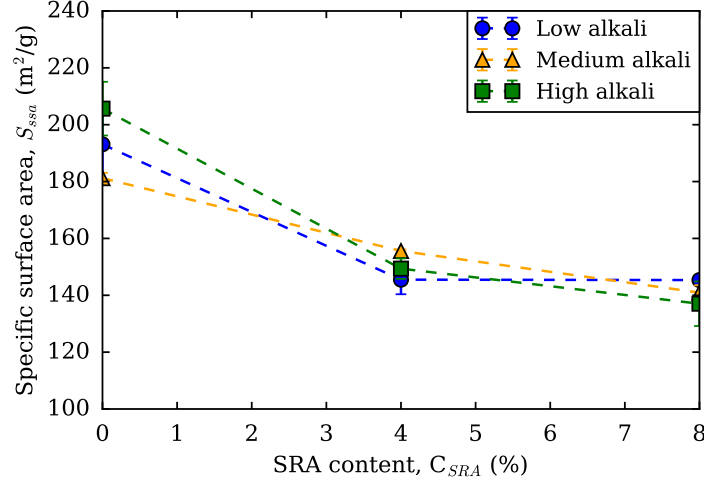
Figure 4.14: Specific surface area evaluated by BET model applied to water sorption isotherms of cement pastes as a function of the SRA content.

area decreases significantly for cement pastes containing SRA relatively to plain pastes. Moreover, pore volume increases with SRA content as shown in figure 4.15. The BET constant increases with addition of SRA as shown in figure 4.16. This increase is more significant for low alkali content, compared to the medium and high alkali contents. The impact of alkali content on specific surface area on plain pastes is minor: surface area obtained by BET model applied to water sorption isotherms is independent of alkali content, in contrast to the decrease observed for surface area based on nitrogen sorption isotherms. This observation may be interpreted, in the light of the model of Jennings (2008) for C-S-H, by the fact that the presence of alkali may lead to the formation of a lower fraction of LD C-S-H at a constant amount C-S-H. In fact, the SSA evaluated by nitrogen may be linked in first order to the SSA of LD C-S-H, since LD C-S-H is mostly accessible to nitrogen. The fact that the degree of hydration of plain paste at various alkali contents at mature ages is comparable, and the similar SSA evaluated by BET applied to water adsorption on these plain pastes is an indicator that the amount of C-S-H (LD and HD) is comparable in plain pastes regardless of alkali content. This observation also agrees with results of Juenger and Jennings (2001).
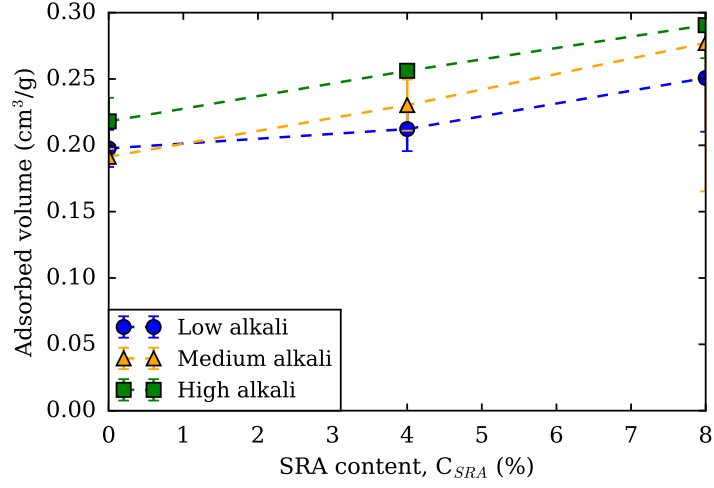
Figure 4.15: Pore volume evaluated from water sorption isotherms at relative humidity of 98% as a function of SRA content of cement pastes.
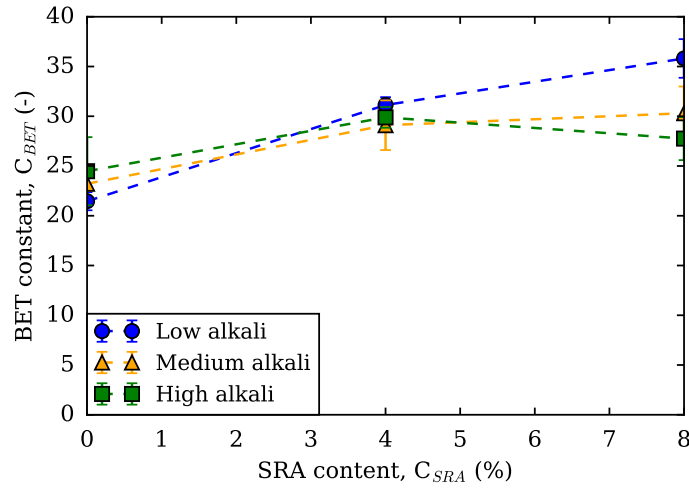
Figure 4.16: BET constant obtained from BET model applied to water sorption isotherms.

The specific surface area evaluated by BET model applied to water sorption isotherms is higher than specific surface area based on nitrogen sorption isotherms by a factor of almost 2 to 3. This observation is well-known, not only for cement pastes, but also for other porous materials and is discussed in detail in section 2.2.3.

Water sorption of zeolite with and without SRA

To examine the role of SRA on the reduction of SSA of cement pastes, a model system is studied: zeolite. The zeolite is studied in presence and absence of SRA. The water sorption isotherms of these two preparations are shown in figure 4.17. The addition of SRA leads to a decrease of maximum adsorbed volume of water, as well as a shift in the kink position. This relative humidity at which the kink occurs is related to the cavitation pressure of the condensed liquid in samples. Assessment of SSA by BET model, BET constant C_{BET}, and the pore volume are presented in the table 4.2.

Sample	SSA (m^2/g)	pore volume (mL/g)	C_{BET} (-)
Zeolite	242	0.24	28
Zeolite + SRA	105	0.14	25

Table 4.2: BET specific surface area, total adsorbed volume, and BET constant C_{BET} evaluated by water adsorption for a zeolite and {zeolite+SRA}.

The SSA of the zeolite that contains SRA decreased by a factor of 2.3 relatively to the zeolite, the BET constant is almost unchanged however. The pore volume is reduced as well by a factor of 1.7. This decrease of SSA and pore volume may be explained by the hindered adsorption of water molecules. In fact, the decrease of both pore volume and SSA may originate from two potential causes: occupation of adsorption sites by SRA molecules, or SRA blocking the access to a fraction of porosity of zeolite. In case only some adsorption sites are hindered, and assuming that capillary condensed water is negligible, one may suppose that sorption isotherms are merely re-scaled and the decrease of pore volume would be explained by the difference of adsorbed volume caused by a difference in surface area. However, re-scaled
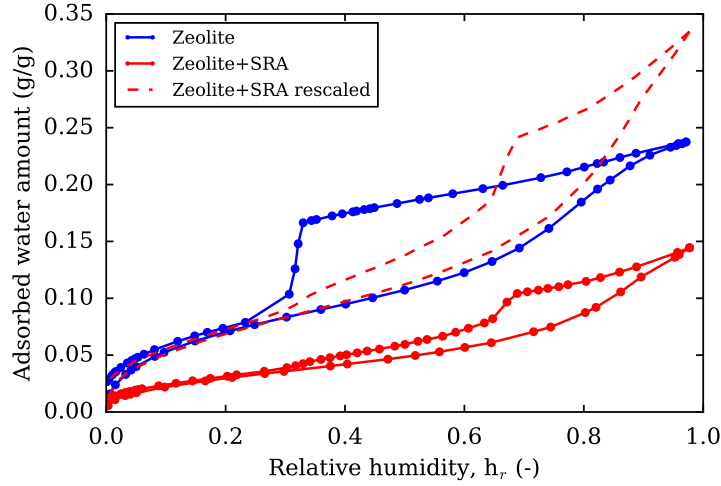
Figure 4.17: Water sorption isotherms of a zeolite and zeolite+SRA. Credits to Jiří Rymeš for measurements on zeolite.

isotherm as shown in figure 4.17 leads to a larger total pore volume, this is an indicator that the uptake of water is not only adsorbed on surfaces but also present as capillary condensate. This leads to the observed difference of the re-scaled pore volume of zeolite that contains SRA and the pore volume of the zeolite.

As observed on water sorption isotherms and nitrogen sorption isotherms, large impact of SRA on the developed pore structure of cement paste are noted. The question of where the SRA is placed at the level of cement hydrates is yet a question that remains. In what follows a primary approach is made to assess the positioning of SRA at the level of cement hydrates. SRA may be located at the large pores of cement paste where bulk water exists; it may also be adsorbed on the solid surfaces, in the interlayer space, or at the necks of small C-S-H pores. The fact that the BET constant of samples decreases for cement paste containing SRA, as shown in figure 4.13, is an indicator that SRA may be adsorbed on surfaces of hydrates, through the drying process. Moreover, pore structure is "better explored" when pore solution is exchanged by solvent (detailed later in section 4.3.3): SSA increases and pore volume as well. This also goes in the sense that SRA hinders adsorption

sites (and by that surfaces seen by nitrogen molecules, although existing, are lower) or makes some pore volume inaccessible to nitrogen/water molecules. Testing on model material (zeolite in this case) showed that SRA not only reduces surface area but also pore volume. This is a strong indicator that SRA may be placed at the entry of some pores making them inaccessible. Note that based on a rudimentary approach, the estimated size of the used molecule in our study is ~ 0.6 nm[1].

Coarsening of microstructure and retardation of hydration

In section 4.2, we observed that cement pastes containing SRA have lower degree of hydration. The decrease of specific surface area observed for cement pastes containing SRA may be partly due to the lower degree of hydration of these pastes, and partly due to the intrinsic presence of SRA in cement pastes. Let us investigate the causes of observed decrease of SSA independently from the observed decrease of degree of hydration. In table 4.3, we show results of plain paste and paste containing 8% SRA cured at RH 95%. Under curing at RH 95%, hydration of cement pastes progresses, and the difference of hydration degree between plain paste and paste containing SRA decreases. In fact, degree of hydration is evaluated based on XRD and TGA measurements, and the degree of hydration of plain paste and paste containing SRA cured at 95% RH (more than 9 months) are estimated to be 0.94 and 0.92 respectively. Therefore, it is reasonable to compare these pastes hence to dissociate the impact of SRA on hydration and on pore structure.

In table 4.3, SSA (evaluated by nitrogen adsorption and water adsorption) remains lower in case of samples containing SRA although hydration is advanced in both plain paste and SRA paste. The pore volume is also lower for paste containing SRA. The coarsening of pore structure is therefore not solely linked to the hydration retardation, but is intrinsic to the presence of SRA.

---

[1]The volumetric mass density of liquid SRA is ρ_{SRA} =0.92 g/cm^3, assuming that the molecule can occupy a volume of cube of characteristic size l, $l = \sqrt[3]{M_{SRA}/(N_A\rho_{SRA})}$, where M_{SRA} is the molar mass of SRA and N_A is the Avogadro number

Sample	Adsorbate	Nitrogen		Water	
	State	SSA (m^2/g)	Ads. volume (mL/g)	SSA (m^2/g)	Ads. volume (mL/g)
PP-L	cured at 95% RH	111	0.18	192	0.18
SR8-L	cured at 95% RH	69	0.16	166	0.16

Table 4.3: SSA and adsorbed volume for curing at 95% RH for plain paste low alkali content and SRA paste at 8% content of SRA and low alkali content. For nitrogen adsorbed volume evaluated at relative pressure 0.99 and for water at 95% RH.

4.3.2 Impact of SRA on pore size distribution

In this section, we present results of the pore size distribution the 9 cement pastes at various SRA and alkali content. The impact of pre-drying will be also addressed.

Pore size distribution obtained by MIP

Results of pore size distribution obtained by MIP measurements on the 9 types of cement pastes are shown in figures 4.18, 4.19 and 4.20 for cement pastes with low alkali content, medium alkali content and high alkali content, respectively. Results show that plain pastes present a bimodal distribution at pore entry diameter of ~ 15 nm and ~ 5 nm, except for low alkali content plain paste where a third family is identified at pores of entry size of 0.3 μm. At any content of alkali, for pastes containing SRA, volume of family of pores of entry diameter ~ 5 nm reduces with increasing content of SRA, while the volume of family of pores of size ~ 15 nm increases. Hence, pastes containing SRA have a coarsened pore structure. We do note that coarsening of pore structure of cement pastes containing SRA is more notable for low alkali content than high alkali content cement pastes.

To examine the impact of alkali content on the pore structure of plain cement pastes, we compare pore size distribution of plain pastes at various alkali contents in figure 4.21. When alkali content increases cement pastes
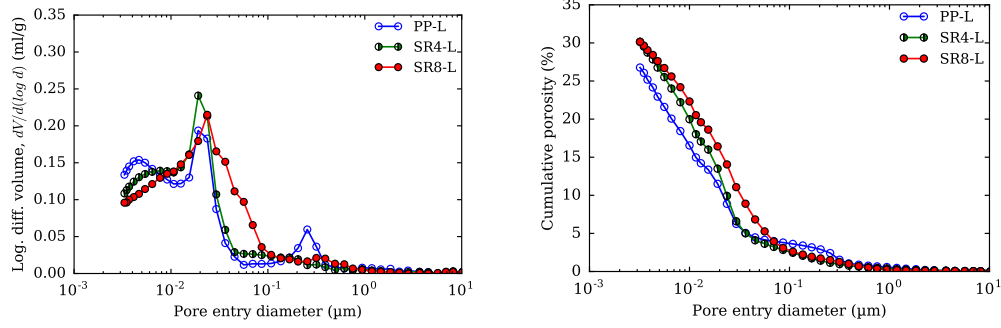
Figure 4.18: Pore size distribution and cumulative porosity obtained by MIP on cement pastes at low alkali content prepared by solvent exchange.
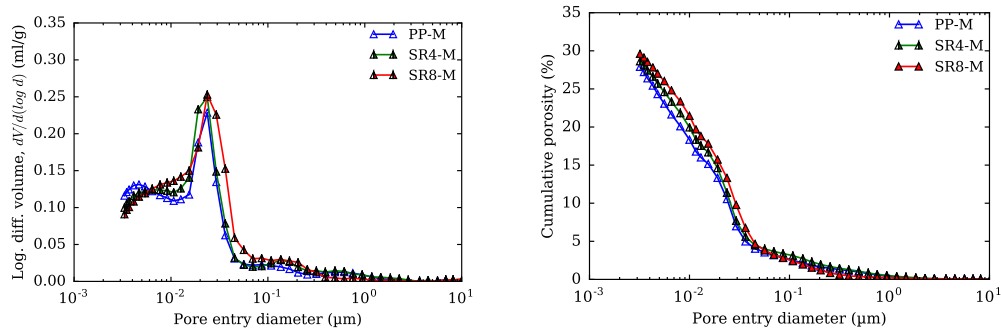
Figure 4.19: Pore size distribution and cumulative porosity obtained by MIP on cement pastes at medium alkali content prepared by solvent exchange.
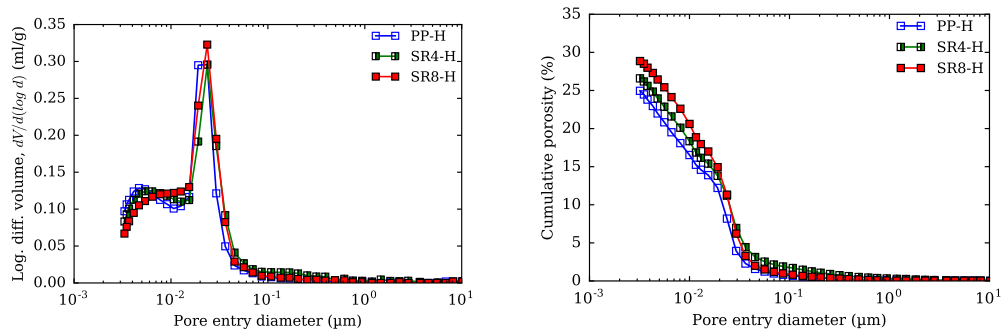
Figure 4.20: Pore size distribution and cumulative porosity obtained by MIP on cement pastes at high alkali content prepared by solvent exchange.

161
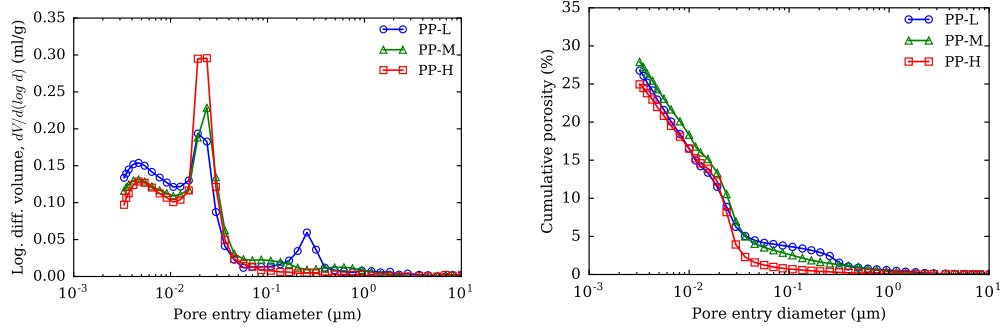
Figure 4.21: Pore size distribution and cumulative porosity obtained by MIP for plain pastes at various alkali content. Cement pastes were prepared by solvent exchane.

develops a pore structure with shared features: 2 family of pore entry diameter $\sim$ 5 nm and $\sim$ 15 nm, low alkali content cement paste also shows a family of pores at larger pore entry diameters. Additionally, the volume of family of pores of size $\sim$ 15 nm increases with increasing alkali content, while volume family of pores of size $\sim$ 5 nm is larger at the lowest alkali content compared to the volume of the same family of pores of other alkali contents.

BJH applied to nitrogen sorption isotherms

Pore structure is also analyzed by BJH applied to nitrogen adsorption branch. Results are shown in figure 4.22 for low alkali content samples at various SRA contents. Volume of family of pores of diameter lower than 10 nm decreases with increasing SRA content. Results confirm the coarsening of pore structure observed by MIP, although nitrogen adsorption allows the assessment of pore sizes rather than pore entry sizes. Hence, addition of SRA leads to a pore structure where volume of smallest pores is lower compared to plain pastes.
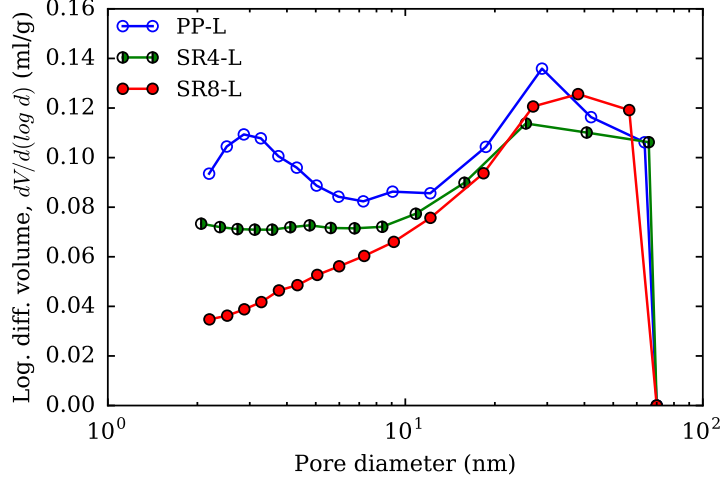
Figure 4.22: Pore size distribution obtained by BJH applied to nitrogen adsorption branch for paste at low alkali content prepared by vacuuming at room temperature.

4.3.3 Impact of pre-drying

Impact of pre-drying evaluated by MIP

Given that pastes were prepared following two pre-drying techniques: solvent exchange and vacuuming at room temperature, we investigate the impact of pre-drying on the obtained pore size distribution and whether the observations with regards of the impact of SRA on pore structure are dependent on the pre-drying method. In figure 4.23 we show the pore size distribution of pastes at low alkali content of a plain paste and paste containing 8% SRA with two pre-drying techniques. For plain paste, when sample is pre-dried by vacuuming at room temperature, only one family of pores of entry diameter ~ 40 nm is distinguished, while for plain paste when prepared by solvent exchange 3 family of pores are identified and the family of pores of the largest volume has a characteristic pore entry diameter of $\sim$15 nm. Vacuuming at room temperature for plain paste leads to a coarsening of pore structure. For paste containing SRA, pore size distribution shows the same characteristic family of pores for both preparation methods, although the family of pores of entry diameter lower than 10 nm has a lower volume when

163
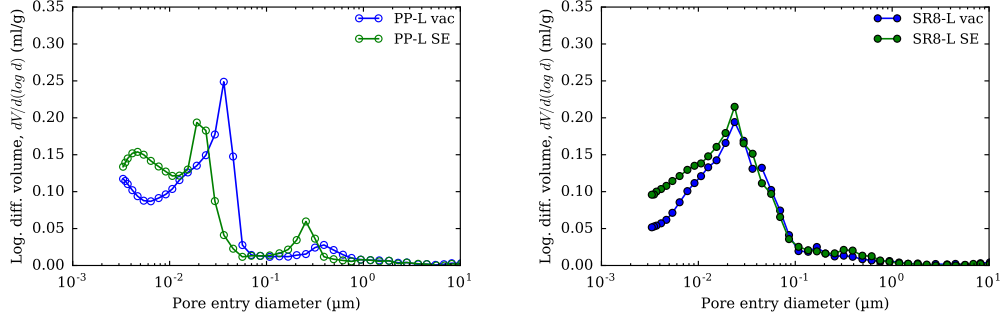
Figure 4.23: Pore size distribution obtained by MIP for plain pastes at low alkali content (PP-L) and at 8% content of SRA (SR8-L) prepared by solvent exchange (SE) and vacuuming at room temperature (vac).

the paste is prepared by vacuuming at room temperature. For paste containing 8% SRA, vacuuming at room temperature does not alter the pore size distribution obtained for a preparation by solvent exchange, while for plain paste the method of preparation alters the obtained pore size distribution. This little impact of vacuuming at room temperature on pore structure of pastes containing SRA relative to solvent exchange can be explained by the presence of SRA in pore solution. In fact, SRA reduces the surface tension, and hence reduces the mechanical impact of drying on the pore structure. The preparation by solvent exchange also allows the reduction of surface tension of the exchanged pore solution, by exchanging the pore solution of cement with solvent. Whatever the pre-drying impact, influence of SRA on pore structure can still be observed as shown in figure 4.24 when comparing cement pastes prepared by the identical methods.

Impact of pre-drying evaluated by nitrogen sorption isotherms

As seen previously, pre-drying impacts the pore structure. We evaluate the impact of pre-drying here on specific surface area obtained by BET model on nitrogen sorption isotherms. Two pre-drying techniques were used: vacuuming at room temperature and solvent exchange. Results of the evaluated specific surface area are shown in figure 4.25. For plain pastes, pre-drying using solvent exchange or vacuuming at room temperature leads to compara-
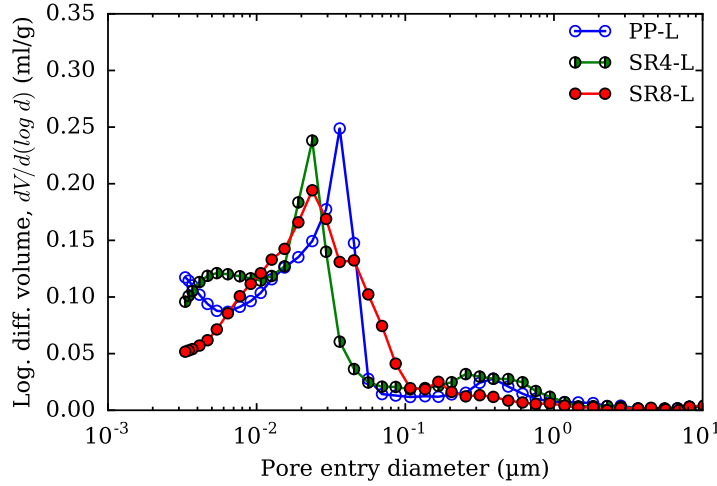
Figure 4.24: Pore size distribution of pastes with and without SRA at low alkali content obtained by MIP on samples prepared by vacuuming at room temperature.

ble values for specific surface area. However, as the content of SRA increases in cement paste, specific surface area obtained when samples are pre-dried using solvent exchange is always higher than specific surface area obtained on samples dried by vacuuming at room temperature. As an illustration, a factor of 1.8 is noted in case of sample SR8-H (which is cement paste at high content of alkali and 8% content of SRA).

This observation may be explained by the possible collapse of microstructure when pre-dried by vacuuming at room temperature relatively to solvent exchange. Assuming a collapse of microstructure occurs on pre-drying, and based on the higher SSA for SRA pastes prepared by solvent exchange, the difference of specific surface areas obtained by the two pre-drying methods would mean that this collapse is more prominent for samples containing SRA than plain pastes. This goes against the results of MIP, for which SRA containing pastes are slightly impacted by drying technique, in contrast to plain paste. A more probable explanation, is the hindered adsorption of nitrogen in case of samples containing SRA. In fact, when cement pastes are dried using solvent exchange, pore solution is exchanged and a significant fraction of
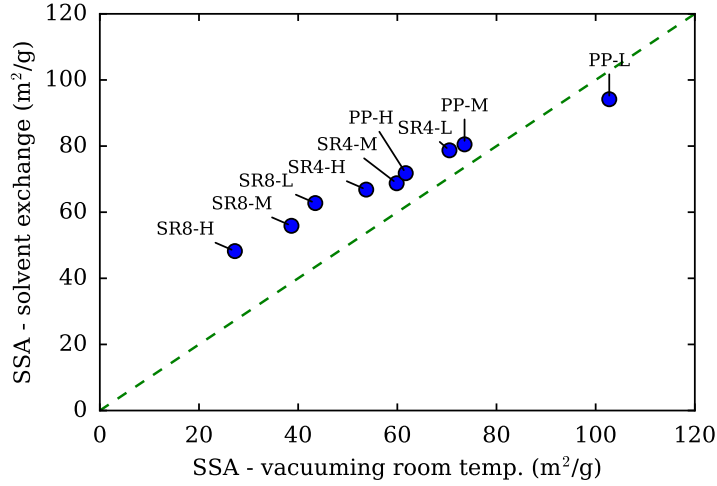
Figure 4.25: Specific surface area evaluated by BET model applied to nitrogen adsorption isotherm using solvent exchange or vacuuming at room temperature to pre-dry the sample.

SRA may be removed as well. This leads to the liberation of a pore space, as well as the adsorption sites that are not seen in case of drying by vacuuming at room temperature.

Furthermore, we compare the BET constant C_{BET} of the 9 types of cement pastes as evaluated by nitrogen sorption isotherms, for the two pre-drying techniques (solvent exchange and vacuuming at room temperature) in figure 4.26. Results show that when samples are pre-dried by solvent exchange, C_{BET} is independent of alkali content and SRA content: solvent exchange buffers the impact of alkali and SRA on the solid surface properties in regards to its interaction with nitrogen as adsorbate, in contrast to vacuuming at room temperature, as discussed in the previous paragraph. The impact of the method of drying, specifically of solvent exchange on the BET constant, was also reported in (Aligizaki, 2006, p. 137). This observation serves as an indicator that solvent exchange may enable the removal of SRA. It could be interesting to test the amount of remaining SRA in samples after using these two pre-drying techniques, although not conducted in this study.

The impact of SRA and alkali was examined making use of MIP, nitrogen

Figure 4.26: BET constant C$_{BET}$ of the 9 types of cement pastes for pre-drying methods of solvent exchange and vacuuming at room temperature.

sorption isotherms and water sorption isotherms, after curing and before the prolonged first drying, to which cement pastes are subjected. Let us investigate in the next section the influence of this first drying on the microstructure of cement pastes, and how alkali and SRA influence the evolution of pore structure through drying.

4.4 Pore structure of cement pastes after drying

Gas adsorption techniques are employed to investigate the influence of drying on pore structure, using water and nitrogen as adsorbates. Note that, in the following section only 4 types of cement pastes are investigated: we choose to study plain paste at low alkali content and high alkali content, as well as samples containing 8% content of SRA at low alkali content and high alkali content.

In the following we investigate the impact of drying on pore structure of cement pastes by nitrogen sorption isotherms and water sorption isotherms. Results of plain pastes are first discussed, followed by results of pastes con-

taining SRA.

4.4.1 Pore structure evolution: investigation by nitrogen sorption

Samples equilibrated at various relative humidities in a range of [11%-95%], were characterized by measurements of nitrogen sorption isotherms. Their specific surface area and pore volume was evaluated. Results of specific surface area of plain pastes in terms of relative humidity of drying is shown in figure 4.27 (upper figure for nitrogen adsorption and lower figure based on water adsorption), results of pore volume in terms of relative humidity of drying of cement paste is shown in figure 4.28.

Specific surface area (based on nitrogen adsorption) of plain pastes decreases linearly with decreasing RH, and reaches a plateau when dried to relative humidities smaller than 60% RH. This tendency is consistent for both tested alkali content. SSA decreases significantly and reaches a decrease of 80% for low alkali content, for high alkali content it decreases by 70%. Moreover, specific surface area of samples at dry state (dried at RH≤60%) is similar for both low alkali content and high alkali content and is equal to $\sim$ 20 m^2/g. Note also that for cement pastes kept at 95% RH specific surface area increases compared to the state at sealed conditions. This can be explained by the progress of hydration of cement pastes in such high conditions of RH.

Figure 4.28 describes the evolution of pore volume with the decreasing relative humidity of drying. The pore volume decreases with decreasing RH and reaches a minimum at 60% RH. When sample is subjected to RH lower than 60%, the pore volume increases back, with further decrease of RH, however it does not reach the pore volume at sealed conditions. The volume of kink is also evaluated from desorption branch of nitrogen sorption isotherm based on the volume of jump observed on nitrogen desorption at relative pressure $\sim$0.42. As the RH decreases, i.e., when conditions of drying becomes more severe, the volume of kink decreases and becomes almost null at RH≤60%. When the kink volume becomes null, this means that nitrogen

cavitation does not occur on desorption for these cement pastes.

Influence of SRA on the evolution of pore structure as seen by nitrogen sorption isotherms was also examined: specific surface area and pore volume are assessed for a sample containing 8% SRA at low content of alkali and at high content of alkali. Figure 4.29 (down) shows results of specific surface area versus the relative humidity. SSA decreases by almost 30% (decrease estimated for the lowest recorded SSA relative to sealed state sample). Samples kept at 95% RH show higher SSA relatively to the sealed state, which may also be linked to a progress of hydration. Figure 4.30 shows results for pore volume and volume of kink (that is observed on desorption branch of nitrogen). Pore volume varies with decreasing relative humidity with regards to the samples kept under sealed state conditions, and stays in a range of ± 0.05 mL/g. For low alkali content it marks a minimum at 75% RH. The observed decrease of SSA and of pore volume is more pronounced in case of plain pastes than for pastes containing SRA.

4.4.2 Pore structure evolution: investigation by water sorption

Figure 4.27 (down) shows results of SSA evaluated by water sorption isotherms, using BET model, for cement pastes dried at decreasing RH from 95% down to 11% RH. Results show that SSA decreases by almost half when sample is dried at 11% RH. This decrease is linear with regards to RH, and reaches a plateau for paste at low alkali content when sample is dried at RH ≤ 33%. The decrease of SSA with decreasing RH of drying does not depend on the alkali content. Figure 4.31 shows results of evolution of adsorbed amount of water evaluated by water sorption isotherms (volumetric method) in a range of [0-40%] and [40%-95%]. Note that the volume of pore filled in the range of RH of [40%-95%] can be interpreted as the volume of large gel pores, which is also the porosity accessible to nitrogen according to Jennings (2000). The volume of pores filled at a range of [0-40%] can be associated to the small gel pores and interlayer water. Results in figure 4.31 show that volume of water adsorbed in RH range of [0-40%] evolves with the RH of drying as does the

169
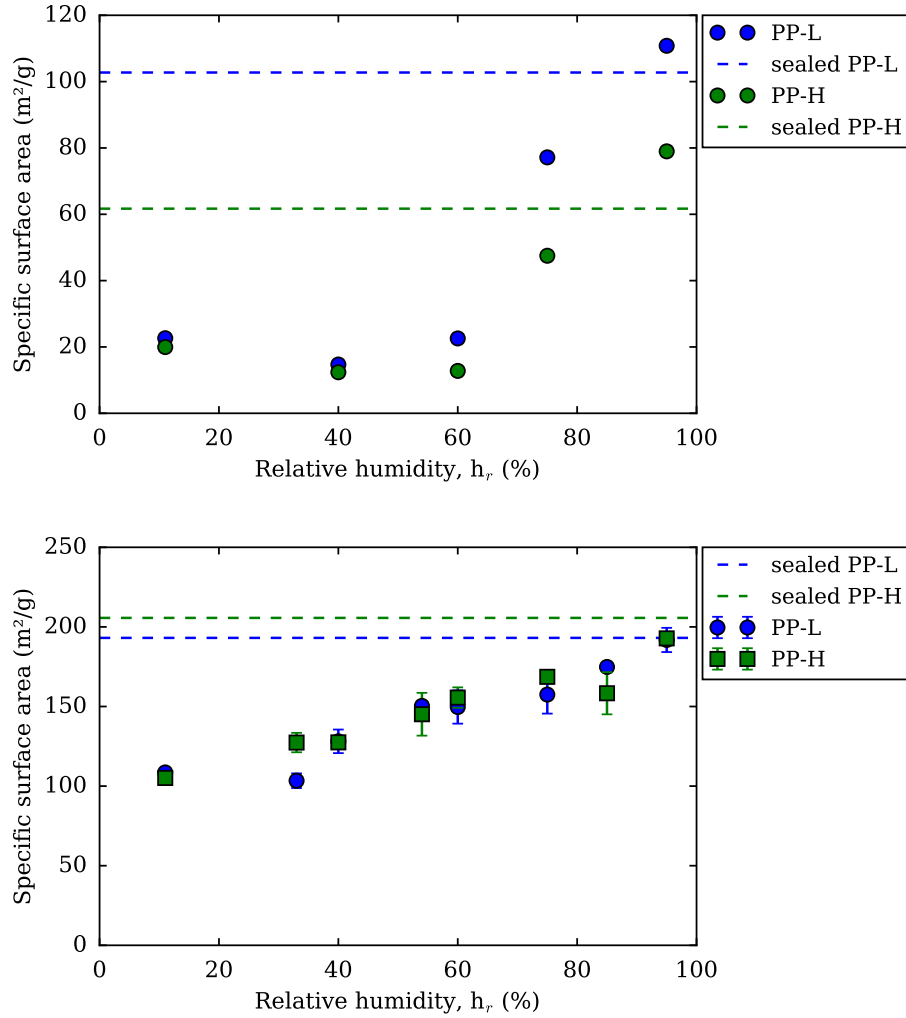
Figure 4.27: Specific surface area based on nitrogen adsorption (top) and water adsorption (bottom) of plain pastes (symbols) with low alkali content (PP-L) and high alkali content (PP-H) in terms of relative humidity at which cement pastes were dried. Dashed lines correspond to specific surface of samples after curing at sealed state.
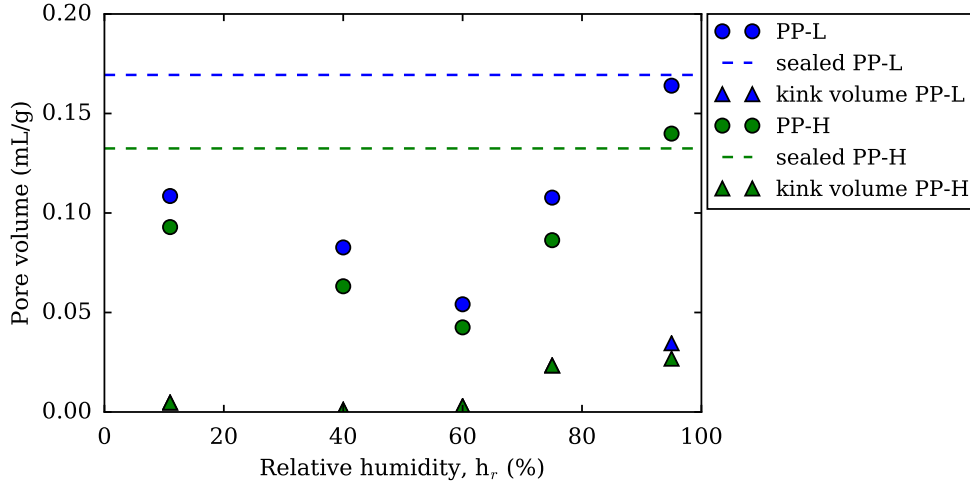
Figure 4.28: Pore volume based on nitrogen adsorption of plain pastes (adsorbed volume at relative pressure of N_2 of 0.97) and kink volume with low alkali content (PP-L) and high alkali content (PP-H) in terms of relative humidity of drying of cement pastes. Dashed lines correspond to pore volume of samples after curing at sealed state.

specific surface area. Moreover, the amount of adsorbed water corresponding to a RH range of [40%-95%] reaches a minimum at 54% RH. The pore volume filled in this range follows a trend similar to the amount of pore volume accessible to nitrogen.

Figure 4.29 (down) shows the results of SSA for samples containing SRA at low alkali content and high alkali content in terms of relative humidity of drying. Results show that SSA decreases with decreasing RH, in contrast to results of SSA evaluated by nitrogen sorption isotherms where the observed decrease is minor. The decrease of SSA is observed regardless of alkali content. In fact, SSA decreases with decreasing RH and reaches a plateau at low RH. For low alkali content SRA paste, SSA reaches a constant value of $\simeq 90$ m^2/g when sample is dried at RH $\leq 60\%$ RH. For high alkali content, the critical RH is 40% RH instead, and the reached constant SSA is $\simeq 100$ m^2/g.

Figure 4.32 shows the results of volume of adsorbed water in a range of RH of [0-40%] and [40%-95%] in terms of RH of drying for cement pastes with

171
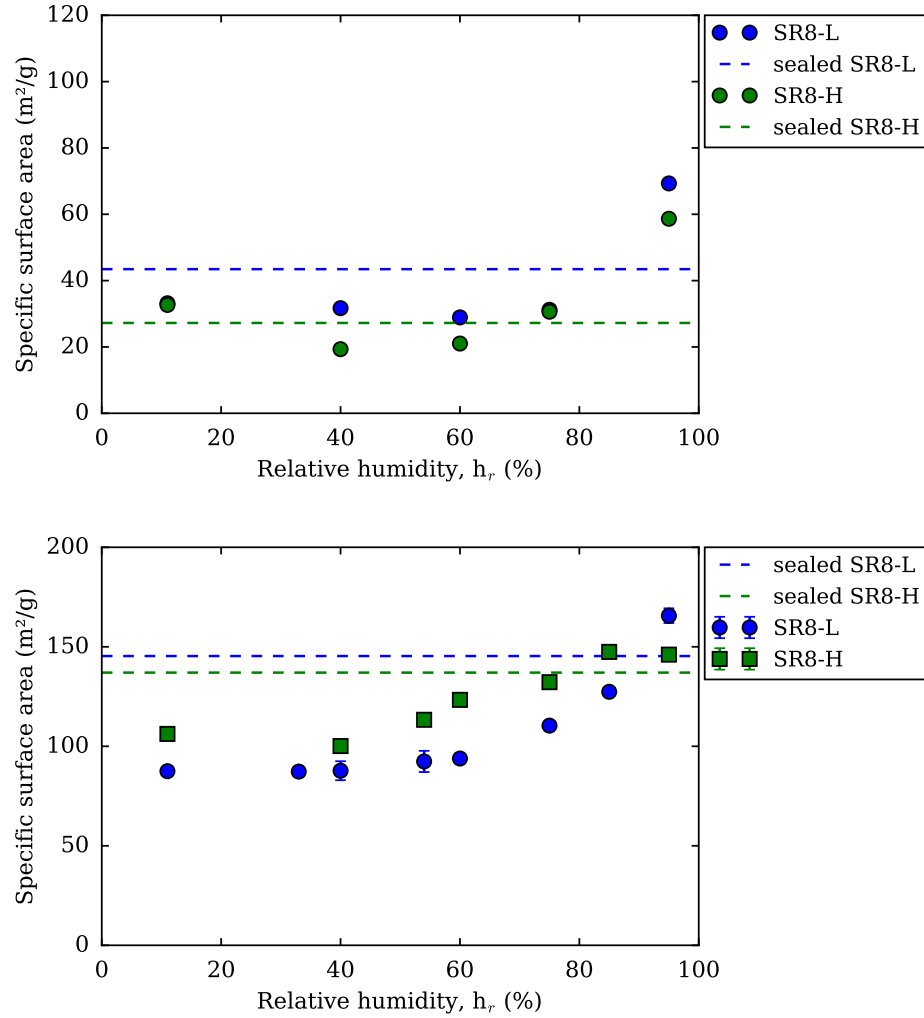
Figure 4.29: Specific surface area based on nitrogen adsorption (top) and water adsorption (bottom) of SRA pastes (symbols) with low alkali content (SR8-L) and high alkali content (SR8-H) in terms of relative humidity at which cement pastes were dried. Dashed lines correspond to specific surface of samples after curing at sealed state.
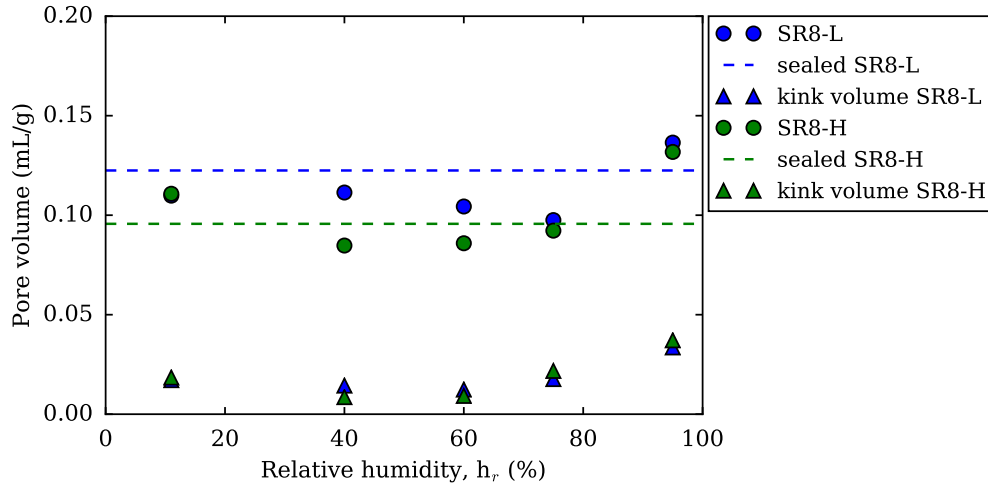
Figure 4.30: Pore volume based on nitrogen adsorption of SRA pastes at low alkali content (SR8-L) and high alkali content (SR8-H) in terms of relative humidity of drying of cement pastes. Dashed lines correspond to pore volume of samples after curing at sealed state.
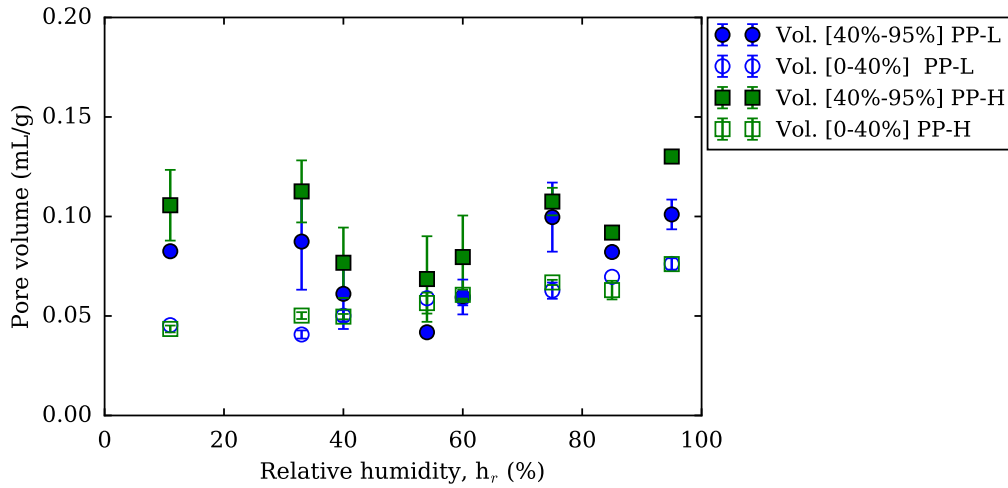
Figure 4.31: Volume of adsorbed amount of water obtained from water sorption isotherms (volumetric method) in terms of relative humidity of drying of cement pastes.

173
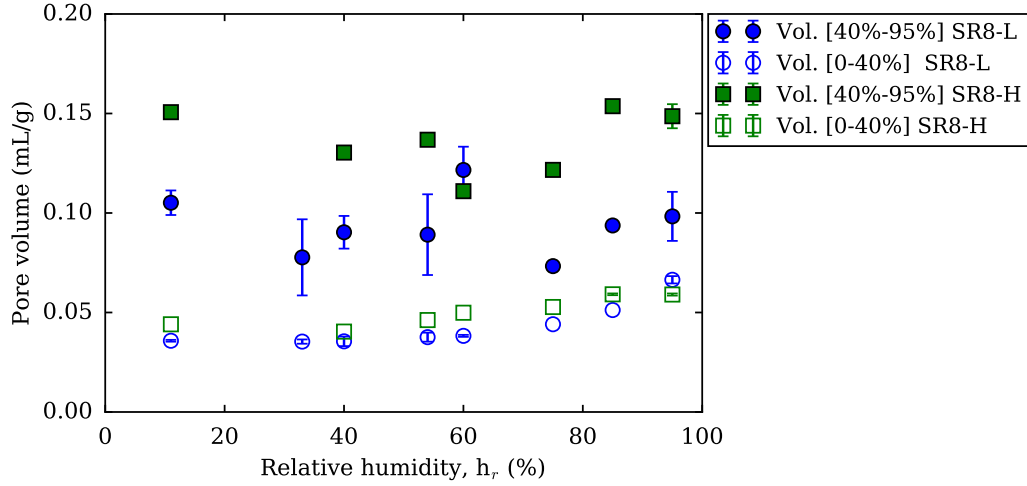
Figure 4.32: Volume of adsorbed amount of water obtained from water sorption isotherms (volumetric method) in terms of RH of drying, for pastes containing 8% SRA at low content of alkali (SR8-L) and high alkali content (SR8-H).

8% SRA content. Results show that volume of pores filled in the range of RH [0-40%] decreases with decreasing RH of drying in a way similar to SSA. The pore volume filled in the range of [40%-95%] is almost constant through drying. The volume of these pores (referred to as mesopores) is higher for cement paste at high alkali content than for the paste at low alkali content.

4.4.3 Discussion on the evolution of microstructure

In this section we review the changes of the pore structure upon drying. Note that the measurements such as water sorption isotherms measurements and pore volume measurements by water immersion are conducted at short periods, and assumed as not altering significantly the microstructure. Measured quantities through these techniques are thus considered representative of the long-term changes that occur during drying.

For plain pastes, drastic changes in pore structure are noted upon drying. These changes were examined by evolution of both pore volume and SSA, measured by water sorption isotherms and nitrogen sorption isotherms. Fig-

ure 4.33 shows t-plot for plain paste at low alkali content and at 3 conditions: 1) for a sample that was kept at sealed state (i.e., measured after curing under sealed conditions), 2) for a sample dried at 11% RH after the sealed state conditions, 3) and for a sample that was re-humidified to 95% RH after drying at 11% RH. The t-plot of the latter sample will be discussed later. T-plot of both samples kept under sealed conditions and sample dried at 11% RH indicate that nitrogen adsorption does not reflect the presence of micropores, since the t-plot follows a linear behavior in terms of thickness of adsorbed layer lower than 1 nm. In fact, the adsorption occurs as if it occurred on a non-porous surface of the same surface area as the cement paste of interest. At the sealed state, pore structure of cement paste indicates the presence of mesopores of widespread distribution. When sample is dried to RH 11%, the t-plot reflects the presence of capillary condensation on nitrogen adsorption, since the t-plot deviates towards higher values than the linear trend at the origin. In fact, when cement paste is dried, pore structure is reorganized such that volume of mesopores increases, and the volume of small pores decreases. Further, comparing the results for sample kept under sealed conditions and sample dried to 11% RH, it is noted that the two plots are almost parallel for thicknesses of adsorbed film larger than 1.1 nm, meaning that the volume of family of pores of size lower than 1.1 nm decreased on drying, and are at the origin of the re-organization of pore structure, as emphasized by nitrogen adsorption.

The re-organization of pore structure is confirmed by water sorption isotherms as shown in figure 4.31. In fact, volume of mesopores (pores filled in the range of RH [40%-95%]) decreases at decreasing RH and passes by a minimum. The fact that a minimum is observed may be linked to the mechanisms leading to the pore structure collapse, as the SSA measured by both nitrogen adsorption and water adsorption decreases with decreasing RH, as well as the volume of micropores (pores filled in the range of RH of [0%-40%]). The presence of a minimum may be related to a change of the dominant mechanisms driving drying shrinkage: at high RH capillary effects contribute largely to the drying shrinkage, whereas at the lower RH drying shrinkage is dominated by surface effects. In figure 4.34, we show the mea-

sured total pore volume by drying to 105 °C and immersion in water of 9 types of cement pastes dried at the various RH. The changes of pore structure occur at a constant total pore volume as characterized by re-saturation in water. Jennings et al. (2015) also studied the water vapor sorption isotherms of cement pastes (obtained by dynamic vapor sorption based on gravimetric method) on a cycles of drying and re-humidification. Jennings et al. (2015) observed that as long as the cement pastes were not dried below 25% RH (on first drying) the pore volume at near saturation (98%) before drying and after drying is found unvarying. Gajewicz et al. (2016) studied by means of 1H NMR the drying and rewetting of cement pastes: the cement pastes were dried by severe methods (oven drying, prolonged periods ∼1 month) and less severe methods (salt solutions, short periods) and they were rewetted subsequently by immersion in solution (saturated in CH). The pore volume and its distribution into a finer porosity (pores less than 10 nm) and coarser one (pores larger than 10 nm) is monitored upon immersion from 2 hours to 12 days. The total pore volume is found to be constant over the rewetting period, however, the distribution of the water into a finer porosity and coarser one evolves on rewetting, and moisture exchange between the two population of pores is observed for the severe drying cases. For the less severe drying, both the total pore volume and its distribution after 2 hours rewetting are found unvarying through time.

In figures 4.35 and 4.36 we plot the pore volume in terms of SSA, evaluated by nitrogen sorption and water sorption, respectively. In first order, measured volume of mesopores decreases linearly with decreasing SSA.

Specific surface area evaluated by water sorption is consistently higher than specific surface area evaluated by nitrogen sorption. The potential causes of this common feature were detailed in section 2.2.3. Moreover, observations regarding the evolution of SSA on long-drying of cement pastes with and without SRA reveal tendencies that do not agree with each other. Let us recapitulate the observations for pastes with and without SRA. For cement pastes, as shown in figure 4.27:

- Based on nitrogen sorption, SSA decreased with decreasing RH of dry-
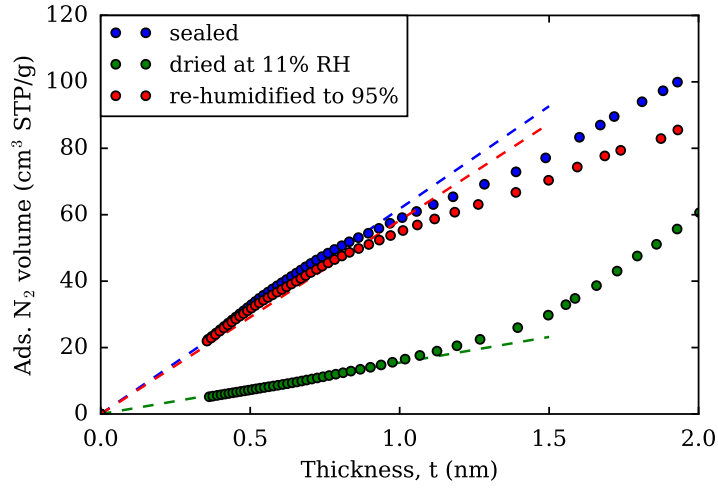
Figure 4.33: t-plot for plain paste at low alkali content (PP-L) for a sample cured at sealed conditions, a sample dried to RH 11% after the sealed curing, and a sample re-humidified to 95% RH after drying at 11% RH.
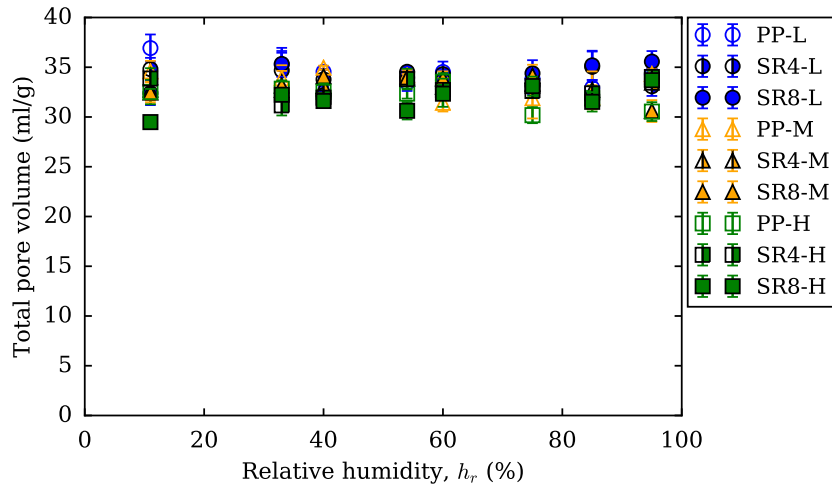
Figure 4.34: Total pore volume of cement pastes measured by weighting samples that were dried at the various RH, the sample is dried at 105°C and resaturated under deionized water.

177
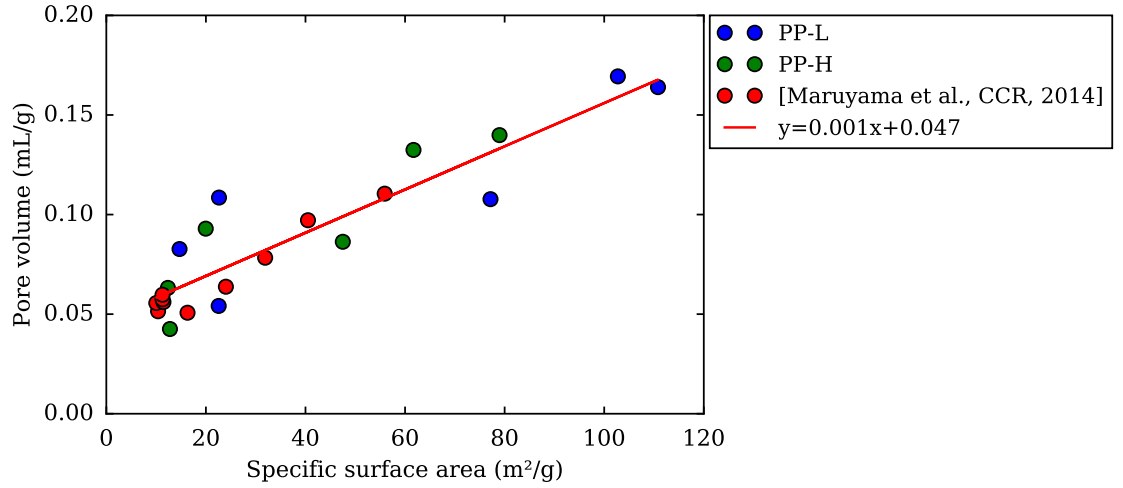
Figure 4.35: Evolution of pore volume evaluated by adsorbed volume of nitrogen at relative pressure of 0.97 in terms of BET specific surface area evaluated from nitrogen adsorption isotherm.
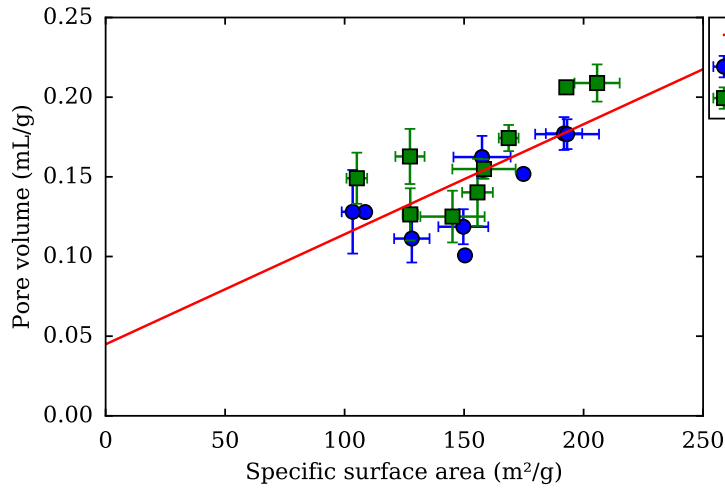
Figure 4.36: Evolution of pore volume evaluated by adsorbed volume of water at 95% RH and BET specific surface area evaluated from water adsorption isotherm.

ing and reached a plateau when cement paste is dried at RH lower than 60%.

- Based on water sorption, SSA decreased with decreasing RH of drying.

For pastes containing SRA, as shown in figure 4.29:

- Based on nitrogen sorption, SSA decreased slightly relatively to sealed state with decreasing RH of drying and reached a plateau when cement paste is dried at RH lower than 75%.

- Based on water sorption, SSA decreased with decreasing RH of drying and reached a plateau.

The fact that for SRA pastes a significant decrease of SSA evaluated by water sorption with decreasing RH is observed while a minor decrease is observed on SSA evaluated by nitrogen sorption isotherms may be linked to the accessible porosity evaluated by each technique, and the fact that each porosity behaves differently on drying. A tentative interpretation of this behavior, in the light of Jennings (2008) model is that the SSA evaluated by nitrogen sorption is that of small and large gel pores. These pores would not collapse on drying or only a small fraction of these pores would collapse. The SSA evaluated by water sorption isotherms on the other hand decreases significantly with decreasing RH and reaches a constant value when cement paste is dried below 60%, indicating that the inaccessible porosity to nitrogen, among which interlayer space, would shrink on drying. The potential collapse of this porosity is however not translated to a length change of cement paste, since measured drying shrinkage for pastes containing SRA below 75% is almost constant as shown in figures 3.8, 3.9 and 3.10. Moreover, when cement pastes are dried at low RH, we observe that SSA based on water sorption reached is ~ 90 to 100 m^2/g for both plain pastes and pastes containing SRA, suggesting that the SSA at dry state is a characteristic of C-S-H regardless of the presence of SRA. The volume of the sharp decrease/kink observed on nitrogen desorption becomes almost null for plain pastes dried below 60% RH. In such cases, pores that are connected to the outside by small entries making

179

it possible for cavitation to occur are no longer "seen" by nitrogen. This suggests two possibilities: either the necks of pores collapse, and these pores become inaccessible to nitrogen or the large pores themselves collapse. For pastes containing SRA, the volume of kink evaluated by nitrogen desorption decreases but does not become null, further confirming that in these cement pastes the magnitude of collapse of pore structure is significantly reduced.

Variability of SSA measured by nitrogen adsorption with drying conditions was a question thoroughly investigated by several authors. In fact, Parrott et al. (1980) investigated the drying shrinkage of alite pastes, and the microstructural changes it undergoes. Our results are in line with their results: SSA measured by nitrogen decreased from 100 m^2/g to 20 m^2/g for paste of water/alite ratio of 0.4. Moreover, the decrease of SSA on drying is reversible when samples are resaturated in limewater for 14 days, pore volume however cannot be fully recovered. Parrott et al. (1980) interpret this by the closure of mesopores which is induced by capillary tension. Litvan and Myers (1983) also reported dependency of nitrogen SSA on RH of conditioning of cement pastes. SSA decreases with decreasing RH, however SSA slightly increases back below 40% RH. Litvan and Myers (1983) also reported the recovering of SSA when sample is re-humidified to RH larger than 75%. The authors link this microstructural change to the gradient of moisture that cement pastes experience, which leads to the creation of new contacts in C-S-H structure.

More recently, Maruyama et al. (2014) studied extensively the microstructural changes of cement pastes during drying shrinkage. Maruyama et al. (2014) reported a drastic decrease of SSA as measured by nitrogen adsorption when pastes are dried to 54% RH, value below which SSA reaches a constant value. This result support results obtained here for cement pastes. Figure 4.35 shows a compilation of results obtained by Maruyama et al. (2014) and our results. SSA measured by water adsorption also decreases gradually with decreasing RH, however the decrease at high RH occurs at higher slope in our case (e.g., SSA decreases to 140 m^2/g vs. 175 m^2/g in Maruyama et al. (2014) at 40% RH). This pore structure re-organization is thought to be due to a consolidation of globule clusters due to surface ef-

fects at low RH range and the creation of mesopores by means of globules densification at RH range below 40% RH. Maruyama et al. (2017) further studied the pore structure evolution by means of Small-angle X-ray scattering (SAXS). Results confirmed the evolution of pore structure during drying, and indicate a stacking of the C-S-H agglomerates below 60% RH, as they are brought closer to each other.

Cement pastes containing SRA are however impacted in minor manner by the pore structure collapse when characterized by nitrogen sorption isotherms as seen in figures 4.29 and 4.30. SRA may act on the drying shrinkage reduction through its action on the pore structure collapse. We remind however, that SSA measured by water adsorption shows a decrease with decreasing RH of drying. This may indicate that at the level of C-S-H microstructural changes do occur, which are not translated however to a macroscopic shrinkage, nor a re-organization of the mesopores volume as shown in figures 4.29, 4.30 and 4.32.

The evolution of pore structure during first drying was confirmed for plain pastes as examined by water sorption isotherms and nitrogen sorption isotherms. The features of this re-organization of the pore structure are identified by the decrease of SSA as the drying RH decreases, and the non-monotonic decrease of volume of mesopores. In what follows, we investigate the reversibility of the pore structure evolution observed during the first desorption, by studying the pore structure of re-humidified cement pastes.

4.5 Reversibility of evolution of pore structure

To investigate the reversibility of pore structure evolution, we compare SSA and pore volume for cement pastes that were kept under sealed conditions, samples that were dried at RH 11% and samples that were re-humidified to 95% after being dried at 11%. Results displayed in table 4.4 show that SSA of cement pastes is regained after re-humidifying to 95%. Pore volume increases back to a comparable value to sealed state pore volume. Results are

shown in the table 4.4. For plain paste at low alkali content, the t-plot for a re-humidified paste is shown in figure 4.33, which illustrates the reversibility of the changes of SSA and pore volume through the similarity of the t-plot of sample kept under sealed conditions and sample re-humidified.

Sample	Adsorbate	Nitrogen		Water	
	State	SSA (m^2/g)	Ads. volume (mL/g)	SSA (m^2/g)	Ads. volume (mL/g)
PP-L	sealed	103	0.19	193	0.18
	dried-11% RH	23	0.16	109	0.13
	dried + re-humidified	99	0.19	178	0.17
SR8-L	sealed	43	0.16	145	0.19
	dried-11% RH	33	0.14	87	0.14
	dried + re-humidified	59	0.16	157	0.17

Table 4.4: Specific surface area and adsorbed volume at sealed state (cured for 3 months under sealed conditions), dried to 11% RH and re-humidified to 95% RH for plain paste low alkali content and SRA paste at 8% content of SRA and low alkali content, for nitrogen adsorbed volume evaluated at relative pressure 0.99 and for water at 95% RH.

It is noted that re-humidification of paste containing SRA leads to an increase of SSA as evaluated by BET model applied to water adsorption and nitrogen adsorption relatively to sealed state. This may be linked to an increased hydration as it still progresses at RH 95%.

The evolution of pore structure induced by drying is significant, and can be examined by the evolution of SSA and pore volume of dried samples, by using water sorption isotherms and nitrogen sorption isotherms. Although the SSA and pore volume undergo large decrease on drying, upon saturation the SSA and pore volume increase back to values comparable to the sealed state. Pearson and Allen (1985) and Winslow and Diamond (1974) also demonstrated by means of SANS and SAXS, respectively, that the surface area of dried cement pastes can be recovered by resaturation, which goes in line with the reversibility of the pore structure changes. Baroghel-Bouny (2007) also indicated by water vapor sorption isotherms on a first desorption

and subsequent cycle of adsorption and second desorption the absence of permanent irreversible microstructural changes.

However, this large evolution of pore structure is reversible since re-humidifying sample to higher RH leads to a re-organization of pore structure such that SSA and pore volume increase back to values comparable to the sealed state.

4.6 Conclusions

In this chapter we evaluated the influence of SRA on microstructure of cement pastes.

First, the chemical composition of 9 types of cement pastes with various alkali contents and SRA contents was assessed by means of XRD and TGA measurements. The alkali impacts the hydration degree in the early ages. Impact of SRA on hydration of cement pastes is evaluated. SRA retards hydration without stopping it. The retardation of hydration concerned both silicate and aluminate phases (namely ferrite phase). By mass balance back calculation, a C/S ratio for the C-S-H was evaluated. The SRA may modify the stoichiometry of the C-S-H. Moreover, the SRA is thought to cause carbonation of cement pastes on TGA measurements.

Second, effect of SRA on pore structure is examined, by means of MIP, nitrogen sorption isotherms and water sorption isotherms. Results indicate a coarsening of pore structure in presence of SRA, where volume of pores of small radii reduces (as shown in figures 4.18, 4.19 and 4.20) and specific surface area decreases with increasing content of SRA regardless of alkali content (as shown in figures 4.12 and 4.14). The impact on pore structure may not be explained solely by hydration retardation, but also intrinsically linked to the presence of SRA. The pre-drying of the cement pastes impacts the pore structure, dependently on the presence of the SRA. MIP measurements indicate potential collapse on drying of plain pastes when dried by vacuuming at room temperature compared to solvent exchange, whereas pastes containing SRA were impacted slightly. The nitrogen adsorption measurements on cement pastes indicated that the SRA is adsorbed on the solid surfaces after

the pre-drying by vacuuming at room temperature, and that the SRA may hinder some adsorption sites.

Moreover, evolution of pore structure through the prolonged drying was evaluated by means of nitrogen sorption isotherms and water sorption isotherms. Drastic changes of pore structure were observed for plain pastes. For plain pastes, SSA evaluated by nitrogen sorption decreased with decreasing RH down to RH $\sim 60\%$, below which SSA reached a plateau as shown in figure 4.27. The total adsorbed volume of nitrogen, associated to mesopores, passes by a minimum at RH $\sim 54\%$ as shown in figure 4.28. The fact that a minimum is observed at this characteristic RH is interpreted by a change in the dominant drying mechanisms: at high RH capillary effects contribute to the drying shrinkage while at the low RH surface effects may dominate the drying shrinkage. SSA evaluated by water sorption showed a continuous decrease with decreasing RH as shown in figure 4.27. The evolution of volume of mesopores, evaluated by the volume of water adsorbed between 40% and 95% RH, confirm the observations based on nitrogen sorption isotherms, where the volume of mesopores pass by a minimum at RH of 54% as shown in figure 4.31.

SRA significantly reduces the pore structure collapse, as measurement of SSA by nitrogen adsorption are almost constant over the range of tested RH as shown in figure 4.29, except at RH 95% where SSA was found higher than the SSA under sealed conditions, which is due to the progress of hydration. SSA evaluated by BET model applied to water adsorption reflected however a decrease of SSA as the RH of drying decreases as shown in figure 4.29. The volume of mesopores evaluated by both nitrogen sorption and adsorbed water volume between 40% and 95% RH are almost constant with decreasing RH as shown in figures 4.30 and 4.32.

The specific surface area and pore volume of plain cement pastes increase back to the initial values at sealed state when re-humidified to 95% RH and after drying at 11% RH.

The impact of SRA on pore structure before and after the long drying was investigated in this chapter. In the next chapter we investigate the properties of SRA in pore solution of cement pastes, and their potential interaction with

the cement paste.

Chapter 5

Physico-chemical characterization of SRA in cement paste

In this chapter we study the physico-chemical characterization of the SRA in the cement paste, using multiple techniques. We conducted leaching experiments on cement paste containing SRA to evaluate whether the SRA is adsorbed on cement matrix, and quantify the adsorbed amount when necessary. Moreover, we characterize the pore solution of studied cement pastes, and the impact of SRA on its properties (ionic composition, organic carbon and surface tension). The pore solutions are extracted from hydrated cement pastes, and characterized by a combination of techniques to evaluate the properties of the pore solution in presence of SRA.

5.1   Context

Eberhardt (2010) conducted leaching experiments, and used prisms of mortar and cement paste which are kept in contact with deionized water for 28 days, after which the solution is renewed and a new cycle is launched; a total of 8 cycles are conducted. The amount of SRA retrieved from the samples is estimated at the end of each cycle. Eberhardt (2010) found that SRA
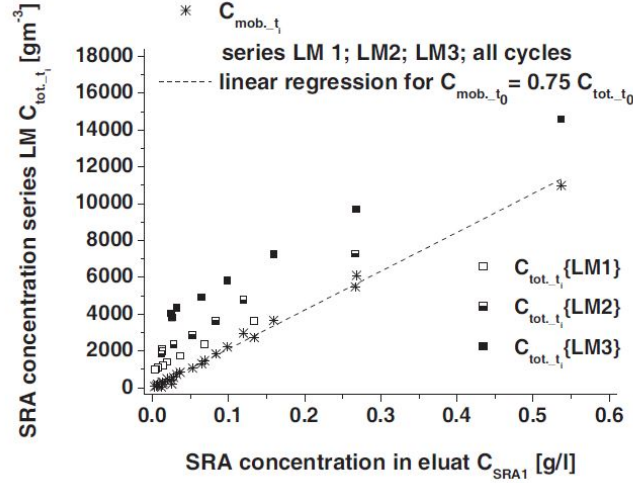
Figure 5.1: Remaining concentration of SRA in samples in terms of measured concentrations in eluates (Eberhardt, 2010). The intercepts for LM1 (1% content of SRA), LM2 (2% content of SRA) and LM3 (3% content of SRA) are not null and indicate the presence of an immobile fraction of SRA.

(commercial SRA with DPTB as major component) adsorbs on hydrates based on these leaching experiments and also on measurements of extracted pore solution. In figure 5.1, we show the results obtained by Eberhardt (2010) based on the leaching experiments; measured content of SRA is plotted in terms of the theoretical concentration in case no adsorption occurs. The fact that the intercept of the plot in not null is an indicator of the presence of non "leachable" SRA. Eberhardt (2010) concluded that SRA in cement pastes and mortars have a "mobile" part and an "immobile" part. Measurements on extracted pore solution were also conducted in the same study by Eberhardt (2010) and corroborated the adsorption of SRA.

Previous studies also questioned the potential adsorption of SRA on cement hydrates. Ai and Young (1997) studied the adsorption of a commercial SRA (DPTB) prepared in suspension of clinker and hydrated cement paste; the amount of SRA in solution was monitored and it has been concluded that SRA does not adsorb. Hence, we aim at investigating the potential adsorption of SRA by means of leaching measurements, and the properties of SRA in pore solution by means of pore solution extractions.

5.2 Materials and methods

5.2.1 Materials

For leaching experiments, studied cement pastes are prepared with the same procedure than the one detailed in section 3.1. The cement pastes are cured under sealed conditions for more than 6 months.

For pore solution extraction, cement pastes are prepared with mix design specified in table 3.3. The cement pastes are prepared with high shear rate mixer at LafargeHolcim Centre de Recherche at Lyon, and poured in molds of cylindrical shape and of diameter 6 cm and height 7 cm. This geometry is adapted for the pore solution extraction by the hydraulic press. The cement paste are cured under sealed conditions for at least 9 months, to ensure pastes have reached an advanced hydration degree, before extraction of pore solution is conducted.

5.2.2 Techniques for characterization of solutions

In this section we introduce the techniques for characterization of extracted pore solution and for leaching measurements. We introduce the total organic carbon measurements (TOC), inductively coupled plasma atomic emission spectroscopy (ICP-AES) and Wilhelmy plate method. The TOC and ICP-AES are used for characterization of extracted pore solutions and leaching measurements. Wilhelmy plate method is used for extracted pore solution only. A summary of the techniques used for each measurement (pore solution extraction and leaching experiments) can be found in figure 5.4.

The TOC allows the evaluation of the organic carbon of a solution, thus allowing to evaluate the amount of SRA. Device used for TOC measurements is TOC V CSH SHIMADZU. The measurements consist of measuring the total carbon amount and the inorganic carbon amount. Total organic carbon is evaluated by subtracting the total inorganic carbon from the total carbon amount. At first, the total carbon is obtained by heating samples to 720°C; carbon in the sample is transformed into CO_2 that is measured in infrared cell based on the wavelength of the carbon. Then a second sampling is intro-

duced in a reactor containing phosphoric acid. As such, only carbonates and
bicarbonates are transformed into CO_2. The amount of inorganic carbon is
therefore obtained. The collected samples are acidified using hydrochloric
acid to reach desired pH 3∼4 level for measurements and to avoid precipita-
tion of hydrates. They are stored in refrigerator until measurements.

To analyze ionic compositions of solutions Inductively coupled plasma
atomic emission spectroscopy (ICP-AES) is conducted. Device used is ICP
Varian 720-ES. Solutions prior to measurements are also acidified using hy-
drochloric acid and stored in refrigerator until measurements.

To measure surface tension device used is Tensio 3S provided by GBX,
based on Wilhelmy method. The plate, made of platine, is cleaned prior
to measurement and after each measurement using deionized water, then
isopropanol and finally exposing it to a flame. The measurement consists in
immersing a plate in the solution of interest. The device detects the surface
of the solution upon immersion and then pulls out the plate as illustrated in
figure 5.2, the force required to pull the plate of the solution is proportional
to the surface tension, following:

$$F = P_{plate} \times \gamma_l \times \cos\theta \tag{5.1}$$

where P_{plate} is the wetted perimeter of the plate, γ_l is the surface tension of the
liquid and θ is the contact angle of the plate. The liquid is generally assumed
perfectly wetting: here we consider θ=0. Prior to every measurement, we
verify, on 5 successive measurements, the surface tension of ultra-pure water
(obtained by PURELAB Ultra provided by ELGA LabWater).

5.2.3 Pore solution extractions

Pore solution of mature pastes is extracted using a hydraulic press (Duch-
esne and Bérubé, 1994). The collected pore solution is first analyzed by the
measurement of the surface tension based on Wilhelmy plate method. The
samples are then acidified and tested for ionic composition based on ICP-AES
measurements and organic content based on TOC measurements.
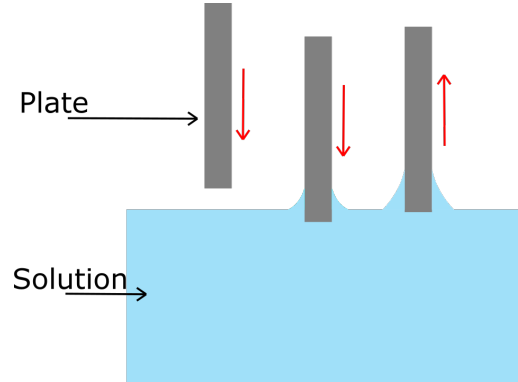
Figure 5.2: Illustrating figure for the Wilhelmy plate measurement of surface tension of a solution. Red arrows indicate direction along which the plate is moved during the measurements (from left to right): the plate is moved down towards the solution until contact is realized then pulled out.

5.2.4 Leaching experiments

To evaluate the potential adsorption of SRA on cement hydrates, we conducted leaching experiments on cement pastes containing SRA in a synthetic pore solution. Leaching experiments consist in putting the studied solid sample (here hydrated cement paste) in contact with a liquid to evaluate the leached species of interest. Few standards (e.g., NF X 31-210 / NF EN 12457-2 concerning granular materials) are developed for leaching experiments on hardened cement pastes. The goal of the existing standards for leaching experiments is to evaluate leached traces of organic and inorganic matter in severe environmental conditions (acid environment at controlled pH) or not (deminineralized water). The standards specify, among others, the solid to liquid ratio, the particle size (in case of granular material) and the contact duration. The tests may be conducted in static conditions where the liquid is not renewed (NF X 31-210 / NF EN 12457-2), or dynamic ones where the liquid is renewed constantly since a constant flow and renewal of the solution is imposed (Moudilou et al. (2002) based on the designed device CTG-LEACHCREATE for cement based materials).

Synthetic pore solution and leaching protocol

The aim of leaching experiments in this study is to evaluate amount of SRA
that is potentially adsorbed on cement hydrates, and hence would not be
present in the bulk phase or in the liquid-gas interface. We choose to conduct
the leaching experiments making use of a synthetic pore solution (SPS),
which mimics the in-situ environment of the pore solution of a cement paste
without SRA. The choice of a synthetic pore solution also helps avoiding the
inevitable dissolution of hydrates in case cement paste is left in contact with
deionized water, hence the evaluation of potential adsorbed amount of SRA
on cement hydrates may be influenced. For each content of alkali, a synthetic
pore solution is prepared.

   The synthetic pore solution is prepared following the protocol below:

1. Plain paste of the desired alkali content is prepared and cured under
   sealed conditions for 7 days.

2. After demolding the plain paste is crushed and sieved, the fraction of
   particles between 250 μm and 1.1 mm is selected and air blown for few
   seconds to remove fine particles.

3. Crushed plain paste is immersed in deionized water for 7 days at a ratio
   solid to liquid of 140 g/L.

4. Letting the solution sediment, the solid fraction and solution can be
   separated, and the synthetic pore solution is ready for use.

   Once the synthetic pore solution for the considered alkali content is pre-
pared, leaching experiments of pastes containing SRA are launched as a suc-
cession of cycles. The first cycle consists in:

1. Pastes containing SRA are crushed and sieved between 250 μm and 1.1
   mm.

2. Obtained particles are immersed in the synthetic pore solution at a
   solid to liquid ratio of 5 g of paste per 0.2 L of synthetic pore solution
   for 7 days.

At the end of each cycle, solution is removed and analyzed for its ionic composition and organic carbon amount. The solution is renewed by addition of synthetic pore solution, a new cycle is hence launched. A total of 4 cycles is conducted per type of cement paste. All 6 types of pastes containing SRA (4% and 8% content of SRA) at the 3 alkali contents (low, medium and high) are studied. A reproducibility set is conducted on paste SR8-L (paste containing 8% SRA and at low alkali content) where the leaching experiment is conducted on 3 sets. A summary of the samples and conditions of the leaching experiments is summarized in table 5.1.

Sample	Alkali content of SPS	Number of measurements	Solid to liquid ratio	Number of cycles
SR4-L	Low alkali content	1		
SR8-L		3	5 g of solid to 200 mL of solution	4
SR4-M	Medium alkali content	1		
SR8-M		1		
SR4-H	High alkali content	1		
SR8-H		1		

Table 5.1: Summary of samples for leaching experiments and parameters of the measurement.

Choice of duration of each leaching cycle

A preliminary study is first conducted to validate the leaching protocol and to confirm the duration chosen per cycle of leaching. To do so, we study a chosen subset of samples: samples SR4-H and SR8-H (pastes at high alkali content and at 4% SRA content and 8% SRA content respectively). A synthetic pore solution is prepared using plain paste containing high alkali content similarly to the procedure described earlier with noted differences, namely plain pastes is cured here for 3 days. To prepare the SPS, the plain paste is left in contact with deionized water for 3 days. Then pastes containing SRA are prepared according to the leaching protocol described earlier and immersed in the synthetic pore solution. For each paste (SR4-H or SR8-H), six sets of SRA paste in contact with synthetic pore solution are prepared. Each preparation served for a sampling after a given contact duration: 1, 2,
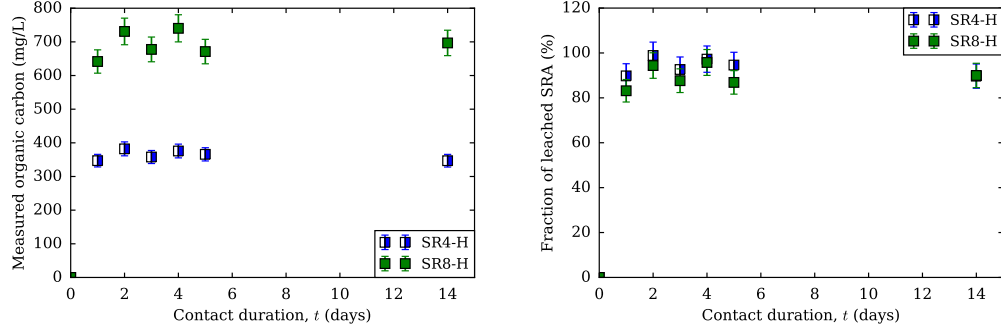
Figure 5.3: Measured organic carbon in sampled solutions as a function of the contact duration (left hand) and corresponding fraction of leached SRA to the initial amount of SRA estimated from mix design (right hand) for pastes at high content of alkali, at 4% SRA content (SR4-H) and 8% content (SR8-H). Error bars estimated from the propagation of errors of measurement.

3, 4, 5 and 14 days. The sampling is analyzed in terms of organic carbon, allowing to measure the amount of leached SRA.

Figure 5.3 shows the measured amount of organic carbon in each sampling in terms of the contact duration. Results confirm that 7 days are enough for the leached SRA to reach equilibrium. Moreover, we observe that a large fraction of SRA is removed: larger than 80% of the SRA content of paste, evaluated from the mix design.

Evaluation of leached SRA in the absence of adsorption

Given that the amount of SRA is known from the mix design, and assuming that all SRA can be leached, we can assess the amount of SRA leached on the successive cycles of leaching.

By means of TOC measurements, we evaluate the concentrations of organic carbon present in tested solutions: measurements on the solutions of leaching experiments and on the synthetic pore solution. Measurements of organic carbon in synthetic pore solution allow to correct the measured concentration of organic carbon in leaching solutions and to obtain organic carbon originating from SRA only (in fact low amount of organic carbon may be present in the cement paste, originating from grinding agents used in the

processing of clinker).

The measured concentrations $C_{meas,raw}$ are corrected for the content of organic carbon present in the synthetic pore solution C_{SPS}, as follows:

$$C_{meas} = C_{meas,raw} - C_{SPS} \tag{5.2}$$

Based on the mix design m_C, the mass of organic carbon originating from SRA present in cement paste, can be evaluated as follows:

$$m_C = \frac{C_{SRA}}{(1 + C_{SRA} + w/c)} \times m_{hcp} \times m_{carbon} \tag{5.3}$$

where m_{carbon} is the content of carbon in SRA, for SRA used in this work $m_{carbon} = 6 \times M_C / M_{C_6H_{14}O_2}$, $M_C = 12$ g/mol is the molar mass of carbon and $M_{C_6H_{14}O_2} = 118$ g/mol is the molar mass of SRA, C_{SRA} is the SRA content expressed in mass fraction relative to the clinker, w/c is the water-to-cement ratio and $m_{hcp} \simeq 5$ g is the mass of hardened cement paste for leaching measurements.

The theoretical concentration of SRA after a cycle of leaching in case all SRA may be removed (i.e., SRA is mobile) can be assessed as follows:

$$C_{th,1} = \frac{m_C}{V} \tag{5.4}$$

$$C_{th,n} = C_{th,n-1} - \frac{C_{meas,n-1}(V - V_{left})}{V} \tag{5.5}$$

where: $C_{th,n}$ is the estimated concentration of SRA at leaching cycle n if we assume that no adsorption occurred and that all SRA can be leached out, $C_{meas,n}$ is the measured organic carbon concentration in removed solution at leaching cycle n, V is the volume of solution equal to 200 mL and V_{left} is the remaining amount of solution at the end of a cycle. The amount of fluid present in the cement paste is neglected with regards to the leaching solution.
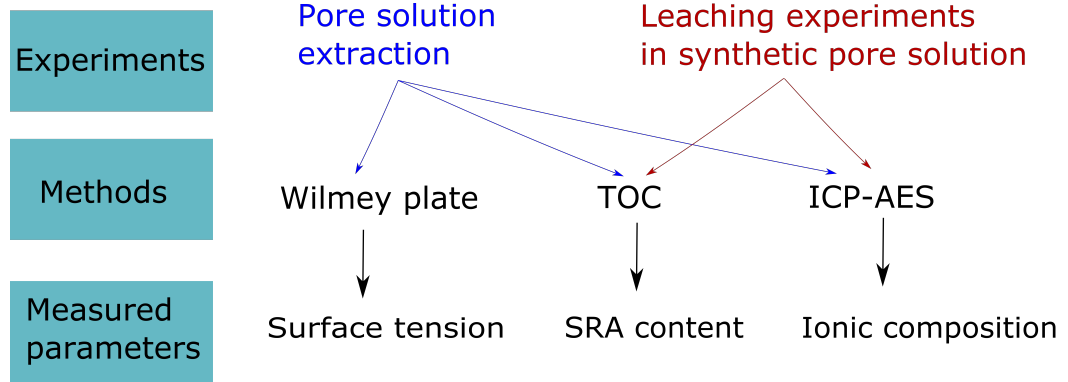
Figure 5.4: Summary of the materials and methods used to characterize SRA
in the pore solution of cement pastes.

5.2.5 Summary of materials and measurements

A summary of the methods employed in this chapter along with concerned
materials can be found in figure 5.4. For pore solution extraction and analy-
sis, 9 types of cement pastes are tested, at the various contents of alkali and
SRA tested. For leaching measurements, 6 types of pastes are tested: pastes
containing SRA at the various alkali content.

5.3 Results on characterization of pore solu-
tion

In this section, we present results for characterization of extracted pore solu-
tion of hardened cement pastes, by means of ICP-AES measurements, TOC
measurements and surface tension measurements. The 9 types of cement
pastes, with various contents of alkali and SRA, are cured under sealed con-
ditions for at least 9 months.

5.3.1 Composition of solutions

Ionic composition of extracted pore solutions plotted as a function of SRA
content is shown in figure 5.5 for the pastes at various contents of alkali
studied. The calcium concentration in pore solution are low in the extracted

Figure 5.5: Measured concentrations of extracted pore solutions for cement pastes at various alkali contents in terms of SRA content.

pore solutions, which can be explained by the fact that concentrations of calcium remain close to the saturation with regards to portlandite (Duchesne and Bérubé, 1994; Gartner et al., 2001).

Results show that sulfates are present in minor concentrations relatively to potassium in the pore solutions. An explanation for this observation is the incorporation of sulfates by hydrates (e.g., ettringite).

Results show that absolute concentration of alkalis (potassium and sodium) decreases consistently with increasing content of SRA. We remind that alkali content is tuned in cement pastes by addition of potassium sulfates to mix water. The consistent decrease of alkali ions in pore solution with increasing content of SRA agrees with results of Rajabipour et al. (2008). In fact, Rajabipour et al. (2008) measured ionic composition on extracted pore solution and found that K^+ and Na^+ have lower concentrations in cement pastes containing SRA, compared to plain paste. They related this observation to the action of SRA on the solubility of alkali sulfates, translated by a reduction of solubility of alkali sulfates and a reduced rate of their dissolution as well. It should be noted that in our study, the potassium sulfate is first dissolved in the mixing water then mixed with clinker. Furthermore, it is noticeable that the decrease of the content of alkali in pore solution with regard to SRA content is higher for higher contents of alkali (that is the slope of potassium content in terms of SRA is larger for large alkali content). As an illustration, for low alkali content the concentration of K decreases from 93 to 28 mmol/L whereas for high content of alkali, K decreases from 614 to 178 mmol/L. In figure 5.6 we show the normalized concentration of alkali (potassium and sodium) in extracted pore solutions, where we normalize the concentrations with regard to the concentrations of the alkali ion in the pore solution of plain paste. Results show that the ratios of concentration of potassium and sodium in the pore solution of the paste containing SRA to the same concentrations in pore solution of plain paste decrease with increasing SRA content, and that this decrease is independent of the alkali content.

Pore solutions are also characterized by TOC measurements. These measurements allow to evaluate content of SRA present in extracted pore solutions. In figure 5.7 we show the results of measured content of SRA for the
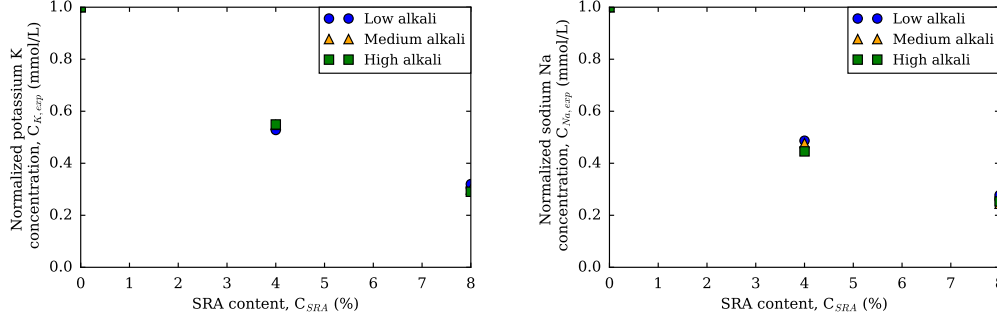
Figure 5.6: Normalized concentrations of extracted pore solutions of alkali (potassium and sodium) in terms of SRA content.

9 types of pastes considered in this study in terms of the SRA content of the samples based on mix design. Note that for paste containing 8% SRA at low alkali content, two measurements are conducted; the measured SRA content is repeatable and is found to vary by 6% on the two samples. Results show a consistent agreement in the content of SRA at the various alkali contents considered. To express the measured concentration of SRA per gram of clinker, exact knowledge of the extracted pore volume is needed. The inverse of the slope of the linear function plotted in figure 5.7 allows an estimation of this extracted pore volume to 0.20 mL per gram of clinker, which is reasonable (and lower) than the assessed total pore volume of 0.35 mL per gram of clinker, based on MIP measurements. The measured content of SRA based on pore solution extraction agrees with the content of SRA based on mix design and assuming no adsorption occurred.

5.3.2 Surface tension of solution

Figure 5.8 displays results of surface tension measured by Wilhelmy method on extracted pore solutions for the 9 types of cement pastes at the various contents of SRA (0, 4 and 8%) and alkali (low, medium and high). The results show that surface tension of pore solution decreases with the presence of SRA. The surface tension of pore solution of paste at low alkali content and containing 8% of SRA (SR8-L) decreases by 42% relatively to the plain paste at the same content of alkali. Moreover, plain pastes showed that the surface
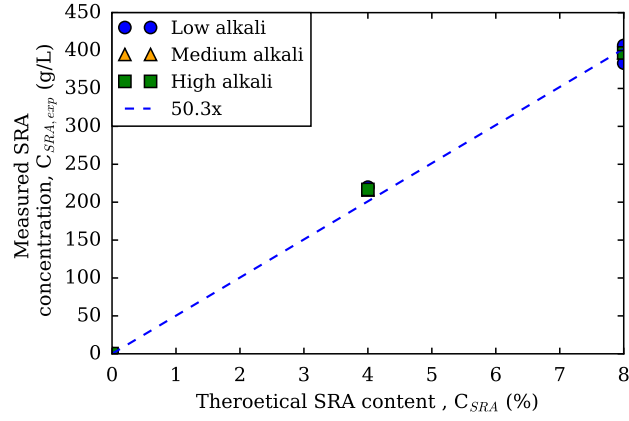
Figure 5.7: Measured content of SRA obtained from pore solution extraction in terms of the SRA content obtained from mix design.
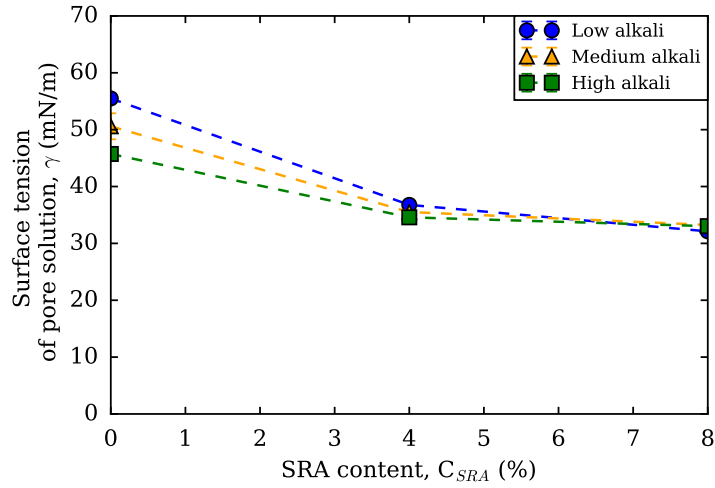
Figure 5.8: Surface tension measured by Whilmey plate method on extracted pore solutions of cement pastes at the 3 contents of alkali in terms of the content of SRA.

tension decreases with increasing alkali content: a decrease of 18% is noted for the high alkali content relatively to the low alkali content. However, for pastes containing SRA, the impact of alkali content on the surface tension of pore solution is minor: at 4% content of SRA, a decrease of 5% of surface tension is noted for the high alkali content relatively to the low alkali content and, at 8% content of SRA, surface tension at high content of alkali increased by 2% relatively to low alkali content.

Reference	Solution	Content	SRA	Surface tension (mN/m)
Bentz et al. (2001)	Distilled water	0	-	76.5
	Distilled water	6%	Eclipse SRA	32.5
Rajabipour et al. (2008)	Synthetic pore solution	0	-	54
	Deionized water	10%	Tetraguard AS20	34
	Synthetic pore solution	10%		31
Eberhardt (2010)	Aqueous solution	10%	Commercial SRA	50
	Synthetic pore solution	10%		49

Table 5.2: Reported values in the literature for the surface tension measurement in SRA/synthetic pore solution or synthetic pore solution only.

In table 5.2 some reported values for mixtures of SRA in synthetic pore solutions or in aqueous solutions can be found. Obtained values concur with the values obtained in this work for measured surface tension in extracted pore solutions with and without SRA. Pease (2005) also confirmed that the surface tension is reduced with various commercial SRAs (Tetraguard, Eclipse, Eclipse Plus, and Eclipse Floor) to approximately 30 mN/m. SRAs allow to
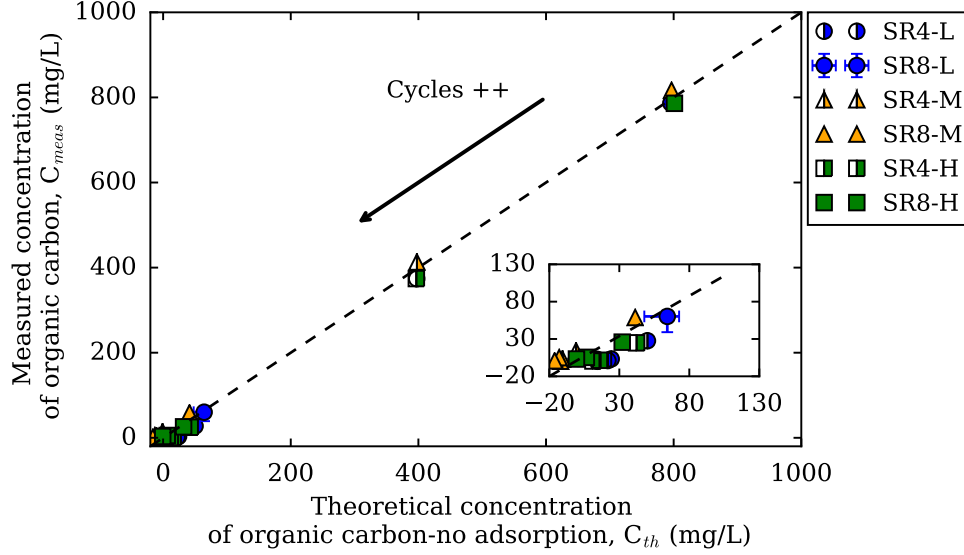
Figure 5.9: Amount of organic carbon originating from SRA leached from
the cement pastes as a function of the theoretical organic carbon expected if
no adsorption of SRA is assumed. Plotted error bars for SR8-L correspond to
the maximum and minimum observed values on the set of 3 measurements.
The inset plot is a zoom on the low region of recorded concentrations.

reduce surface tension in both aqueous solutions and in synthetic pore solutions. The reduction of surface tension is larger in an aqueous solution (76.5 mN/m for water down to 30 mN/m) than in the pore solution (54 mN/m down to 31 mN/m). Values of surface tension reported for synthetic pore solutions concur with the values obtained in this work for extracted pore solution of plain pastes at the various contents of alkali.

5.4 Results of the leaching of SRA from cement pastes

In figure 5.9 we plot the measured concentration C_{meas} of organic carbon in solutions as a function of the theoretical concentration C_{th} computed as detailed in section 5.2.4. With increasing number of cycles, the concentration of organic carbon amount decreases in the solution. Moreover, the mea-

sured organic carbon amount corresponds to the theoretical organic carbon amount in the solution computed under the assumption that no adsorption occurred. Both amounts tend to low values, indicating that organic carbon is completely depleted, and hence SRA can be removed entirely by leaching experiments. Furthermore, a significant amount of SRA is removed at the first cycle, further confirming the preliminary results for determining the leaching protocol detailed in section 5.2.4, and shown in figure 5.3, where a large fraction of the SRA is leached out of the cement pastes in only one cycle. We do note that negative values for the theoretical organic concentrations are encountered at the last cycles for some cement pastes meaning that more organic carbon is released than expected. However this may be explained by an accumulation of errors in the computation of these values of organic carbon concentrations: error bars on the set on SR8-L are on the same order of magnitude as the variation of these negative values. We conclude that the SRA used in this study can be leached out from the cement pastes regardless of alkali content, hence all of the SRA is "mobile" under the definition given by Eberhardt (2010).

Results of ionic composition of leaching solutions are shown in figures 5.10 and 5.11 for pastes at the various contents of alkali for pastes containing 4% content of SRA and pastes containing 8% content of SRA, respectively, where we plot the total content of compounds (calcium, potassium, sulfate and sodium). Cycle 0 corresponds to synthetic pore solutions, and shows that the synthetic pore solutions is composed of calcium ions, potassium ions and sodium ions in majority. Results show that calcium and potassium have the largest concentrations in the solutions of leaching experiments, indicating that the leaching in deionized water (as for the preparation of SPS) leads to the dissolution of the calcium bearing phases (e.g., portlandite and ettringite).

Let us examine the alkali content of the synthetic pore solution, corresponding to cycle 0 on the figures 5.10 and 5.11. If we assume that the potassium in solution is that of the alkali added to the cement paste, we find for the medium alkali content, based on mix design, the molar fraction amount of potassium per gram of hardened cement paste (saturated)
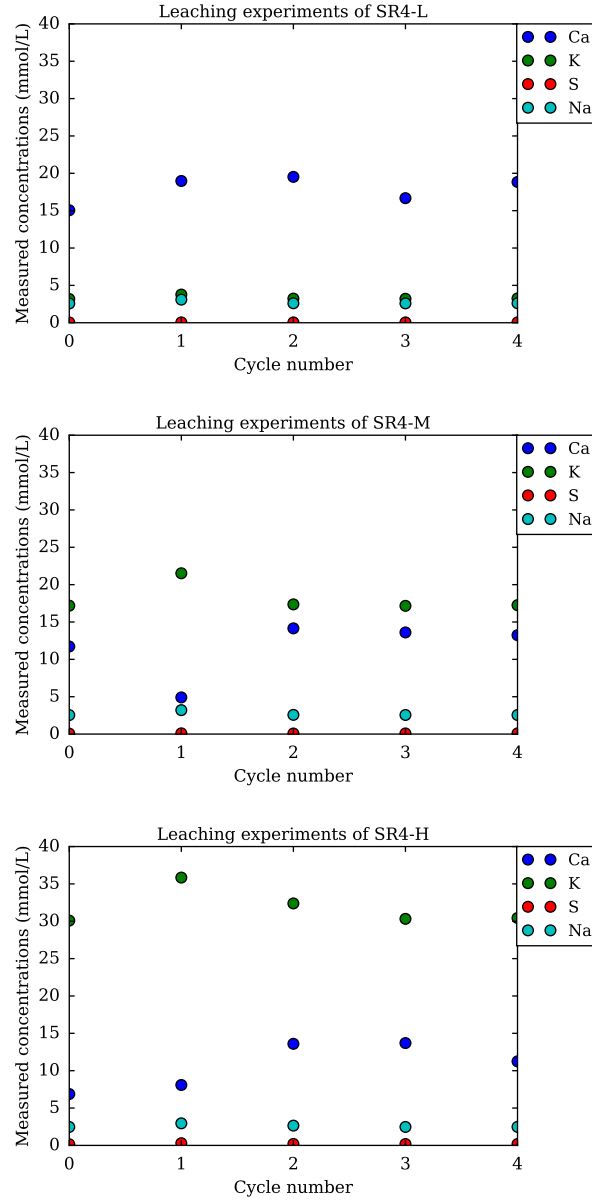
Figure 5.10: Measured concentrations of ionic composition of solutions for leaching cycles on cement pastes at 4% content of SRA at various contents of alkali. Cycle number 0 refers to the synthetic pore solution prepared for leaching experiments.

is: $m_{K_2SO_4}/m_{hcp} \times 2/M_{K_2SO_4}$, where $M_{K_2SO_4} = 174$ g/mol is the molar mass of K_2SO_4, hence the concentration of potassium in leaching solution (due to enrichment in alkali) $\simeq 14$ mmol/L. The difference between the amount of potassium for synthetic pore solution at medium alkali content and the amount of potassium for synthetic pore solution at low alkali content yields $\simeq 14$ mmol/L, and the difference between high alkali content and low alkali content gives $\simeq 27$ mmol/L. This indicates that potassium added to cement paste can be recovered in the eluate. The amount of potassium measured in the synthetic pore solutions corresponds well to the amount of enrichment in alkali.

We also note that the concentration of calcium in the pore solution is reduced with increasing alkali concentration. Concentration of sulfate in the synthetic pore solution and the eluates through leaching cycles remains low. Given that enrichment of cement paste in alkali content is conducted by means of addition of potassium sulfate to the mixing water, 1 mole of potassium sulfate added corresponds to 2 moles of potassium and 1 mole of sulfate. The low values of sulfate concentrations in the eluate, compared to potassium, indicates that the sulfates are incorporated in the aluminate phases, namely ettringite. This observation is also confirmed by measurements on extracted pore solutions. Furthermore, the composition of solutions varies only slightly compared to synthetic pore solutions (corresponding to cycle 0), confirming that hydrates dissolution is prevented by conducting leaching measurements using synthetic pore solutions.

5.5 Conclusions

In this chapter, a physico-chemical characterization of the SRA in the cement pastes is performed. We analyzed the potential adsorption of SRA on cement hydrates by means of leaching experiments conducted using synthetic pore solutions. Pore solution extractions are also conducted, and the obtained pore solutions are analyzed for their content of SRA, their ionic composition and their surface tension is measured. We concluded based on the set of this experimental campaign, summarized in figure 5.4, that:
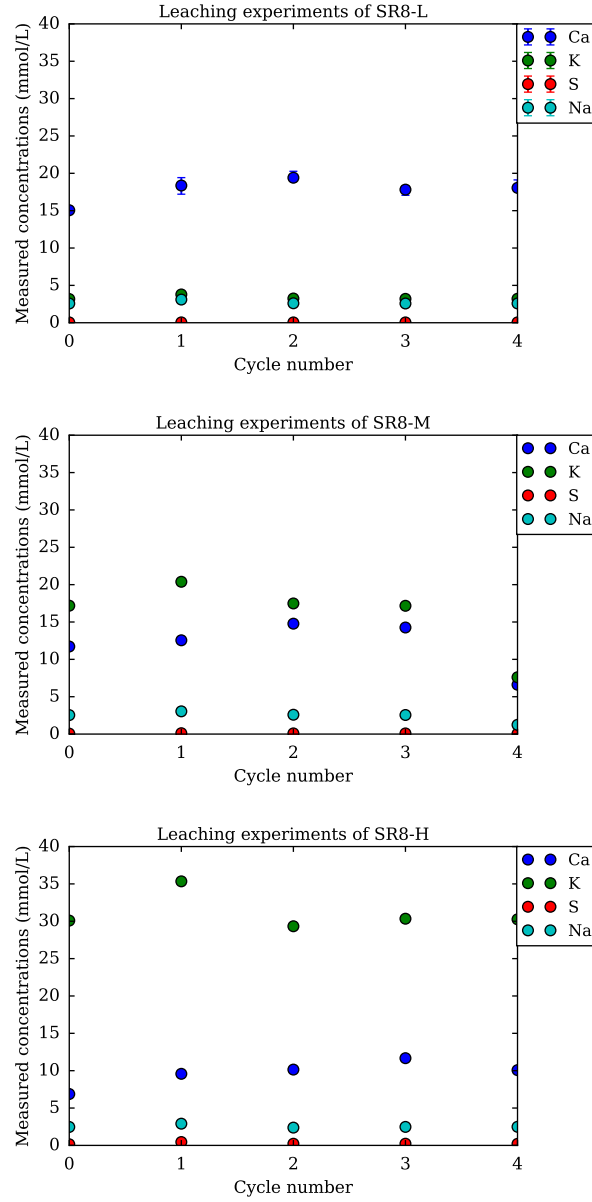
Figure 5.11: Measured concentrations of ionic composition of solutions for leaching cycles on cement pastes at 8% content of SRA at various contents of alkali. Cycle number 0 refers to the synthetic pore solution prepared for leaching experiments.

- SRA used in this study does not adsorb on cement hydrates and can be leached out of the cement pastes, regardless of alkali content as shown in figure 5.9. The amount of SRA leached out and in the pore solution can be assessed from the mix design.

- Alkalis are depleted in presence of SRA since amount of alkali in pore solution decreases consistently with SRA content, as shown in figure 5.6.

- Surface tension of pore solution is reduced in presence of SRA, and the surface tension in presence of SRA is slightly dependent of the alkali content for investigated contents of SRA as shown in figure 5.8.

- Surface tension of pore solution of plain pastes decreased with increased content of alkali for plain pastes, as shown in figure 5.8.

Chapter 6

Modeling of water content

This chapter addresses the modeling of water content of the 9 types of cement pastes with various contents of SRA and alkali, on drying and rehumidification. The water content that we aim at modeling is the water content obtained by gravimetric method. Understanding water distribution in cement pastes, and quantifying the contribution of different types of water to the water content of cement pastes is important to understand and model the strains induced by each type subsequently. To estimate the water content, and resolve it into different types, knowledge of pore structure is necessary. We use the pore size distribution and specific surface area distribution as an input to estimate the water content of cement pastes. Two models are presented in this chapter based on the discrimination of water in the pore space:

1. Water in capillary pores, water adsorbed on surfaces and water in micropores based on nitrogen sorption istoherms.

2. Water in capillary pores, water adsorbed on surfaces based on water sorption isotherms (obtained by volumetric method).

6.1   Inputs of model and framework

In this section we introduce the inputs of the model and how they are quantified, as well as the model workflow. We model the water content of cement

pastes measured by gravimetric method (i.e., weighing the cement pastes equilibrated at set RH for several months). The pore structure characterization is used as an input for the model. The pore structure is analyzed either by nitrogen sorption isotherms or by water sorption isotherms (volumetric method, obtained by equilibrating the cement pastes, dried prior to measurement, at set RH for few hours).

6.1.1 Identification of types of water: model 3W and model 2W

In this section, we detail the method for quantifying the water in pore space under the scope of:

- Model 3W, based on nitrogen sorption isotherms, and considering 3 types of water: water in capillary pores, water adsorbed on surfaces and water in micropores.

- Model 2W, based on water volumetric sorption isotherms, and considering 2 types of water: water in capillary pores and water adsorbed on surfaces.

Amount of water in capillary pores is denoted as w_{cap}. Amount of water adsorbed on surfaces of pores that had been emptied of their condensate is denoted as w_{ads}, and water present in micropores is denoted as w_μ. Note that these water types are expressed in fraction of mass per mass of dry cement paste (dried at 105°C under vacuum). The water content w of cement paste is assessed, in the scope of model 3W, as follows:

$$w = w_{cap} + w_{ads} + w_\mu \tag{6.1}$$

In the scope of model 2W, the water content is assessed as follows:

$$w = w_{cap} + w_{ads} \tag{6.2}$$

To resolve water content w in cement paste into these three forms (capillary, adsorbed on surfaces, and in micropores), or two forms (capillary,

adsorbed on surfaces), and model their evolution during drying and re-humidification, knowledge of pore structure is required.

When a pore is desaturated, i.e., filled by gaseous phase, a film of water remains adsorbed on the pore walls. The thickness of adsorbed layer is assessed from the Badmann t-plot (Badmann et al., 1981) at the considered relative humidity. Based on the latter, the pore radius r_c of the pores, where the capillary meniscus is formed at a given relative humidity h_r, is corrected to account for the presence of the adsorbed layer t, following:

$$r_k(h_r) = r_c(h_r) - t(h_r) \tag{6.3}$$

where r_k is the Kelvin radius evaluated by equation 2.11.

We do note that we assume that the t-plot is a characteristic function of the cement paste, and is independent of alkali or SRA content. This assumption is verified in figure 6.1, where we assessed t-plot from water vapor adsorption isotherms (volumetric method), following:

$$t = \frac{V_{ads}}{S_{ssa}} \tag{6.4}$$

where V_{ads} is the adsorbed volume obtained from the adsorption isotherm (volumetric method) at a given RH on the cement pastes, and S_{ssa} is the specific surface area evaluated by BET model. The assessed t-plot concurs with Badmann t-plot, and is independent of the contents of SRA and alkali.

From BJH analysis of nitrogen sorption isotherms, we obtained the cumulative pore volume, and the cumulative surface area as a function of the pore radius r. The amount of water in capillary pores that remain saturated at a given relative humidity can be deduced, which allows to estimate the amount of capillary water present in cement paste at the considered relative humidity following:

$$w_{cap} = (V_{total} - V(r \geq r_c)) \times \rho_w \tag{6.5}$$

where V_{total} is the total volume of pores, and $V(r \geq r_c)$ is the volume of pores of a radius larger than r_c, i.e., volume of empty pores.
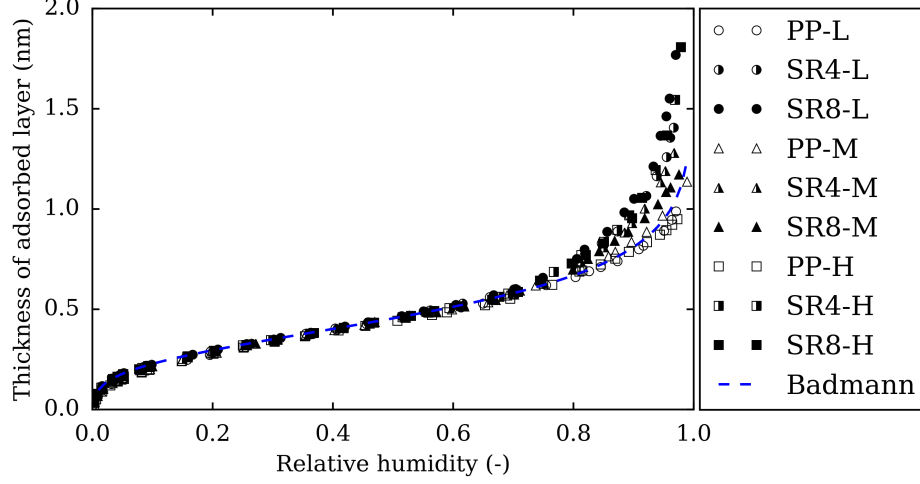
Figure 6.1: Statistical thickness of the adsorbed water based on water vapor sorption isotherms compared to Badmann t-plot.

The surface area of pores that are empty is known as well. Using the Badmann t-plot, the amount of adsorbed water can be computed following:

$$w_{ads} = (S_{ssa}(r \geq r_c) \times t) \times \rho_w \tag{6.6}$$

where $S_{ssa}(r \leq r_c)$ stands for the specific surface area of pores of radius larger than r_c expressed in m^2 per g of dry cement paste, and t is the thickness of the adsorbed layer. We assume that $\rho_w= 1$ g/cm^3.

To account for the ink-bottle effect (introduced in section 2.2.3) in the drying and re-humidification of cement pastes, the microstructure is analyzed by nitrogen sorption isotherms by applying BJH analysis to adsorption branch when re-humidification of the cement pastes is considered, whereas BJH analysis is conducted on desorption branch of nitrogen sorption isotherms for the drying of the cement pastes.

For model 3W, note that when BJH analysis is conducted on desorption branch of nitrogen sorption isotherms, we are limited by the presence of the cavitation. The BJH analysis cannot be carried out below the cavitation pressure of nitrogen occurring at a relative pressure ~ 0.42. Below the

corresponding radius $r_{cavitation} \simeq 2.1$ nm[1], water is assumed to be present as adsorbed water on the total exposed surfaces. This means that $w_{cap}=0$ and $w_{ads} = S_{ssa} \times t \times \rho_w$, where S_{ssa} is the specific surface area evaluated by BET model on the adsorption isotherms. This assumption will be later investigated by the use of microstructure analyzed by mercury intrusion porosimetry, given that MIP makes it possible to intrude pores of an entry size smaller than $r_{cavitation}$. As for the adsorption branch of nitrogen isotherms, we choose the same limit for pore size (i.e., 2.1 nm) below which the capillary condensate is considered to be emptied, and water is present only in adsorbed form on all the exposed surface area, as estimated by BET theory.

For model 3W, the difference between the capillary water and adsorbed water on one hand and the measured water content on the other hand is assigned to water in micropores. In the first instance, we examine the evolution of amount of water in micropores during drying and re-humidification, then we attempt to model it in order to estimate water content of cement paste as will be detailed in following sections.

6.1.2 Model 3W: water in micropores during a desorption-adsorption cycle

In the following, we disregard the impact of the evolution of microstructure on the water content of cement pastes, and we consider the microstructure of cement pastes at the sealed state as an input for the estimations of types of water. The pore structure is analyzed by BJH applied to nitrogen sorption isotherms.

Based on estimation of water adsorbed on surfaces (based on equation 6.6) and water in capillary pores (based on equation 6.5) we can evaluate water in micropores the amount w_μ accounting for the measured water content

---

[1]This size is estimated for a relative pressure 0.51 as the sum of Kelvin radius and thickness of adsorbed layer (evaluated by Harkins and Jura (1944)).

(gravimetric), as follows:

$$w_\mu = w_{exp} - w_{cap} - w_{ads} \tag{6.7}$$

where w_{exp} is measured water content by gravimetric method (i.e., by weighing the samples kept in the desiccators).

We plot the amount w_μ of water in micropores on desorption-adsorption cycle in terms of relative humidity as shown in figure 6.2. Most of the water content in micropores is removed and regained in the high range of relative humidity. In fact, for RH<60% water in micropores increases only slightly and remains lower than 0.02 g/g. Above this relative humidity a significant amount of water in micropores is regained. In contrast, on desorption branch for plain pastes, water content in micropores decreases almost linearly until reaching a water content of 0.02 g/g at 40%. For pastes containing SRA, on desorption branch, most of the water content in micropores is removed at 54%.

In first order, water content in micropores during desorption and water content in micropores during adsorption follow each a master curve, regardless of alkali content and SRA content. Water content in micropores can be described by the following equation:

$$w_\mu(h_r) - w_\mu(11\%) = \alpha_1 \exp(\alpha_2 h_r) \tag{6.8}$$

where $\alpha_1 = \alpha_{1,ads} = 2.4 \times 10^{-4}$ g/g$_{d105}$ and $\alpha_2 = \alpha_{2,ads} = 6.6$ in case of adsorption (re-humidification) of cement paste, and $\alpha_1 = \alpha_{1,des} = 3.6 \times 10^{-3}$ g/g$_{d105}$ and $\alpha_2 = \alpha_{2,des} = 4$ in case of desorption (i.e., drying) of cement paste.

At any relative humidity, water content in micropores is higher on desorption branch than in adsorption branch, indicating that hysteresis is present in the process of adsorption and desorption of water in micropores.
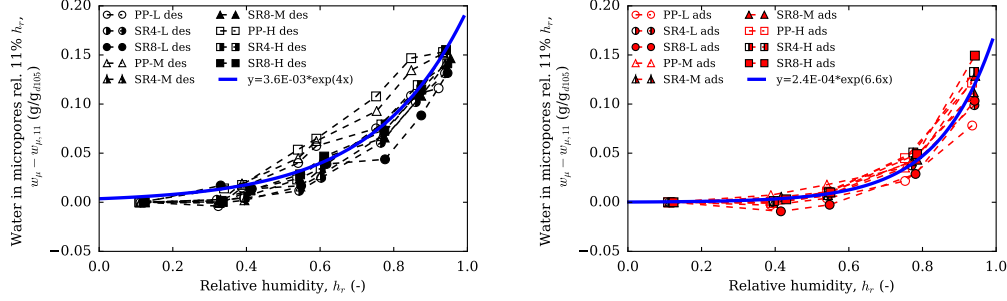
Figure 6.2: Water in micropores on first desorption (left) and adsorption (right) relatively to state at 11% relative humidity. By default, dashed lines are plotted as a visual guide, unless specified otherwise.

6.1.3 Workflow of models

In figures 6.3 and 6.4 we show the workflow of the model 3W and of the model 2W respectively.

6.2 Results of modeling of water content

In this section we present results of modeling of water content for cement pastes on drying and re-humidification based on two models:

- Model 3W: based on nitrogen sorption isotherms, resolves 3 types of water: water in capillary pores, water adsorbed on surfaces and water in micropores.

- Model 2W: based on water sorption isotherms, resolves 2 types of water: water in capillary pores and water adsorbed on surfaces.

The pore structure is considered not evolving on drying and re-humidification, and is based on measurements of samples kept at sealed state. Impact of neglecting the evolution of microstructure on the evolution of pore structure will be later verified.
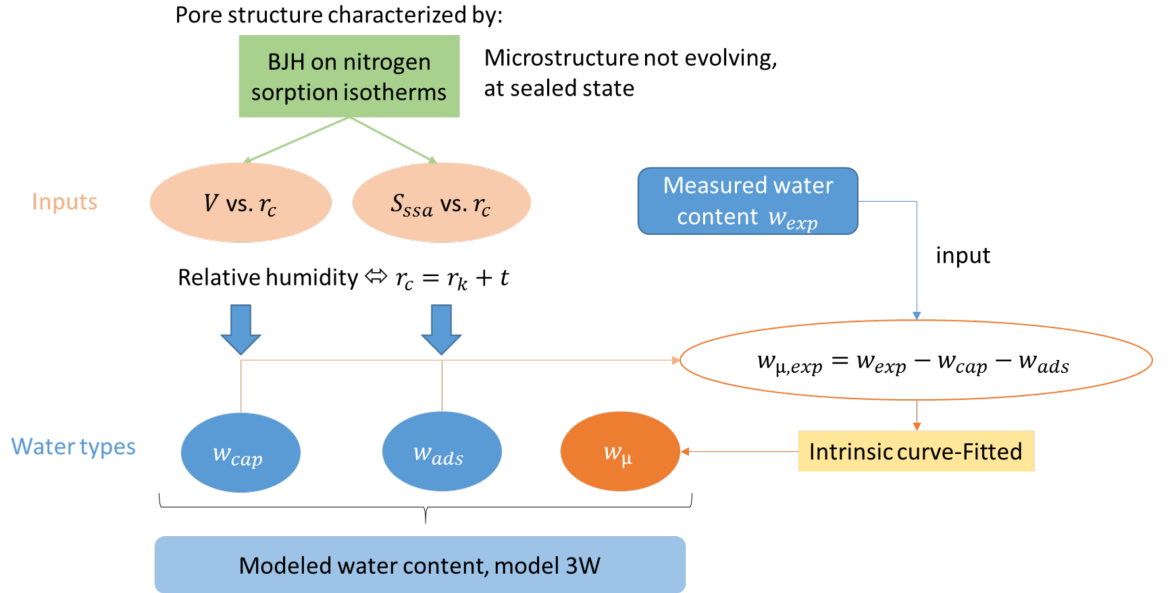
Figure 6.3: Workflow of the model 3W for the water content of cement pastes based on three types of water.
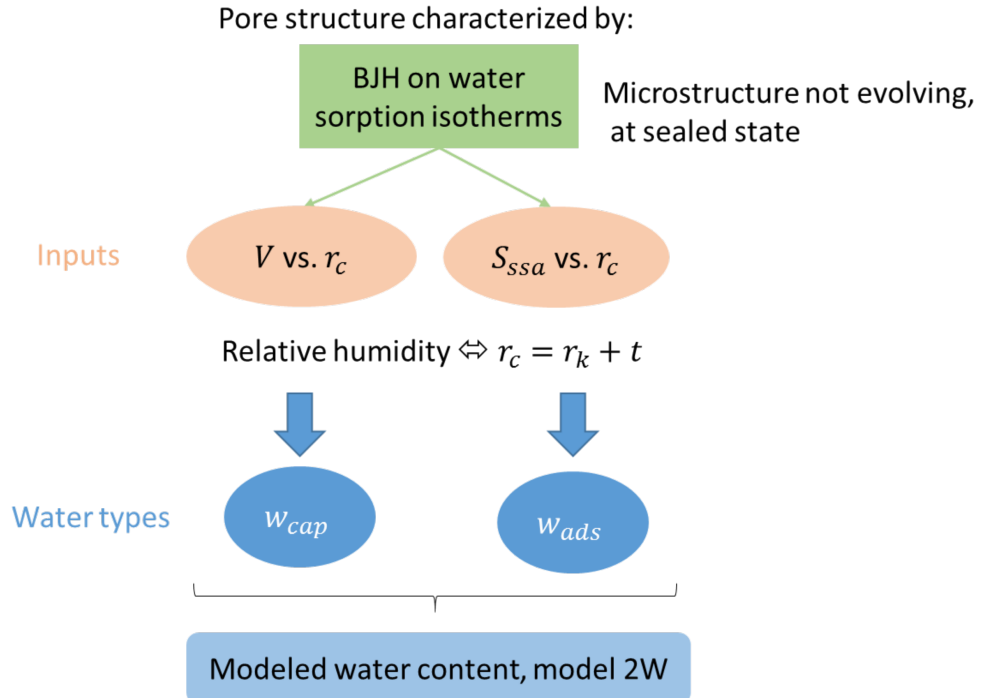
Figure 6.4: Workflow of the model 2W for the water content of cement pastes based on two types of water.

6.2.1 Results of modeling of water content based on model 3W

Considering the empirical function obtained for water in micropores as a function of relative humidity given in equation 6.8, we can estimate water content of cement pastes during re-humidification and drying.

The results of water content estimations resolved into water in capillary pores, water adsorbed on surfaces, and water in micropores are shown in figure 6.5 for two types of cement pastes during the adsorption. During the re-humidification of cement pastes, water in cement pastes evolves such that water in capillary pores is regained gradually after reaching about 60% or 75% relative humidity for plain paste and paste containing SRA, respectively. Adsorbed water, relatively to the state at 11%, increases with increasing h_r. Adsorbed water reaches a maximum at the same relative humidities where water in capillary pores is depleted. Note that water adsorbed on surfaces is computed relatively to state at relative humidity of 11%, where all surface area is considered to be covered by an adsorbed layer. The computed water adsorbed on surfaces at 11% RH can surpass adsorbed water at higher relative humidities, which leads to negative values of the computed adsorbed water relative to state at 11% RH. Water in micropores varies only slightly for relative humidities lower than 60%. At relative humidities higher than 60%, water content consists mostly in water in micropores and water in capillary pores.

Water content estimations for 9 types of cement pastes studied here are shown in figures 6.6, 6.7 and 6.8 for pastes at low alkali content, medium alkali content and high alkali content, respectively. Results show a general agreement between experimental values and the ones estimated with the model 3W.
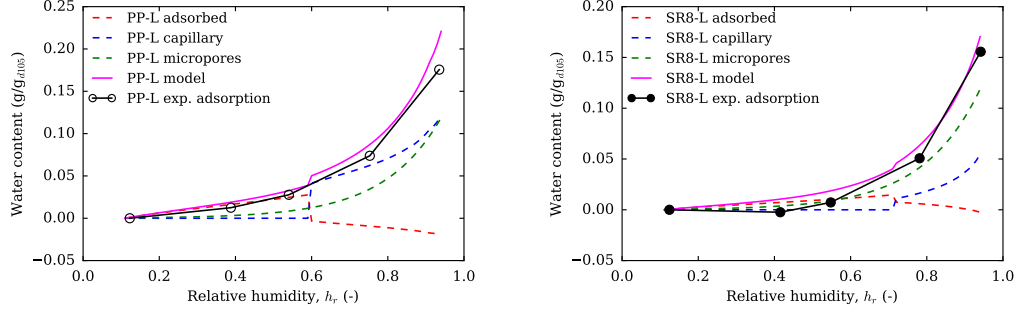
Figure 6.5: Estimated water content on adsorption branch and contribution of adsorbed water, water in capillary pores and water in micropores to the water content for a plain paste low alkali (left) and SRA paste containing 8% SRA low alkali (right).

6.2.2 Results of modeling of water content based on model 2W

We use water sorption isotherms measured by volumetric method to model water content, and resolve it into water in capillary pores and water adsorbed on surfaces, based on equations 6.5 and 6.6. In equation 6.5 V_{total} corresponds to the volume of pores of a size lower than 35 nm in radius, this pore radius is imposed by the maximum pore size used for the model 3W, dictated by the BJH analysis applied to the nitrogen sorption isotherms.

The results of the modeled water content and measured water content are shown in figures 6.9, 6.10 and 6.11 for pastes at low alkali content, medium alkali content and high alkali content, respectively.

Below the cavitation pressure of water, water is considered adsorbed on surfaces. The surface area is evaluated by BET applied to water sorption isotherms, and is equal on both drying and re-humidification. Hence, on the low range of RH, the model predicts no hysteresis of the water content.

We compare the difference between measured water content (gravimetric method, long-term) and modeled water content based on water sorption isotherms (volumetric method, short-term) in figure 6.12 on drying and re-humidification. We observe that for plain pastes, the difference between es-

218
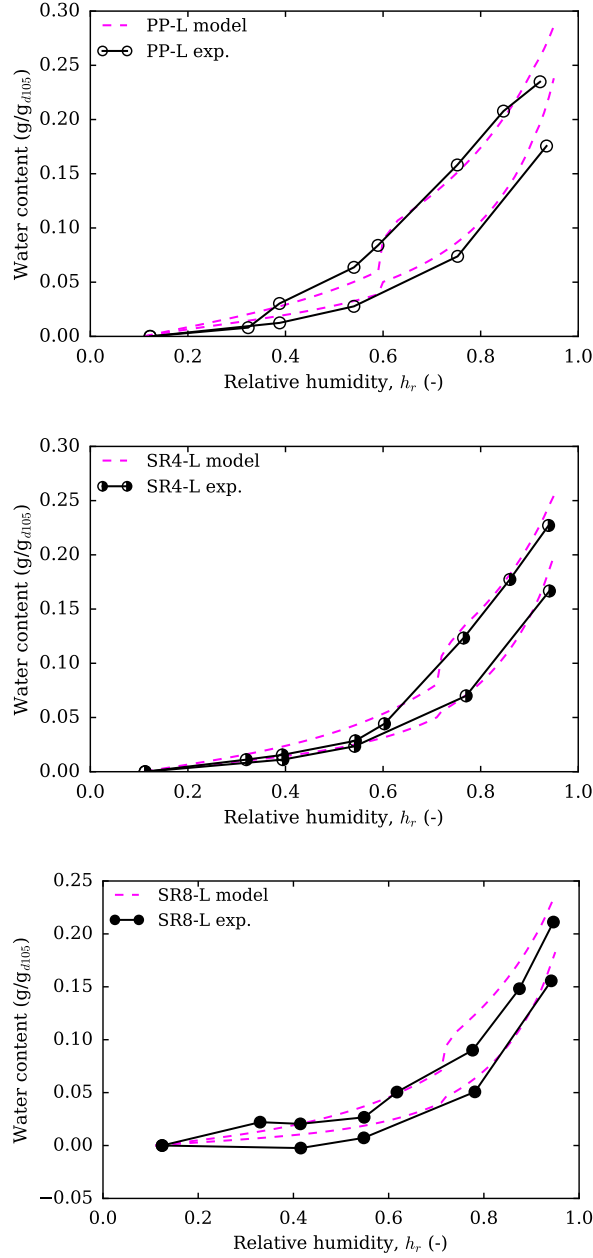
Figure 6.6: Estimated water content of cement pastes based on model 3W and experimental values relative to water content at 11% relative humidity, when pore structure is analyzed by BJH applied to nitrogen sorption isotherms, for pastes at low alkali content.

219
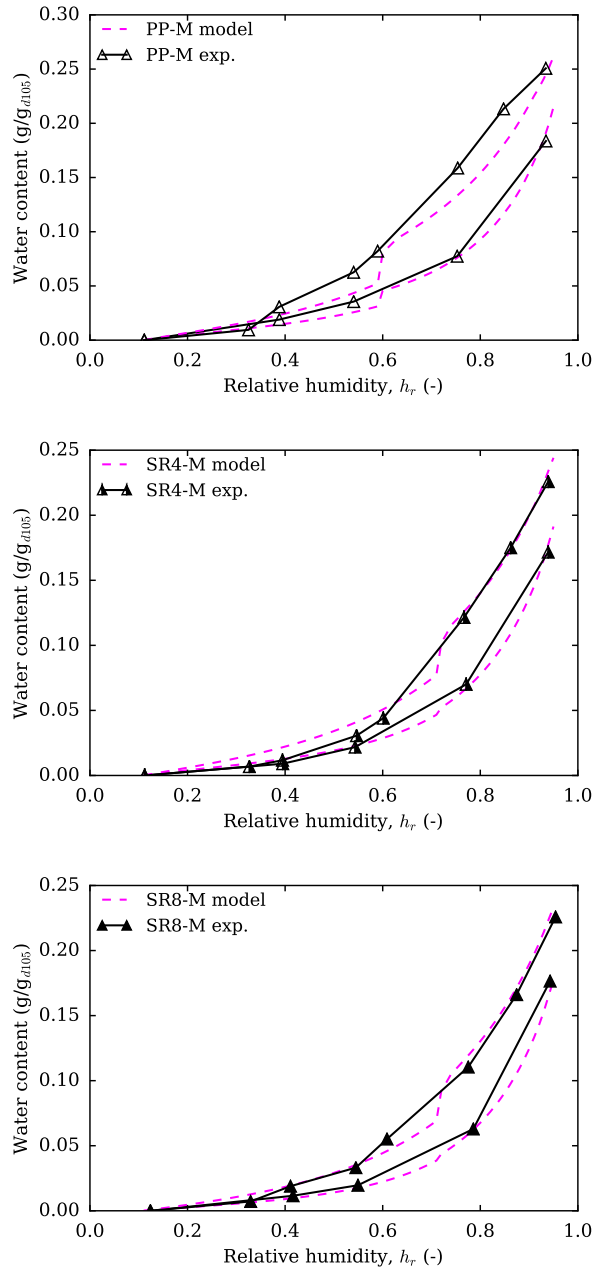
Figure 6.7: Estimated water content of cement pastes based on model 3W and experimental values relative to water content at 11% relative humidity, when pore structure is analyzed by BJH applied to nitrogen sorption isotherms, for pastes at medium alkali content.
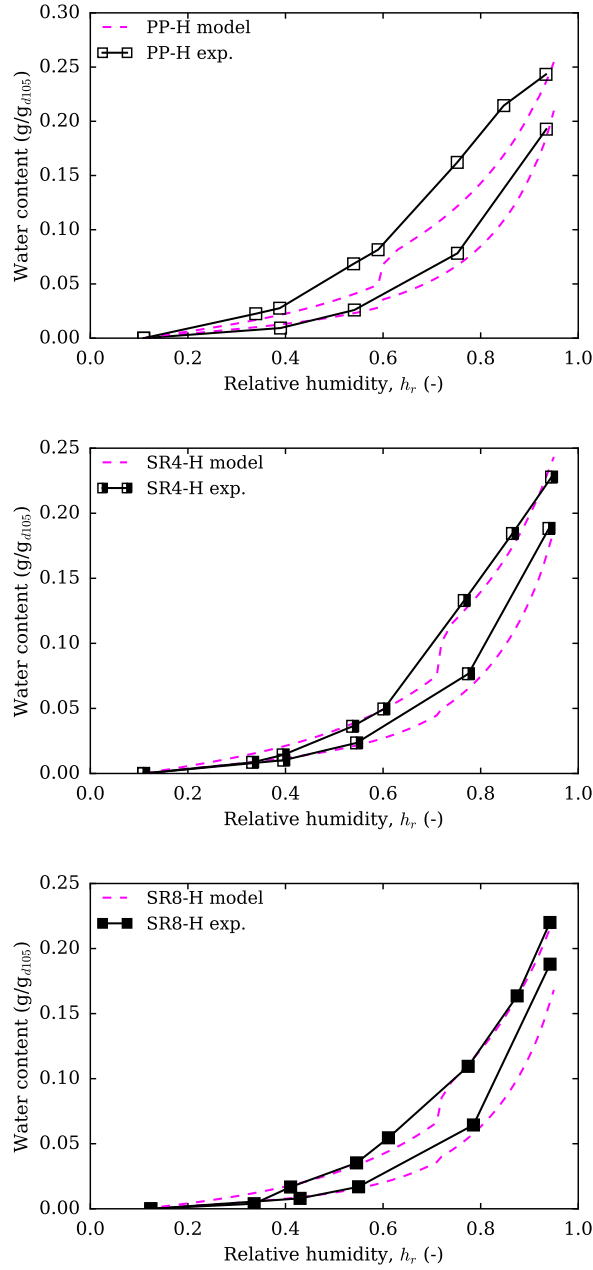
Figure 6.8: Estimated water content of cement pastes based on model 3W and experimental values relative to water content at 11% relative humidity, when pore structure is analyzed by BJH applied to nitrogen sorption isotherms, for pastes at high alkali content.
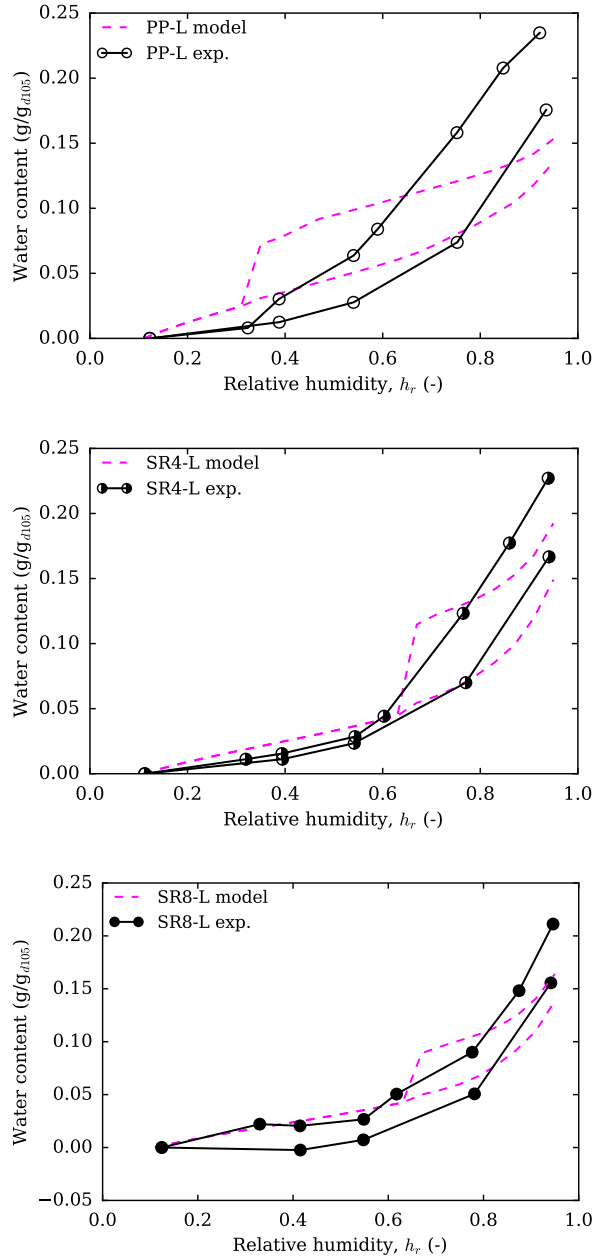
Figure 6.9: Predicted water content of cement pastes based on model 2W and experimental values relative to water content at 11% relative humidity when microstructure is analyzed by BJH on water sorption isotherms, for pastes at low alkali content.
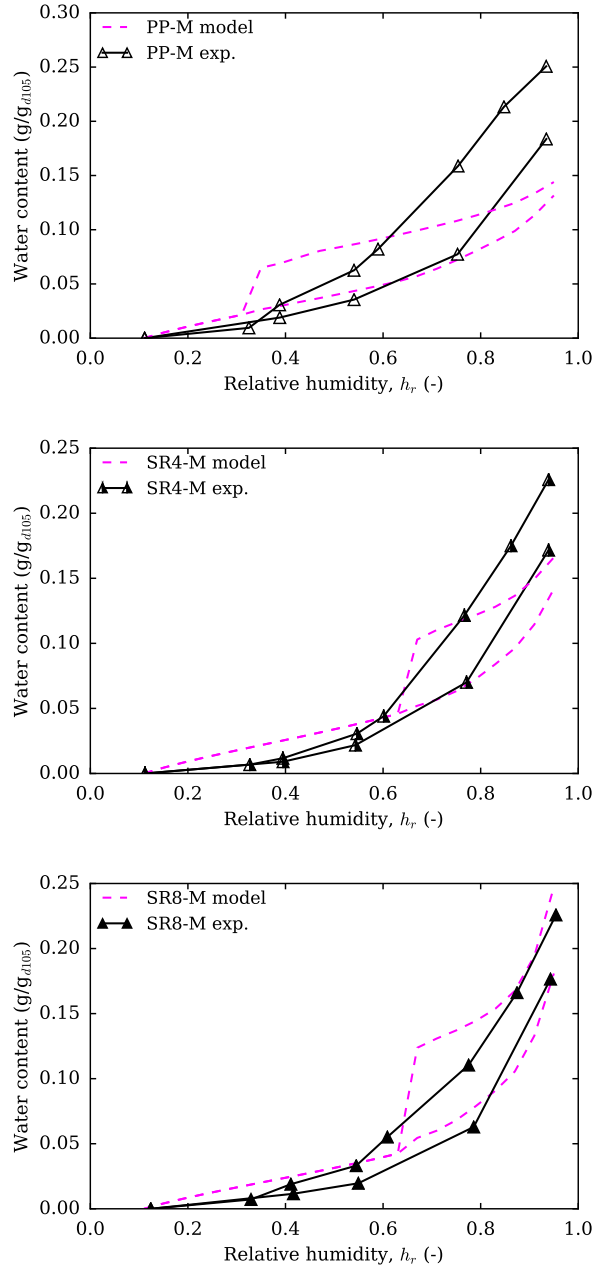
Figure 6.10: Predicted water content of cement pastes based on model 2W and experimental values relative to water content at 11% relative humidity when microstructure is analyzed by BJH on water sorption isotherms, for pastes at medium alkali content.
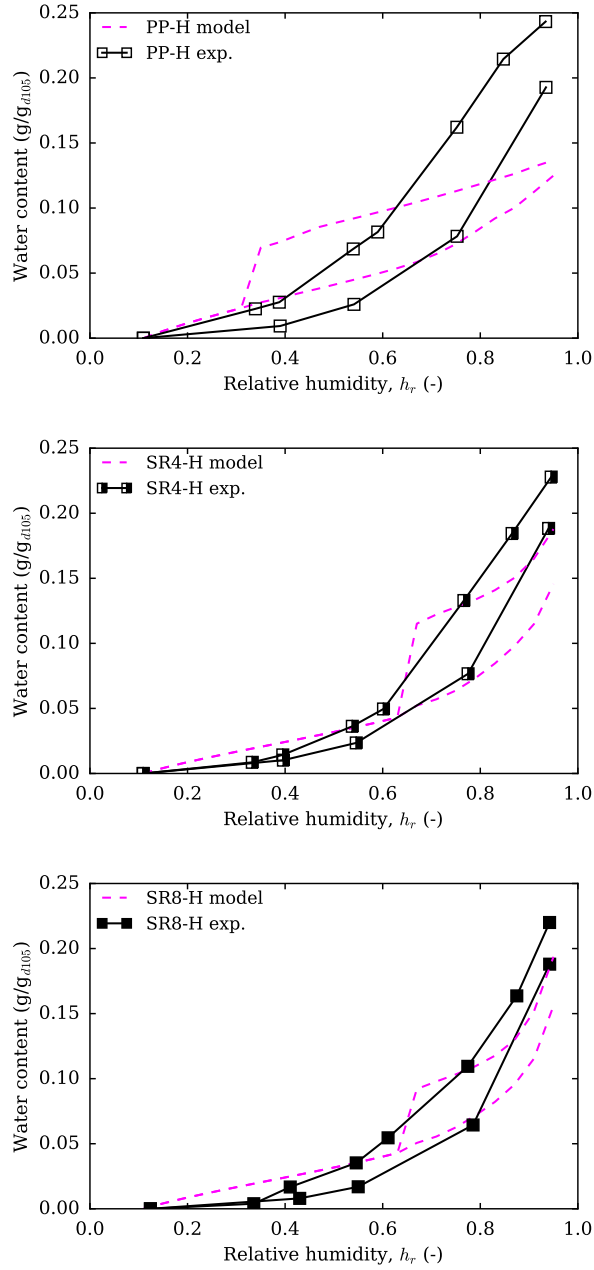
Figure 6.11: Predicted water content of cement pastes based on model 2W and experimental values relative to water content at 11% relative humidity when microstructure is analyzed by BJH on water sorption isotherms, for pastes at high alkali content.
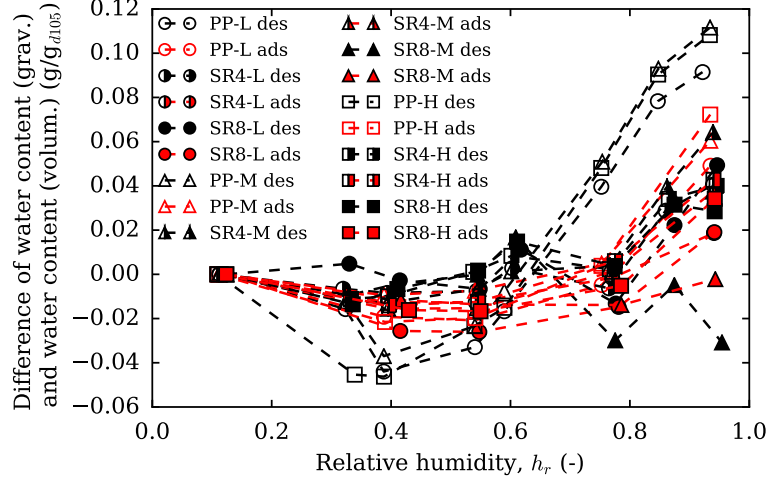
Figure 6.12: Difference between water content based on gravimetric measurements and on volumetric measurements. Red symbols correspond to adsorption branch, and black symbols correspond to first desorption.

timated water content (sum of capillary and adsorbed water) and measured water content is non negligible, especially at RH higher than 60%. This may originate from the underestimation of capillary water. In fact, the input used here (that is water sorption isotherms measured on pre-dried powder sample) is limited to the maximum relative humidity that is observed during the measurements. In the high range of relative humidities (>95%) controlling the set relative humidity may be an issue, and may lead to an underestimation of the total pore volume. The volumetric water sorption isotherms are also conducted on cement pastes dried prior to the measurements (by vacuuming at room temperature). Although the drying method is meticulously chosen to limit the impact of drying, this latter may not be completely eliminated. Further, the differences observed on low RH may also be linked to the reorganization of the pore structure on long-term drying for the measurements of the gravimetric water content of cement pastes (detailed in section 4.4). In this case, water content of cement paste on long-term measurements is lower than the modeled water content based on the volumetric water sorption (at sealed state), since the surface area decreases on long-term drying.

225

6.3 Impact of assumptions of analysis on modeled water content

In this section we examine the impact of hypotheses made in the modeling of water content. Firstly, we verify the influence of the choice of cut size of pores below which all pores are emptied of their condensate, and covered by an adsorbed layer on model 3W. Secondly, we examine the impact of disregarding the influence of evolution of pore structure.

6.3.1 Impact of choice of threshold radius for capillary water of model 3W

In model 3W, pore structure is used as input and analyzed by nitrogen sorption isotherms. When pore structure is analyzed by nitrogen sorption isotherms, we are confronted to cavitation of nitrogen that occurs on desorption branch. Cavitation of the saturating fluid, which is under significant tensile stresses, is translated into the emptying of pores at a critical relative pressure. To overcome the cavitation of nitrogen on desorption branch for the analysis of microstructure by BJH model, microstructure is assumed to be described only by its specific surface area assessed by BET model for pores where cavitation on nitrogen occurs. The cavitation of nitrogen occurs for pores of entry size of 2.1 nm. In figure 6.13 we plot the estimated desorption branch of water content based on model 3W where we choose, in addition to the cut equal to 2.1 nm, a second cut size equal to 2.5 nm. The grayed zone in figure 6.13 corresponds to the zone bound by RH where cavitation of water indeed occurs and the RH that corresponds to the size of pores where cavitation of nitrogen occurs, and where we approximate water content by the adsorbed water on BET specific surface area. The largest observed error for the examined pastes is $\sim$0.03 g/g.

An alternative method to describe the microstructure on desorption is mercury intrusion porosimetry (MIP). In fact, the intrusion of mercury is equivalent to an invasion of the pores by a non-wetting phase. Therefore, mercury intrusion porosimetry allows the description of the pore entries (Ali-
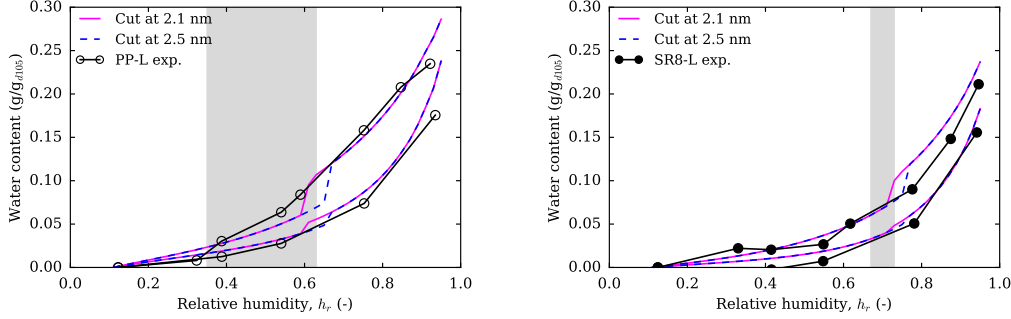
Figure 6.13: Impact of the choice of cut size on estimations of water content for a low alkali content plain paste (PP-L) and paste containing 8% SRA (SR8-L). The grayed zone corresponds to the range of RH where water is assumed adsorbed on surfaces as dictated by the characterization of pore structure by nitrogen on desorption branch.

gizaki, 2006, p.80-81), as detailed in section 2.2.2. Given that the smallest intruded entry of pore is ~ 1.6 nm, MIP allows us to assess microstructure below the entry radius of pores at which cavitation occurs around 2.1 nm. Making use of both cumulative pore volume and cumulative specific surface area obtained by MIP as a function of pore entry radius, we derive capillary water and adsorbed water. Considering water in micropores as obtained by equations 6.7, we compute the water content. We show results for two pastes at low alkali content, plain paste and paste containing 8% SRA content in figure 6.14. We examine the impact of both the technique used (MIP and nitrogen desorption branch) and the choice of cut size for presence of capillary condensate. Results show that both MIP and nitrogen sorption isotherms for pore structure input allow to approximate the water content of cement pastes. For plain paste the use of MIP as input for modeling of water content leads to an absolute error for plain paste low alkali content of 0.06 g/g for RH higher than 60%. The choice of cut size for MIP has little impact on the obtained results.
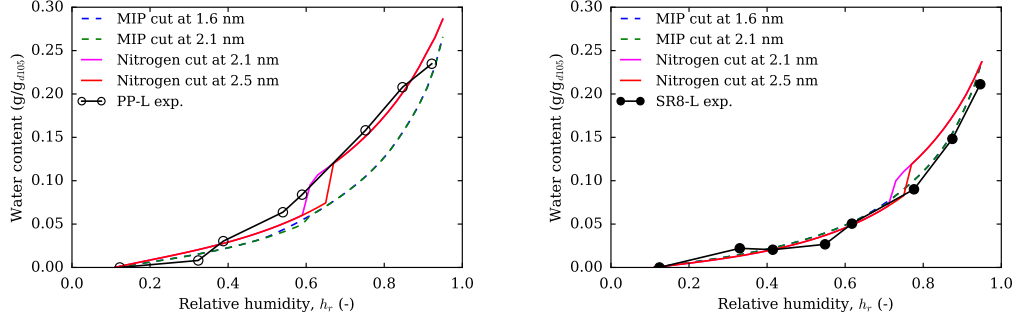
Figure 6.14: Estimations of water content on drying based on model 3W and using as input desorption branch of nitrogen to characterize pore structure with two cut sizes 2.1 nm and 2.5 nm and using MIP with two cut sizes 1.6 nm and 2.1 nm. An illustration is given for plain paste at low alkali content (left) and paste containing 8% SRA at low alkali content (right).

6.3.2 Impact of evolution of pore structure on estimation of water content

In this section, we address the impact of the pore structure of plain cement pastes on the estimated water content.

In section 4.4, an evolution of the microstructure is observed for cement pastes, regardless of alkali content and SRA content. Indeed, microstructural changes during drying are captured by a decrease of specific surface area, evaluated by BET model applied to nitrogen sorption isotherms and to water sorption isotherms, as well as changes of pore volume. The evolution of microstructure is significant in the case of plain pastes, as opposed to pastes containing SRA. We remind that SSA of plain pastes drops when drying to 11% by 80% and 50% as evaluated by BET theory applied to nitrogen sorption isotherms and water sorption isotherms, respectively (cf. figure 4.27), while it drops by 30% for both SSA of pastes containing SRA evaluated by BET theory applied to nitrogen sorption isotherms and to water sorption isotherms (cf. figure 4.29). Therefore, accounting for microstructural changes may be relevant for plain pastes and disregarded for pastes containing SRA. To account for the evolution of microstructure for plain pastes, induced by drying and re-humidification, evolution of specific surface

area and pore volume need to be included in the estimations of capillary and adsorbed water. To do so, at each relative humidity, knowledge of the "new" microstructure must be implemented in the estimations of capillary water and adsorbed water.

Results (detailed in section 4.4, figure 4.27) showed that specific surface area evolves through drying depending on the relative humidity range. For plain pastes, at relative humidities greater than $h_{r,critical}$=60% for SSA evaluated by nitrogen sorption or $h_{r,critical}$=33% for SSA evaluated by water sorption, specific surface area decreases with decreasing relative humidity following a linear function. Below $h_{r,critical}$, specific surface area reaches a plateau. The volume of pores can be described by a decreasing function of specific surface area, as shown in figures 4.35 and 4.36. After re-humidifying cement paste (paste dried at relative humidity 11% and re-humidified to 95%), we found that for plain paste at low alkali content, specific surface area increases back to its value under sealed conditions, and volume of pores as well. We assume that microstructural changes, as seen by specific surface area and volume of pores, are similar for both drying and re-humidification, i.e., evolution of pore structure is reversible and without a hysteresis. Therefore, at a given relative humidity, on drying branch or re-humidification branch, total specific surface area can be evaluated following:

$$\frac{S_{ssa}(h_r)}{S_{ssa,0}} = \begin{cases} \alpha = \dfrac{S_{ssa}(11\%)}{S_{ssa,0}} & h_r < h_{r,critical} \\ \dfrac{1-\alpha}{1-h_{r,critical}}(h_r - 1) + 1 & h_r \geq h_{r,critical} \end{cases} \tag{6.9}$$

where $S_{ssa}(h_r)$ is the estimated specific surface area of cement paste dried at relative humidity h_r, $S_{ssa,0}$ is the initial specific surface area at sealed state, $h_{r,critical}$ is the critical relative humidity for the evolution of pore structure.

The pore volume is also evaluated as follows:

$$\Delta V_{total} = a_{microchange} \times \Delta S_{ssa} \tag{6.10}$$

where $a_{microchange}$ is the factor of proportionality of the changes of surface area upon drying to the changes of pore volume, V_{total} is the total pore volume

of cement paste, and ΔS_{ssa} is the change of specific surface area with regards to sealed state.

When pore structure is studied by nitrogen sorption isotherms, parameter $a_{microchange}$=0.001 g/m^2, as shown in figure 4.35. When pore structure is studied by water sorption isotherms, parameter $a_{microchange}$=0.0007 g/m^2, as shown in figure 4.36.

To quantify the distribution of pore volume and specific surface area, we assume that microstructure evolves, such that for a family of pores of a characteristic size r at a given relative humidity the specific surface area and pore volume are proportional to the initial surface area and pore volume, respectively. The factor of proportionality is taken as the ratio of total specific surface area of the cement paste dried at h_r to the specific surface area at the sealed state. For the pore volume, the factor of proportionality is equal to the ratio of the pore volume of the cement paste at h_r to the pore volume at the sealed state.

Specific surface area of the family of pores of size r of the cement paste dried at relative humidity h_r is estimated as follows:

$$S_{ssa}(r, h_r) = \frac{S_{ssa}(h_r)}{S_{ssa,0}} S_{ssa,0}(r) \tag{6.11}$$

where $S_{ssa}(h_r)$ is the estimated specific surface area of cement paste dried at a given relative humidity h_r, $S_{ssa,0}$ is the specific surface area of cement paste at sealed state, and $S_{ssa}(r, h_r)$ and $S_{ssa,0}(r)$ are the specific surface areas of family of pores of characteristic size r dried at relative humidity h_r, and specific surface area of the same family of pores at initial sealed state, respectively.

Total pore volume of dried cement paste is estimated as follows:

$$V(r, h_r) = \frac{V_{total}(h_r)}{V_{total,0}} V_0(r) \tag{6.12}$$

where $V_{total}(h_r)$ is the estimated total pore volume of cement paste dried at given relative humidity h_r, $V_{total,0}$ is the initial total pore volume (at sealed state), $V(r, h_r)$ is the pore volume of family of pores of characteristic size r

of dried cement paste at given h_r and $V_0(r)$ is the pore volume of the family of pores at initial sealed state.

Knowing how the microstructure evolves, the estimated volumes of capillary water and adsorbed water are corrected, making use of the new implemented pore structure and using equations 6.5, 6.6 and 6.8 to compute the contribution of water in capillary pores, water adsorbed on surfaces and water in micropores (for model 3W) to the total water content, respectively. Results are shown in figure 6.15 for model 3W and figure 6.16 for model 2W. We observe that the impact of the evolution of microstructure on the estimated water content is notable for relative humidities lower than 80% and 60% based on model 3W and model 2W, respectively. In this range of relative humidity, contribution of water adsorbed on surfaces to the total water content is large. The water adsorbed on surfaces being directly proportional to surface area, multiplying the surface area by a factor comes to multiplying the adsorbed water by the same factor. The estimated water content is thus sensitive to the evolution of pore structure in the low range of RH and may provide a better approximation of the experimental values. However, for the modeling of water content, we neglect the evolution of the pore structure and consider the pore structure at sealed state as an input for the model.

6.4 Discussion of estimated water content

6.4.1 Comparison with resolution of water obtained from NMR

When pore structure is analyzed by BJH applied to nitrogen sorption isotherms, water content is resolved into three types of water: water in capillary pores, water adsorbed on surfaces and water in micropores. Water in micropores accounts for the fraction of porosity that is inaccessible to nitrogen. This "unexplored" pore space can be interpreted as internal surfaces of C-S-H in the cement paste (see section 2.2.3). The adsorbed water assessed from nitrogen sorption isotherms can be interpreted as a water adsorbed on the external surfaces of pores of the cement paste accessible to nitrogen. Therefore, we
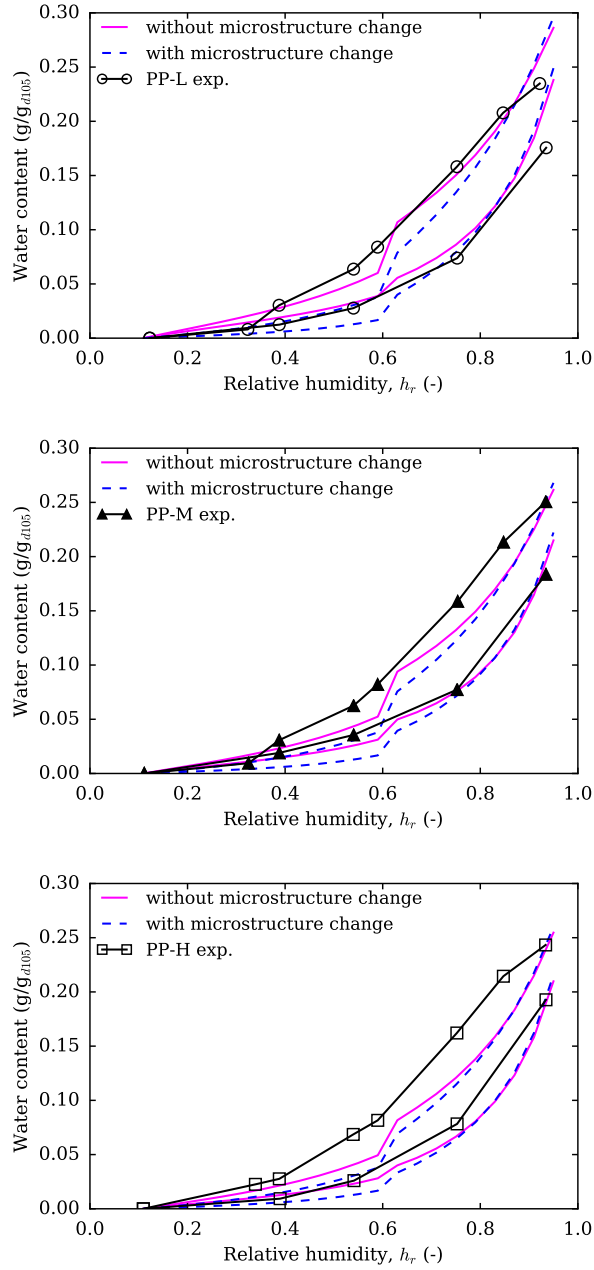
Figure 6.15: Impact of the evolution of pore structure on estimated water content for plain pastes at low (PP-L), medium (PP-M) and high alkali content (PP-H), based on model 3W using pore structure analyzed by nitrogen sorption isotherms.

Figure 6.16: Impact of the evolution of pore structure on estimated water content for plain pastes at low (PP-L), medium (PP-M) and high alkali content (PP-H), based on model 2W using pore structure analyzed by water sorption isotherms.

compare the sum of water adsorbed on internal and external surfaces, i.e., water adsorbed on surfaces and water in micropores respectively, to the values given in the literature for the evolution of water in C-S-H during desorption and adsorption.

Gajewicz (2014) studied the evolution of water in cement pastes through drying, using proton NMR. This author resolved water content during desorption into water in capillary pores, gel water and interlayer water, making use of the three pore families identified by proton NMR measurements. Given that original data was expressed in molar H/S ratio, we use $C_{1.5}$-S-$H_{1.9}$ for dry C-S-H to convert the molar H/S ratio to a water content of gram per gram of dry C-S-H. Roosz et al. (2016) later conducted measurements on synthesized C-S-H. They have measured water sorption isotherms (adsorption and desorption) on synthesized C-S-H of three C/S ratios (0.6, 1.2 and 1.6). Here, we use the adsorbed water of synthesized C-S-H of a C/S ratio of 1.6 for comparison purposes.

Results of comparison of water adsorbed on C-S-H estimated here and the values reported in the literature are shown in figure 6.17. The values retrieved from literature (Roosz et al., 2016) compare well with the values assessed here. For desorption branch however, the values from Gajewicz (2014) for interlayer water are lower than our values for water in C-S-H for relative humidities larger than 60%. However, below relative humidity of 40%, water content attributed to C-S-H is lower than interlayer water and is comparable to gel water. This may be originating from the differences in definitions of the types of water we consider, relatively to the definitions of water in interlayer, and gel water. In fact, the gel water may include a fraction of what we call in this work water in capillary pores. Further investigation of how the pore space characterized by proton NMR relates quantitatively to that measured by nitrogen sorption can be useful to rigorously define how the interlayer and gel water obtained from proton NMR compare to water in capillary pores, water adsorbed on surfaces and water in micropores as defined in this work.
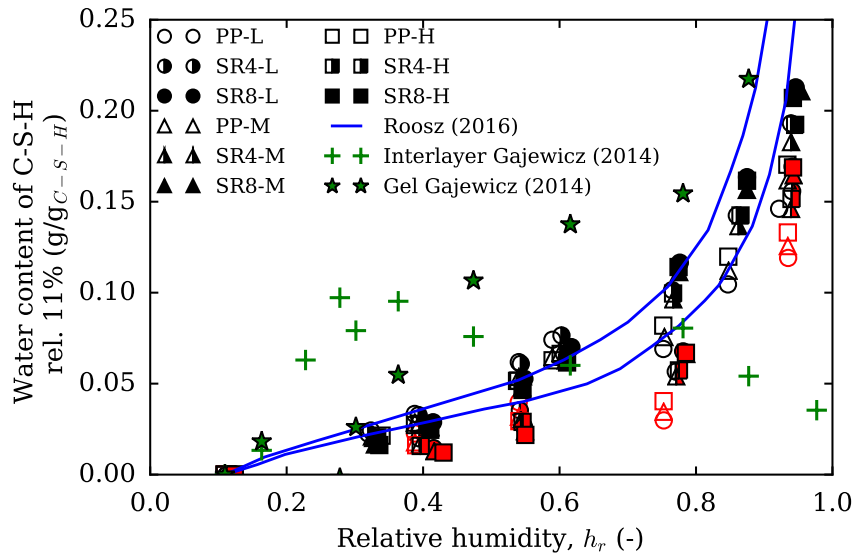
Figure 6.17: Water in C-S-H (water adsorbed on surfaces and water in micropores) in a desorption-adsorption cycle. Values from the literature for water in C-S-H are adapted from Gajewicz (2014) and Roosz et al. (2016). Red symbols stand for the adsorption branch and black symbols stand for the desorption branch.

6.4.2 Hysteretical behavior of adsorption in C-S-H and in cement paste

The hysteresis of water content in cement paste can be taken into account considering two origins: 1) ink-bottle effect and 2) hysteresis of the water content of micropores. In fact, due to the ink-bottle effect, water in capillary pores and water adsorbed on surfaces exhibit a hysteresis phenomenon, since water adsorbed on surfaces is attributed to surfaces of capillary pores emptied of their condensate and filled pores stand for the water-filled capillary pores. As shown in figure 6.2, water content in micropores on desorption branch is greater than the water content in micropores on the adsorption branch when plotted as a function of relative humidity: water in micropores thus shows a hysteresis loop.

Pinson et al. (2015) studied the hysteresis of water sorption and shrinkage in cement paste. Pinson et al. (2015) consider the presence of water under 4 forms: water in capillary pores, gel water, water adsorbed on surfaces and water in interlayer, as shown in figure 6.18. Their results show that the hysteresis can be well taken into account by two mechanisms, first the pore blocking (ink-bottle) mechanism on desorption branch and thermodynamic equilibrium for the adsorption branch, second, from the hysteresis of drying and refilling of the interlayer space. The latter empties until reaching a relative humidity of 20% but refills gradually on the entire range of relative humidity based on results of molecular models. Our results are corroborated by those obtained by Pinson et al. (2015) for considering that the hysteresis can be explained partly by the ink-bottle effect on the adsorbed water and water in capillary pores. However, we do not consider that water in interlayer is removed only when reaching a relative humidity of 20%: water in micropores in our work is considered to be removed gradually on the whole range of RH.

Roosz et al. (2016) observed by means of water sorption measurements on synthesized C-S-H that the interlayer hydration shows an irreversibility: water re-enters the interlayer space at the high range relative humidity during adsorption and cannot be removed unless C-S-H undergoes a severe drying.
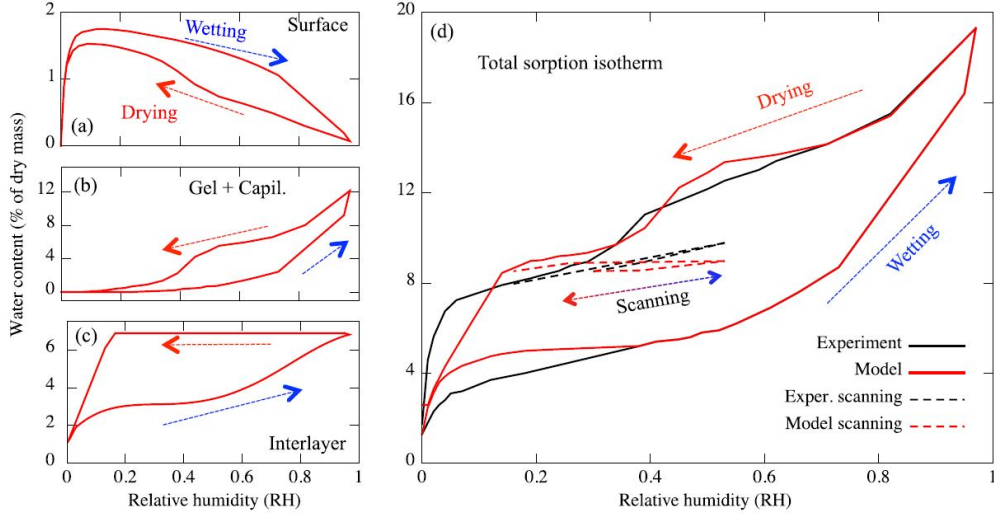
Figure 6.18: Water in cement paste and origin of hysteresis at the various scales considered: capillary and gel water, water adsorbed on surfaces and water in interlayer, after Pinson et al. (2015)).

Resuls of Roosz et al. (2016) are plotted relatively to state at 11% on the corresponding sorption branch in figure 6.17. Their results compare well with water in C-S-H (water in micropores and water adsorbed on surfaces) in model 3W showing a hysteresis loop upon a desorption-adsorption cycle. Bonnaud et al. (2012) also studied by means of atomistic simulations water inside of a C-S-H globule (intragranular) and in-between two C-S-H globules (intergranular) and its contribution to the cohesive behavior of C-S-H. Their results show that the adsorption and desorption of the intragranular water is reversible, and reaches its maximum at a relative humidity as low as 20%; however for the intergranular model with a pore width of 1 nm, hysteresis arises below relative humidity of 20% as shown in figure 6.19. Also, at the level of cement paste, a multiscale porosity is present with widespread pore sizes. Accounting for it could be more relevant to understand the hysteresis of water in cement pastes based on atomistic simulations.
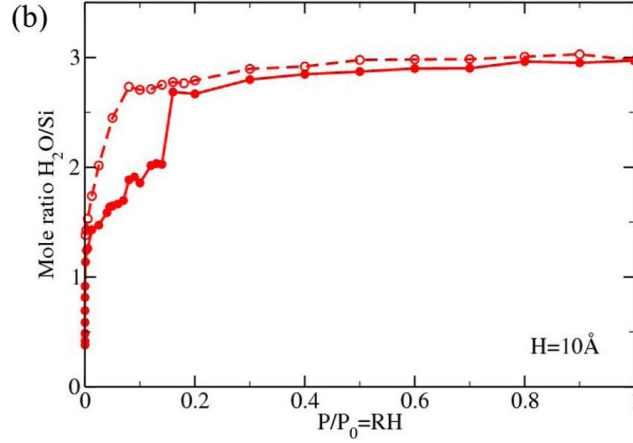
Figure 6.19: Modeled adsorption (filled symbols) and desorption (hollow symbols) for slit-shaped pore between C-S-H grains of width 1 nm (after Bonnaud et al., 2012).

6.5   Conclusions

In this chapter we modeled the water content measured by long-term gravimetric method of 9 types of cement pastes studied here following two models: model 3W and model 2W. The two models are summarized as follows:

- Model 3W is based on pore structure characterized by nitrogen sorption isotherms, and water is resolved into three types of water: water in capillary pores, water adsorbed on surfaces and water in micropores.

- Model 2W is based on pore structure characterized by water sorption isotherms, and water is resolved into two types of water: water in capillary pores and water adsorbed on surfaces.

Water in capillary pores and water adsorbed on surfaces are evaluated by taking into account the pore structure of cement paste, as characterized by nitrogen sorption isotherms (for model 3W) or water sorption isotherms (for model 2W). Water in micropores is found to follow a master curve, independently of the alkali and SRA content, and this intrinsic curve is used as an input to model the water content of cement pastes for model 3W. Combining the three types of water or two types of water in cement paste,

the water content on desorption and adsorption can be estimated, for model 3W and model 2W respectively.

The characteristic hysteresis of water content of cement pastes in a desorption-adsorption cycle is accounted for by two effects:

1. The ink-bottle effect for water in capillary pores and adsorbed on exposed surfaces.

2. Hysteresis of water in micropores.

Water adsorbed on surfaces and water in micropores can be interpreted as water adsorbed on external surfaces, which are accessible to nitrogen, and water adsorbed on internal surfaces of C-S-H which are inaccessible to nitrogen respectively. This water in C-S-H compares well with values given in the literature for water in C-S-H obtained on synthetic C-S-H (Roosz et al., 2016) and has the order of magnitude obtained for gel water and interlayer water cement pastes analyzed by proton NMR (Gajewicz, 2014). The hysteretical behavior of water in C-S-H concurs with the results obtained on synthetic C-S-H.

The quantification of contribution of each type of water to the water content of cement paste allows us in the next chapter to evaluate the strain generated by each type of water, and to model the drying shrinkage upon drying and re-humidification.

Chapter 7

Modeling of drying-induced strain

In this chapter, firstly an empirical model is proposed to estimate the drying shrinkage of cement pastes, depending on their content in alkali and SRA. Secondly, we model strain of the 9 types of cement pastes during drying and re-humidification, based on physical mechanisms. This physics-based modeling approach accounts for capillary forces, surface effects and, when considered, strain induced by adsorption in micropores. In the previous chapter, water in cement pastes was resolved into three types of water (i.e., water in capillary pores, water adsorbed on surfaces, and water in micropores) or two types of water (i.e., water in capillary pores, and water adsorbed on surfaces): two physics-based models are derived, one corresponding to the resolution into 3 types of water (coined model 3W) and one corresponding to the resolution into 2 types of water (coined model 2W). Each type of water induces a strain. The re-humidification branch is used to calibrate the model. A blind prediction is then applied on the first drying shrinkage. The role of SRA is examined and its action on strain on drying and re-humidifying is analyzed. The hysteresis and irreversibility of drying shrinkage is also discussed in the light of the herein proposed models.

7.1 Phenomenological model

In this section we present a phenomenological model to estimate the uniaxial strain during the first drying of cement pastes. The model depends on both alkali content C_{alkali} and SRA content C_{SRA}.

The strain, estimated relatively to the state at a relative humidity of 95%, is obtained as follows:

$$\varepsilon(h_r) - \varepsilon(95\%) = \alpha \ln(-\ln(h_r)) - \alpha \ln(-\ln(95\%)) + \beta \exp(h_r) - \beta \exp(95\%) \tag{7.1}$$

where:

$$\alpha = \alpha(C_{alkali}, C_{SRA}) = a_1 C_{alkali} C_{SRA} + a_2 \tag{7.2}$$

$$\beta = \beta(C_{SRA}) = b_1 C_{SRA}^2 + b_2 C_{SRA} + b_3 \tag{7.3}$$

The function given in equation 7.1 is fitted on the measured drying shrinkage of the 9 types of cement pastes by means of the least square method. The constants are found as: $a_1 = -5.83 \times 10^{-5}, a_2 = -7.13 \times 10^{-4}, b_1 = 4.16 \times 10^{-5}, b_2 = -7.08 \times 10^{-4}, b_3 = 1.54 \times 10^{-3}$, and C_{SRA} is the content in SRA expressed in g per 100 g of clinker, and C_{alkali} is the content in alkali $NaO_{2(eq)}$ expressed in g per 100 g of clinker.

The phenomenological model proposed here is a sum of two functions: a negative function (i.e., a shrinkage) and a positive function (i.e., a swelling, when SRA content is larger than 2.5%). The negative contribution to the modeled strain is dependent on the alkali and SRA contents, since the performance of the SRA is modified by the presence of alkali, which leads to larger drying shrinkage. The positive contribution depends on the SRA content only. In fact, experimentally, the presence of SRA in cement pastes leads to a constant drying shrinkage in the range of relative humidities [33%-75%]. In the phenomenological model, the positive contribution gives place to a swelling which counterbalances the negative contribution and leads to an almost constant drying shrinkage in this range of relative humidities.

The strains estimated using equation 7.1 versus the strains measured, for

the 9 types of cement pastes studied in this work at the 8 relative humidities ranging from 11% to 95%, are plotted in figure 7.1. Most estimated strains fall in a range of error of $\pm20\%$. The mean error of the estimations[1] is 12.4%. We plot the estimated strain and the measured strain as a function of relative humidity in figures 7.2, 7.3 and 7.4.
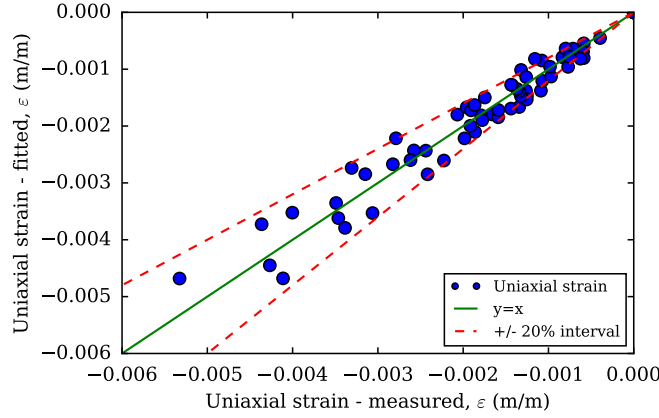
Figure 7.1: Uniaxial strain estimated using the phenomenological model in terms of the measured uniaxial strain of the 9 types of cement pastes dried on the 8 relative humidities.

The relative humidities of interest for engineering applications are usually larger than 50%. Using a least square method to fitting the equation 7.1 on the measured drying shrinkage in the range of relative humidities [54%-95%], the parameters are found as follows: $a_1 = -6.55 \times 10^{-5}, a_2 = -7.79 \times 10^{-4}, b_1 = 5.07 \times 10^{-5}, b_2 = -7.86 \times 10^{-4}, b_3 = 1.34 \times 10^{-3}$. In figure 7.5, we show, on the restrained range of relative humidities [54%-95%], the strains fitted on this restrained range in terms of the measured strains. The mean error of the estimation is 11.7%. The estimated strains and the measured strains are plotted in terms of relative humidity in figures 7.6, 7.7 and 7.8.

In the next section, we present a modeling approach based on the physical mechanisms of drying shrinkage.

---

[1]the error is evaluated by $\frac{1}{n}\sum_0^n |1 - \varepsilon_{fitted,i}/\varepsilon_{measured,i}|$
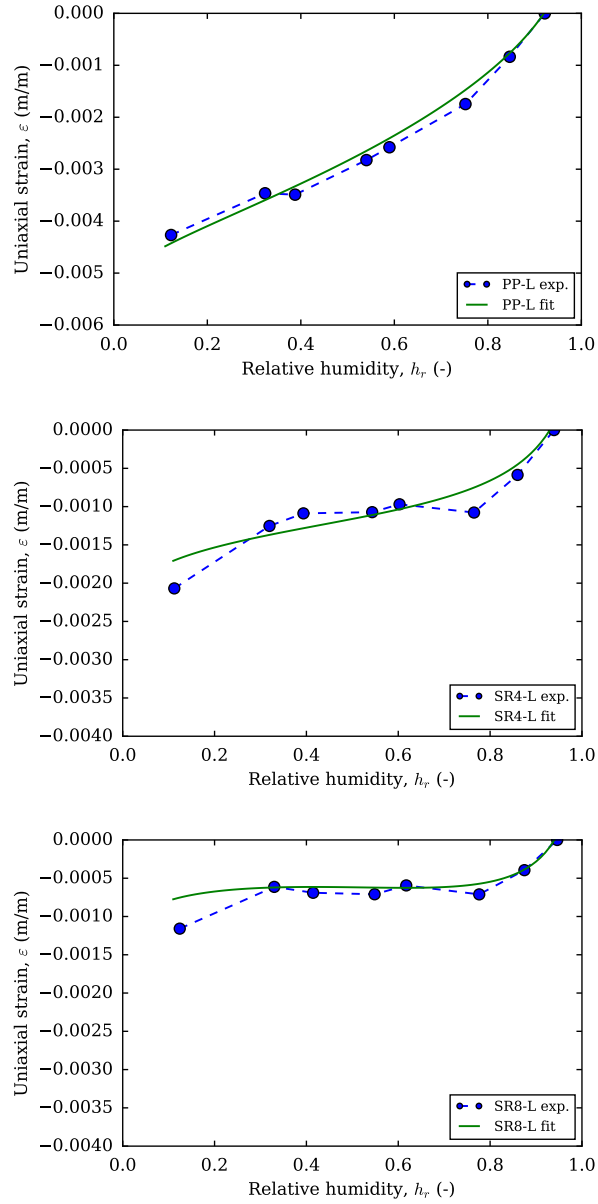
Figure 7.2: Fitted uniaxial strain (denoted as "paste" fit) and measured uniaxial strain (denoted as "paste" exp.) for the cement pastes at low alkali content in terms of relative humidity.
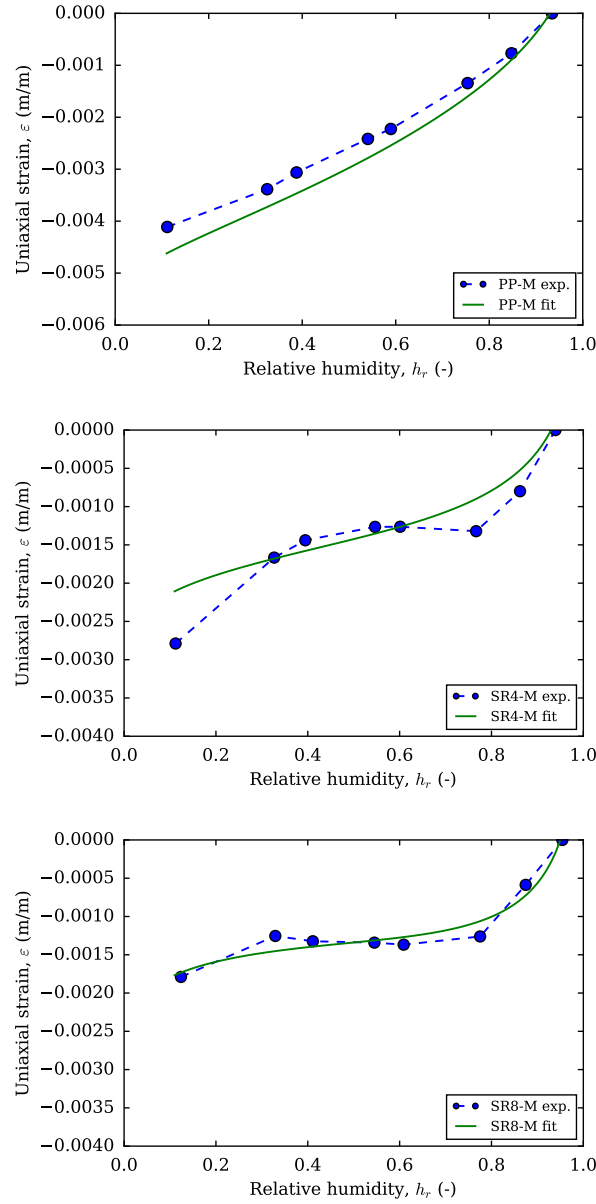
Figure 7.3: Fitted uniaxial strain (denoted as "paste" fit) and measured uniaxial strain (denoted as "paste" exp.) for the cement pastes at medium alkali content in terms of relative humidity.
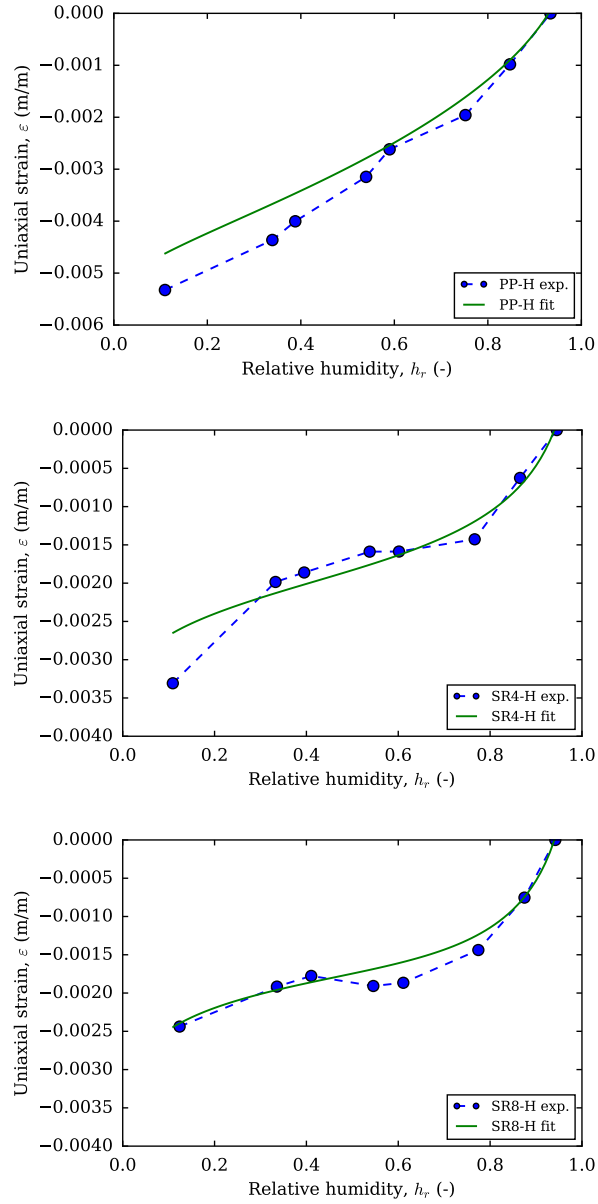
Figure 7.4: Fitted uniaxial strain (denoted as "paste" fit) and measured uniaxial strain (denoted as "paste" exp.) for the cement pastes at high alkali content in terms of relative humidity.
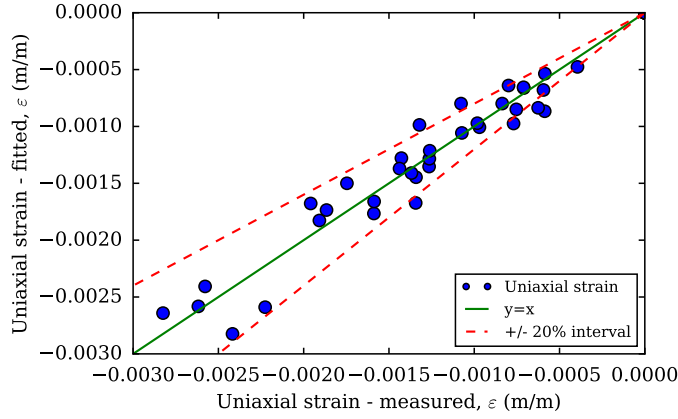
Figure 7.5: Uniaxial strains estimated for relative humidities larger than 54% using the phenomenological model in terms of the measured uniaxial strains of the 9 types of cement pastes dried on the 8 relative humidities.

7.2 Model concept

As seen in chapter 6, water in pore space can be separated into either 3 contributions:

1. Water in capillary pores,

2. Water adsorbed on surfaces,

3. Water in micropores,

or into 2 contributions only (i.e., water in capillary pores and water adsorbed on surfaces).

Each type of water contributes to the total strain of the cement paste, as illustrated in figure 7.9:

1. Water in capillary pores induces a strain ε_{cap} governed by capillary forces,

2. Water adsorbed on surfaces induces a strain ε_{ads} governed by surface effects,

3. Water in micropores induces a strain ε_{μ}, function of the water content in micropores.

247
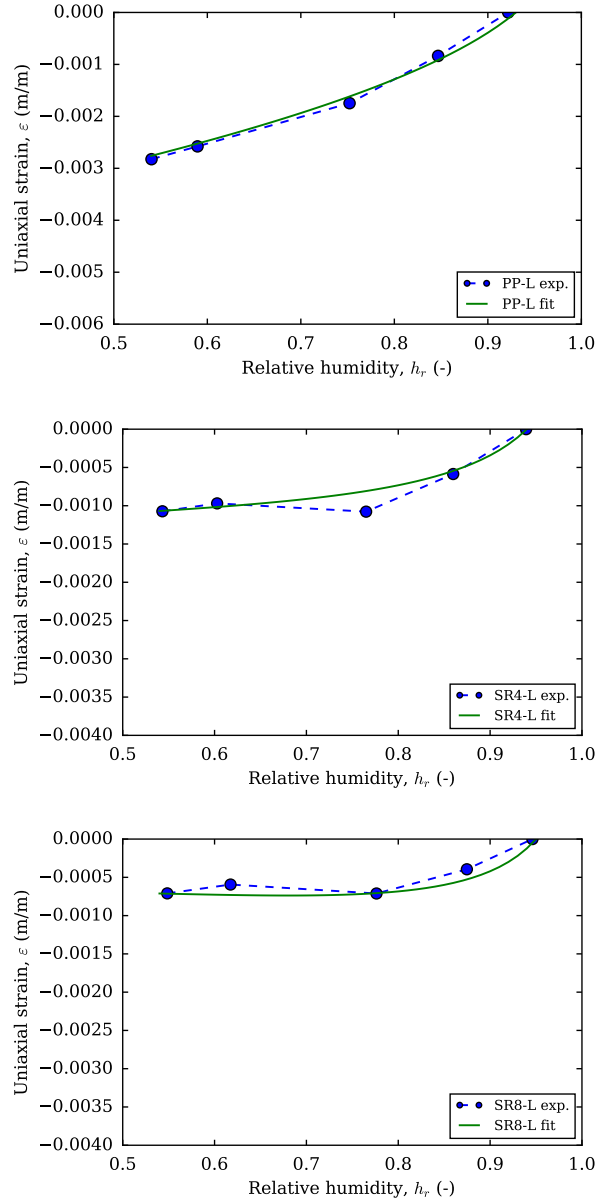
Figure 7.6: Fitted uniaxial strain (denoted as "paste" fit) and measured uniaxial strain (denoted as "paste" exp.) for the cement pastes at low alkali content, in terms of relative humidity on the restrained range [54%-95%].
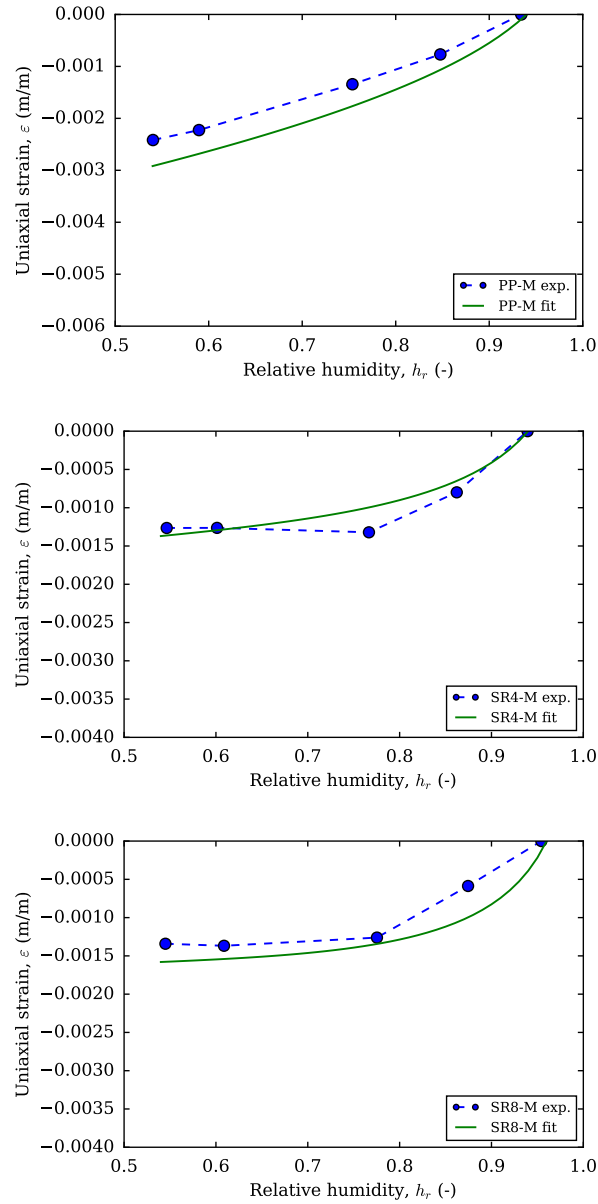
Figure 7.7: Fitted uniaxial strain (denoted as "paste" fit) and measured uniaxial strain (denoted as "paste" exp.) for the cement pastes at medium alkali content, in terms of relative humidity on the restrained range [54%-95%].
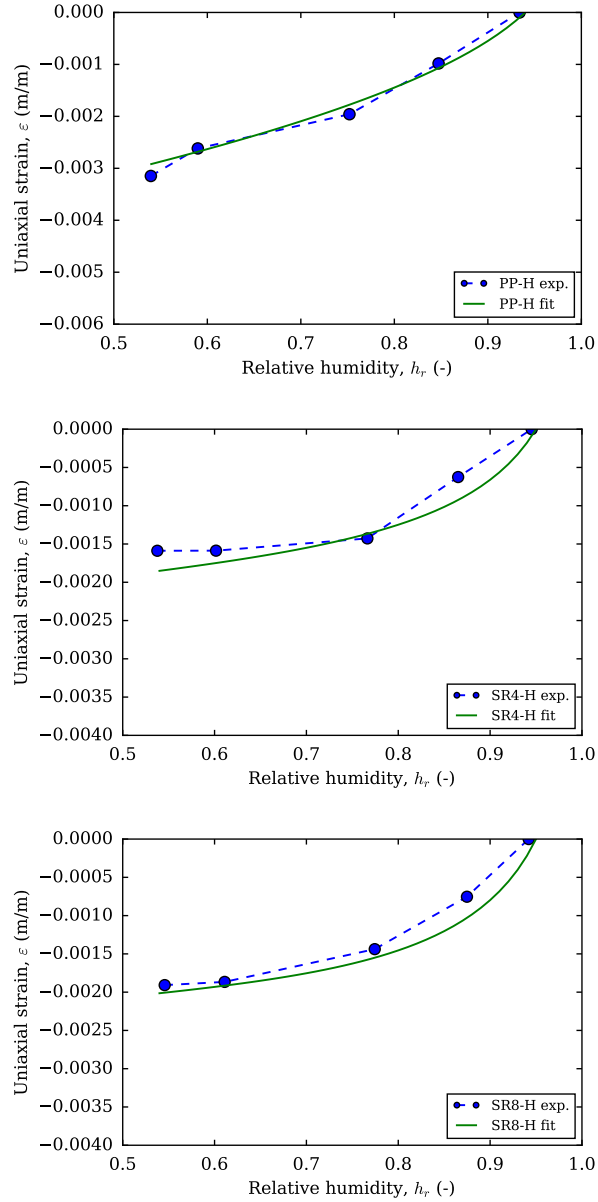
Figure 7.8: Fitted uniaxial strain (denoted as "paste" fit) and measured uni-axial strain (denoted as "paste" exp.) for the cement pastes at high alkali content, in terms of relative humidity on the restrained range [54%-95%].

The total strain ε is assumed to be equal to the sum of these three contributions:

$$\varepsilon = \varepsilon_{cap} + \varepsilon_{ads} + \varepsilon_{\mu} \tag{7.4}$$
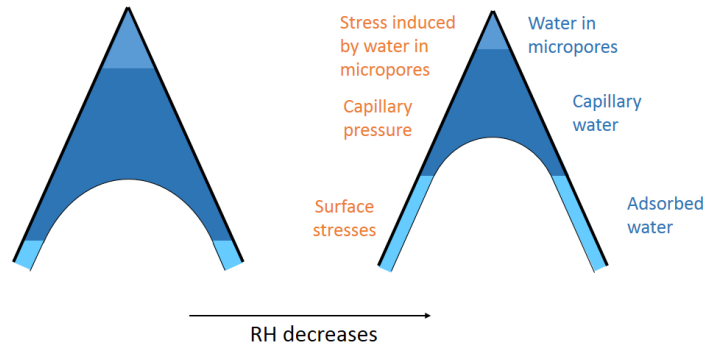
Figure 7.9: Schematic of water in pore space and strain each type induces (based on an idea by R. Barbarulo).

In the next sections we address the modeling of strain induced by each type of water. First, we detail the strain induced by water in capillary pores, followed by the strain induced by water adsorbed on surfaces, then we introduce the strain induced by water in micropores.

7.2.1 Strain induced by water in capillary pores

As shown in section 2.3.2, capillary forces can induce a deformation of a porous material. This strain is considered to depend on the saturation degree, and on the bulk modulus and Biot coefficient of the porous material.

Di Bella et al. (2017) reviewed three models to estimate the ultimate drying shrinkage, developed in the framework of poroelasticity. The three models take into account the capillary depression of the pore fluid. They are: 1) the Biot-Bishop model, referring to the classical approach for computing

stresses induced by capillary forces as $S_l p_{cap}$; 2) the Coussy model, referring to the model proposed in Coussy et al. (2004); 3) the Vlahinić et al. (2009) model. Di Bella et al. (2017) discussed the parameters influencing the results of estimated strain, and demonstrated that how the saturation degree is computed is of major influence on the estimated strain. The saturation degree was assessed in their work by two methods, by computing the water content relative to the dry mass of the sample at 50 °C and to the dry mass of the sample at 105 °C. The bulk modulus K_s of the solid skeleton was found to impact less the estimation of the ultimate drying shrinkage. They also found that the models in the high range of relative humidities concur and agree well with experimental data, and that they start diverging at low relative humidity (i.e., below 40%).

In our present work, the saturation degree S_l is estimated as follows:

$$S_l = \frac{V_{cap}}{V_{total}} \tag{7.5}$$

where V_{cap} is the volume of water in capillary pores, and V_{total} is the volume of mesopores. When the pore structure is characterized with nitrogen sorption isotherms, V_{total} is estimated as the adsorbed volume of nitrogen at relative pressure of 0.97, corresponding typically to pores of size lower than 35 nm. When the pore structure is characterized with water sorption isotherms, V_{total} is taken as the pore volume of pores of size lower than 35 nm, corresponding to a relative humidity of 98%. Note that the mesopore volume assessed by water is consistently larger than the one evaluated by nitrogen sorption, with a difference comprised between 20% to 60% for the 9 types of cement pastes.

We estimate the strain induced by capillary forces with the model proposed by Coussy et al. (2004). Hence the strain ε_{cap} at a given relative humidity h, relative to a reference state at a reference relative humidity h_0, can be computed as follows (Coussy et al., 2004):

$$\begin{aligned}
\varepsilon_{cap} &= \frac{1}{3}\frac{b}{K}\int_{h_{r,0}}^{h_r} -S_l dp_{cap} \\
&= \frac{1}{3}\frac{b}{K}\frac{\rho RT}{M_v}\int_{h_{r,0}}^{h_r} -S_l d\ln(h)
\end{aligned} \tag{7.6}$$

where b is the Biot coefficient, K is the bulk modulus, R is the ideal gas constant, T is the absolute temperature, ρ is the bulk density of water, M_v is the molar mass of water. For the computation of strain, the following parameters are chosen: the Biot coefficient is $b = 0.69$ (Ghabezloo, 2010) and the bulk modulus is $K = 5$ GPa (based on elastic measurements on the cement pastes detailed in appendix C.1).

7.2.2 Strain induced by water adsorbed on surfaces

A film layer remains adsorbed on the surface of pores emptied from their capillary condensate. This adsorbed water leads to a strain ε_{ads} following the Gibbs-Bangham mechanism, as explained in section 2.3.2, where a decrease in surface energy caused by adsorption on surfaces leads to a swelling of the material, following:

$$\varepsilon_{ads} = \lambda_{ads}\Delta\gamma \tag{7.7}$$

where γ is the surface energy and λ_{ads} is the proportionality factor linking the changes of surface energy to the strain at the macroscopic level.

The parameter λ_{ads} depends on the properties of the material. Bangham and Maggs (1944) postulated the factor λ_{ads} of proportionality between strain and changes of surface energy for a generic porous structure as:

$$\lambda_{ads} = \frac{\rho S_{ssa}}{E_s} \tag{7.8}$$

where ρ is the density of the porous material (i.e., cement paste in our case), S_{ssa} is its specific surface area, and E_s is the Young's modulus of the solid skeleton.

Parikh (1958) and Scherer (1986) related the factor λ_{ads} to the properties

of the material of cylindrical geometry following:

$$\lambda_{ads} = \lambda_{ads,Scherer} = \frac{\rho S_{ssa}(1-\nu)}{E_s} \qquad (7.9)$$

where ν is the Poisson's ratio of the solid skeleton. λ_{ads} computed using equation 7.9 will be referred to as $\lambda_{ads,Scherer}$.

In case of a geometry made of a stack of cylinders as shown in figure 7.10, the parameter can be written as (Scherer, 1986):

$$\lambda_{ads} = \frac{\rho S_{ssa}}{E_s} \times f(x,\nu)$$

where $f(x,\nu)$ is a function of the geometrical parameter $x = a/l$ and ν is the Poisson's ratio of the solid skeleton. Values of $f(x,\nu = 0.2)$ range between 0.800 and 1.232 for x between 0 and 0.5.
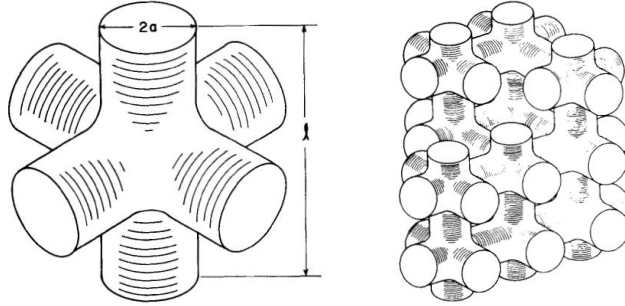
Figure 7.10: Building block (left) of the geometry made of stacked cylinders (right) after (Scherer, 1986).

Vandamme et al. (2010) studied adsorption-induced strains in the framework of poroelasticity. The authors underlined that, for a material with given specific surface area and porosity, depending on whether the microstructure is made of spherical pores or of stacked spheres, the strain induced by adsorption can vary by a factor of $\frac{K_s}{K}$, where K_s is the bulk modulus of the solid skeleton and K is the bulk modulus of the porous material. Vandamme et al. (2010) also distinguish surface stress and surface energy, the surface stress being the driving force for adsorption-induced strains. However, Gor and Bernstein (2016) indicated that the variations of surface stresses can be

approximated by the variations of surface energy, for amorphous materials in which adsorption is mostly incommensurate, thus justifying Bangham's law. The variations of surface energy are evaluated following Gibbs' isotherm:

$$\mathrm{d}\gamma = -\Gamma d\mu \tag{7.10}$$

where $\Gamma = N_{ads}/S$ is the excess adsorbed amount of fluid per unit area of solid surface, and μ is the chemical potential of the adsorbed fluid.

The strain ε_{ads} induced by adsorption on solid surfaces exposed at a given relative humidity h_r, relative to a reference state at a reference relative humidity $h_{r,0}$, is computed as follows (Hansen, 1987):

$$\varepsilon_{ads} = \frac{\rho_w RT}{M_v} \int_{h_{r,0}}^{h_r} \lambda_{ads} \frac{V_{ads}}{S_{ssa}} d\ln(h) \tag{7.11}$$

where ρ_w is the mass density of water, R is the ideal gas constant, T is the absolute temperature, V_{ads} is the volume of adsorbed water, S_{ssa} is the specific surface area affected by an adsorbed film layer.

Note that, during drying, the specific surface area S_{ssa} in equation 7.11, which refers to the surface area of the pores emptied of their condensate and in which an adsorbed film remained, depends on the relative humidity. In fact, when the capillary pores are saturated, $S_{ssa} = 0$. When the relative humidity decreases, the capillary pores are gradually emptied of their condensate and this specific surface S_{ssa} increases. Under the assumption of cylindrical geometry for the pores, the function $S_{ssa}(h_r)$ can be calculated if the pore size distribution is known. Indeed, by noting $V(h_r)$ the volume of pores of characteristic size r that are emptied at a given relative humidity h_r, the following relation holds:

$$S_{ssa}(h_r) = \frac{2}{r}V(h_r) \tag{7.12}$$

Hansen (1987) found that estimating the adsorption-induced strain by using equation 7.8 for assessing the proportionality factor accounted for only 33% of the strain. He linked the strain not captured by the Gibbs-Bangham theory to microstructural changes of the interlayer upon drying, which may

be leading to irreversible shrinkage. In absence of an accurate description of the pore structure of cement pastes, we will fit the adsorption parameter λ_{ads}.

7.2.3 Strain induced by water in micropores

For microporous materials, such as clay or coal (Carrier et al., 2013; Hol and Spiers, 2012), strain is found experimentally to be roughly a linear function of the adsorbed fluid in the material, as shown in figure 7.11. One can imagine
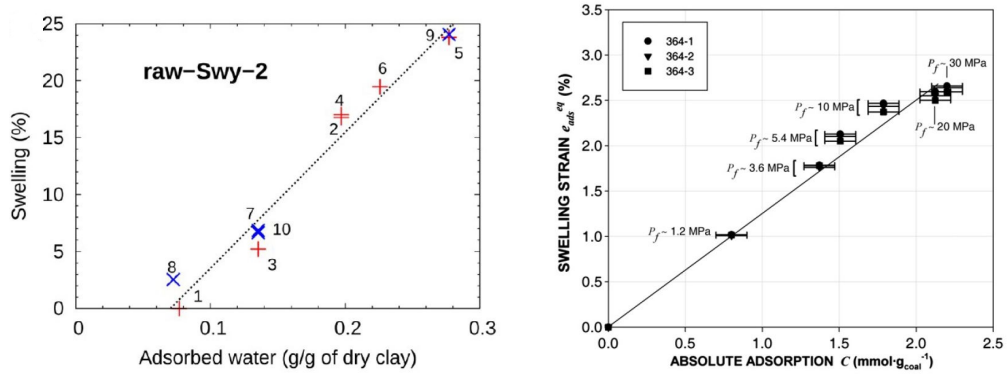
Figure 7.11: Strain measured in terms of content in adsorbed fluid, in case of clay-based material (left, (Carrier et al., 2013)) and coal (right, (Hol and Spiers, 2012)).

that the strain is generated by geometric accommodation of the micropores, such that the micropores remain saturated.

The strain induced by water in micropores is assumed to be a linear function of the water content in micropores:

$$\varepsilon_\mu = \lambda_\mu \times w_\mu \tag{7.13}$$

Consequently, the strain generated by a variation of water content in the micropores is proportional to this variation. This assumption of linear behavior is a simplification of the actual and complex behavior of strain induced by water in micropores, e.g., (Kowalczyk et al., 2008; Espinoza et al., 2013). Kowalczyk et al. (2008), among others, studied the adsorption-induced strain

in microporous carbon by means of molecular simulations, and found that how strain depends on the pressure of the fluid depends strongly on the size of the micropores and can even exhibit a nonmonotonic behavior.

7.2.4 Model workflow

We develop 2 models relying on the physical mechanisms leading to drying shrinkage: a model coined 3W considers that water in the pore space can be present in capillary pores, adsorbed on solid surfaces, or in micropores; a model coined 2W considers that water in the pore space can only be present in capillary pores and adsorbed on solid surfaces.

As we have seen in chapter 4, first drying is accompanied by an irreversible drying shrinkage. Helmuth and Turk (1967) reported that subsequent drying cycles are reversible, as the first drying shrinkage allows alteration of the pore structure leading to a stabilized microstructure. Hence, we focus at first instance on re-humidification of cement paste. We assume that the pore structure does not evolve and that the surface tension is constant on drying. However, it should be noted that Eberhardt (2010) indicated that, on drying, the surface tension of pore solution of cement pastes containing SRA increases back to that of the pore solution without SRA.

In the models, there is no free parameter in the estimation of the strain ε_{cap} induced by capillary effects. In contrast, the parameter λ_{ads}, which links variations of surface energy with the strain induced by adsorption on solid surfaces according to the Gibbs-Bangham effect, will be fitted, for both models 2W and 3W. In addition, for model 3W which also considers water in micropores, the parameter λ_{μ}, which relates water content in micropores with strain induced by micropores, will also be fitted. Once those fits will have been performed, on the re-humidification branch, a blind application to the first drying shrinkage will be conducted.

Figures 7.12 and 7.13 illustrate the workflow, for models 3W and 2W, respectively. For model 3W, nitrogen sorption isotherms will be used as input, as they allow to determine what fraction of water is present in the capillary pores, adsorbed on solid surfaces, or present in micropores (see

section 6.1.1 and 6.1.2). In contrast, for model 2W, water sorption isotherms will be used as input, as they allow to determine what fraction of water is present in the capillary pores or adsorbed on solid surfaces (see section 6.1.1).
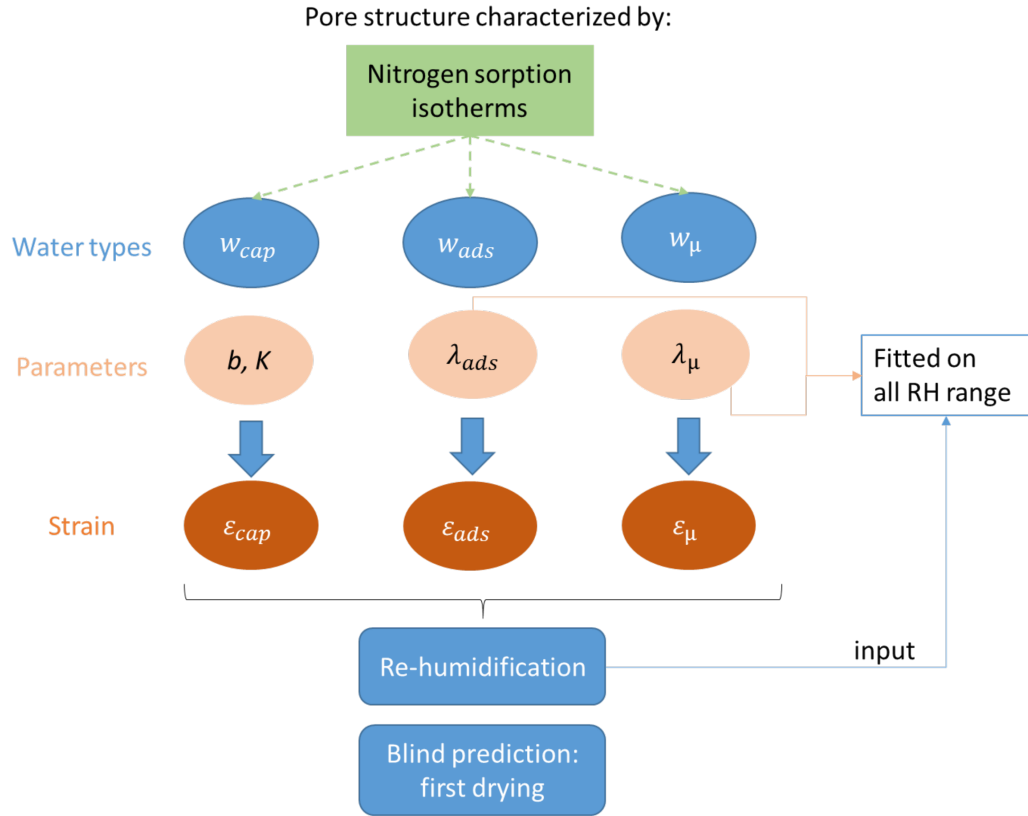
Figure 7.12: Schematic illustrating the workflow of drying shrinkage model based on consideration of three contributions to strain (model 3W): strain induced by water in capillary pores, by water adsorbed on surfaces and by water in micropores.

Since samples are re-humidified from a relative humidity of 11% to a relative humidity of 95%, we will compute strain and water content relative to the state at a relative humidity of 11%. The pore structure is considered unchanging, as we demonstrated in section 6.3.2 that changes in pore structure have little impact on the estimated quantities of water in capillary pores, adsorbed on surfaces and in micropores.
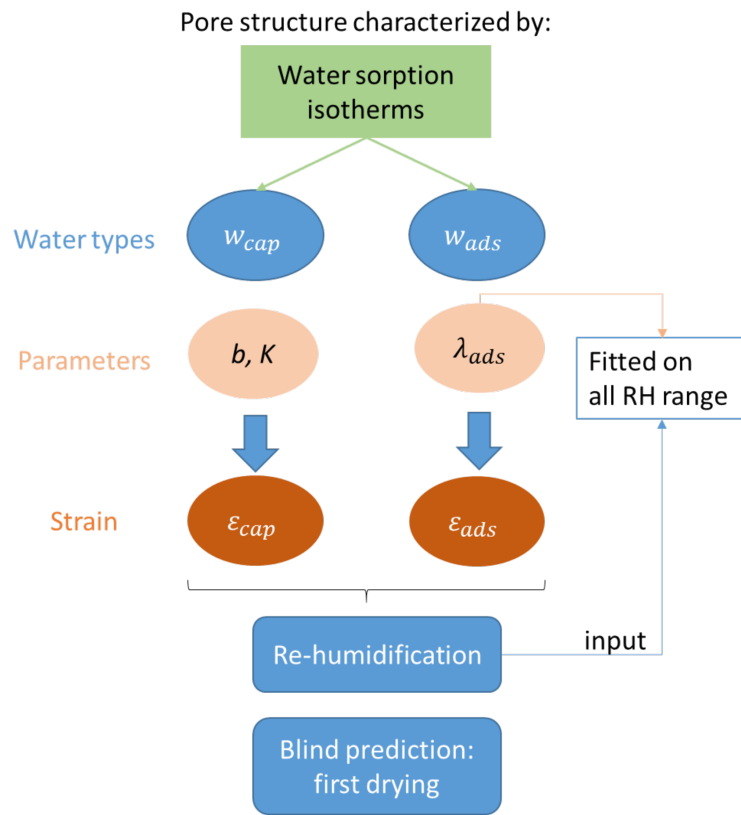
Figure 7.13: Schematic illustrating the workflow of drying shrinkage model based on consideration of two contributions to strain (model 2W): strain induced by water in capillary pores and by water adsorbed on surfaces.

7.3 Application to re-humidification

In this section, we present first the model based on the discrimination of the water in the pore space of the cement paste into 3 types (i.e., model 3W): water in capillary pores, water adsorbed on surfaces and water in micropores. Then we present results of the model considering 2 types of water (i.e., model 2W): water in capillary pores and water adsorbed on surfaces. We determine the parameters needed for the estimation of the strain induced by water adsorbed on surfaces (for models 2W and 3W) and water in micropores (for model 3W), based on experimental measurements of strain on the re-humidification branch.

7.3.1 Modeling strain based on model 3W

Following the previous chapter, the water content is discriminated into 3 contributions, based on the pore structure analyzed with nitrogen sorption isotherm, as detailed in section 6.1.1. The amounts of water in capillary pores and water adsorbed on surfaces are estimated based on the pore structure analysis, as back-calculated from the BJH analysis of the nitrogen sorption isotherms. The water content in micropores is estimated from the fitted function 6.8.

In this section, we determine the parameters λ_{ads} and λ_{μ} of the model, where λ_{ads} governs the strain induced by adsorption on surfaces and the parameter λ_{μ} governs the strain induced by water in micropores. The parameters λ_{ads} and λ_{μ} are obtained by fitting the sum $\varepsilon_{ads} + \varepsilon_{\mu}$ of modeled strain induced by adsorption on surfaces and by water in micropores on the difference $\varepsilon_{exp} - \varepsilon_{cap}$ between the measured strain ε_{exp} and the strain induced by water in capillary pores ε_{cap}, on the range of relative humidities [11%-95%]. Indeed, note that the strain ε_{cap} is evaluated based on the parameters defined in section 7.2.1 and does not require any fitting.

The results of the modeled strain and measured strain are shown in figures 7.14, 7.15 and 7.16 for pastes at low alkali content, at medium alkali content and at high alkali content, respectively. Considering the total strain to result from the contribution of three mechanisms captures the swelling of the 9 types

of cement pastes considered in this study: the mean relative error (i.e., the mean of relative error on each relative humidity and for each type of cement paste) on the modeled strain is of 9%, the mean absolute error is 75 μm/m. For relative humidities below 85%, a large contribution to the total strain is the strain induced by adsorption on solid surfaces.

The fitted parameters λ_{ads} are shown in figure 7.17. The ratios $\lambda_{ads}/\lambda_{ads,Scherer}$ and the values of $\lambda_{ads,Scherer}$ are given in figure 7.18. Note that values of λ_{ads} and $\lambda_{ads,Scherer}$ are given in the case where the total surface area is affected by an adsorbed film layer (i.e., when no water is present in capillary pores). λ_{ads} is found to decrease with decreasing SRA content, regardless of alkali content. Moreover, for plain paste (i.e. with no SRA) the factor λ_{ads} increases with increasing alkali content. For pastes containing SRA, a high content of alkali leads to a larger λ_{ads} as well.

The parameter λ_{ads} is higher than the theoretical value estimated by $\lambda_{ads,Scherer}$ (based on equation 7.9 for ρ=2.604 g/cm^3 (Allen et al., 2007), E_s=24.4 GPa and ν=0.24 (Acker et al., 2001)) by a factor between 1 and 5. The decrease of λ_{ads} with increasing content of SRA may be partly explained by the impact of SRA on pore structure, since, at increasing content of SRA ,the surface area was found to decrease (cf. figure 4.11). In fact, $\lambda_{ads,Scherer}$ in equation 7.9 also predicts a decrease with decreasing surface area. Let us examine the increase of λ_{ads} with increasing alkali content. Assuming that the parameters ρ, E_s and ν are identical from paste to paste in equation 7.9, and given that an increase in alkali content leads to a decrease of the surface area (evaluated by nitrogen adsorption on surfaces, cf. figure 4.12), an increase in alkali content would lead to a decrease of the parameter $\lambda_{ads,Scherer}$, whereas the fitted λ_{ads} showed an opposite trend. The impact on surface area is hence not sufficient to explain uniformly the impact of SRA and alkali on the parameter λ_{ads}. We also observe that, at a given content in alkali, the ratio $\lambda_{ads}/\lambda_{ads,Scherer}$ is almost constant, except for the paste containing 8% SRA and a medium amount of alkali. The fact that the ratio is not dependent of the SRA content may be interpreted by the fact that the SRA does not impact the geometry (i.e., the topological features) of the C-S-H microstructure. These features may be influenced by the alkali content and

Figure 7.14: Measured and modeled strains on the re-humidification branch for pastes at low alkali content, in terms of relative humidity. The strain modeled with model 3W is decomposed into a strain induced by capillary effects (with no fitting parameter), a strain induced by adsorption on surfaces (with one fitting parameter λ_{ads}) and a strain induced by micropores (with one fitting parameter λ_{μ}).
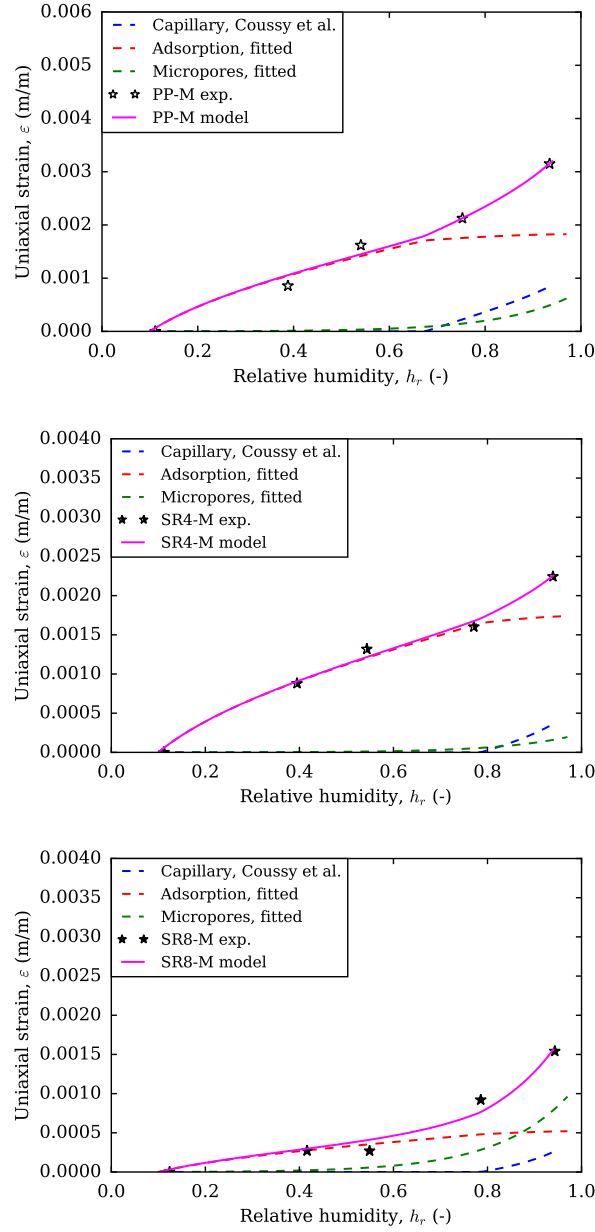
Figure 7.15: Measured and modeled strains on the re-humidification branch for cement pastes at medium alkali content, in terms of relative humidity. The strain modeled with model 3W is decomposed into a strain induced by capillary effects (with no fitting parameter), a strain induced by adsorption on surfaces (with one fitting parameter λ_{ads}) and a strain induced by micropores (with one fitting parameter λ_μ).
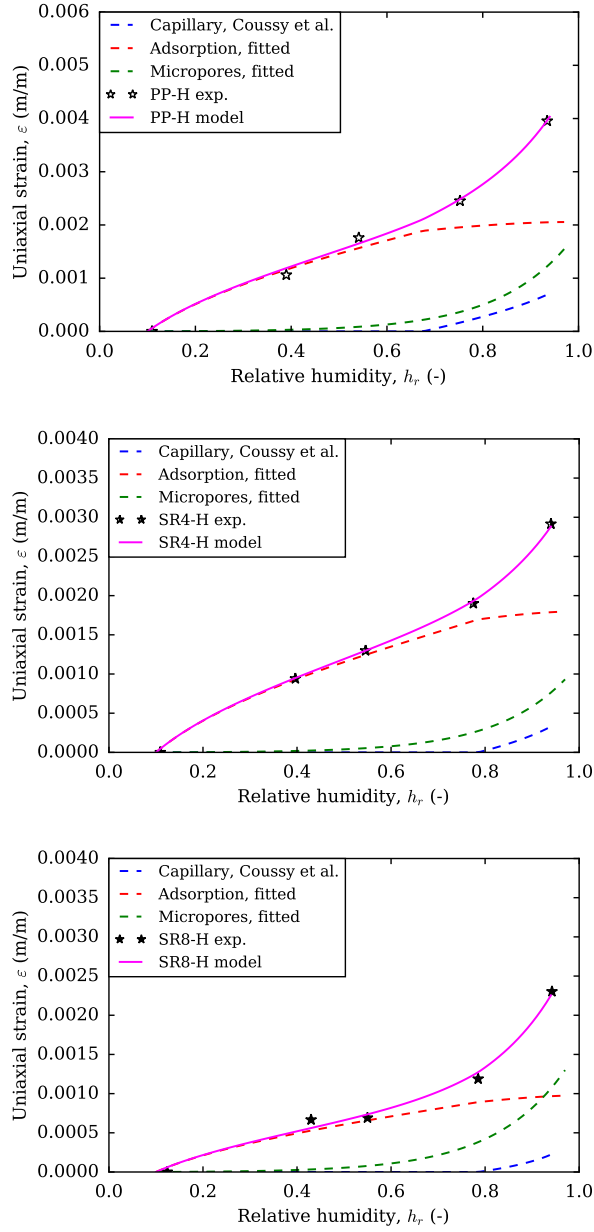
Figure 7.16: Measured and modeled strains for cement pastes at high alkali content on the re-humidification branch, in terms of relative humidity. The strain modeled with model 3W is decomposed into a strain induced by capillary effects (with no fitting parameter), a strain induced by adsorption on surfaces (with one fitting parameter λ_{ads}) and a strain induced by micropores (with one fitting parameter λ_{μ}).

264
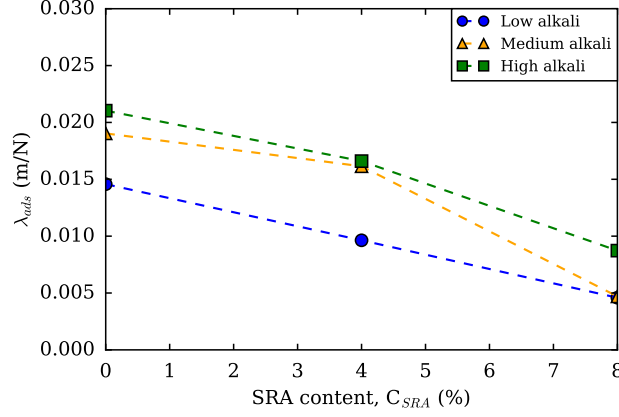
Figure 7.17: Fitted factor λ_{ads} of proportionality govering the strain induced by adsorption on surfaces (Gibbs-Bangham model), obtained under the scope of model 3W based on three types of water.

lead to a higher ratio $\lambda_{ads}/\lambda_{ads,Scherer}$ when the alkali content is increased.
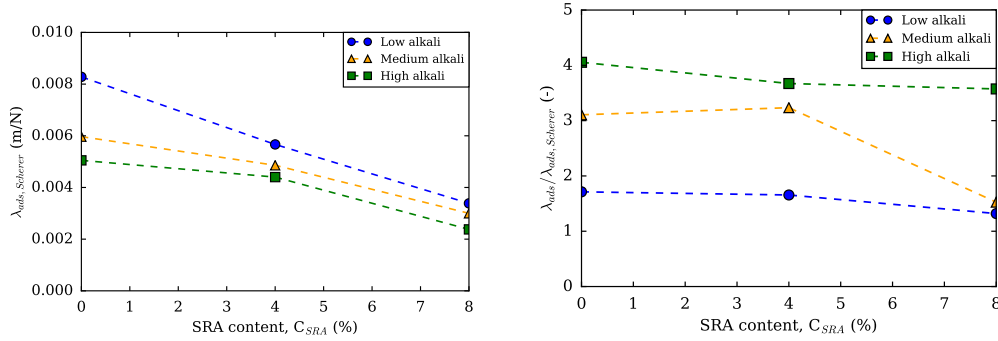
Figure 7.18: Factor $\lambda_{ads,Scherer}$ relating the variations of surface energy to the strain induced by adsorption on surfaces (left) and ratio $\lambda_{ads}/\lambda_{ads,Scherer}$ (right) obtained under the scope of model 3W based on three types of water.

The fitted factor λ_μ, linking the variation of water content in micropores to the induced strain is shown in figure 7.19. The results show that the factor λ_μ is the largest for paste containing high alkali content. For low alkali content, λ_μ is found to decrease when the SRA is present in the mix. For the medium alkali and high alkali content, λ_μ does not follow a monotonic behavior with the content in SRA. The values of λ_μ show that, for a variation

of the water content in the micropores of the order of 0.01 g/g, the induced strain is of the order of 100 μm/m, which is low compared to the order of magnitude of the strain measured on cement pastes upon re-humidification. The contribution of strain induced by water in micropores to the total strain of the cement pastes is low, in particular at low relative humidity. However, at high relative humidity, where the water content in micropores increases, the fraction of the total strain that is induced by water in micropores becomes significant.
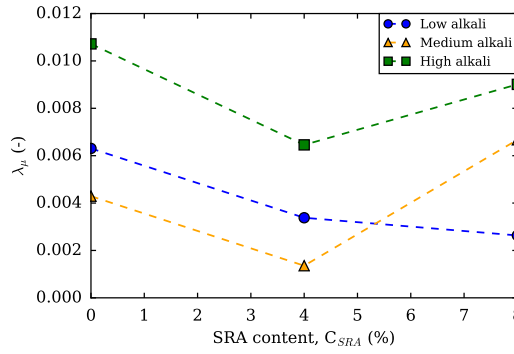
Figure 7.19: Factor of proportionality λ_μ for strain induced by micropores and the change of water content of micropores.

7.3.2 Modeling strain based on model 2W

In this section, water in the cement paste is distinguished into two types: water in capillary pores and water adsorbed on surfaces. Following the methodology described in the section 6.1.1, the pore structure is characterized with water vapor sorption isotherms (volumetric method) to identify the contribution of the adsorbed water and water in capillary pores to the estimated total water content of cement paste. The only parameter to be fitted for model 2W is the parameter λ_{ads}. This parameter λ_{ads} is obtained by fitting the strain ε_{ads} induced by adsorption on surfaces on the difference $\varepsilon_{exp} - \varepsilon_{cap}$ between the measured strain ε_{exp} and the strain induced by water in capillary pores ε_{cap}, on the range of relative humidities [11%-95%]. Indeed, we recall

that the strain ε_{cap} is evaluated based on the parameters defined in section 7.2.1 and does not require any fitting.

Once the obtained factor λ_{ads} to estimate the adsorption-induced strain is fitted, the strain of the cement pastes upon re-humidification can be estimated. The results of the modeled strain (thus modeled with model 2W, which considers only capillary effects and adsorption on surfaces) are shown in figure 7.20. The model captures well the order of magnitude of strain and the shape of the measured strain. The mean relative error (i.e., the mean of the relative error at each relative humidity and for each type of cement paste) of the modeled strain is of 15%, the mean absolute error is 140 μm/m. The model considering 2 types of water only leads to an error larger than the one obtained with the model considering 3 types of water.

The fitted parameter λ_{ads} is shown in figure 7.21. The results show that this parameter λ_{ads} decreases consistently with an increasing SRA content, and that the decrease is independent of the alkali content, since the plots of λ_{ads} in terms of SRA content are almost parallel to each other. The parameter $\lambda_{ads,Scherer}$ computed using equation 7.9 and the ratio $\lambda_{ads}/\lambda_{ads,Scherer}$ are shown in figure 7.22. The parameter $\lambda_{ads,Scherer}$ decreases with an increasing content in SRA, which is due to the decrease observed in the surface area evaluated by water sorption isotherm with an increasing content in SRA (cf. figure 4.14). The ratio $\lambda_{ads}/\lambda_{ads,Scherer}$ lies in the range [0.25-2], which is lower than the one found in the previous section (as shown in figure 7.18), which is a consequence of the fact that the parameter $\lambda_{ads,Scherer}$ depends on the surface area, which is larger when evaluated with water sorption isotherms than with nitrogen sorption isotherms.

7.4 Blind prediction of first drying shrinkage

In this section, we make a blind prediction of the strain on first drying, in the framework of the two aforementioned models (i.e., models 3W and 2W). The modeling of the first drying shrinkage is therefore conducted under the framework of poroelasticity: the first drying shrinkage is considered elastic. The first model takes into account the strain induced by water in capillary
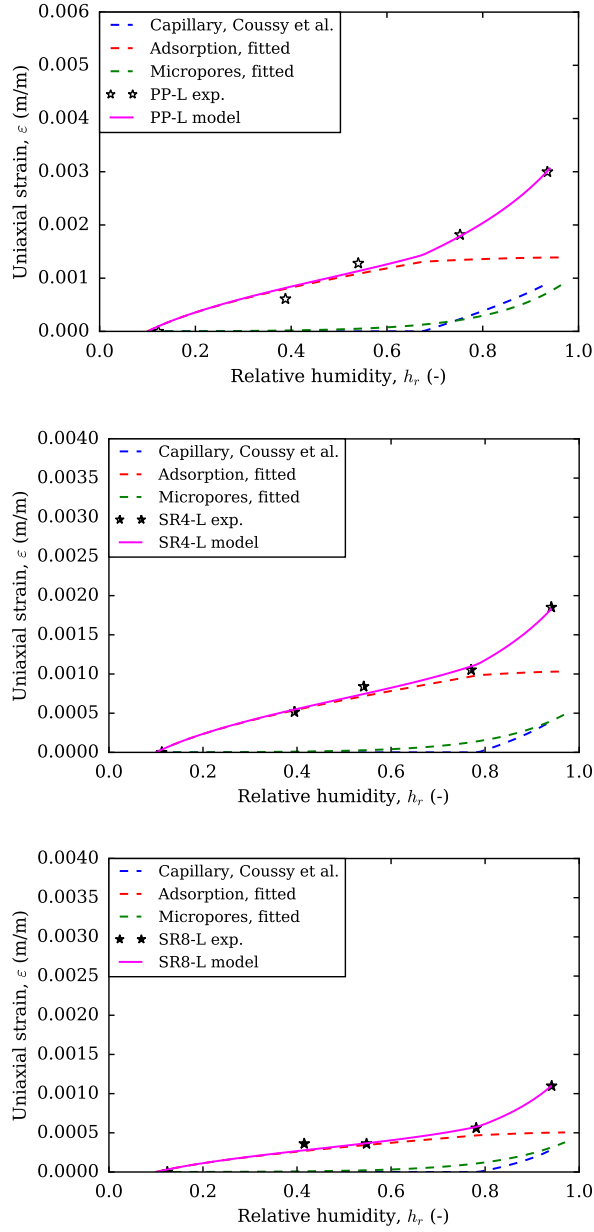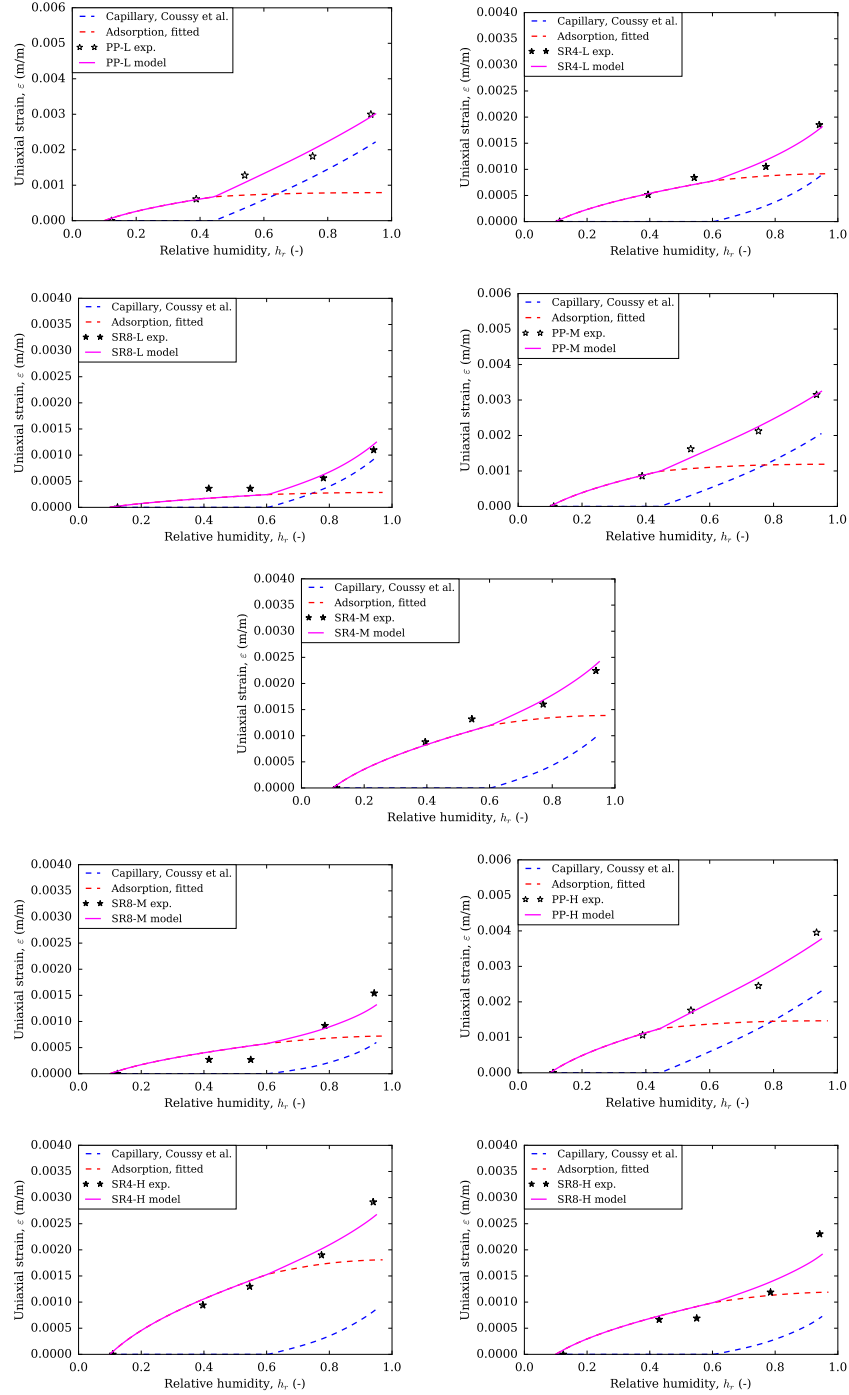
Figure 7.20: Measured and modeled strains on the re-humidification branch, in terms of relative humidity. The strain modeled with model 2W is decomposed into a strain induced by capillary effects (with no fitting parameter) and a strain induced by adsorption on surfaces (with one fitting parameter λ_{ads}).

Figure 7.21: Fitted factor λ_{ads} of proportionality govering the strain induced by adsorption on surfaces (Gibbs-Bangham model), obtained under the scope of model 2W based on two types of water.
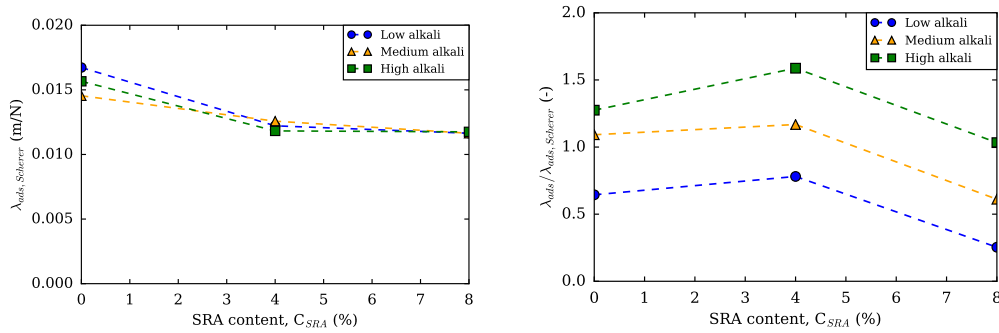
Figure 7.22: Factor $\lambda_{ads,Scherer}$ relating the variations of surface energy to the strain induced by adsorption on surfaces (left) and ratio $\lambda_{ads}/\lambda_{ads,Scherer}$ (right) obtained under the scope of model 2W based on two types of water.

269

pores, water adsorbed on surfaces and water in micropores, based on model 3W. As for the second model, it accounts for water in capillary pores and water adsorbed on surfaces, based on model 2W. The factors λ_{ads} (cf. figure 7.17) and λ_μ (cf. figure 7.19) for the model that accounts of 3 contributions were determined based on the re-humidification branch, as shown in section 7.3.1. For the model based on 2 contributions to strain (strain induced by water in capillary pores and strain induced by water adsorbed on surfaces), the factor λ_{ads} was obtained from the re-humidification branch, as detailed in section 7.3.2 and shown in figure 7.21.

7.4.1 Estimation of first-drying strain based on model 3W

The results of the strain estimated with model 3W for the first drying and the resolution of water into 3 types, as well as the measured strain on the first drying, are shown in figures 7.23, 7.24 and 7.25 for the low, medium, and high alkali contents, respectively. We also show in these figures the increments of strain on two successive relative humidities, which allows to judge the accuracy of the model independently of the considered reference state. The estimated strain and measured strain show a fair agreement: the mean relative error of the estimated strain is 23%, the mean absolute error is 290 μm/m. The mean error on the increment of strain on the considered intervals is equal to 170 μm/m.

Examining closely the increments of strain on successive intervals, for plain pastes the largest difference between the model and the measured strain is in the range of relative humidities [40%-54%], and also in the range of relative humidities [60%-75%] for plain pastes at high alkali content.

As for the pastes containing SRA, except for paste SR8-H (i.e., paste at high alkali content and at 8% content in SRA), the increments on modeled strain and measured strain recorded the largest difference in the range of relative humidities [11%-33%] and [60%-75%]. For paste SR4-M (i.e., paste at medium alkali content and 4% content in SRA), in addition to these intervals (i.e., [11%-33%] and [60%-75%]), the error between increments of modeled

Figure 7.23: Strain on first drying estimated with model 3W (blind prediction) and its decomposition into a strain induced by capillary effects, a strain induced by adsorption effects, and a strain induced by micropores, confronted to the measured length change, as a function of relative humidity for pastes at low alkali content.

Figure 7.24: Strain on first drying estimated with model 3W (blind prediction) and its decomposition into a strain induced by capillary effects, a strain induced by adsorption effects, and a strain induced by micropores, confronted to the measured length change, as a function of relative humidity for pastes at medium alkali content.

Figure 7.25: Strain on first drying estimated with model 3W (blind prediction) and its decomposition into a strain induced by capillary effects, a strain induced by adsorption effects, and a strain induced by micropores, confronted to the measured length change, as a function of relative humidity for pastes at high alkali content.

strain and measured strain was also significant in the range [85%-95%]. These differences for pastes containing SRA, on the low range of relative humidities [11%-33%] is an indicator that the strain induced by adsorption on surfaces may be underestimated by the model, given that in the low range of relative humidities, a large contribution to the strain is that of the strain induced by adsorption on surfaces.

7.4.2 Estimation of first-drying strain based on model 2W

In this section we examine the strain estimated with model 2W for the first drying. Using the factor λ_{ads} determined on the re-humidification branch (cf. figure 7.21), the strain induced by adsorption on surfaces is computed. The strain induced by capillary effects is computed using the saturation degree and the parameters (i.e., Biot coefficient and bulk modulus) defined in section 7.2.1. In figure 7.26, we show an illustration of the computed saturation degree for pastes at low alkali content, where a decrease in saturation degree in the presence of SRA is observed compared to plain paste, at any relative humidity. We note that the sudden decrease of the saturation at characteristic RH (45% and 65%) is related to the cavitation of water at the considered RH, which leads to the emptying of capillary water. The total strain is assessed for the 9 types of cement pastes. The results are shown in figures 7.27, 7.28, and 7.29. We show both increments of strain and absolute value for the modeled strain (and its decomposition into the contributions of adsorption on surfaces and capillary effects) and measured strain.

Results show that, for plain pastes, modeled strain and measured strain agree fairly, with a mean relative error of 26% and an absolute error of 270 μm/m. For both plain pastes and pastes containing SRA, the increment of the strain in the range of relative humidities [11%-33%] is underestimated by the model. For pastes containing SRA, the increment of the modeled strain on the range of relative humidities [60%-75%] is also larger than the measured increment. This overestimation by the model may be related to the estimation of water in capillary pores, where pores are considered emptied at
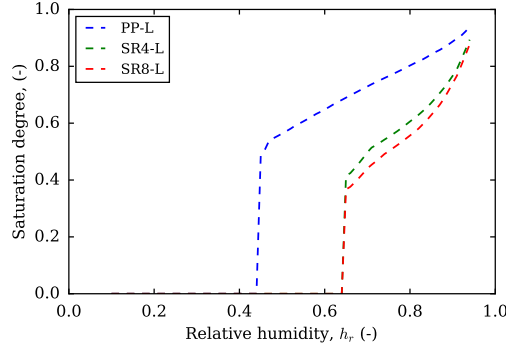
Figure 7.26: Saturation degree computed based on model 2W (i.e., when water is distinguished into water in capillary pores and water adsorbed on surfaces). The saturation degree here displays only takes into account water in capillary pores and excludes water adsorbed on exposed surfaces.

a relative humidity of $\sim 65\%$. Considering that the relative humidity below which water in capillary pores is emptied is larger than 65%, in case of pastes containing SRA, may provide a better approximation of the measured strain.

7.4.3 Discussion of modeling of strain based on model 3W and model 2W

Both the model 3W (which differentiates water into water in capillary pores, water adsorbed on surfaces and water in micropores) and model 2W (which differentiates water into water in capillary pores and water adsorbed on surfaces) estimate reasonably well the measured strain. The models accuracy, when evaluated based on the error on the increment of strain on the considered intervals of relative humidities, is of the same order of magnitude.

We note that the plateau of strain observed for pastes containing SRA in a range of relative humidities [33%-75%] upon first drying is not captured by any of the 2 models. In fact, in the framework of the models, a plateau cannot be reproduced, since for all mechanisms considered (i.e., capillary effects accounted for with Coussy model, surface effects accounted for with Gibbs-Bangham model, and strain induced by water in micropores), a monotonic behavior of strain with regards to relative humidity is expected. One may
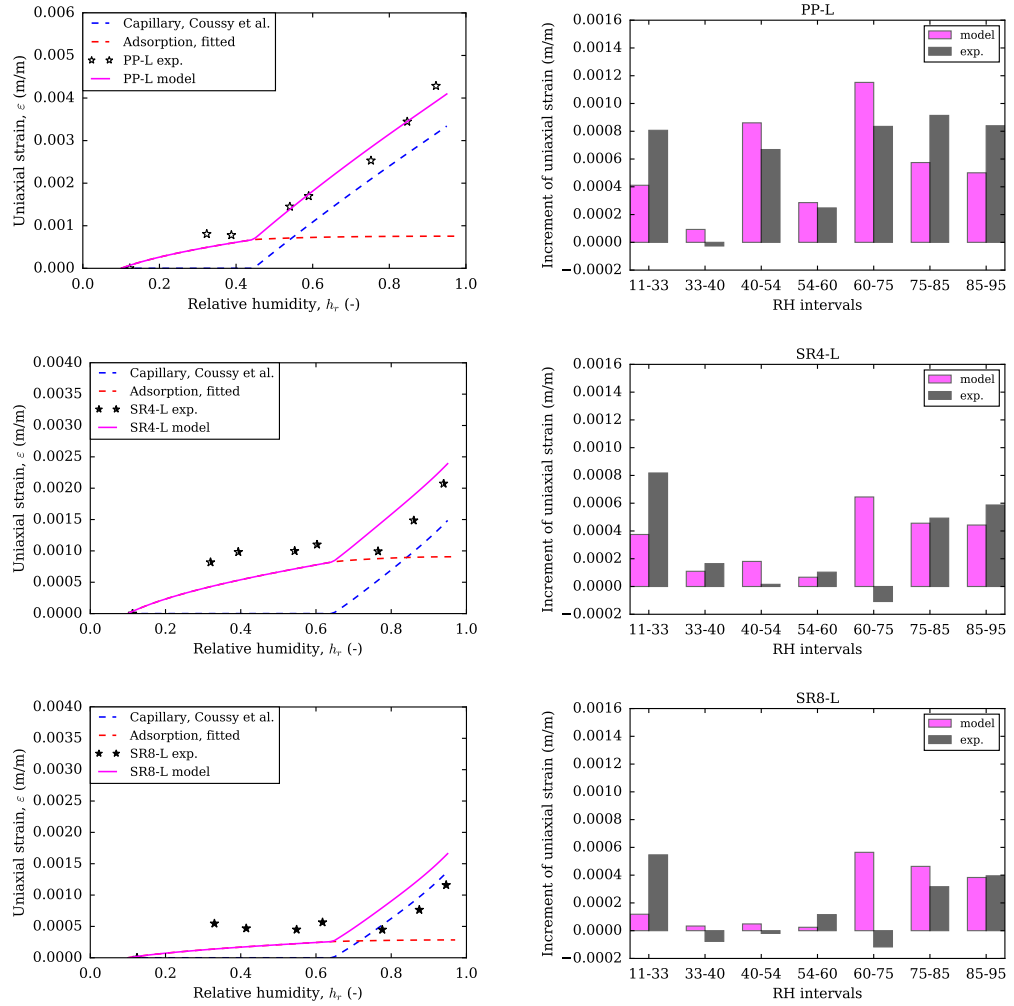
Figure 7.27: Strain on first drying estimated with model 2W (blind prediction) and its decomposition into a strain induced by capillary effects and a strain induced by adsorption effects, confronted to the measured length change, as a function of relative humidity, for pastes at low alkali content.
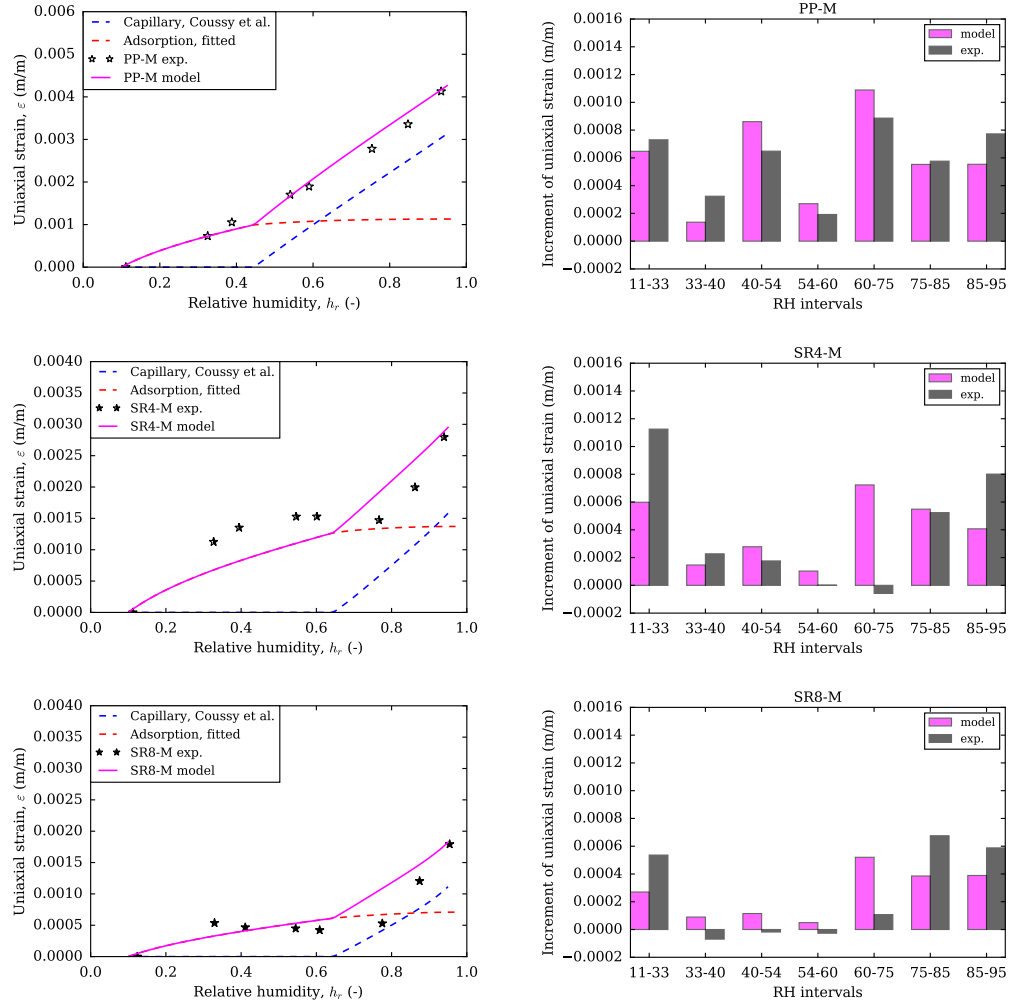
Figure 7.28: Strain on first drying estimated with model 2W (blind prediction) and its decomposition into a strain induced by capillary effects and a strain induced by adsorption effects, confronted to the measured length change, as a function of relative humidity, for pastes at medium alkali content.
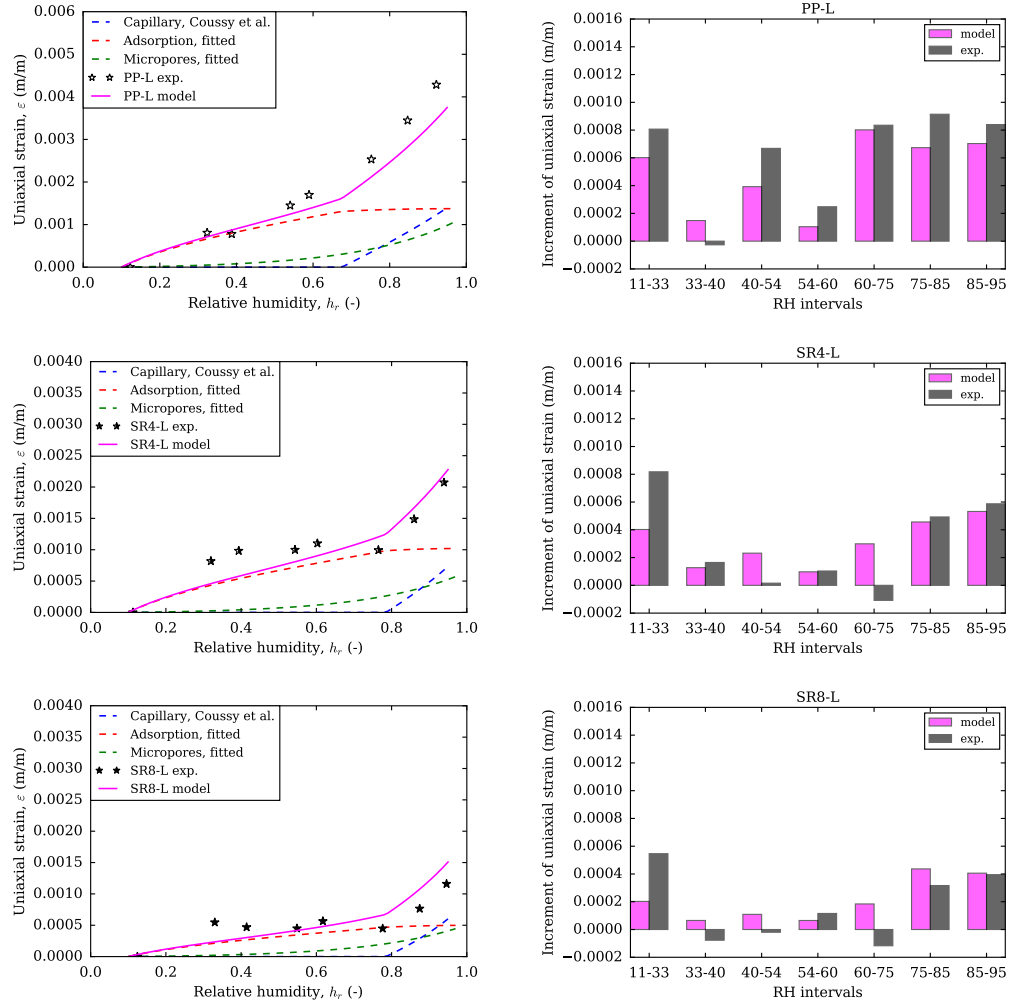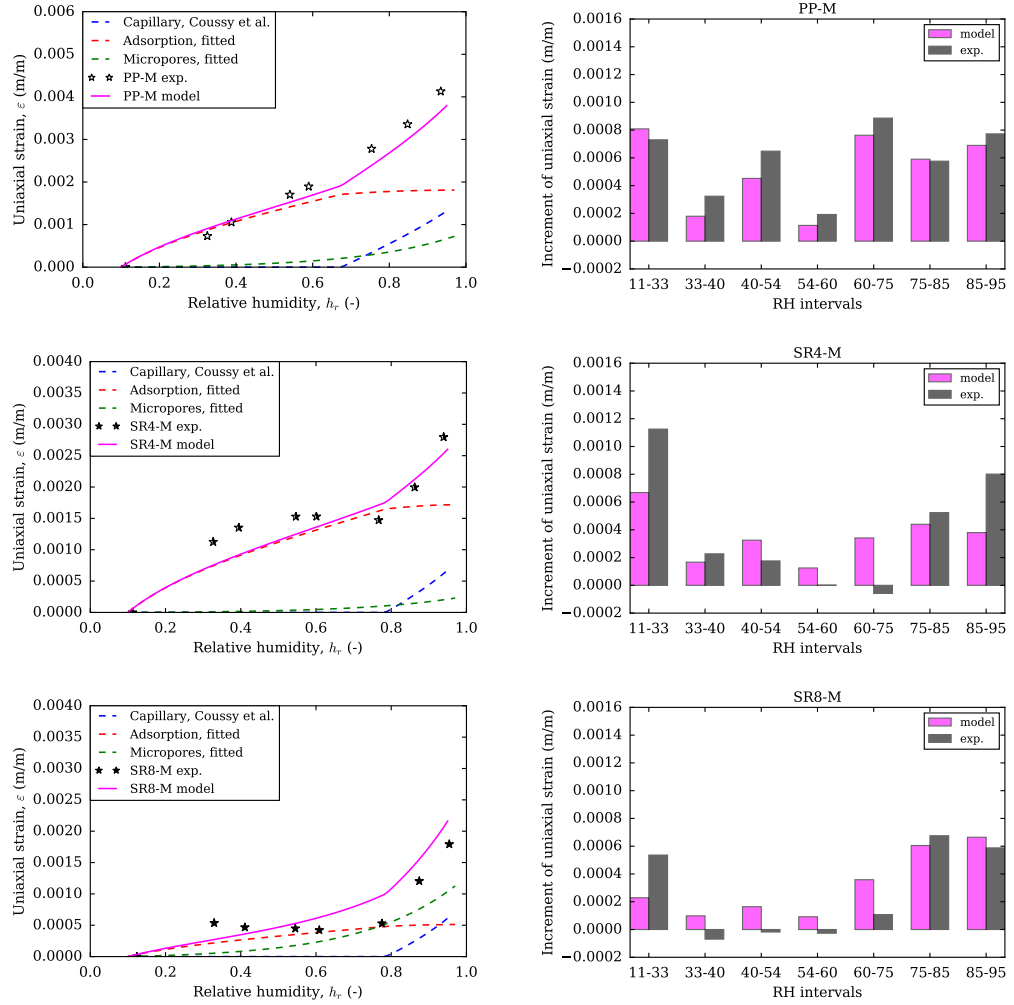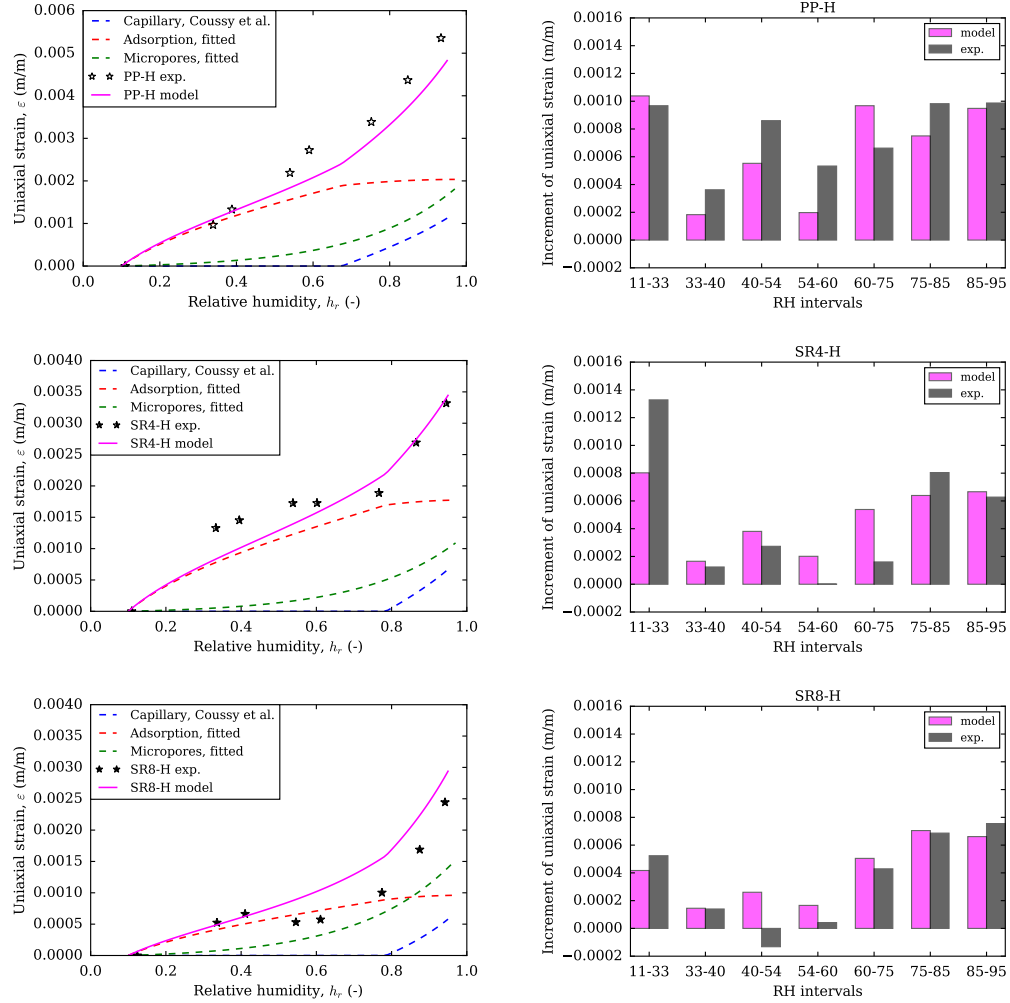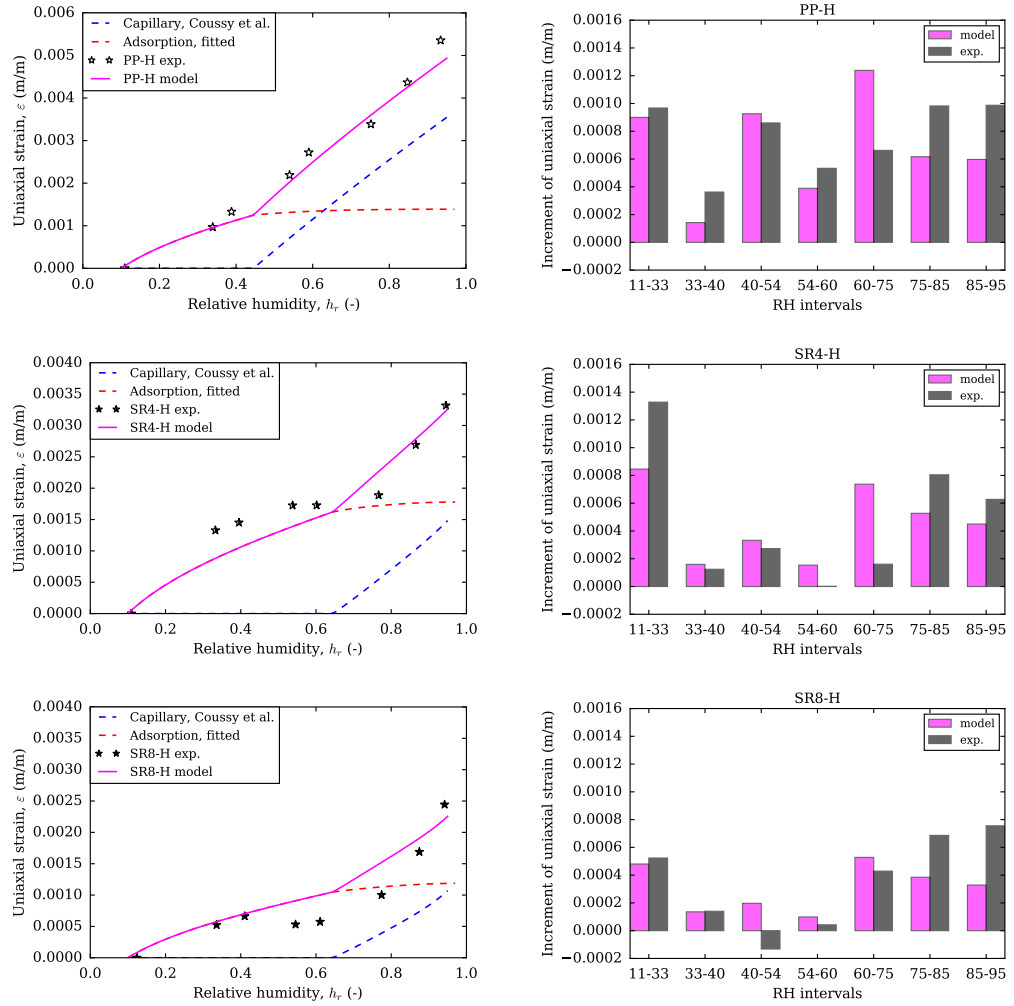
Figure 7.29: Strain on first drying estimated with model 2W (blind prediction) and its decomposition into a strain induced by capillary effects and a strain induced by adsorption effects, confronted to the measured length change, as a function of relative humidity, for pastes at high alkali content.

imagine that a swelling may be induced by the presence of SRA upon drying, caused for instance by an enhanced adsorption of SRA at decreasing relative humidity, which would lead to an apparent plateau of the strain with regards to relative humidity.

7.4.4 Modeling hysteresis and irreversibility

In this section we examine the hysteresis and irreversibility of shrinkage, observed when drying cement pastes and subsequently re-humidifying them, under the scope of models 3W and 2W. The parameters implemented for the model 3W (λ_{ads} and λ_{mu}) and the model 2W (λ_{ads}) are determined as detailed in section 7.3, based on the re-humidification branch. The modeling of the hysteresis is enabled by the fact that the modeled water content, which are used as input for modeling of strain, is dependent on the drying or re-humidification and shows a hysteresis.

Results of strain estimated with model 3W are shown in figure 7.30. The model captures the hysteresis of drying shrinkage and re-humidification qualitatively. However, quantitatively, for plain pastes, at the various alkali contents here considered, the hysteresis is underestimated, since the model underestimates strain on the first drying of cement pastes at relative humidities larger than 40%. To quantify the hysteresis, we compute:

$$\Delta\varepsilon = \varepsilon_{des}(h_r) - \varepsilon_{ads}(h_r) \tag{7.14}$$

where $\varepsilon_{des}(h_r)$ is the strain on the desorption branch at a given relative humidity h_r and $\varepsilon_{ads}(h_r)$ is the strain on the adsorption branch at the same relative humidity h_r. The range of relative humidities considered is the relative humidities considered on the re-humidification branch.

In figure 7.31 we plot the hysteresis $\Delta\varepsilon$ estimated with model 3W, in terms of the measured one. For plain pastes, the model underestimates the hysteresis, whereas for pastes containing SRA, the estimated hysteresis is closer to the measured one.

For model 2W, results of the estimated strain are shown in figure 7.32. In figure 7.33, we plot the estimated hysteresis in terms of the measured
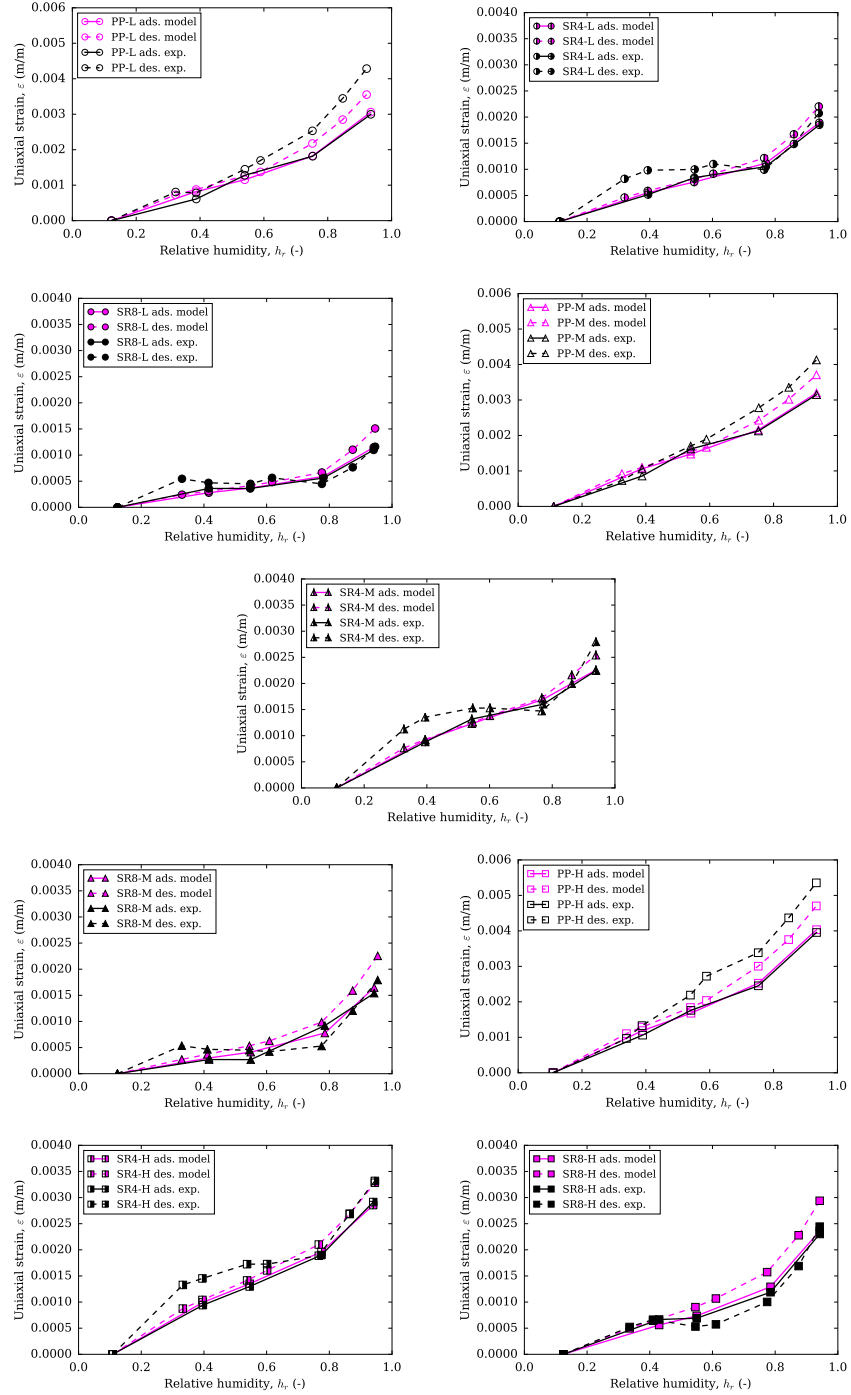
Figure 7.30: Strain upon first drying and subsequent re-humidification, modeled with model 3W and measured.
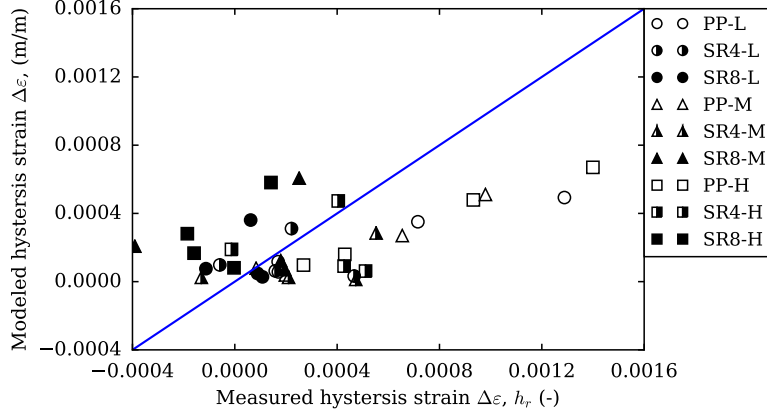
Figure 7.31: Hysteresis estimated with model 3W, in terms of the measured hysteresis.

one. The model 2W captures the hysteresis and its order of magnitude, since it estimates well the strains measured upon the first drying and the subsequent re-humidification for plain pastes. The model 2W captures better the hysteresis of the strain in terms of RH, than the model 3W.

On the low range of relative humidities, where capillary effects are not occurring, both model 3W and model 2W predict that strain on both drying and re-humidification coincide because, with both models, at those low relative humidities, the whole surface area of the sample is affected by an adsorbed film layer upon drying and re-humidification. Also, the factor λ_{ads} relating the changes of surface energy to the strain they induce is considered the same on drying and re-humidification, which leads to no hysteresis at low relative humidities, which is consistent with the measurements for plain pastes. In contrast, for pastes containing SRA, experiments show some hysteresis of the drying shrinkage and swelling at low relative humidity.

Overall, the models 3W and 2W succeed in capturing most of the hysteresis and irreversiblity observed experimentally, while those models are poroelastic. This observation shows that the hysteresis and irreversibility of drying shrinkage (when strain is plotted versus relative humidity) can be accounted for by the hysteresis of the water content in the cement pastes on drying and re-humidification. In fact, with both models 3W and 2W, we account for
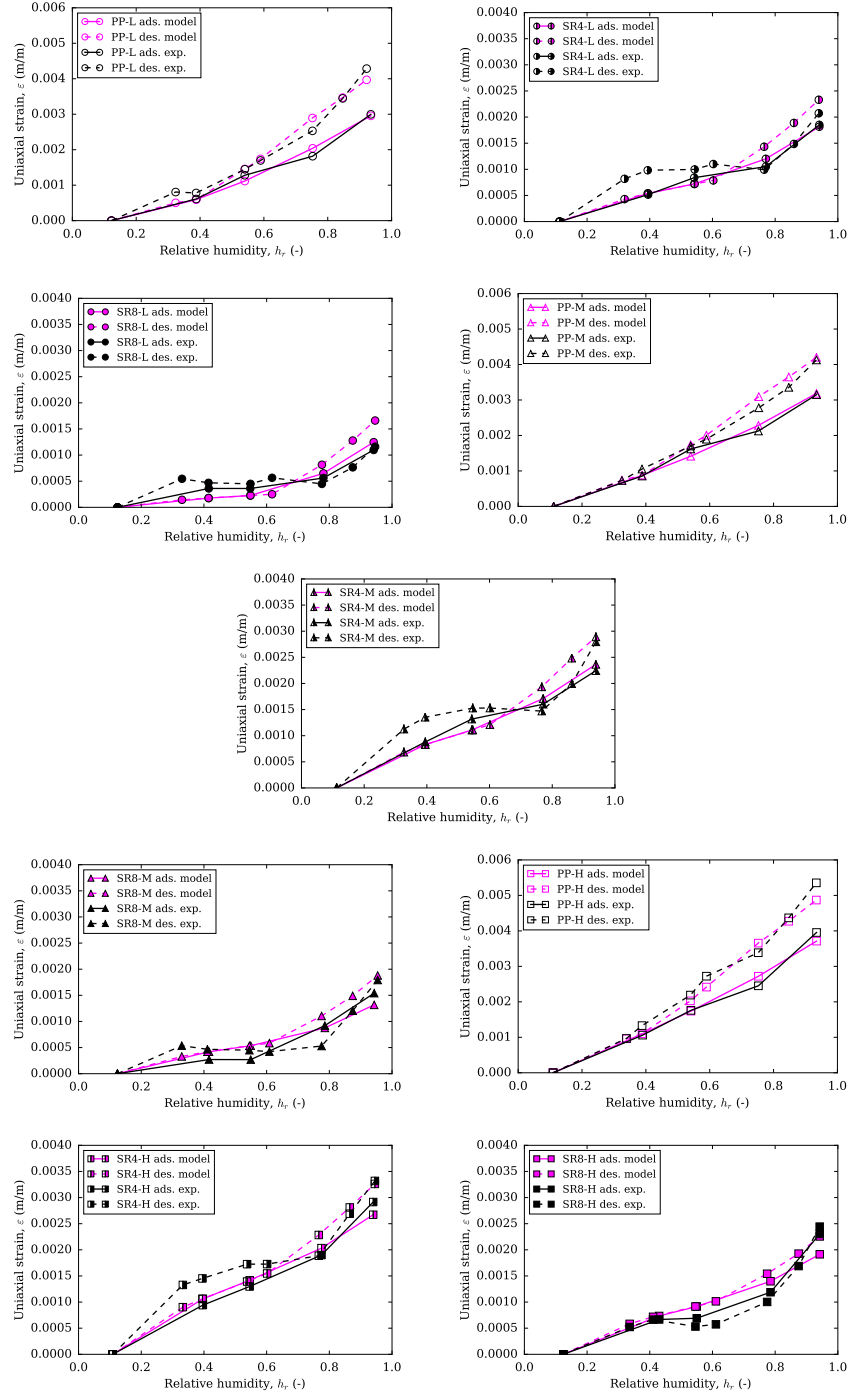
Figure 7.32: Strain upon first drying and subsequent re-humidification, modeled with model 2W and measured.
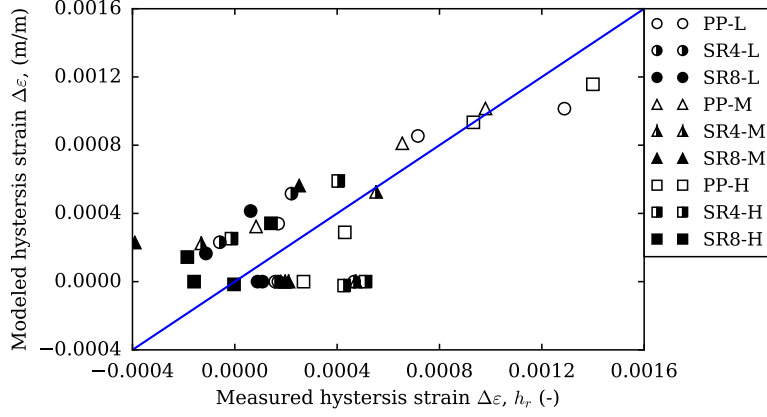
Figure 7.33: Hysteresis estimated with model 2W, in terms of the measured hysteresis.

the ink-bottle effect for water in capillary pores and water adsorbed on surfaces. In addition for model 3W, we also account for the hysteresis of water in micropores (cf. figure 6.2). Di Bella et al. (2017) showed that the first drying shrinkage can be well accounted for in the poroelasticity framework, regardless of the reported irreversibility of this first drying shrinkage.

The hysteresis is better approached by the model considering water in capillary pores and water adsorbed on emptied pores (i.e., model 2W) than the model considering the water as a contribution of 3 types of water (i.e., model 3W). In fact, modeling strain based on model 2W is based on the water vapor sorption isotherms. The water vapor sorption isotherms allow exploring a larger fraction of the pore space, so that the hysteresis due to water in capillary pores and water adsorbed on surfaces can be better captured. In contrast, with nitrogen sorption isotherms, cavitation of nitrogen on the desorption branch limits the range of the pore space that can be probed. Hence, the ink-bottle effect is not as well captured on the full range of considered relative humidities with model 3W as with model 2W.

7.5 Role of SRA in drying shrinkage reduction

In this section we review the role of SRA in reducing drying shrinkage, in light of the two models proposed in the previous sections. We examine the role of SRA as highlighted by the models based on 2 types of water (i.e., model 2W) or 3 types of water (i.e., model 3W).

Based on model 3W, the action of SRA on capillary effects occurs by the reduction of saturation degree caused by the reduction of surface tension and the impact of SRA on the developed pore structure. The SRA also acts on the strain induced by adsorption on surfaces. In fact, the factor λ_{ads} of proportionality between changes of surface energy and strain induced by adsorption on surfaces decreases with addition of SRA (see figure 7.18). An addition of 1% of SRA in mix (mass percentage of clinker) leads to a reduction of the factor λ_{ads} by 9% (with regards to plain paste). This impact of the SRA on the factor λ_{ads} may be linked to the impact of the SRA on the surface area of cement pastes, which decreases as well when SRA is added. The strain induced by water in micropores, for pastes at low alkali content and high alkali content, is, at first order, reduced by addition of SRA, since the factor λ_{μ} decreases when SRA is added (see figure 7.19). However, for the paste with medium alkali content, the strain induced by micropores is found to be larger for paste containing 8% of SRA than for other pastes.

In model 2W, SRA also acts on the capillary effects. The action of the SRA translates not only into a reduction of the saturation degree (cf. figure 7.26) but also into a reduction of the range of relative humidities at which capillary effects occur, given that cavitation of water occurs at higher relative humidities. Like for model 3W, the SRA acts on the strain induced by adsorption on surfaces, by inducing a consistent reduction of the factor λ_{ads} (cf. figure 7.21).

7.6 Conclusions

In this chapter, two approaches for modeling of strain were presented. The first approach is an empirical model allowing to estimate the first drying shrinkage strain of a cement paste at given SRA content and alkali content, and at a give relative humidity. The second approach is based on the physical processes at the origin of drying shrinkage. Two physics-based models were proposed, based either on the distinctions of water in pore space into 3 types (model 3W, with which water can be in capillary pores, adsorbed on surfaces, or in micropores) or into 2 types (model 2W, with which water can be in capillary pores or adsorbed on surfaces). Water in capillary pores deforms the material through capillary effects, modeled with Coussy model. Water adsorbed on surfaces is assumed to deform the material according to Gibbs-Bangham surface effects. Water in the micropores is assumed to deform the material linearly with respect to the water content in the micropores.

For the strain induced by adsorption on surfaces (that plays a role in both models 3W and 2W), the parameter λ_{ads} linking changes of surface energy to strain was fitted. In addition, for model 3W only, the parameter λ_μ that relates strain to the water content in micropores was fitted also. Both parameters were fitted on the re-humidification branch. Both models were then used to perform a blind prediction of the first drying shrinkage. The accuracy of the models was evaluated by the mean error on the increments of strain on the intervals of relative humidities, and was found to be equal to 170 μm/m for model 3W and to 200 μm/m for model 2W. Model 2W is satisfactory in capturing the qualitative behavior and magnitude of the strain upon first drying, while requiring only one fitting parameter λ_{ads} (fitted on the re-humidification branch).

The models, developed in the scope of poroelasticity, suggest that SRA acts on:

- Strain induced by water in capillary pores,

- Strain induced by adsorption on surfaces of pores emptied of their condensate,

- Strain induced by water in micropores.

SRA reduces the capillary forces. This reduction of the capillary forces by the SRA is due to 1) the lowering of the saturation degree at any given relative humidity (cf. figure 7.26) caused by the reduction of surface tension as well as by a coarsening of the pore structure in presence of SRA and to 2) the reduction of the range over which capillary forces act due to a shift of the cavitation pressure of water in pastes containing SRA toward higher relative humidities.

The action of the SRA on the adsorption-induced strain is based on the reduction of the factor λ_{ads} of proportionality between changes of surface energy and strain induced by adsorption. The factor λ_{ads} is found to decrease consistently upon addition of SRA, regardless of alkali content (as shown in figures 7.18 and 7.22). This decrease may be linked to the impact of the SRA on the pore structure, namely on the surface area affected by an adsorbed film layer. Furthermore, the factor λ_{ads} differs from the theoretical value $\lambda_{ads,Scherer}$. The ratio $\lambda_{ads}/\lambda_{ads,Scherer}$ is found independent of the SRA content (as shown in figures 7.18 and 7.22) and increases with increasing alkali content. This feature may be interpreted by the fact that the SRA would not modify the morphology of C-S-H while alkali would.

The action of SRA on the strain induced by micropores is manifested by the decrease of the parameter λ_μ (as shown in figure 7.19). The variations of strain induced by water in micropores are significant only at high relative humidities.

Both models capture qualitatively the hysteresis and irreversibility of the first drying shrinkage. Since both models are poroleastic, the irreversibility observed experimentally may at least partly not be due to a mechanical irreversibility. The hysteresis and irreversibility of drying shrinkage of cement pastes can be captured at first order by the hysteresis of the water content with relative humidity (as shown in figures 7.31 and 7.33), found for all 3 types of water, and linked to the ink-bottle effect for what concerns water in capillary pores and water adsorbed on surfaces. Quantitatively, model 2W captures better the hysteresis than model 3W, which is attributed to the fact that model 2W uses water sorption isotherms as inputs while model 3W uses

nitrogen sorption isotherms as inputs, and that the former ones are able to quantify the ink-bottle effect on a wider pore size distribution than the latter ones.

Chapter 8

Conclusions and perspectives

8.1 Conclusions

How a shrinkage reducing admixture (namely hexylene glycol) is able to reduce drying shrinkage of cement-based materials was examined in this work, to the light of an extensive experimental campaign, which served as a basis for deriving models to estimate water content in cement pastes and drying shrinkage. The efficiency of the SRA in cement pastes at various alkali contents was examined. The potential mechanisms of action of the SRA were identified and modeled. The derived models can help optimize the amount of SRA to add to the mix to reach a targeted drying shrinkage reduction, and tailor this amount to the cement formulation, namely to its alkali content.

The first part of this study was based on an extensive experimental characterization of cement pastes containing various contents in SRA and alkali. Drying shrinkage isotherms and water sorption isotherms on a full cycle of drying and re-humidification were measured after both long-term drying and short-term drying (see chapter 3). The ability of the SRA to reduce drying shrinkage was examined at various relative humidities, contents in SRA, and contents of alkali. The SRA was found to reduce most efficiently drying shrinkage in the range of relative humidities of 75% down to 33%: in this range, after long-term drying, a plateau of drying shrinkage was observed, such that drying shrinkage and weight loss were not correlated. In pastes

containing SRA, drying shrinkage increased with an increasing alkali content, while, for plain pastes, the drying shrinkage did not depend much on the alkali content. Further, the irreversibility of the drying shrinkage was investigated by re-humidification of the samples. The SRA was found to reduce the irreversible drying shrinkage significantly, when compared to plain pastes. Finally, at low RH, the short-term drying shrinkage was found larger than long-term drying shrinkage. For plain pastes, the short-term drying shrinkage exhibited a larger irreversible drying shrinkage than the long-term drying.

To gain a better understanding of how cement pastes are impacted by SRA, after both short-term and long-term drying, we characterized the microstructure of the cement pastes. The SRA was found to lead to a consistent retardation of hydration regardless of the alkali content. The pore structure of the cement pastes was also impacted by the SRA: the pore structure of cement pastes containing SRA was coarser than that of plain pastes, as illustrated by the decrease of the specific surface area and the modification in the pore size distribution, as evaluated with mercury intrusion porosimetry and gas sorption techniques (with water vapor and nitrogen), as shown in section 4.3. The evolution of the pore structure upon drying was also examined. The pore structure of the plain cement pastes underwent dramatic evolutions, as illustrated by the variations of specific surface area and of pore volume, measured with both nitrogen and water sorption. In contrast, the magnitude of the evolutions of the pore structure of pastes containing SRA observed upon drying, as investigated by nitrogen sorption, was less significant than for the plain pastes (see section 4.4). Finally, we found that the large evolutions of pore structure of the plain cement pastes are mostly reversible when re-humidifying to 95% RH (see section 4.5).

A physico-chemical investigation of the SRA was conducted by means of pore solution extractions and of leaching measurements (see chapter 5). The SRA influenced the properties of the pore solution by reducing its surface tension, regardless of the alkali content. The SRA was found to impact also the composition of the pore solution: the content of alkali in the pore solution decreased with an increasing amount of SRA. Moreover, the SRA

was found to be mobile, as the SRA could be leached out of the cement paste: in saturated conditions our SRA of interest was not adsorbed on the solid surfaces of the cement pastes, whatever their alkali content was.

Other conclusions regarding the experimental campaign are:

- The addition of SRA after hydration of cement pastes was tested, and proven beneficial in reducing drying shrinkage.

- The SRA was responsible for a shift of the cavitation pressure of water in both cement pastes and in zeolites towards larger relative humidities.

- SRA hindered the adsorption (of water and nitrogen) in zeolite and in cement pastes, as illustrated by the combination of pre-drying methods (solvent exchange and vacuuming at room temperature) and of characterization techniques (MIP, nitrogen sorption and water sorption).

The second part of this work focused on modeling how water content and drying-induced strain of the cement pastes evolve with relative humidity. For what concerns water content (see chapter 6), modeling required knowledge of the pore structure of the cement pastes (from sorption isotherms) and of the features of the pore solution (namely, its surface tension). A first model was phenomenological. Then, 2 models more physically based were proposed, depending on how the pore structure was analyzed. When the pore structure was characterized by BJH analysis of nitrogen sorption isotherms, water in the pore space was divided into three contributions: water in capillary pores, water adsorbed on solid surfaces and water in micropores. This model was referred to as model 3W. The amounts of water attributed to the micropores and to the water adsorbed on solid surfaces were found to compare well with literature data for water adsorbed on synthetic C-S-H. Also, their magnitude compared reasonably well with literature data obtained with NMR. When the pore structure was characterized by BJH analysis of water sorption isotherms (volumetric method), water in the pore space was divided into two contributions: water in capillary pores and water adsorbed on solid surfaces. This model was referred to as model 2W. Both model 3W and model 2W modeled water content on a cycle of first drying and subsequent re-humidification.

For what concerns drying shrinkage (see chapter 7), first we proposed a phenomenological model that estimates the drying shrinkage as a function of relative humidity, by taking into account the content of alkali and SRA in the paste. This model can readily be used by the engineer to optimize the amount of SRA to add to the mix. To capture the plateau observed experimentally at medium relative humidities, we needed to consider that there exists some swelling mechanism that gets activated in this range of relative humidities to counterbalance the shrinkage induced by the classical physical processes (capillary effects,...) involved during drying.

For what concerns drying shrinkage, we also derived two models with a more physical basis than the phenomenological model. The two models to estimate the water content in the cement paste were used as inputs for the two models to estimate the drying shrinkage of cement pastes. Both models were poroelastic. In model 2W, drying shrinkage was considered to result from capillary effects induced by water in capillary pores and from Gibbs-Bangham-type effects induced by adsorption of water on solid surfaces. In addition, for model 3W, drying shrinkage was also considered to result from variations of the water content in micropores. The models were first calibrated on the strains measured on the re-humidification branch. For model 3W, two parameters were fitted: a parameter linking the variations of surface energy to the strain they induce, and a parameter linking the variations of water content in the micropores to the strain they induce. For model 2W, only one parameter was fitted, which links the variations of surface energy to the strain they induce. Then a blind prediction of the first drying shrinkage was performed. The models were able to capture the hysteresis and irreversibility of drying shrinkage, which indicates that these features (i.e., hysteresis and irreversibility) are not due so much to mechanical irreversibilities, but are mostly due to irreversibilities in how water content evolves with relative humidity (i.e., ink-bottle effect for capillary pores, but also hysteresis of water content in micropores). As for the action of SRA on drying shrinkage, the model made it possible to identify the individual effect of the SRA on each shrinkage mechanism. For what concerns capillary effects, the SRA acts through a reduction of the degree of saturation at a

given relative humidity, and through a reduction of the range over which capillary effects occur, as cavitation of water in presence of SRA is shifted toward larger relative humidities. Indeed, cavitation occurred at a relative humidity of about 65% when the paste contained the SRA, while it occurred at a relative humidity of about 35% for plain pastes. The SRA also acts on the strain induced by adsorption on surfaces by reducing the magnitude of the parameter that translate variations of surface energy into strain.

8.2 Perspectives

This study can be further improved, on both the experimental and the modeling levels.

On the experimental level, several improvements can be made:

- For what concerns the drying shrinkage measurements, parts of the differences noted between pastes could be attributed to the fact that the hydration degree of the various pastes was different, even though the pastes were tested at the same age. Such difference was attributed to the hydration retardation due to the SRA, which persisted even at mature ages (i.e., for pastes older than 3 months). Consequently, it may be useful to compare pastes at a given hydration degree.

- In the same spirit, to characterize the effect of the SRA other than its effect on the microstructure, an alternative would be to study hydrated cement pastes to which the SRA is added after curing.

- We investigated the pore structure of the various cement pastes and their evolution during the first drying. In addition, investigating their evolution on the re-humidification branch could have provided interesting information, in particular regarding a potential reversibility or irreversibility of those evolutions.

- The evolution of the pore structure over time upon drying and re-humidification may also provide insight into the differences observed between short-term drying and long-term drying.

- At medium relative humidities, a plateau was observed on the long-term drying shrinkage strains of the cement pastes containing SRA (i.e., in spite of the decrease of relative humidity, the cement pastes did not shrink more). We attributed this plateau to an enhanced adsorption of SRA molecule on the surfaces of pores of cement pastes, which may lead to a swelling of the cement paste countering the shrinkage induced by desorption of water, and hence to an apparent plateau. To verify experimentally such behavior, and to determine where the SRA is located during drying (e.g., on solid interfaces, or at liquid-gas interfaces), we may conduct a double isotherm experiment, as proposed by late Dr. Ellis Gartner. The double isotherm would consist in measuring the relative pressure of the SRA in the gaseous phase in the pore space of the cement paste, after equilibration at a given relative humidity. If the relative pressure would remain equal to the saturated vapor pressure of the SRA, this could be an indicator that the SRA would be located at the interfaces gas/solid or gas/liquid.

On the modeling level, several improvements to the proposed models 3W and 2W can be made as well:

- 2 parameters have been back-calculated, which govern how adsorption on surfaces and how variations of water content in the micropores translate into a strain. Being able to link the magnitude of those parameters to microstructural features (morphology of the pore, properties of the microscopic phases,...) would bring confidence in the modeling.

- Another aspect that requires improvement is the thermodynamic formulation of the models. Presently, the total strain was assumed to result from the concatenation of various individual contributions (i.e., capillary effects, Gibbs-Bangham-type effects, and effects due to water in the micropore). A proper thermodynamic derivation of the strain induced by those various effects would be needed.

Common to both experiments and modeling, one question that we did not tackle is that of the time-dependent behaviors, although our experiments

showed that the duration of the drying plays a critical role on the evolution of the microstructure. We did not address what role the viscous behavior of the material plays, in this process specifically, and more generally on the drying shrinkage strains.

Finally, we note that the approach here adopted, which mixed extensive experiments with modeling, could be replicated with other SRAs, to help decipher their own modes of action.

Appendices

Appendix A

Preparation of cement pastes

Mixing of cement pastes at high high alkali content and in presence of SRA by the mixing method of the low and medium alkali pastes led to an inhomegenous paste with apparent lumps as illustrated in figure A.1. The lumps are agglomerations of few millimeters in size that can be visually noticed in the mix.

To investigate these formed lumps at high alkali content in the presence of SRA, we conducted semi-quantitative XRD measurements on a cement paste prepared at high alkali content and with 8% SRA content, mixed with Renfert mixer at a speed of 250 rpm. 10 minutes after mixing, the paste is dried under nitrogen flow for 1 hour. In figure A.2 the obtained chart of the identified phases, and in table A.1 the percentage of identified phases with a semi-quantitative approach. It is worth noting that Eberhardt (2010) also observed, by means of ESEM wet mode observation, large crystals for cements pastes containing SRA at early age, which were identified as syngenite. The precipitation of syngenite is enhanced by SRA, Eberhardt (2010) indicated also that syngenite is no longer observed at 12 hours hydration.

Figure A.1: Formed lumps during mixing of pastes at high alkali content and in presence of SRA.
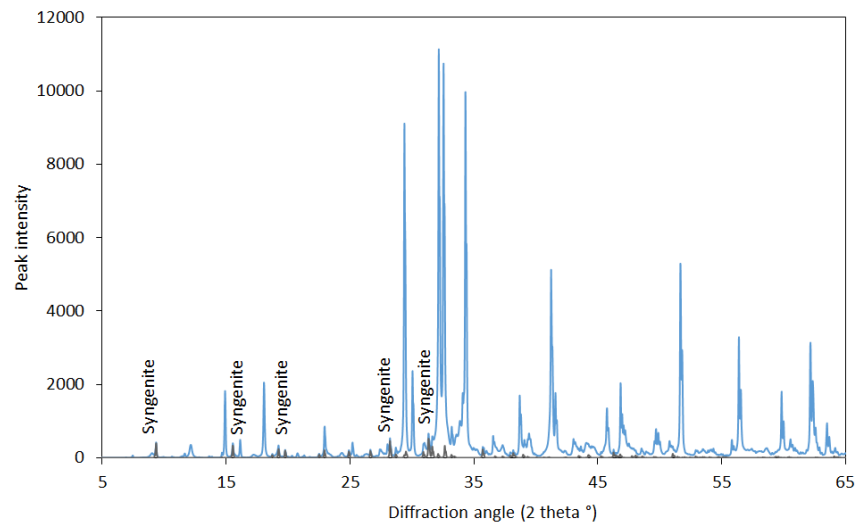
Figure A.2: XRD chart of the formed lumps during mixing.

Phase	Mass fraction, percentage (%)
C_3A	0.12
C_4AF	5.9
C_3S	60.9
C_2S	19.9
Bassanite	0.2
Gypsum	0.4
Periclase	0.8
Hydrogarnet	1.3
Ettringite	1.8
Calcite	2.5
Portlandite	2.5
Syngenite	3.6

Table A.1: Identified phases of the cement paste at high alkali content and 8% SRA 10 minutes after mixing.

APPENDIX A. PREPARATION OF CEMENT PASTES

Appendix B

Drying shrinkage measurements

B.1 Measurements of relative humidity of samples after curing

After sealed curing, the relative humidity of the 9 types of samples was measured by crushing the cement paste into centimetric samples, then placing the sample into the Aqualab 4TE to measure the water activity. The Aqualab 4TE is a water activity meter provided by Meter group. The device is calibrated prior to a series of measurements by salt solutions provided by the supplier corresponding to a given RH. The relative humidity of the 9 types of cement pastes is plotted in terms of the SRA content of the samples in figure B.1. Results show that the relative humidity of the samples increased with increasing SRA content, and decreases with increasing alkali contents. These measurements explain the swelling and weight gain of some samples placed in 95% RH. We do note that these measurements of RH and the internal RH may differ, for kinetic reason (sample has to be left in the measuring device for long periods to measure its internal RH) or that some drying occurs on the preparation of the samples for the measurements. However, assuming these effects occur in all samples at the same magnitude, the tendencies observed would still be relevant.
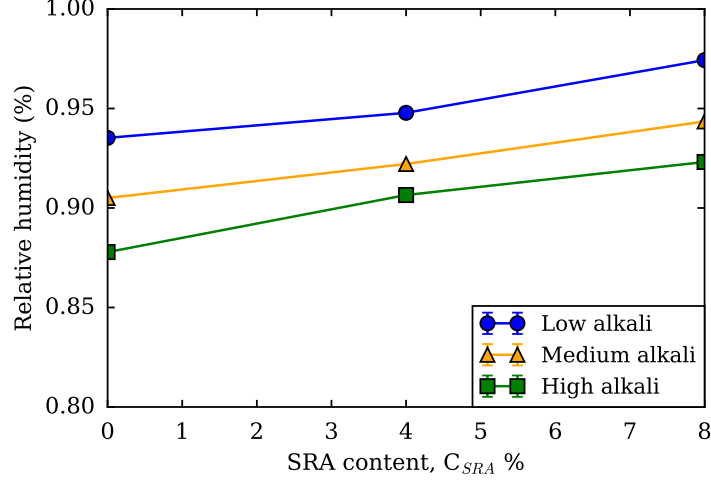
Figure B.1: Relative humidity of cement pastes just after curing (and before drying) in terms of the SRA content.

B.2 Monitoring mass and strain on drying and re-humidification

For the drying shrinkage measurements, note that the error bars stands for the standard deviation of the data, computed as follows:

$$s = \sqrt{\frac{\sum_{i=1}^{N}(x_i - \bar{x})^2}{N}} \tag{B.1}$$

To confirm that cement pastes have reached equilibrium, samples in box A, where we monitored both drying shrinkage and weight loss on drying. Figures B.2, B.3 and B.4 show the results of the measurements on drying for pastes at low alkali content, medium alkali content and high alkali content, respectively. The figures B.5, B.6 and B.7 show the results of monitoring on re-humidification, for samples at low alkali content, medium alkali content and high alkali content, respectively.

Figure B.2: Monitoring measurements of weight loss (left) and drying shrink-
age (right) of cement pastes in the box A (2 specimens) for samples at low
alkali content.
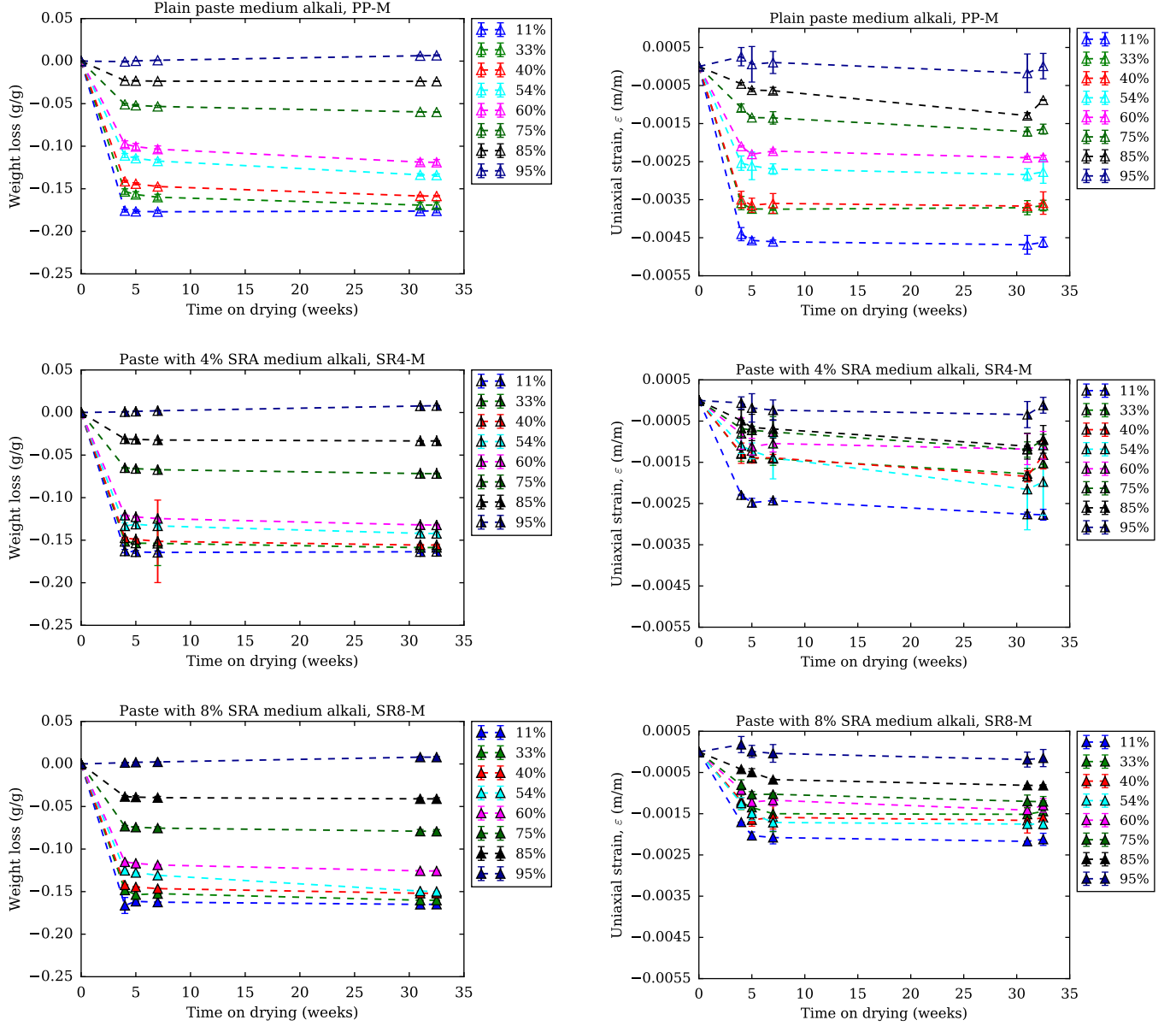
Figure B.3: Monitoring measurements of weight loss (left) and drying shrinkage (right) of cement pastes in the box A (2 specimens) for samples at medium alkali content.

Figure B.4: Monitoring measurements of weight loss (left) and drying shrinkage (right) of cement pastes in the box A (2 specimens) for samples at high alkali content.

Figure B.5: Monitoring measurements of weight loss (left) and strain on re-humidification (right) of cement pastes in the box A (2 specimens) for samples at low alkali content.

Figure B.6: Monitoring measurements of weight loss (left) and strain on re-humidification (right) of cement pastes in the box A (2 specimens) for samples at medium alkali content.

Figure B.7: Monitoring measurements of weight loss (left) and strain on re-humidification (right) of cement pastes in the box A (2 specimens) for samples at high alkali content.

Figure B.8: Weight loss (left) and drying shrinkage (right) in terms of relative humidity for cement paste at low alkali content, prepared by the high shear mixing procedure (PP-L-rep) and the low shear mixing procedure (PP-L).

B.3 On the impact of mixing on drying shrinkage measurements

The mixing procedure is not the same for set of samples at low and medium alkali content on the on hand and the samples at high alkali content on the other. We denote the mixing procedure of cement pastes at low and medium alkali content by the low shear mixing procedure, and the high shear mixing procedure for the mixing procedure of cement paste at high alkali content. Both mixing procedures are detailed in section 3.1. To confirm that the mixing procedure does not impact the results of the drying shrinkage and weight loss of samples, we chose 2 types of cement pastes that are mixed at the high shear rate mixer and for which the drying shrinkage and mass loss isotherms are measured. We studied the plain paste at low alkali (PP-L) and the paste at medium alkali content and at 8% content of SRA (SR8-M). The samples are dried at 6 relative humidities from 95% to 11%. The drying shrinkage and weight loss of cement pastes is shown in figures B.8 and B.9 for PP-L and SR8-M. Results confirm that the impact of mixing procedure on the drying and mass loss isotherms is negligible.
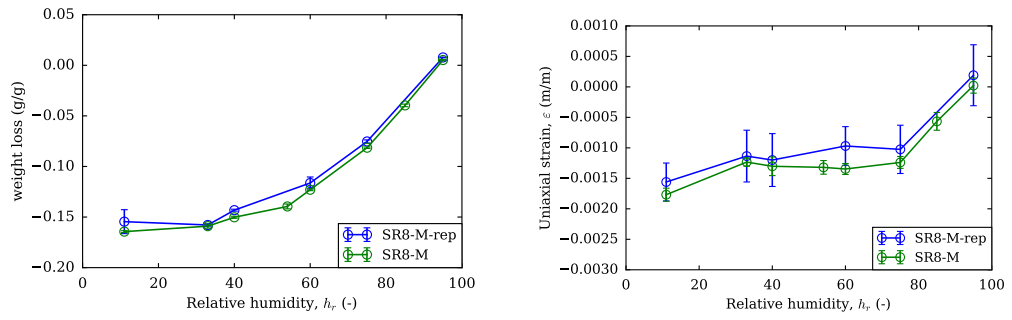
Figure B.9: Weight loss (left) and drying shrinkage (right) in terms of relative humidity for cement paste at medium alkali content with 8% SRA content, prepared by the high shear mixing procedure (SR8-M-rep) and the low shear mixing procedure (SR8-M).

Appendix C

Mechanical characterization

C.1   Results of bending test

Cement pastes were characterized for their mechanical properties by means of a three point bending test. The flexural strength and Young's modulus of the samples of 3 mm thickness was measured. The results of the flexural strength and the Young's modulus are plotted in terms of the SRA content in figure C.1. For the estimation of the bulk modulus of the cement pastes before drying, implemented for the modeling of drying induced strain, the following formula is used:

$$K = \frac{E}{3(1 - 2\nu)} \tag{C.1}$$

where E is the Young's modulus, and ν is the Poisson's ratio.

Young's modulus can be expressed as follow:

$$E = \frac{Fl^3}{48yI} \tag{C.2}$$

Where:

F: Force applied at the center of the measured sample

l: length of the sample

I: quadratic moment m^4

y: measured displacement m
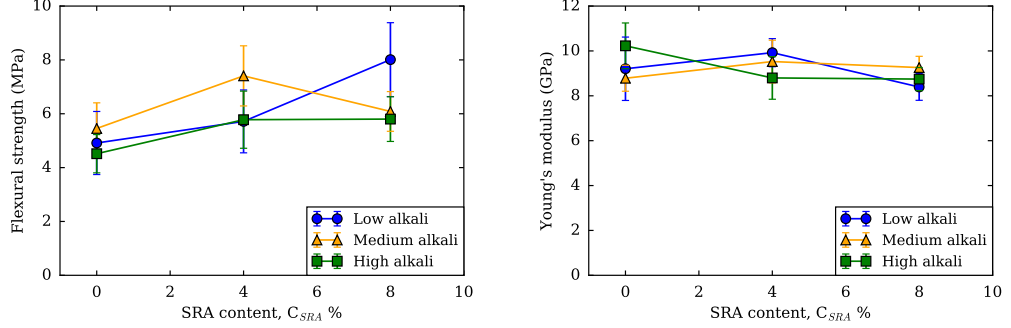
Figure C.1: Flexural strength (left) and Young's modulus (right) of the cement pastes after the sealed curing and before the drying.

At least 3 samples are measured per type of sample. Every sample is tested twice, for a span of 6 cm

C.2 Results of ultrasonic pulse velocity measurements

The ultrasonic pulse velcoity of the P-wave (i.e., the longitudinal wave) and the S-wave (i.e., shearwave velocity) of the specimens of geometry $3{\times}13{\times}100$ mm^3 was measured using an ultrasonic probe (V103-RM and V153-RM, Panametrics-NDT), and a pulse receiver (5077PR, Panametrics-NDT). The measurement parameters are detailed in Maruyama et al. (2014). The voltage of the pulse oscillator is -400 V, the pulse repetition frequency was 100 Hz for the transmission method and the frequency is 1.0 MHz. The measurement is conducted over the 13 mm thickness of the samples.

Measurement of P-wave and S-wave velocities, and knowledge of bulk density of samples, we can deduce the dynamic Poisson's ratio and the Young's modulus, that are related to the P-wave and S-wave velocities v_p and v_p,

Figure C.2: The P-wave (left) and S-wave (right) velocities for cement pastes after curing for 3 months at sealed conditions and before drying.

respectively, following:

$$v_p = \sqrt{\frac{E(1 - \nu)}{\rho(1 + \nu)(1 - 2\nu)}}. \tag{C.3}$$

$$v_s = \sqrt{\frac{E}{2\rho(1 + \nu)}}. \tag{C.4}$$

The bulk density of cement pastes can be assessed by the archimedes method: mass of specimens is measured as it is, then they are saturated under vacuum for 24 hours, and then mass in water is measured, therefore volume of sample is computed.

Appendix D

Phase assemblage

In figure D.1, we show the histogram for the Si/Ca ratio on the tested samples, slight increase of the mean value of the Gaussian fit is observed for paste containing 8% SRA content with regards to the plain paste at low alkali content.
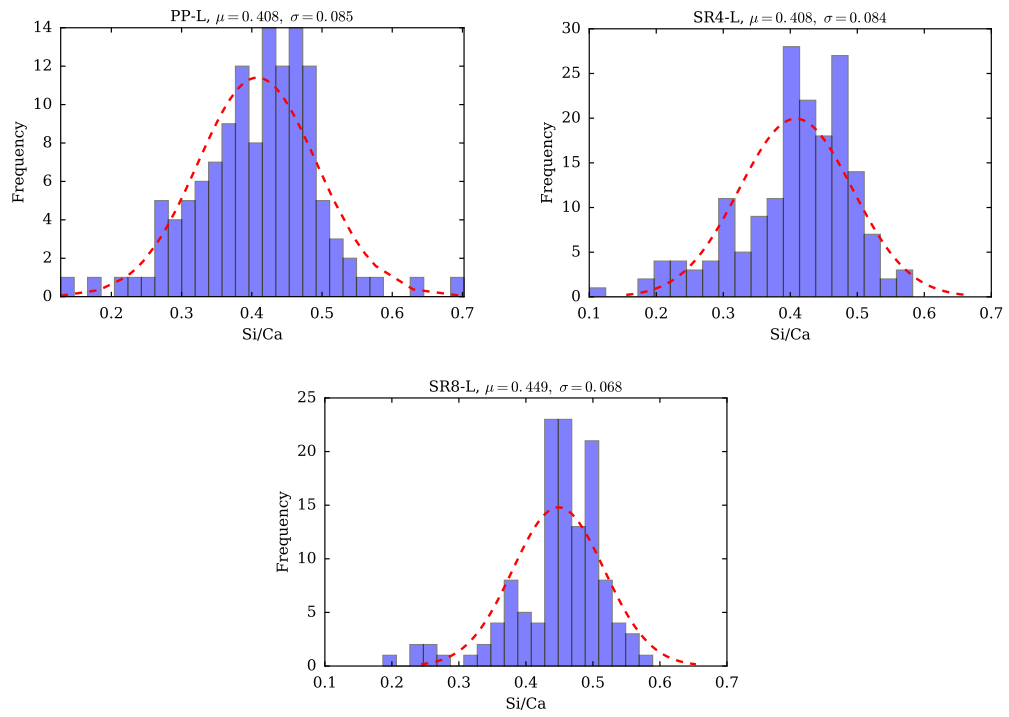
Figure D.1: Distribution of the Si/Ca ratio at low alkali content of plain paste (PP-L), paste at 4% SRA content (SR4-L) and paste at 8% SRA content (SR8-L).

Appendix E

Reproducibility of measurements

In this chapter, we verified the reproducibility of sorption isotherms measurements and short-term drying measurements, by conducting the measurements at least twice on two sets of samples prepared separately. The results of the measurements are as detailed below:

- Nitrogen sorption isotherms in figure E.1.

- Water sorption isotherms in figure E.2.

- Short-term drying measurements in figure E.3.
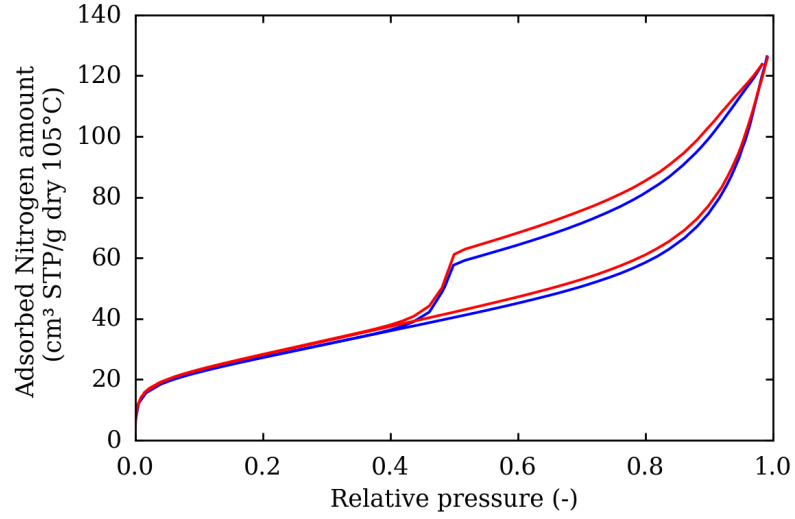
Figure E.1: Nitrogen sorption isotherm measured on a plain paste at low alkali. 2 samples were measured
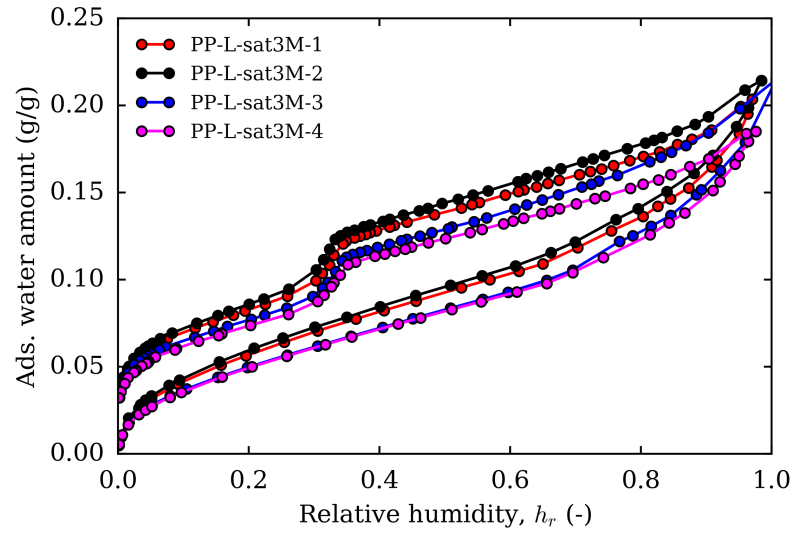
Figure E.2: Water sorption isotherm measured on a plain paste at low alkali. 4 samples were measured.
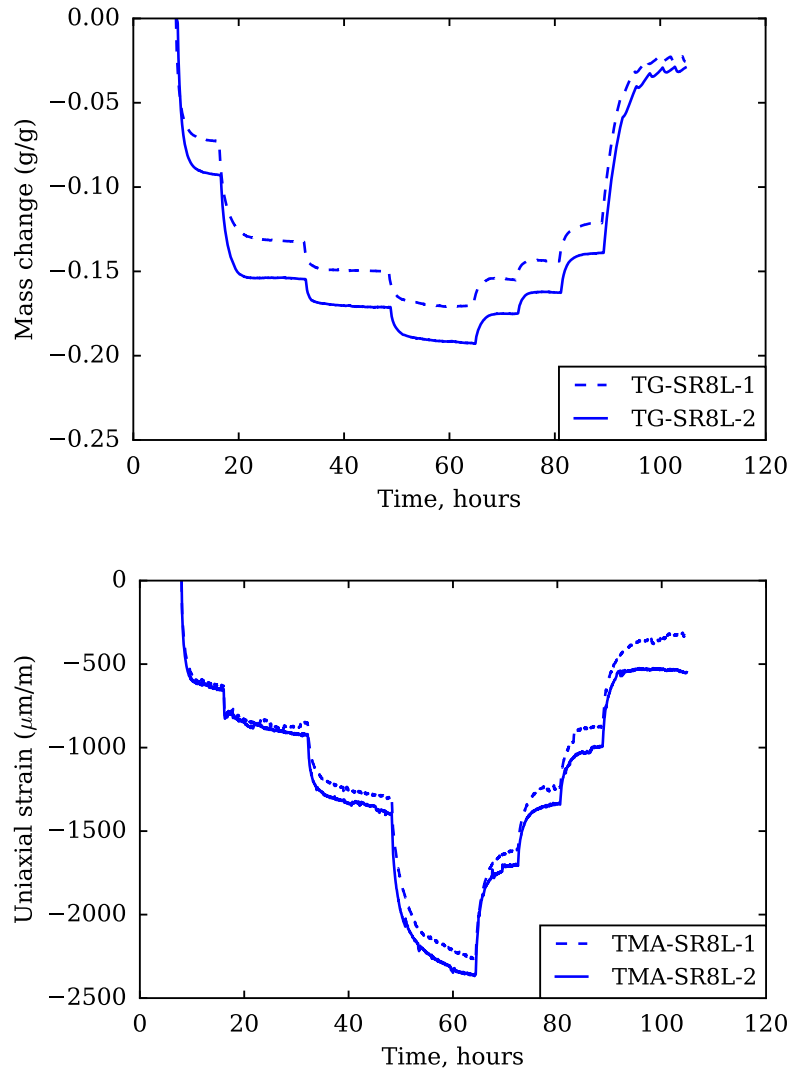
Figure E.3: Mass change and strain on short-term drying in terms of time for a paste at low alkali content with 8% SRA content, 2 samples were measured.

APPENDIX E. REPRODUCIBILITY OF MEASUREMENTS

Bibliography

Acker, P. and Ulm, F. J. (2001). Creep and shrinkage of concrete: Physical origins and practical measurements. *Nuclear Engineering and Design*, 203(2-3):143–158. *Cited page 62*

Acker, P., Ulm, F.-J., Bazant, Z., and Wittmann, F. (2001). Micromechanical analysis of creep and shrinkage mechanisms. In *Creep, Shrinkage and Durability Mechanics of Concrete and other Quasi-Brittle Materials*, pages 15–25. Cambridge. *Cited page 261*

Ai, H. and Young, J. F. (1997). Mechanism of shrinkage reduction using a chemical admixture. In *Proceedings of the 10th International Conference on the Chemistry of Cement, vol. 3, Göteborg, Sweden*, pages 18–22. *Cited pages 38, 76, 77, 79, 80, 145, and 188*

Aïtcin, P. C. (2000). Cements of yesterday and today - concrete of tomorrow. *Cement and Concrete Research*, 30(9):1349–1359. *Cited page 37*

Aligizaki, K. K. (2006). *Pore structure of cement based materials Testing interpretation and requirements.* Taylor & Francis, london. *Cited pages 16, 51, 55, 56, 60, 61, 135, 166, and 226*

Allen, A. J., Thomas, J. J., and Jennings, H. M. (2007). Composition and density of nanoscale calcium-silicate-hydrate in cement. *Nature Materials*, 6(4):311–316. *Cited page 261*

Badmann, R., Stockhausen, N., and Setzer, M. J. (1981). The statistical thickness and the chemical potential of adsorbed water films. *Journal of Colloid And Interface Science*, 82(2):534–542. *Cited pages 57 and 211*

Balogh, A. (1996). New Admixture Combats Concrete Shrinkage. *Concrete Construction*, 1996:5.   *Cited page 77*

Bangham, D. H., Fakhoury, N., and Mohamned, A. F. (1932). The Swelling of Charcoal. Part II. - Some Factors Controlling the Expansion Caused by Water, Benzene and Pyridine Vapours. *Proceedings of the Royal Society A*, 138(834):162–183.   *Cited page 65*

Bangham, D. H. and Maggs, F. A. P. (1944). The strength and elastic constants of coals in relation to their ultra-fine structure. In *Conference on the Ultra-Fine Structure of Coals and Cokes.*, pages 118–30, London. British Coal Utilization Research Association.   *Cited page 253*

Baroghel-Bouny, V. (2007). Water vapour sorption experiments on hardened cementitious materials. Part I: Essential tool for analysis of hygral behaviour and its relation to pore structure. *Cement and Concrete Research*, 37(3):414–437.   *Cited page 182*

Baroghel-Bouny, V. and Godin, J. (2000). Experimental study on drying shrinkage of ordinary and high-performance cementitious materials. In *International RILEM Workshop on Shrinkage of Concrete (Shrinkage 2000)*, pages 215–232, Paris.   *Cited pages 64 and 65*

Barrett, E. P., Joyner, L. G., and Halenda, P. P. (1951). The Determination of Pore Volume and Area Distributions in Porous Substances. I. Computations from Nitrogen Isotherms. *Journal of the American Chemical Society*, 73(1):373–380.   *Cited page 56*

Bažant, Z. P. and Raftshol, W. J. (1982). Effect of cracking in drying and shrinkage specimens. *Cement and Concrete Research*, 12(2):209–226.   *Cited page 75*

Beltzung, F. and Wittmann, F. H. (2005). Role of disjoining pressure in cement based materials. *Cement and Concrete Research*, 35(12):2364–2370.   *Cited pages 16, 66, and 69*

Benboudjema, F., Meftah, F., and Torrenti, J. M. (2007). A viscoelastic approach for the assessment of the drying shrinkage behaviour of cementitious materials. *Materials and Structures/Materiaux et Constructions*, 40(2):163–174. *Cited page 74*

Bentur, A., Berger, R. L., Lawrence, F. V., Milestone, N. B., Mindess, S., and Young, J. F. (1979). Creep and drying shrinkage of calcium silicate pastes III. A hypothesis of irreversible strains. *Cement and Concrete Research*, 9(1):83–95. *Cited page 67*

Bentz, D. P. (2005). Curing with Shrinkage-Reducing Admixtures. *Concrete international*, pages 55–60. *Cited page 123*

Bentz, D. P. (2006). Influence of Shrinkage-Reducing Admixtures on Early-Age Properties of Cement Pastes. *Journal of Advanced Concrete Technology*, 4(3):423–429. *Cited pages 39, 77, 80, 82, and 129*

Bentz, D. P., Garboczi, E. J., and Quenard, D. A. (1998). Modelling drying shrinkage in reconstructed porous materials: application to porous Vycor glass. *Modelling and Simulation in Materials Science and Engineering*, 6(3):211. *Cited page 72*

Bentz, D. P., Geiker, M., and Hansen, K. (2001). Shrinkage-reducing admixtures and early-age desiccation in cement pastes and mortars. *Cement and Concrete Research*, 31(7):1075–1085. *Cited pages 39, 76, 82, 110, 129, and 201*

Bentz, D. P. and Jensen, O. M. (2004). Mitigation strategies for autogenous shrinkage cracking. *Cement and Concrete Composites*, 26(6):677–685. *Cited page 76*

Bisschop, J. and Wittel, F. K. (2011). Contraction gradient induced microcracking in hardened cement paste. *Cement and Concrete Composites*, 33(4):466–473. *Cited page 92*

Bonnaud, P. A., Ji, Q., Coasne, B., Pellenq, R.-M., and Vliet, K. (2012). Thermodynamics of Water Confined in Porous Calcium-Silicate- Hydrates. *Langmuir*, 28(31):11422–11432. *Cited pages 28, 237, and 238*

Brunauer, S., Emmett, P. H., and Teller, E. (1938). Gases in Multimolecular Layers. *Journal of the American Chemical Society*, 60(1):309–319. *Cited page 55*

Carrier, B., Wang, L., Vandamme, M., Pellenq, R. J., Bornert, M., Tanguy, A., and Van Damme, H. (2013). ESEM study of the humidity-induced swelling of clay film. *Langmuir*, 29(41):12823–12833. *Cited pages 29 and 256*

Chanvillard, G. (1999). *Le matériau béton : connaissances générales.* *Cited page 68*

Chen, J. J., Sorelli, L., Vandamme, M., Ulm, F. J., and Chanvillard, G. (2010). A coupled nanoindentation/SEM-EDS study on low water/cement ratio portland cement paste: Evidence for C-S-H/Ca(OH)2 nanocomposites. *Journal of the American Ceramic Society*, 93(5):1484–1493. *Cited page 146*

Collepardi, M., Borsoi, A., Collepardi, S., Ogoumah Olagot, J. J., and Troli, R. (2005). Effects of shrinkage reducing admixture in shrinkage compensating concrete under non-wet curing conditions. *Cement and Concrete Composites*, 27(6):704–708. *Cited pages 75 and 76*

Collier, N. C., Sharp, J. H., Milestone, N. B., Hill, J., and Godfrey, I. H. (2008). The influence of water removal techniques on the composition and microstructure of hardened cement pastes. *Cement and Concrete Research*, 38(6):737–744. *Cited page 49*

Coussy, O. (2010). *Mechanics and Physics of Porous Solids.* *Cited pages 16, 54, 70, and 71*

Coussy, O., Dangla, P., Lassabatère, T., and Baroghel-Bouny, V. (2004). The equivalent pore pressure and the swelling and shrink-

age of cement-based materials. *Materials and Structures*, 37:15–20.
Cited pages 71, 72, 73, and 252

Cranston, R. W., Inkley, F. A., and Adalbert, F. (1957). The Determination of Pore Structures from Nitrogen Adsorption Isotherms. *Advances in Catalysis*, Volume 9:143–154. *Cited page 57*

D'Ambrosia, M., Altoubat, S., and Park, C. (2001). Early age tensile creep and shrinkage of concrete with shrinkage reducing admixtures. In Ulm, F., Bazant, Z., and Wittman, F. H., editors, *Creep, Shrinkage and Durability Mechanics of Concrete and other Quasi-Brittle Materials, CONCREEP*, volume 3, pages 685–90, BOSTON. *Cited page 81*

Damgaard Jensen, A. and Chatterji, S. (1996). State of the art report on micro-cracking and lifetime of concrete - Part 1. *Materials and Structures*, 29(2):3–8. *Cited page 38*

Dang, Y., Qian, J., Qu, Y., Zhang, L., Wang, Z., Qiao, D., and Jia, X. (2013). Curing cement concrete by using shrinkage reducing admixture and curing compound. *Construction and Building Materials*, 48:992–997 Contents. *Cited pages 123 and 124*

Derjaguin, B. V. and Churaev, N. V. (1978). On the question of determining the concept of disjoining pressure and its role in the equilibrium and flow of thin films. *Journal of Colloid And Interface Science*, 66(3):389–398. *Cited page 65*

Deshpande, R., Hua, D.-W., Smith, D. M., and Brinker, C. J. (1992). Pore Structure Evolution in Silica Gel during Aging/Drying. III. Effects of Surface Tension. *Journal of Non-Crystalline Solids*, 144(1992):32–44. *Cited page 129*

Di Bella, C., Wyrzykowski, M., and Lura, P. (2017). Evaluation of the ultimate drying shrinkage of cement-based mortars with poroelastic models. *Materials and Structures/Materiaux et Constructions*, 50(1):1–13. *Cited pages 251, 252, and 283*

Diamond, S. (2000). Mercury porosimetry: an inappropriate method for the measurement of pore size distributions in cement-based material. *Cement and Concrete Research*, 30(10):1517–1525. *Cited page 50*

Doerr, S. H., Shakesby, R. A., and Walsh, R. P. (2000). Soil water repellency: Its causes, characteristics and hydro-geomorphological significance. *Earth Science Reviews*, 51(1-4):33–65. *Cited page 129*

Duchesne, J. and Bérubé, M. A. (1994). Evaluation of the validity of the pore solution expression method from hardened cement pastes and mortars. *Cement and Concrete Research*, 24(3):456–462. *Cited pages 190 and 198*

Eberhardt, A. B. (2010). *On the mechanisms of shrinkage reducing admixtures in self consolidating mortars and concretes.* PhD thesis. *Cited pages 24, 38, 39, 76, 78, 80, 145, 187, 188, 201, 203, 257, and 299*

Eberhardt, A. B. and Kaufmann, J. (2006). Development of shrinkage reduced self compacting concrete. In Malhotra, V. M., editor, *International Conference on Recent Advances in Concrete Technology*, pages 13–30, Montreal. *Cited page 76*

Espinoza, D. N., Vandamme, M., Dangla, P., Pereira, J. M., and Vidal-Gilbert, S. (2013). A transverse isotropic model for microporous solids: Application to coal matrix adsorption and swelling. *Journal of Geophysical Research: Solid Earth*, 118(12):6113–6123. *Cited page 256*

Feldman, R. F. and Beaudoin, J. J. (1991). Pretreatment of hardened hydrated cement pastes for mercury intrusion measurements. *Cement and Concrete Research*, 21(2-3):297–308. *Cited page 49*

Feldman, R. F. and Sereda, P. J. (1968). A Model of Hydrated Portland Cement Paste as Deduced from Sorption Length Change and Mechanical Properties. *Materials and Structures*, 1(6):509–519. *Cited pages 15, 45, 46, 60, and 67*

Ferraris, C. F. and Wittmann, F. H. (1987). Shrinkage mechanisms of hardened cement paste. *Cement and Concrete Research*, 17:453–464.
Cited page 66

Flatt, R. J., Roussel, N., and Cheeseman, C. R. (2012). Concrete: An eco material that needs to be improved. *Journal of the European Ceramic Society*, 32(11):2787–2798. *Cited page 37*

Folliard, K. J. and Berke, N. S. (1997). Properties of high-performance concrete containing shrinkage-reducing admixture. *Cement and Concrete Research*, 27(9):1357–1364. *Cited page 75*

Gajewicz, A. M. (2014). *Characterisation of cement microstructure and pore – water interaction by 1H Nuclear Magnetic Resonance Relaxometry*. PhD thesis, University of Surrey. *Cited pages 27, 234, 235, and 239*

Gajewicz, A. M., Gartner, E., Kang, K., McDonald, P. J., and Yermakou, V. (2016). A1H NMR relaxometry investigation of gel-pore drying shrinkage in cement pastes. *Cement and Concrete Research*, 86:12–19.
Cited page 176

Gallé, C. (2001). Effect of drying on cement-based materials pore structure as identified by mercury intrusion porosimetry - A comparative study between oven-, vacuum-, and freeze-drying. *Cement and Concrete Research*, 31(10):1467–1477. *Cited page 49*

Garci Juenger, M. C. and Jennings, H. M. (2002). Examining the relationship between the microstructure of calcium silicate hydrate and drying shrinkage of cement pastes. *Cement and Concrete Research*, 32(2):289–296. *Cited page 68*

Gartner, E., Maruyama, I., and Chen, J. (2017). A new model for the C-S-H phase formed during the hydration of Portland cements. *Cement and Concrete Research*, 97:95–106. *Cited pages 47, 68, and 78*

Gartner, E., Young, J. F., Damidot, D. a., and Jawed, I. (2001). Hydration of portland cement. In *Structure and performance of cements*, number 2, pages 57–108. *Cited pages 44, 45, and 198*

Gettu, R., Roncero, J., and Martin, M. (2002). Long-term behaviour of concrete incorporating a shrinkage-reducing admixture. *Indian Concrete Journal*, 76(9):586–592. *Cited pages 76 and 81*

Ghabezloo, S. (2010). Association of macroscopic laboratory testing and micromechanics modelling for the evaluation of the poroelastic parameters of a hardened cement paste. *Cement and Concrete Research*, 40(8):1197–1210. *Cited page 253*

Gor, G. Y. and Bernstein, N. (2016). Revisiting Bangham's law of adsorption-induced deformation: Changes of surface energy and surface stress. *Physical Chemistry Chemical Physics*, 18(14):9788–9798. *Cited page 254*

Goto, T., Sato, T., Sakai, K., and Ii, M. (1985). Cement shrinkage reducing agent and cement composition. *Cited pages 38 and 75*

Grasley, Z. C. and Leung, C. K. (2011). Desiccation shrinkage of cementitious materials as an aging, poroviscoelastic response. *Cement and Concrete Research*, 41(1):77–89. *Cited page 74*

Hagymassy, J., Brunauer, S., and Mikhail, R. S. (1969). Pore structure analysis by water vapor adsorption. *Journal of Colloid and Interface Science*, 29(3):485–491. *Cited page 57*

Hansen, W. (1987). Drying Shrinkage Mechanisms in Portland Cement Paste. *Journal of the American Ceramics Societey*, 70(5):323–328. *Cited pages 64, 65, 66, 91, and 255*

Harkins, W. D. and Jura, G. (1944). Surfaces of Solids. XIII. A Vapor Adsorption Method for the Determination of the Area of a Solid without the Assumption of a Molecular Area, and the Areas Occupied by Nitrogen and Other Molecules on the Surface of a Solid. *Journal of the American Chemical Society*, 66(8):1366–1373. *Cited pages 57, 140, and 213*

Helmuth, R. A. and Turk, D. M. (1967). The Reversible and Irreversible Drying Shrinkage of Hardened Portland Cement and Tricalcium Silicate Paste. *Portland Cement Association Journal Research and Development Laboratories*, 9(2):8–21. *Cited pages 16, 67, 68, and 257*

Hewlett, P. (2003). *Lea's chemistry of cement and concrete.* *Cited page 37*

Hol, S. and Spiers, C. J. (2012). Competition between adsorption-induced swelling and elastic compression of coal at CO_2 pressures up to 100 MPa. *Journal of the Mechanics and Physics of Solids*, 60(11):1862–1882. *Cited pages 29 and 256*

Holt, E. and Leivo, M. (2000). Methods of reducing early-age shrinkage. *International RILEM Workshop on Shrinkage of Concrete, Shrinkage*, pages 435–447. *Cited page 76*

Holt, E. and Leivo, M. (2004). Cracking risks associated with early age shrinkage. *Cement and Concrete Composites*, 26(5):521–530. *Cited page 76*

Jawed, I. and Skalny, J. (1978). Alkalies in cement: A review. *Cement and Concrete Research*, 8(1):37–51. *Cited page 143*

Jennings, H. M. (2000). Model for the microstructure of calcium silicate hydrate in cement paste. *Cement and Concrete Research*, 30(1):101–116. *Cited pages 15, 46, 47, and 169*

Jennings, H. M. (2004). Colloid model of C-S-H and implications to the problem of creep and shrinkage. *Materials and Structures*, 37(1):59–70. *Cited page 67*

Jennings, H. M. (2008). Refinements to colloid model of C-S-H in cement: CM-II. *Cement and Concrete Research*, 38(3):275–289. *Cited pages 15, 46, 47, 54, 67, 155, and 179*

Jennings, H. M., Kumar, A., and Sant, G. (2015). Quantitative discrimination of the nano-pore-structure of cement paste during drying: New

insights from water sorption isotherms. *Cement and Concrete Research*, 76:27–36. *Cited page 176*

Juenger, M. and Jennings, H. M. (2001). Effects of highly alkalinity on cement pastes. *ACI Materials Journal*, 98(3):251–255. *Cited pages 143 and 155*

Knapen, E., Cizer, O., Van Balen, K., and Van Gemert, D. (2009). Effect of free water removal from early-age hydrated cement pastes on thermal analysis. *Construction and Building Materials*, 23(11):3431–3438. *Cited page 151*

Konecny, L. and Naqvi, S. (1993). The effect of different drying techniques on the pore size distribution of blended cement mortars. *Cement and Concrete Research*, 23(5):1223–1228. *Cited page 49*

Kovler, K. and Zhutovsky, S. (2006). Overview and Future Trends of Shrinkage Research. *Materials and Structures*, 39(9):827–847. *Cited pages 39, 61, and 63*

Kowalczyk, P., Ciach, A., and Neimark, A. V. (2008). Adsorption-induced deformation of microporous carbons: Pore size distribution effect. *Langmuir*, 24(13):6603–6608. *Cited page 256*

Lide, D. R. (2003). CRC Handbook of Chemistry and Physics. *eBook*, page 3485. *Cited pages 35 and 88*

Lippens, B. C., Linsen, B. G., and Boer de, J. H. (1964). Studies on Pore Systems in Catalysts VIII. The Adsorption of Krypton and Nitrogen on Graphitized Carbon. *Journal of Catalysis*, 3:32–37. *Cited page 57*

Litvan, G. G. (1976). Variability of the nitrogen surface area of hydrated cement paste. *Cement and Concrete Research*, 6(1):139–143. *Cited page 59*

Litvan, G. G. and Myers, R. E. (1983). Surface area of cement paste conditioned at various relative humidities. *Cement and Concrete Research*, 13(1):49–60. *Cited page 180*

Mackenzie, J. K. (1950). The elastic constants of a material containing spherical coated holes. In *Proc. Phys. Soc*, volume 63, pages 223–246.
Cited page 72

Maltese, C., Pistolesi, C., Lolli, A., Bravo, A., Cerulli, T., and Salvioni, D. (2005). Combined Effect of Expansive and Shrinkage Reducing Admixtures to Obtain Stable and Durable Mortars. *Cement and Concrete Research*, 35(12):2244–2251.
Cited pages 39, 76, 79, 80, and 81

Mantellato, S., Palacios, M., and Flatt, R. J. (2015). Reliable specific surface area measurements on anhydrous cements. *Cement and Concrete Research*, 67:286–291.
Cited page 49

Mantellato, S., Palacios, M., and Flatt, R. J. (2016). Impact of sample preparation on the specific surface area of synthetic ettringite. *Cement and Concrete Research*, 86:20–28.
Cited page 146

Maruyama, I. (2010). Origin of Drying Shrinkage of Hardened Cement Paste : Hydration Pressure. *Journal of Advanced Concrete Technology*, 8(2):187–200.
Cited pages 40, 66, 68, and 74

Maruyama, I., Beppu, K., Kurihara, R., and Furuta, A. (2016). Action Mechanisms of Shrinkage Reducing Admixture in Hardened Cement Paste. *Journal of Advanced Concrete Technology*, 14(6):311–323.
Cited pages 16, 78, 80, 81, and 111

Maruyama, I., Gartner, E., Beppu, K., and Kurihara, R. (2018a). Role of alcohol-ethylene oxide polymers on the reduction of shrinkage of cement paste. *Cement and Concrete Research*, 111(May):157–168.
Cited pages 16, 77, 78, and 79

Maruyama, I., Nishioka, Y., Igarashi, G., and Matsui, K. (2014). Microstructural and bulk property changes in hardened cement paste during the first drying process. *Cement and Concrete Research*, 58:20–34.
Cited pages 39, 121, 124, 180, and 314

333

Maruyama, I., Rymeš, J., Vandamme, M., and Coasne, B. (2018b). Cavitation of water in hardened cement paste under short-term desorption measurements. *Materials and Structures*. *Cited page 54*

Maruyama, I., Sakamoto, N., Matsui, K., and Igarashi, G. (2017). Microstructural changes in white Portland cement paste under the first drying process evaluated by WAXS, SAXS, and USAXS. *Cement and Concrete Research*, 91:24–32. *Cited pages 124 and 181*

Mehta, P. K. and Monteiro, P. J. M. (2001). *Concrete: microstructure, properties, and materials*. new york, 2 edition. *Cited pages 37, 44, and 69*

Mikhail, R. S., Copeland, L. E., and Brunauer, S. (1964). Pore structures and surface Areas of hardened Portland Cement Pastes By Nitrogen Adsorption. *Canadian journal of chemisrty*, 42:426–438. *Cited page 59*

Mikhail, R. S. and Selim, S. (1966). Adsorption of organic vapors in relation to the pore structure of hardened Portland cement pastes. *Highway Research Board Special Report*, pages 123–134. *Cited pages 16, 55, and 61*

Mitchell, L. D. and Margeson, J. C. (2006). The effects of solvents on C-S-H as determined by thermal analysis. *Journal of Thermal Analysis and Calorimetry*, 86(3):591–594. *Cited page 151*

Mora-Ruacho, J., Gettu, R., and Aguado, A. (2009). Influence of shrinkage-reducing admixtures on the reduction of plastic shrinkage cracking in concrete. *Cement and Concrete Research*, 39(3):141–146. *Cited page 76*

Moudilou, E., Bellotto, M., Defosse, C., Serclerat, I., Baillif, P., and Touray, J. C. (2002). A dynamic leaching method for the assessment of trace metals released from hydraulic binders. *Waste Management*, 22(2):153–157. *Cited page 191*

Muller, A. C. A. (2014). *Characterization of porosity & C–S–H in cement pastes by 1H NMR*. PhD thesis, Ecole Polytechnique Federale De Lausanne. *Cited pages 49 and 139*

Multon, J., Bizot, H., and Martin, G. (1991). Mesure de l'eau absorbée dans les aliments. In et Documentation, T., editor, *Technique d'analyse et de contrôle dans les industries agro-alimentaires*, chapter Chapitre 1. Lavoisier, Paris. *Cited page 92*

Nair, H., Ozyildirim, C., and Sprinkel, M. M. (2016). Reducing Cracks in Concrete Bridge Decks Using Shrinkage Reducing Admixture. Technical Report 434. *Cited page 38*

Odler, I. (2003). The BET-specific surface area of hydrated Portland cement and related materials. *Cement and Concrete Research*, 33(12):2049–2056. *Cited pages 60 and 61*

Odler, I., Hagymassy, J., Bodor, E. E., Yudenfreund, M., and Brunauer, S. (1972). Hardened Portland cement pastes of low porosity IV. Surface area and pore structure. *Cement and Concrete Research*, 2(5):577–589. *Cited page 60*

Oliveira, M. J., Ribeiro, A. B., and Branco, F. G. (2014). Combined effect of expansive and shrinkage reducing admixtures to control autogenous shrinkage in self-compacting concrete. *Construction and Building Materials*, 52:267–275. *Cited page 76*

Parikh, N. M. (1958). Effect of Atmosphere on Surface Tension of Glass. *Journal of the American Ceramic Society*, 41(1):18–22. *Cited page 253*

Parrott, L. J., Hansen, W., and Berger, R. (1980). Effect of first drying upon the pore structure of hydrated alite paste. *Cement and Concrete Research*, 10(5):647–655. *Cited pages 39 and 180*

Pearson, D. and Allen, A. J. (1985). A study of ultrafine porosity in hydrated cements using small angle neutron scattering. *Journal of Materials Science*, 20(1):303–315. *Cited page 182*

Pease, B. J. (2005). *The Role of Shrinkage Reducing Admixtures on Shrinkage, Stress Development, and Cracking*. M.s.c.e, Purdue University. *Cited pages 76 and 201*

Pinson, M. B., Masoero, E., Bonnaud, P. A., Manzano, H., Ji, Q., Yip, S., Thomas, J. J., Bazant, M. Z., Van Vliet, K. J., and Jennings, H. M. (2015). Hysteresis from multiscale porosity: Modeling water sorption and shrinkage in cement paste. *Physical Review Applied*, 3(6):1–17. *Cited pages 27, 236, and 237*

Pinson, M. B., Zhou, T., Jennings, H. M., and Bazant, M. Z. (2018). Inferring pore connectivity from sorption hysteresis in multiscale porous media. *Journal of Colloid and Interface Science*, 532(July 2015):118–127. *Cited page 54*

Pour-ghaz, M., Spragg, R., Weiss, J., and Lafayette, W. (2010). Moisture Profiles and Diffusion Coefficients in Mortars Containing Shrinkage reducting admixtures. In *International RILEM Conference on Use of Superabsorbent Polymers and Other New Additives in Concrete*, number August. *Cited pages 39 and 82*

Powers, T. C. (1958). Structure and Physical Properties of Hardened Portland Cement Paste. *Journal of the American Ceramic Society*, 41(1):1–6. *Cited pages 15 and 45*

Powers, T. C. (1962). A hypothesis on carbonation shrinkage. *J Res Dev Labs Portland Cement Ass*, 4(2):40–45. *Cited page 63*

Prakash, S. S., Sankaran, C. J., Hurd, A. J., and Rao, S. M. (1995). Silica aerogel films prepared at ambient pressure by using surface derivatization to induce reversible drying shrinkage. *Cited page 129*

Rajabipour, F., Sant, G., and Weiss, J. (2008). Interactions between shrinkage reducing admixtures (SRA) and cement paste ' s pore solution. *Cement and Concrete Research*, 38:606–615. *Cited pages 77, 80, 112, 145, 198, and 201*

Rasmussen, C. J., Vishnyakov, A., Thommes, M., Smarsly, B. M., Kleitz, F., and Neimark, A. V. (2010). Cavitation in metastable liquid nitrogen confined to nanoscale pores. *Langmuir*, 26(12):10147–10157. *Cited page 53*

Ravikovitch, P. I. and Neimark, A. V. (2002). Experimental confirmation of different mechanisms of evaporation from ink-bottle type pores: Equilibrium, pore blocking, and cavitation. *Langmuir*, 18(25):9830–9837.
Cited pages 15 and 53

Ribeiro, A. B., Gonçalves, A., and Carrajola, A. (2006). Effect of shrinkage reducing admixtures on the pore structure properties of mortars. *Materials and Structures/Materiaux et Constructions*, 39(286):179–187.
Cited pages 81 and 82

Rongbing, B. and Jian, S. (2005). Synthesis and evaluation of shrinkage-reducing admixture for cementitious materials. *Cement and Concrete Research*, 35(3):445–448.
Cited page 76

Roosz, C., Gaboreau, S., Grangeon, S., Prêt, D., Montouillout, V., Maubec, N., Ory, S., Blanc, P., Vieillard, P., and Henocq, P. (2016). Distribution of Water in Synthetic Calcium Silicate Hydrates. *Langmuir*, 32(27):6794–6805.
Cited pages 27, 234, 235, 236, 237, and 239

Rougelot, T., Skoczylas, F., and Burlion, N. (2009). Water desorption and shrinkage in mortars and cement pastes: Experimental study and poromechanical model. *Cement and Concrete Research*, 39(1):36–44.
Cited pages 71 and 73

Rouquerol, F., Luciani, L., Llewellyn, P., Denoyel, R., and Rouquerol, J. (2003). Texture des matériaux pulvérulents ou poreux. *Techniques de l'Ingénieur*.
Cited page 58

Saliba, J., Rozière, E., Grondin, F., and Loukili, A. (2011). Influence of shrinkage-reducing admixtures on plastic and long-term shrinkage. *Cement and Concrete Composites*, 33(2):209–217.
Cited pages 39, 75, 76, 80, and 81

Samouh, H., Rozière, E., and Loukili, A. (2018). Shape effect on drying behavior of cement-based materials: Mechanisms and numerical analysis. *Cement and Concrete Research*, 110(April):42–51.
Cited page 92

Sant, G., Eberhardt, A., Bentz, D. P., and Weiss, J. (2010). Influence of Shrinkage-Reducing Admixtures on Moisture Absorption in Cementitious Materials at Early Ages. *Journal of Materials in Civil Engineering*, 22(March):277–287. *Cited pages 39 and 82*

Sant, G., Lothenbach, B., Juilland, P., Saout, G. L., Weiss, J., and Scrivener, K. (2011). The origin of early age expansions induced in cementitious materials containing shrinkage reducing admixtures. *Cement and Concrete Research*, 41(3):218–229. *Cited page 76*

Sant, G., Rajabipour, F., Lura, P., and Weiss, J. (2006). Examining Time-Zero and Early Age Expansion in Pastes Containing Shrinkage Reducing Admixtures (Sra ' S). *Engineering*, (September). *Cited pages 39, 76, and 80*

Sarawade, P. B., Kim, J. K., Hilonga, A., and Kim, H. T. (2010). Preparation of hydrophobic mesoporous silica powder with a high specific surface area by surface modification of a wet-gel slurry and spray-drying. *Powder Technology*, 197(3):288–294. *Cited page 129*

Sasano, H., Maruyama, I., Nakamura, A., and Yamamoto, Y. (2018). Impact of Drying on Structural Performance of Reinforced Concrete Shear Walls. *Journal of Advanced Concrete Technology*, 16:210–232. *Cited page 38*

Scherer, G. W. (1986). Dilatation of Porous Glass. *Journal of the American Ceramic Society*, 69(6):473–480. *Cited pages 29, 65, 253, and 254*

Scherer, G. W. (2015). Drying, Shrinkage, and Cracking of Cementitious Materials. *Transport in Porous Media*, 110(2):311–331. *Cited page 39*

Scrivener, K. L., Snellings, R., and Lothenbach, B. (2016). *A Practical Guide to Microstructural Analysis of Cementitious Materials.* CRC Press, Taylor & Francis Group. *Cited pages 135 and 138*

Shah, S. P., Karaguler, M. E., and Sarigaphuti, M. (1992). Effect of shrinkage reducing admixtures on restrained shrinkage cracking of concrete. *ACI Materials Journal*, 89(3):289–295. *Cited pages 39, 75, 76, 80, and 81*

338

Sharp, J. H., Gartner, E., and Macphee, D. E. (2010). Novel cement systems (sustainability). In *Session 2 of the Fred Glasser Cement Science Symposium. Advances in Cement Research*, pages 195–202. *Cited page 37*

Shokri, N., Lehmann, P., and Or, D. (2008). Effects of hydrophobic layers on evaporation from porous media. *Geophysical Research Letters*, 35(19):1–4. *Cited page 129*

Sika (2012). Sika ® Control-60. Technical Report 2. *Cited page 38*

Snoeck, D., Velasco, L. F., Mignon, A., Van Vlierberghe, S., Dubruel, P., Lodewyckx, P., and De Belie, N. (2014). The influence of different drying techniques on the water sorption properties of cement-based materials. *Cement and Concrete Research*, 64(October):54–62. *Cited page 49*

Swenson, E. G. and Sereda, P. J. (1968). Mechanism of the carbonatation shrinkage of lime and hydrated cement. *Journal of Applied Chemistry*, 18(4):111–117. *Cited page 63*

Taylor, H. F. W. (1990). *Cement Chemistry.* *Cited pages 62, 145, and 151*

Tazawa, E.-i. and Miyazawa, S. (1995). Influence of cement and admixture on autogenous shrinkage of cement paste. *Cement and Concrete Research*, 25(2):281–287. *Cited page 76*

Tennis, P. D. and Jennings, H. M. (2000). Model for two types of calcium silicate hydrate in the microstructure of Portland cement pastes. *Cement and Concrete Research*, 30(6):855–863. *Cited page 46*

Termkhajornkit, P., Barbarulo, R., and Chanvillard, G. (2015). Microstructurally-designed cement pastes: A mimic strategy to determine the relationships between microstructure and properties at any hydration degree. *Cement and Concrete Research*, 71:66–77. *Cited page 136*

Thommes, M., Smarsly, B., Groenewolt, M., Ravikovitch, P. I., and Neimark, A. V. (2006). Adsorption hysteresis of nitrogen and argon in pore networks and characterization of novel micro- and mesoporous silicas. *Langmuir*, 22(2):756–764. *Cited page 53*

Van Damme, H. (2018). Concrete material science: Past, present, and future innovations. *Cement and Concrete Research*, (January):0–1. *Cited page 38*

Vandamme, M., Brochard, L., Lecampion, B., and Coussy, O. (2010). Adsorption and strain: The CO2-induced swelling of coal. *Journal of the Mechanics and Physics of Solids*, 58(10):1489–1505. *Cited page 254*

Vlahinić, I., Jennings, H. M., and Thomas, J. J. (2009). A constitutive model for drying of a partially saturated porous material. *Mechanics of Materials*, 41(3):319–328. *Cited pages 71, 73, 74, and 252*

Washburn, E. W. (1921). The dynamics of capillary flow. *Physical Review*, 17(3):273–283. *Cited page 50*

Weiss, J., Lura, P., Rajabipour, F., and Sant, G. (2008). Performance of Shrinkage-Reducing Admixtures at Different Humidities and at Early Ages. *ACI Materials Journal*, 105(5). *Cited pages 76 and 111*

Whim, B. P. and Johnson, P. G. (2012). *Directory of solvents*. Springer Science & Business Media. *Cited pages 35 and 88*

Winslow, D. N. and Diamond, S. (1974). Specific Surface of Hardened Portland Cement Paste as Determined by Small-Angle X-Ray Scattering. *Journal of the American Ceramic Society*, 57(5):193–197. *Cited page 182*

Wittmann, F. H. (1973). Interaction of Hardened Cement Paste and Water. *Journal of the American Ceramic Society*, 56(8):409–415. *Cited page 66*

Wu, M., Johannesson, B., and Geiker, M. (2014). Application of water vapor sorption measurements for porosity characterization of hardened cement pastes. *Construction and Building Materials*, 66:621–633. *Cited page 57*

Ye, H. and Radlińska, A. (2016). A Review and Comparative Study of Existing Shrinkage Prediction Models for Portland and Non-Portland Cementitious Materials. *Advances in Materials Science and Engineering*, 2016:10–14. *Cited page 39*

Ye, H. and Radlińska, A. (2017). Effect of Alkalis on Cementitious Materials: Understanding the Relationship between Composition, Structure, and Volume Change Mechanism. *Journal of Advanced Concrete Technology*, 15(4):165–177. *Cited page 40*

Ye, H., Radlińska, A., and Neves, J. (2017). Drying and carbonation shrinkage of cement paste containing alkalis. *Materials and Structures/Materiaux et Constructions*, 50(2). *Cited page 69*

Zhang, J. and Scherer, G. W. (2011). Comparison of methods for arresting hydration of cement. *Cement and Concrete Research*, 41(10):1024–1036. *Cited pages 15, 48, 49, and 151*

Zhang, Z. and Scherer, G. W. (2017). Supercritical drying of cementitious materials. *Cement and Concrete Research*, 99(May):137–154. *Cited page 48*

Zhou, X., Zhong, L., and Xu, Y. (2008). Surface modification of silica aerogels with trimethylchlorosilane in the ambient pressure drying. *Inorganic Materials*, 44(9):976–979. *Cited page 129*